Examining structural and functional connectivity change in animal models of cerebrovascular disease

Gerard Ronald Hall, Bsc, Msc

Thesis submitted to The University of Nottingham for the degree of Doctor of Philosophy

March 2021

Abstract

Cerebrovascular disease is a leading cause of death worldwide and is associated with a wide range of cognitive impairments. Using graph theory on structural and functional connectomes generated through MRI is emerging as a promising tool in revealing network change in patients with VCI. Though animal models can offer mechanistic insight into disease progression, there is a lack of tools for processing preclinical MRI data when compared to the clinics, especially for advanced analysis investigating network changes. Therefore, the primary aim of this thesis was to develop an MRI processing pipeline from gold standard human approaches that is adapted for non-human preclinical models. During development, the pipeline was used to process and analyse data from a bilateral carotid artery stenosis (BCAS) mouse model widely used to emulate vascular cognitive impairment (VCI). The subsequent second aim therefore was to identify potential neuroimaging biomarkers of VCI. The most notable changes in the BCAS brains were reductions in functional connectivity in the sensorimotor network, and an increase in structural connectivity in the visual association area at the chronic timepoints. The pipeline was further validated in a contrasting sheep model of cerebrovascular disease, known as the middle cerebral artery occlusion (MCAO) model of stroke. Post-stroke timepoints displayed more specific and focused damage in the white matter on the injured side, this was coupled with a widespread increase in functional connectivity. Our approach represents a significant contribution to preclinical connectivity literature, and future work could help refine and update the tools chosen in the pipeline.

Acknowledgements

Without the help of others none of this would be possible, I always struggle to say thanks and could write another thesis on all the people who have helped me. I would like to begin thanking Jewel, when I first arrived you helped in every way to make me feel welcome and since then have become a close friend and a top lad. Although you may support Liverpool FC, you're still top lad and one day I hope to show you the pool myself. You also helped form the group of friends in E27/28 that the majority of my happy memories were formed from, thank you. In addition to everyone in E27/28, Matt, I hope I made you feel as welcome as Jewel did for me, in turn you became almost a younger brother to me, from your travelling stories to your quick wit that kept me laughing, thank you. To Nash, where do I begin... your continuation and dedication to having a tea break close before I have a break down due to stress (usually resulting from coding or writing) is legendary. From deep conversations, to arguing about why I am always correct, you definitely made the PhD process far more exciting and enjoyable.

I am also very lucky to have a dedicated and inspirational supervisor to learn from, Thank you Dr. Tracy Farr for not only giving me this opportunity, but also going the extra mile every single time. From making sure I was settled in when I first came to Nottingham, to spotting and checking over job applications. In particular, the ability to manage a lab with so many multi-disciplinary topics in science has been highly inspirational to me. The fearlessness to learn unfamiliar topics from completely different fields (for example learning programming), whilst still being comfortably advanced in your own field, is an attitude I hope to adopt in my future projects. My secondary supervisor Dr. Stam Sotiropoulos, even five-minute meetings with you would save weeks' worth of work, without your in-depth technical knowledge in MRI, I wouldn't have been able to complete this PhD for sure. It was an honour to learn from someone as advanced in their field as you. I would also like to thank Dr Rebecca Trueman, although you were not an official supervisor, sitting in meetings and presentations, and always giving sound advice has been super helpful, thank you.

To my family, Mum watching you battle with illness was hard but seeing your unwavering ability to never give up and always keep strong and smiling, was truly inspirational. During tough days, I would only have to think about your courage, and I could continue. Dad, you

have never stopped protecting and caring for us all. You used to feel guilty when you couldn't help when I had problems with homework, but you taught me more than I can imagine. Though you might not have the grades, you're one of the wisest people I know, your advice and help throughout this PhD has been crucial. To my little sister Megan, you almost rung me every single night to check on me. Your gossip about school and stories on our many sports like ballet always make me smile, I hope to see you all again soon.

Lastly, I would like to thank my partner, Robyn. You have always been supportive, from helping me practice my presentation for my PhD application, to moving to Nottingham with me without question. I could go on forever, you have always looked after me. Whilst I'm probably tougher to deal with than most of the kids in your nursery, you always keep me on track and somehow are psychic to when I'm feeling down and always help me get back up. Although I may be second behind our cat Leo, I'll happily accept my position since he is such a good boy. I hope one day now I can do the same to you and help you achieve your career goals too.

Abbreviations

28D	28-Day
3m	3 Month
6D	6-day
6m	6 Month
ACA	Anterior Cingulate Area (possible change)
ACAr	Anterior Cerebral Artery
Acb	Nucleus Accumbens
AD	Axial Diffusivity
AIDAmri	Atlas-based Imaging Data Analysis of structural and functional mouse brain MRI
AMCA	Allen Mouse Brain Connectivity Atlas
ANOVA	Analysis of Variance
ANTs	Advanced Normalization Tools
ATS	Atherosclerosis
AUC	Area Under the Curve
AUD	Auditory Area
AZ	Alzheimer's disease
Aβ	Amyloid Beta
BBB	Blood Brain Barrier
BBR	Boundary Based Registration
BCAS	Bilateral Carotid Artery Stenosis
BCCAO	Bilateral Common Carotid Artery Occlusion
BET	Brain Extraction Tool
BOLD	Blood Oxygen Level Dependant
C	Cingulate
CAA	Cerebral Amyloid Angiopathy
Cau	Caudate
CBF	Cerebral Blood Flow
cc	Corpus Callosum
Ce	Cerebellum
CEnt	Caudomedial Entorhinal Cortex

Cg1	Cingulate Cortex 1
Cg2	Cingulate Cortex 2
CPu	Caudate Putamen
CS	Cortical Subplate
CSF	Cerebrospinal Fluid
Cst	Corticospinal Tract
CT	Computed Tomography
CTRL	Control
CTX	Cortex
CUPR	Cuprizone
DICOM	Digital Imaging and Communications in Medicine
DLB	Dementia with Lewy Bodies
DMN	Default Mode Network
dMRI	Diffusion weighted MRI
DTI	Diffusion Tensor Imaging
ECT	Ectorhinal Cortex
EPI	Echo-Planar Imaging
FA	Fractional Anisotropy
FAST	FMRIB's Automated Segmentation Tool
FDR	False Discovery Rate
ff	Fornix
FIX	FMRIB's ICA-based Xnoiseifier
FLAIR	Fluid Attenuated Inversion Recovery
FLIRT	FMRIB's Linear Image Registration Tool
fMRI	Functional Magnetic Resonance Imaging
FMRIB	Functional Magnetic Resonance Imaging of the Brain
FNIRT	FMRIB's Non-linear Image Registration Tool
FrA	Frontal Association Cortex
FSL	FMRIB Software Library
FWE	Family Wise Error Rate
FWHM	Full Width Half Maximum
GE	Gradient Echo
GIFT	Group ICA of fMRI Toolbox
GLM	General Linear Model

GP	Globus Pallidus
HPF	Hippocampal Formation
Hps	Hippocampus
Hy	Hypothalamus
Hz	Hertz
Ic	Internal Capsule
ICA	Independent Component Analysis
ICAr	Internal Cerebral Artery
In	Insular
LADIS	The Leukoaraiosis And DISability
M	Motor
M1	Pre and Post-Cruciate Gyrus
MCA	Middle Cerebral Artery
MCAO	Middle Cerebral Artery Occlusion
MCAr	Middle Cerebral Artery
MD	Mean Diffusivity
Md	Midbrain
Mdb	Midbrain Behavioural
Mdm	Midbrain Motor
Mds	Midbrain Superior Colliculus
Me	Medulla
MEnt	Medial Entorhinal Cortex
MICO	Multiplicative Intrinsic Component Optimization
MOC	Medial Orbital Cortex
MP-RAGE	Magnetization Prepared Rapid Acquisition Gradient Echo
MRI	Magnetic Resonance Imaging
NICE	National Institute for Health and Care Excellence
NIFTI	Neuroimaging Informatics Technology Initiative
NINDS-AIREN	National Institute of Neurological Disorders and Stroke Association Internationale pour la Recherche et l'Enseignement en Neurosciences’
NQA	Normalised Quantitative Anisotropy
OB	Orbitofrontal Gyrus
Occ	Occipital lobe
Olf	Olfactory

Or	Orbital frontal Gyrus
Pa	Pallidum
PaS	Parasubiculum
Pf	Prefrontal Cortex
PH	Parahippocampal Gyrus
Pl	Prelimbic
Po	Pons
POpt	Pre-Optic Nuclei
Ppva	Posterior Parietal Visual Association
Pr	Perirhinal
Pre	Pre-Stroke
PrL	Prelimbic Cortex
PSD	Post Stroke Dementia
PTLp	Periaqueductal Grey
Pu	Putamen
QSDR	q Space Diffeomorphic Reconstruction
rad/s	Radians Per Second
rBET	Rodent Brain Extraction Tool
RD	Radial Diffusivity
Rh	Rhinal Cortex
rHps	Retrohippocampal
rHy	Right Hypothalamus
RK4	Runge-Kutta fourth order
ROI	Region of Interest
RS	Retrosplenial
rs-fMRI	resting state functional Magnetic Resonance Imaging
RSCg	Retrosplenial Granular Cortex
RSD	Retrosplenial Dysgranular Cortex
RSN	Resting-State Network
RUN DMC	Radboud University Nijmegen Diffusion Tensor and Magnetic Resonance Cohort
S	Sensory
S1	Anterior Sygmoideus Gyrus
S2	Sylvian Gyrus

SC	Superior Colliculus
SCANS	St George's Cognition and Neuroimaging in Stroke Study
Sep	Septal Nuclei
SG	Sylvian Gyrus
SNR	Signal-to-Noise ratio
SPACE	Sampling Perfection with Application-optimized Contrasts using Different Flip Angle Evolution
SPM8	Statistical Parametric Mapping 8
SS	Suprasylvius Gyrus
SSp	Primary Somatosensory Area
STP	Serial Two-Photon
STR	Striatum
TBSS	Tract base spatial statistics
TeA	Temporal Association
Th	Thalamus
TL	Temporal Lobe
V	Visual
V1	Primary Visual Area
VA	Visual Association
VCI	Vascular Cognitive Impairment
VD	Vascular Dementia
VICCCS	Vascular Impairment of Cognition Classification Consensus Study
VIS	Visual Area
WM	White Matter
WMH	White Matter Hyperintensities

List of figures

Chapter 1 – General Introduction

Figure 1. 1. Venn diagram of the inclusion criteria of VCI within Alzheimer's and vascular dementia....2
Figure 1. 2. Chart displaying the major sub-types of VCI based of the VICCCS....3
Figure 1. 3. Cartoon illustrations of: (a) Differing types of vascular pathology associated with VCI. (b) Vascular coverage of a single brain hemisphere....4
Figure 1. 4. Transverse MRI images of VCI patents: (a) FLAIR image displaying WM hyperintensities and lacunar infarction. (b) T_2* weighted image displaying different microbleeds....5
Figure 1. 5. Effects of WM damage on diffusivity distributions measured with dMRI....7
Figure 1. 6. Process of building a structural connectome....9
Figure 1. 7. Circular graph illustrating small worldness....10
Figure 1. 8. Different RSNs in the human....13
Figure 1. 9. Simplified diagram of the BCAS procedure in the mouse....15
Figure 1. 10. Reconstruction of the corpus callosum in the mouse using tractography....18
Figure 1. 11. Structural connectome differences in a similar study between a demyelinating condition group and control mice....20
Figure 1. 12. Illustration of the mouse DMN using rs-fMRI....22
Figure 1. 13. Hierarchy matrix of the mouse RSNs identified using the ICA technique....23
Figure 1. 14. Overview of the different types of prominent RSNs in the mouse....24
Figure 1. 15. Differences in connectivity between structural viral tracing and functional rs-fMRI in the mouse model....25

Chapter 2 – Methods

Figure 2. 1. T_2 weighted structural template generated from the mouse study sample....28
Figure 2. 2. Differences between bias and non-bias corrected image....29
Figure 2. 3. Flow chart of the rs-fMRI pipeline....30
Figure 2. 4. Study T_2 weighted template registered to AMCA template....32
Figure 2. 5. Skull stripped T_2 weighted study template....33

Figure 2. 6. Illustration of the slice-by-slice time course from a rs-fMRI dataset.....34
Figure 2. 7. Skull stripped rs-fMRI dataset.....34
Figure 2. 8. Fsleyes view of ICA classification of noise and signal.....36
Figure 2. 9. Subsequent output of the dual-regression analysis.....38
Figure 2. 10. Hierarchical connectivity matrix output of RSN components 39
Figure 2. 11. The AMCA template rendered into a 3D projection for glass brain figures 40
Figure 2. 12. Flow chart illustration of the dMRI pipeline.....42
Figure 2. 13. Subject average template of the dMRI B0 images 44
Figure 2. 14. dMRI scalar map output of an individual subject 45
Figure 2. 15. Average FA skeleton of all subjects.....46
Figure 2. 16. Voxelwise comparisons of FA values between groups.....47
Figure 2. 17. Structural connectivity output matrix generated from the dMRI data of a individual subject.....48

Chapter 3 – Development of the pipeline

Figure 3. 1. Illustration of displaying the primary diffusion directions in order to check for correct anatomical directions.....51
Figure 3. 2. Comparison of the detected bias field output from bias correction tools supplied in FSL and ANTs packages 53
Figure 3. 3. Comparison of registration tools between ANTs and FSL toolboxes.....55
Figure 3. 4. Flow chart of the indirect registration steps of the pipeline 57
Figure 3. 5. Contrast of between the output of indirect and direct registration methods.....58
Figure 3. 6. Differences in the brain mask used for skull stripping between the pipeline and methods widely used in humans.....59
Figure 3. 7. Differences in the brain mask output between the pipeline and rodent specific skull stripping methods.....60
Figure 3. 8. Illustration explaining the shearing phenonium with EPI images during linear registration 61
Figure 3. 9. Comparison of the shearing phenonium when registering to the subject template in contrast to an individual subject 62
Figure 3. 10. Differences in the motion report between a subject with high motion compared to relatively low motion during scanning 65

Figure 3. 11. Spatial maps displaying signal, noise or a mixture from three different components of a single subject rs-fMRI dataset.....67
Figure 3. 12. Differences in timeseries between components classified as signal, noise or a combination of both from single subject ICA 69
Figure 3. 13. Differences in the power spectra between component classified as signal, noise or a combination of both from single subject ICA 71
Figure 3. 14. The range of group level components primarily driven by neural signal when the ICA dimensionality is set to 15 75
Figure 3. 15. The range of group level components primarily driven by neural signal when the ICA dimensionality is set to 30 76
Figure 3. 16. The range of group level components primarily driven by neural signal when MELODIC determines the optimal ICA dimensionality.....77
Figure 3. 17. Detecting artifact driven group level components through viewing the power spectra in relation to other components.....78
Figure 3. 18. Effects of aggressive against unaggressive removal of group based noise components on the overall power spectra average 80
Figure 3. 19. Differences in the hierarchical clustering of group components between partial and full correlation.....82
Figure 3. 20. Illustration of the process of rendering MRI images into a 3-D space for glass brains 83
Figure 3. 21. Group matrices displaying the effect of a global absolute threshold on network density.....85
Figure 3. 22. Group matrices displaying the effect of a proportional threshold on network density.....87
Figure 3. 23. Graph showing the small-worldness value peak between differing thresholds .88
Figure 3. 24. Registration comparisons between using individual B0 or T_2 weighted images to each corresponding template 90
Figure 3. 25. Flow chart displaying the adjustments to certain scripts in the TBSS process ..91
Figure 3. 26. Coronal display of the primary diffusion directions.....92
Figure 3. 27. Structural connectivity matrix of corresponding connectivity histogram of an individual subject.....94
Figure 3. 28. Structural connectivity matrix of corresponding connectivity histogram of an individual subject scaled by a factor of $\log_{10}$.....95

Figure 3. 29. Illustration of the differences in mesoscale and macroscale dimensionalities of the AMCA atlas 96
Figure 3. 30. Adaption of specific parent regions to generate the AMCA parent atlas 97

Chapter 4 – Connectivity in the rodent model

Figure 4. 1. Timeline of experimental design 100
Figure 4. 2. WM skeletons for TBSS analysis 103
Figure 4. 3. AMCA atlas and parent atlas used in analysis 104
Figure 4. 4. Graph displaying CBF at the 24hr, 3m and 6m timepoints 105
Figure 4. 5. Variation in group components as a result of different dimensionalities 106
Figure 4. 6. Hierarchy matrix displaying the highly correlated cluster of components 108
Figure 4. 7. Spatial maps of sensorimotor, visual and limbic clusters 109
Figure 4. 8. Spatial maps of recognition, sensory integration and cognition component clusters 109
Figure 4. 9. Sagittal cartoon of the mouse brain, colour coded based on the location of components in the hierarchy matrix, and a 3D glass brain representation of the positive correlations between the signal components 111
Figure 4. 10. Functional connectomes between sham and hypoperfused subjects displayed as glass brains and circle graphs 113
Figure 4. 11. Differences in correlational strength of functional components between sham and hypoperfused groups 114
Figure 4. 12. Coronal displays of functional components chosen for dual-regression analysis 115
Figure 4. 13. Representative functional connectivity strengths for group components in sham and hypoperfused groups 116
Figure 4. 14. Spatial map differences of a rodent default mode network analogue between sham and hypoperfused groups 117
Figure 4. 15. Graph displaying measures of global efficiency in functional connectivity for sham and hypoperfusion groups 118
Figure 4. 16. Line graph displaying local efficiency measures of functional group components between sham and hypoperfused groups 119
Figure 4. 17. Graphs displaying both measures of segregation (transitivity and modularity) for the functional networks between groups 120

Figure 4. 18. Spatial map differences in FA between sham and hypoperfused mice at the 3-month timepoint....121
Figure 4. 19. Spatial map differences in FA between sham and hypoperfused mice at the 6-month timepoint....122
Figure 4. 20. Spatial map differences in FA for 3m and 6m timepoints with corresponding uncorrected and corrected significance values....123
Figure 4. 21. Group based structural connectivity matrices built using the AMCA regions for the 3m timepoint....125
Figure 4. 22. Group based structural connectivity matrices built using the AMCA regions for the 6m timepoint....126
Figure 4. 23. Spatial maps of FA and tractography for the sham and hypoperfusion groups, with each group average structural connectivity matrices built using the parent AMCA regions for both the 3m and 6m timepoints....127
Figure 4. 24. Diagram of integratory graph theory values of structural connectivity (global and local efficiency) for both groups and timepoints....129
Figure 4. 25. Diagram of segregatory graph theory values of structural connectivity (transitivity and modularity) for both groups and timepoints....130

Chapter 5 – Connectivity in the ovine model

Figure 5. 1. WM skeletons used for TBSS analysis....145
Figure 5. 2. Spatial maps and power spectra of components undergoing the epi unwarping stage and components skipping the process....148
Figure 5. 3. Spatial maps of group components: 1, 7, and 11....150
Figure 5. 4. Spatial maps of group components: 13, 20, 22, and 24....151
Figure 5. 5. Hierarchy matric of rs-fMRI components for the pre-stroke timepoint....153
Figure 5. 6. Hierarchy matric of rs-fMRI components for the pre-stroke (lower corner) and 6D (upper corner) timepoint....154
Figure 5. 7. Hierarchy matric of rs-fMRI components for the pre-stroke (lower corner) and 28D (upper corner) timepoint....155
Figure 5. 8. Box plot comparison of the significant edge difference for the correlation between component 22 and 11 at the pre-stroke and 6D post-stroke timepoint....157

Figure 5. 9. Box plot comparison of the significant edge difference for the correlation between component 22 and 13 at the pre-stroke and 6D post-stroke timepoint 158
Figure 5. 10. Box plot comparison of the significant edge difference for the correlation between component 22 and 20 at the pre-stroke and 6D post-stroke timepoint 159
Figure 5. 11. Box plot comparison of the significant edge difference for the correlation between component 24 and 22 at the pre-stroke and 6D post-stroke timepoint 160
Figure 5. 12. Box plot comparison of the significant edge difference for the correlation between component 20 and 11 at the pre-stroke and 28D post-stroke timepoint 161
Figure 5. 13. Line graph measuring global efficiency of functional connectivity matrices for all the timepoints 162
Figure 5. 14. Line graph measuring modularity of functional connectivity matrices for all the timepoints 163
Figure 5. 15. Line graph measuring transitivity of functional connectivity matrices for all the timepoints 164
Figure 5. 16. Line graph measuring the overall averaged local efficiency of functional connectivity matrices for all the timepoints.....165
Figure 5. 17. Line graph displaying the local efficiency measures of all individual signal components for all timepoints 166
Figure 5. 18. TBSS output of spatial map differences in FA values between the pre-stroke and 6D poststroke timepoints 168
Figure 5. 19. TBSS output of spatial map differences in FA values between the pre-stroke and 28D poststroke timepoints 170
Figure 5. 20. TBSS output of spatial map differences in FA values between both post-stroke timepoints at 6D and 28D 172
Figure 5. 21. WM reconstructions of an individual subject dMRI data using deterministic tractography for all timepoints.....174
Figure 5. 22. Average structural connectivity matrix of the pre-stroke timepoint using the modified unilateral ovine atlas.....176
Figure 5. 23. Average structural connectivity matrix of the 6D poststroke timepoint using the modified unilateral ovine atlas.....177

Figure 5. 24. Average structural connectivity matrix of the 28D poststroke timepoint using the modified unilateral ovine atlas.....178
Figure 5. 25. Line graph displaying global efficiency measures of structural connectivity matrices for all timepoints 179
Figure 5. 26. Line graph displaying measures of average overall local efficiency of the structural connectivity matrices for all timepoints 181
Figure 5. 27. Line graph displaying values of local efficiency at all timepoints for specific areas that displayed significant interactional differences for timepoint, anatomical region and hemispheric side.....181
Figure 5. 28. Line graph displaying transitivity measures of structural connectivity matrices for all timepoints.....182
Figure 5. 29. Line graph displaying modularity measures of structural connectivity matrices for all timepoints.....183

Table of Contents

CHAPTER 1. GENERAL INTRODUCTION 1

1.1. VASCULAR COGNITIVE IMPAIRMENT 1
1.1.1. Underlying Pathology 4
1.2. NEUROIMAGING TECHNIQUES 6
1.2.1. Principles of diffusion weighted imaging 6
1.2.2. The use of dMRI to assess VCI 8
1.2.3. Connectomics and graph theory 8
1.2.4. Structural connectivity in VCI 11
1.2.5. Principles of rs-fMRI 12
1.2.6. Functional connectivity in VCI 13
1.3. ANIMAL MODELS OF VCI 14
1.3.1. Bilateral common carotid artery occlusion 14
1.3.2. Bilateral carotid artery stenosis 15
1.4. NEUROIMAGING IN THE ANIMAL MODEL 17
1.5. STRUCTURAL CONNECTIVITY IN THE MOUSE BRAIN 19
1.6. FUNCTIONAL CONNECTIVITY IN THE MOUSE BRAIN 20
1.7. THESIS AIMS 26

CHAPTER 2. GENERAL METHODS 27

2.1. DATA PRE-PROCESSING 27
2.1.1. Data conversion 27
2.1.2. Orientation confirmation 27
2.1.3. Structural template creation 28
2.1.4. Bias correction 29
2.2. RS-FMRI PIPELINE 30
2.2.1. Correcting for image distortion 31
2.2.2. Structural image registration and skull stripping 31
2.2.3. Functional image registration and skull stripping 33
2.2.4. Independent component analysis 35
2.2.4.1. Removing noise at the single subject level 35
2.2.4.2. Group level independent component analysis 37
2.2.4.3. Dual regression 37
2.2.5. Hierarchical network analysis 38
2.2.5.1. Connectivity images 39
2.2.6. Seed based analysis 41
2.2.7. Graph theory 41
2.3. DMRI PIPELINE 42
2.3.1. Correcting for image distortion 43

2.3.2. Skull stripping *43*
2.3.3. Template creation and image registration *43*
2.3.4. Tract based spatial statistics *44*
2.3.5. Probabilistic tractography *48*
2.3.5.1. Graph theory 48

CHAPTER 3. DEVELOPMENT OF THE DATA PROCESSING PIPELINE FOR EVALUATION OF STRUCTURAL AND FUNCTIONAL CONNECTIVITY IN THE MOUSE 49

3.1. INTRODUCTION 49
3.2. RESULTS AND DISCUSSION 50
3.2.1. Data pre-processing *50*
3.2.1.1. Data conversion 50
3.2.1.2. Orientation confirmation 50
3.2.1.3. Bias correction 52
3.2.2. rs-fMRI pipeline *54*
3.2.2.1. Structural image registration and skull stripping 54
3.2.2.2. Functional image registration and skull stripping 61
3.2.2.3. Determining motion 63
3.2.2.4. Removing noise at the single subject level 66
3.2.2.4.1. Spatial mapping 66
3.2.2.4.2. Timeseries 68
3.2.2.4.3. Power spectral density 70
3.2.2.5. Group level independent component analysis 72
3.2.2.6. Hierarchical network analysis 78
3.2.2.7. Connectivity images 83
3.2.2.8. Graph theory 84
3.2.3. dMRI pipeline *89*
3.2.3.1. Template creation and image registration 89
3.2.3.2. Tract based spatial statistics 91
3.2.3.3. Probabilistic tractography 92

CHAPTER 4. STRUCTURAL AND FUNCTIONAL NETWORK CHANGES IN A MOUSE MODEL OF VASCULAR COGNITIVE IMPAIRMENT 98

4.1. INTRODUCTION 98
4.2. METHODS 100
4.2.1. Experimental design *100*
4.2.2. MRI hardware and acquisition *101*
4.2.3. Processing of MRI data *102*
4.2.3.1. CBF 102
4.2.3.2. rs-fMRI 102
4.2.3.3. dMRI 103

4.2.4. Statistical Analysis ... *104*
4.3. RESULTS ... 105
4.3.1. CBF ... *105*
4.3.2. rs-fMRI ... *106*
4.3.2.1. Independent component analysis ... 106
4.3.2.2. Qualitative network differences between groups ... 112
4.3.2.3. Dual Regression ... 115
4.3.2.4. Default mode network ... 117
4.3.2.5. Graph Theory ... 118
4.3.3. dMRI ... *121*
4.3.3.1. TBSS ... 121
4.3.3.2. Tractography ... 124
4.3.3.3. Graph theory ... 128
4.4. DISCUSSION ... 131
4.4.1. Functional connectivity network ... *132*
4.4.2. Functional connectivity differences between sham and hypoperfused mice ... *134*
4.4.3. Structural connectivity differences between sham and hypoperfused mice ... *137*
4.4.4. Conclusions ... *139*

CHAPTER 5. STRUCTURAL AND FUNCTIONAL NETWORK CHANGES IN AN OVINE MODEL OF CEREBROVASCULAR DISEASE. ... 141

5.1. INTRODUCTION ... 141
5.2. METHODS ... 142
5.2.1. Experimental design ... *142*
5.2.2. MRI hardware and acquistion ... *142*
5.2.3. Processing of MRI data ... *143*
5.2.3.1. Data pre-processing ... 143
5.2.3.1.1. Structural template creation ... 143
5.2.3.2. rs-fMRI ... 143
5.2.3.2.1. Independent component analysis ... 143
5.2.3.2.2. Dual regression ... 143
5.2.3.2.3. Hierarchical network analysis ... 143
5.2.3.3. dMRI ... 144
5.2.3.3.1 Tract based spatial statistics ... 144
5.2.3.3.2. Deterministic tractography ... 146
5.2.3.3.3. Probabilistic tractography ... 146
5.2.4. Statistical analysis ... *146*
5.3. RESULTS ... 147
5.3.1. rs-fMRI ... *147*
5.3.1.1. EPI unwarping process ... 147
5.3.1.2. Independent component analysis ... 149
5.3.1.3. Qualitative network comparisons between timepoints ... 152

5.3.1.4. Edge differences between functional matrices 156
5.3.1.5. Dual regression 162
5.3.1.6. Graph theory 162
5.3.2. dMRI 167
5.3.2.1. Tract based spatial statistics 167
5.3.2.2. Tractography 173
5.3.2.2.1. Deterministic tractography 173
5.3.2.2.2. Probabilistic tractography 175
5.3.2.3. Graph theory 179
5.4. DISCUSSION 184

CHAPTER 6. GENERAL DISCUSSION 192

6.1. THESIS OUTCOME 192
6.2. DMRI PIPELINE 193
6.3. RS-FMRI PIPELINE 195
6.4. BOTH DMRI AND RS-FMRI PIPELINES IN COMBINATION 197
6.5. CONCLUSION 199

APPENDIX A. SCRIPTS 200

A.1. PRE-PROCESSING STEPS 200
A.1.1. Data conversion (Br2Nii, Bruker2Nifti, Dcn2niiX) 200
A.1.2. Orientation deletion, change and confirmation (FSL) 200
A.1.3. Structural template creation (ANTs) 201
A.1.4. Bias correction (ANTs) 201
A.1.5. Skull stripping (ANTs & FSL) 201
A.2. RS-FMRI PIPELINE 202
A.2.1. Unwarp EPI data (FSL) 202
A.2.2. rs-fMRI mask creation and skull stripping (ANTs & FSL) 203
A.2.3. Motion, slice timing (FSL) 204
A.2.4. Single subject ICA (FSL) 204
A.2.5. Single subject component cleaning (FSL) 204
A.2.6. rs-fMRI timeseries registration (FSL & ANTs) 205
A.2.7. Smoothing EPI data (FSL) 206
A.2.8. Group level ICA (FSL) 206
A.2.9. Component analysis (FSL) 206
A.3. DMRI PIPELINE 206
A.3.1. EPI unwarping (FSL) 206
A.3.2. Motion and eddy correction (FSL) 207
A.3.3. dMRI mask creation and skull stripping (FSL & ANTs) 207
A.3.4. Remove B0 image and average (FSL) 207
A.3.5. Creating B0 template (ANTs) 208

A.3.6. Tensor fitting and making scalar maps (FSL) *208*
A.3.7. Creating FA template (ANTs) *208*
A.3.8. TBSS scripts (FSL) *208*
A.3.9. Voxelwise analysis of TBSS skeletons (FSL) *209*
A.3.10. Registration of B0 images (ANTs) *209*
A.3.11. Local modelling of diffusion parameters (FSL) *209*
A.3.12. Probabilistic tractography (FSL) *210*

APPENDIX B. OVINE RESTING STATE COMPONENTS 211

B.1. OVINE COMPONENT 1: SENSORY, VISUAL NETWORK 211
B.2. OVINE COMPONENT 7: SENSORY, MEMORY NETWORK 212
B.3. OVINE COMPONENT 11: POTENTIAL DMN 213
B.4. OVINE COMPONENT 13: UNCLEAR FUNCTIONAL ASSOCIATION 214
B.5. OVINE COMPONENT 20: UNCLEAR FUNCTIONAL ASSOCIATION 215
B.6. OVINE COMPONENT 22: UNCLEAR FUNCTIONAL ASSOCIATION 216
B.7. OVINE COMPONENT 24: UNCLEAR FUNCTIONAL ASSOCIATION 217

REFERENCES 218

Chapter 1. General Introduction

1.1. Vascular cognitive impairment

Worldwide, 35.6 million people are currently diagnosed with dementia, and estimations predict this may reach 115 million by 2050 (Wortmann, 2012). Although the pathological spotlight is often on amyloid beta (Aβ) and Alzheimer's disease (Glenner and Wong, 1984; Kang et al., 1987), vascular pathology has long been known to play a role in the development of dementia (Jellinger, 2006; Bowler, 2007). The term vascular cognitive impairment (VCI) (Hachinski and Bowler, 1993) was coined to encompass the broad range of deficits in cognitive function that have a vascular origin. The link between VCI and modifiable vascular risk factors such as hypertension (Dichgans and Zietemann, 2012), diabetes (Mizrahi et al., 2010; Kim et al., 2012), hyperglycemia (Gorelick et al., 2011; Yang et al., 2015), smoking (Rusanen et al., 2011; Batty et al., 2018), obesity and cholesterol (Anstey et al., 2011; Appleton et al., 2017), and diet and physical activity (Dichgans and Zietemann, 2012) is well established. There are also a variety of non-modifiable risk factors associated with increased risk of developing VCI; the strongest being advanced age (O'Brien and Thomas, 2015) followed by level of education (Elbaz et al., 2013; Zieren et al., 2013), socioeconomic standing, and prior intellectual capability or cognitive reserve (Iadecola, 2013).

The term VCI broadly covers mild cognitive impairment through to severe forms of vascular dementia (Dichgans and Leys, 2017). It can include other dementia sub-types such as Alzheimer's disease and it is now recognized that a combination of sub-types, termed mixed dementia, is likely the most common (Toledo et al., 2013; Montine et al., 2014) (Figure 1.1).

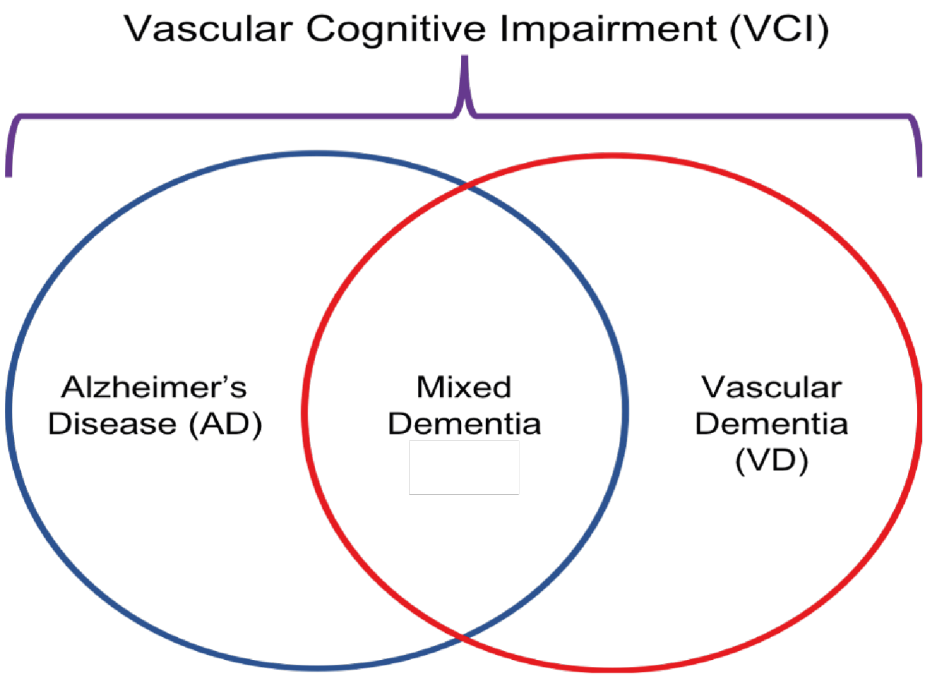


Figure 1. 1. A venn diagram illustrating that VCI can include Alzheimer's disease and vascular dementia, or a combination of the two, recognised as mixed dementia. Modified from (Rosenberg et al., 2016).

Because VCI covers a spectrum of disorders, it lacks a standard collective opinion regarding classification of sub-types. Supported by a multinational group of clinicians and researchers, the Vascular Impairment of Cognition Classification Consensus Study (VICCCS) was designed to obtain a broader agreement regarding classification of VCI sub-types (Skrobot et al., 2017; Skrobot et al., 2018). Overall, the VICCCS suggested use of the terms mild and major to estimate VCI severity and proposed four subtypes of major VCI: post-stroke dementia, multi-infarct dementia, subcortical ischemic vascular dementia, and mixed dementia (Skrobot et al., 2017) (Figure 1.2).

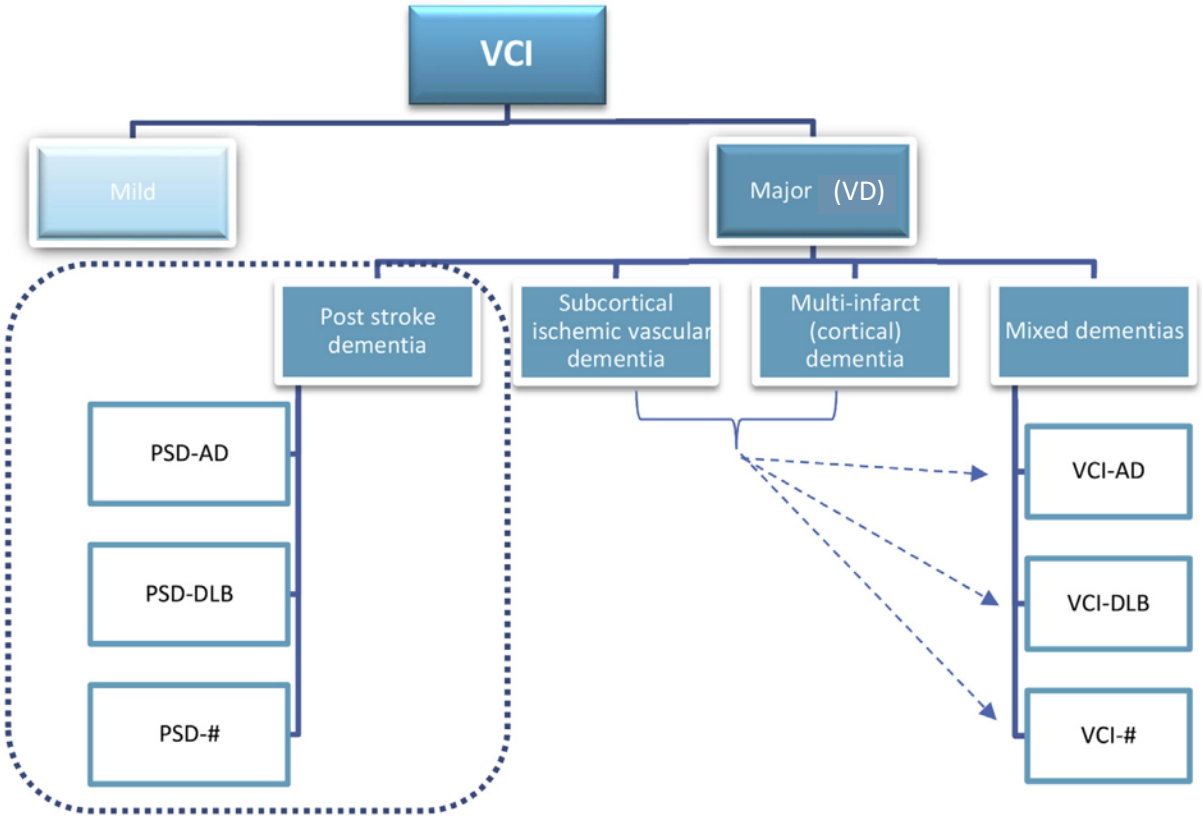


Figure 1. 2. The Vascular Impairment of Cognition Classification Consensus Study (VICCCS) suggested the major sub-types of vascular cognitive impairment include post stroke dementia, subcortical ischemic vascular dementia, multi-infarct (cortical) dementia, and mixed dementias (VD - vascular dementia, PSD - post stroke dementia, AD - Alzheimer's disease, DLB - dementia with Lewy bodies). Modified from (Skrobot et al., 2018).

VCI generally involves a progressive decline in cognitive domains and is often characterized by executive dysfunction and prolonged processing speeds (Smith, 2016). Given the variety of subtypes and comorbidities, a specific VCI diagnosis is not straightforward. In the UK, the National Institute for Health and Care Excellence (NICE) guidelines recommend referral to specialist services so that a wide range of cognitive domains can be examined, including; executive function, attention, learning, processing speed, language, visual constructional perceptual ability, social cognition, spatial orientation and specific motor control (Sachdev et al., 2014).

1.1.1. Underlying Pathology

Vascular risk factors that produce VCI are associated with cerebrovascular pathologies (Alves et al., 2017; Kalaria, 2017); an overview is depicted in (Figure 1.3a).

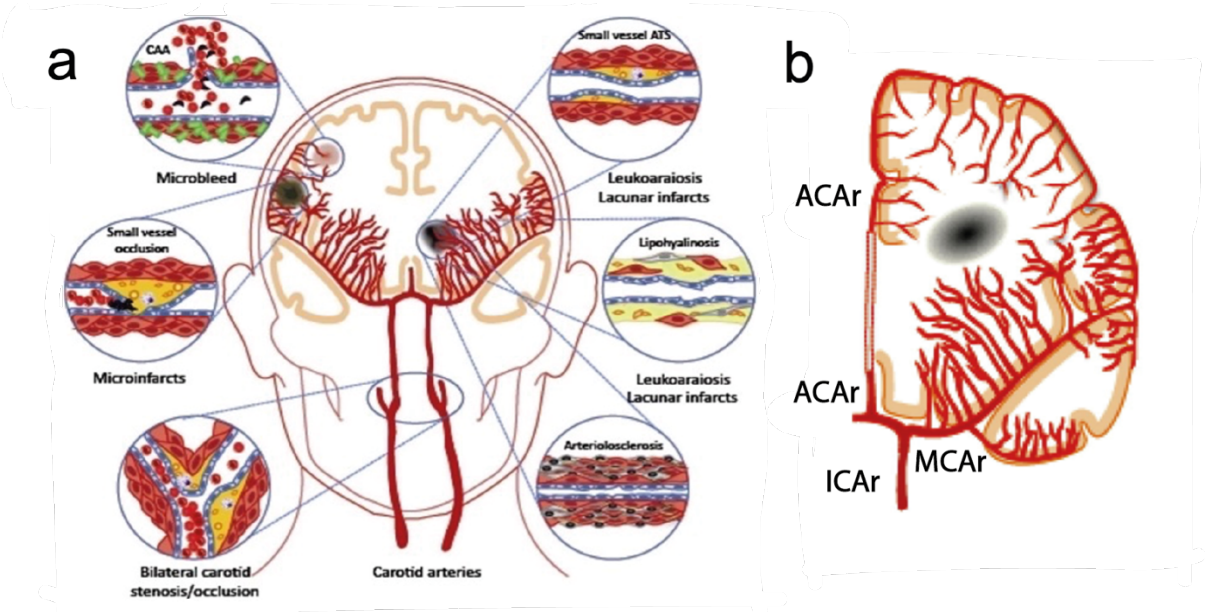


Figure 1. 3. (a) The range of vascular pathologies associated with VCI. (b) Vascular coverage of a hemisphere with the shaded area illustrating hypoxia in deep subcortical white matter. (CAA - cerebral amyloid angiopathy, ATS - atherosclerosis, ACAr - anterior cerebral artery, ICAr - internal carotid artery, MCAr - middle cerebral artery). Image from (Iadecola, 2013).

Cerebral hypoperfusion, as a result of carotid artery stenosis and/or atherosclerosis, is a strong contributor to VCI (Hachinski et al., 2006; Alsop et al., 2010; Chao et al., 2010; Kalaria et al., 2012; Zheng et al., 2013; Duncombe et al., 2017). At rest, the brain is responsible for approximately 20% of overall energy consumption, therefore, it is not unexpected that a range of problems can manifest without a well-regulated continuous supply of blood (Camandola and Mattson, 2017). These manifestations may include occlusion and/or hardening of blood vessels, accumulation of hyaline and fibrin (lipohyalinosis), and leakage. White matter (WM) appears to be particularly susceptible to hypoperfusion (Deary et al., 2003; Bucur et al., 2008; Bastin et al., 2009) due to the outside-in vascular arrangement of the brain (Figure 1.3b). The major cerebral vessels branch to supply the high energy demands of cortical grey matter, but the subcortical WM is perfused by penetrating arterioles that lack

anastomotic branches and overlapping vascular territories (Harris and Attwell, 2012; Iadecola, 2013).

Some of the pathologies depicted in Figure 1.3 are associated with radiological features. Indeed, the use of neuroimaging techniques such as magnetic resonance imaging (MRI) and computed tomography (CT) help exclude certain cerebral pathologies and diagnose VCI. Some of the more prominent radiological features include: microbleeds, lobar and deep haemorrhages, multiple lacunar infarcts, enlarged perivascular spaces, cerebral amyloid angiopathy, and WM hyperintensities or leukoaraiosis (Figure 1.4).

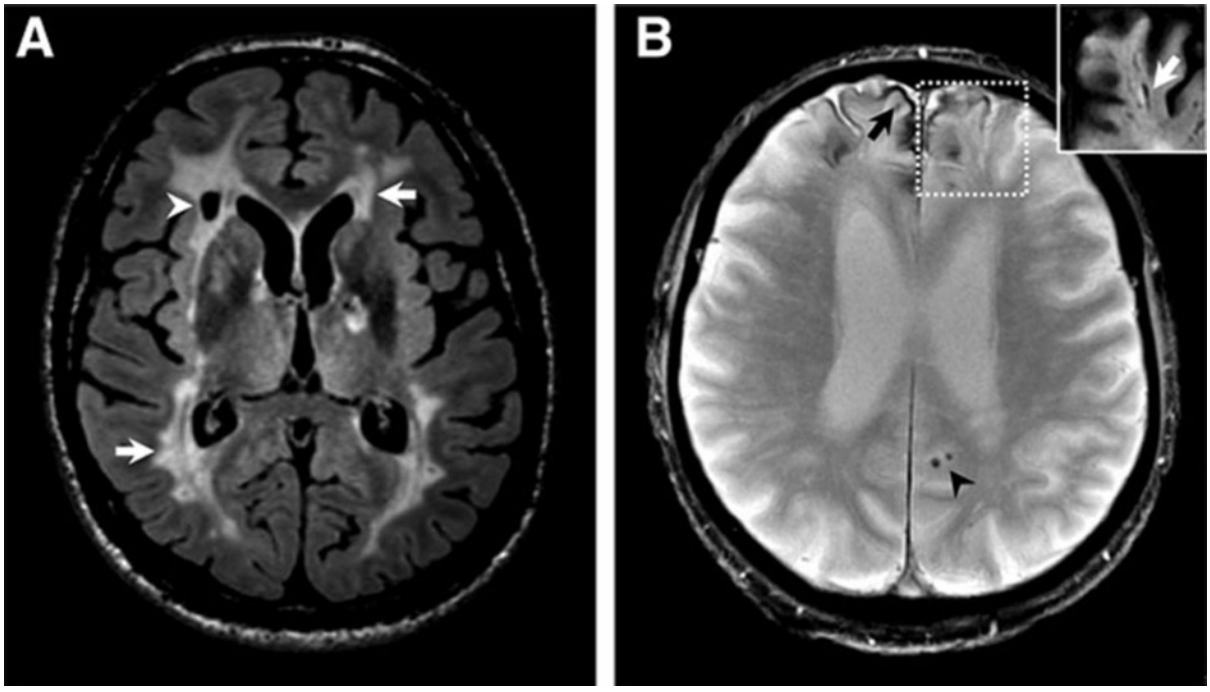


Figure 1. 4. MRI indicators that support a VCI diagnosis. (**A)** Transverse FLuid Attenuated Inversion Recovery (FLAIR) image from a 64-year-old male. The white arrows indicate WM hyperintensities, while the anterior white arrowhead shows a lacunar infarction. (B) A T_2*-weighted gradient echo image from a 52-year-old female patient. The posterior black arrowhead indicates microbleeds while the black arrow indicates accumulation of blood in the sulcus. The white arrow (inset) indicates enlargement of perivascular space. Figure taken from (Dichgans and Leys, 2017).

Generally, no threshold is required for the number of radiological features that constitute a VCI diagnosis (Schneider et al., 2007). However, the National Institute of Neurological Disorders and Stroke Association Internationale pour la Recherche et l'Enseignement en Neurosciences' (NINDS-AIREN) criteria requires cognitive deficits to be coupled with the presence of radiological features. Furthermore, the recently updated VICCCS-2 has recommended MRI as the gold-standard neuroimaging method for VCI diagnosis, including categorising radiological features based on size, amount and anatomical location (Skrobot et al., 2018). In particular, WM hyperintensities are now considered to be a very important neuroimaging correlate of VCI (Debette et al., 2010). The Leukoaraiosis And DISability (LADIS) study was a multi-centre European initiative that concluded severe WM change was a strong predictor of developing dementia across a 3 year follow up (Poggesi et al., 2011).

1.2. Neuroimaging Techniques

1.2.1. Principles of diffusion weighted imaging

Whilst anatomical T_1 and T_2 weighted MRI can identify WM changes and track their progression, it has been suggested that other techniques may offer more information about WM microstructure. Diffusion weighted MRI (dMRI) has long been used to depict features of WM. Grounded on the principles of diffusivity of water molecules, dMRI attempts to model the distribution of diffusion. Compared to other major tissue types, WM generally results in a unique directional dependent diffusion, a principle called anisotropy. In contrast, other cerebral tissues like grey matter and cerebral spinal fluid tend to have a more isotropic (directionally independent) shape of diffusion (Alexander et al., 2007).

The distribution of diffusion can be modelled via a 3D tensor (i.e. 3 x 3 matrix) and is the method used in diffusion tensor imaging (DTI). These tensor models furthermore can be quantified and displayed as scalar parameter maps (Khanna et al., 2015). Commonly reported scalar variables are fractional anisotropy (FA) and mean diffusivity (MD). FA is a unitless value that displays an average gross estimate of the strength of anisotropy in each voxel (0.1 corresponds to minimal whereas 1 is maximal anisotropy). As WM is more anisotropic, it tends to have higher FA values than grey matter. FA is commonly used as an indicator of WM integrity; decreases are associated with tissue deterioration (Floel et al., 2009; Liu et al., 2010; Takeuchi et al., 2010). MD quantifies the diffusion rate of a given voxel; higher values

indicate greater free diffusion and are suggestive of damaged tissue and loss of structure (Soares et al., 2013).

The strength of the principal diffusion direction, and its perpendicular counterpart, are known as axial and radial diffusivity (AD and RD), respectively. In general, decreases in AD have been correlated with axonal damage, while increases in radial diffusivity have been linked with demyelination (Song et al., 2002; Song et al., 2005; Sun et al., 2008; Sun et al., 2011; Khanna et al., 2015). Figure 1.5 highlights the relationship between DTI scalar parameters and potential tissue pathology.

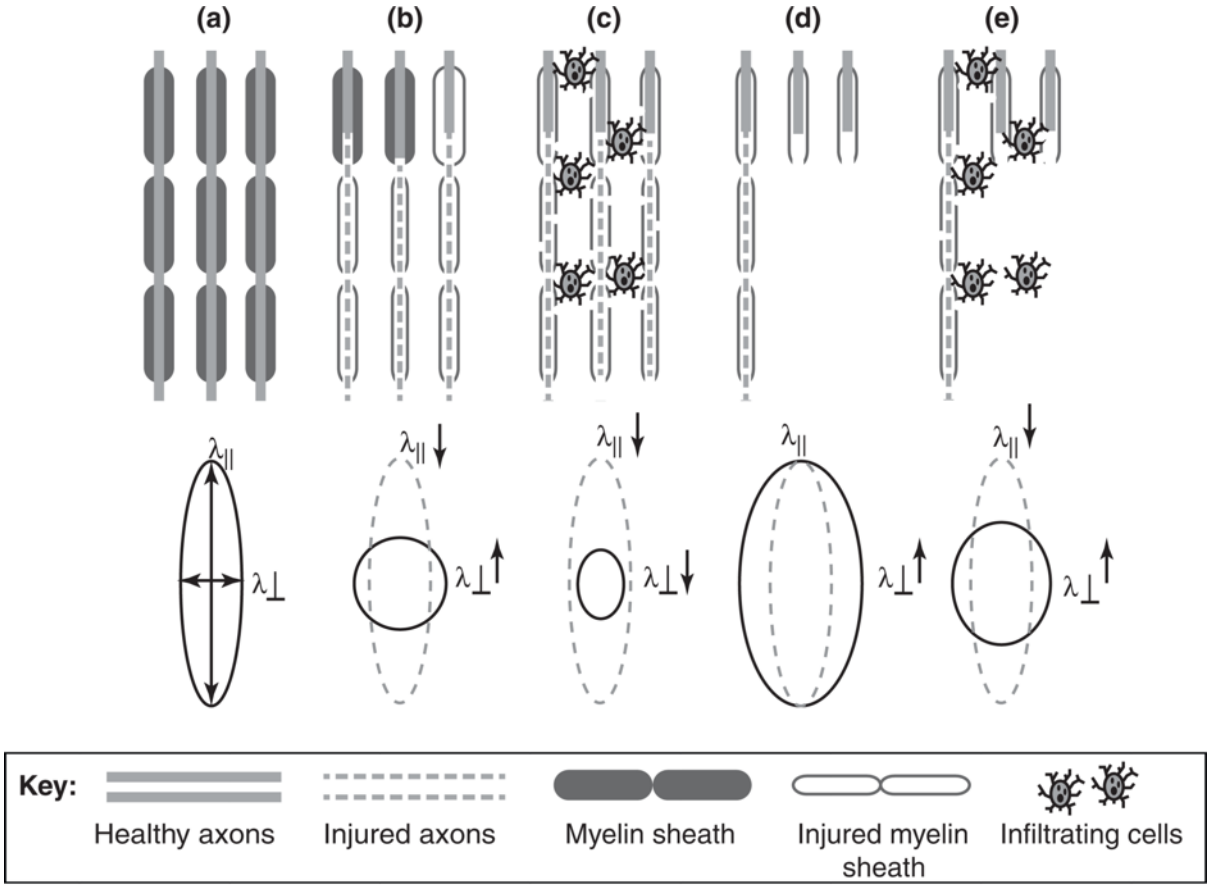


Figure 1. 5. A simplified diagram displaying a range of WM damage and the corresponding effects on diffusivity measures (parallel (λ‖) and perpendicular (λ⊥) eigenvalues represents AD and RD, respectively). (a) Healthy WM with anisotropic diffusion (high AD and low RD). (b) Axonal damage associated with decreased AD and increased RD. (c) Similar damage as in (b), but with infiltrating inflammatory cells, consequentially reducing AD and RD. (d) More severe WM damage with an increase in RD. (e) More severe WM damage with infiltrating inflammatory cells results in an increase in RD. Taken from (Zhang et al., 2012).

It is important to note however, there are numerous factors that can influence these scalar parameters (Jones et al., 2013), these influential factors include; axonal count and direction, packing density, loss of myelin, infiltration of inflammatory cells, oedema, and partial volume effects (Wang et al., 2011; Jones et al., 2013). Though caution should be maintained when making subsequent implications, scalar parameters can still provide useful information about tissue microstructure.

1.2.2. The use of dMRI to assess VCI

Clinical studies incorporating dMRI to investigate VCI generally report decreases in FA coupled with an increase in MD in the WM (Chen et al., 2006; Zhou et al., 2011; Biesbroek et al., 2017; Chen et al., 2018). This pattern is suggestive of an enlargement of extracellular space due to demyelination and axonal damage. Both FA and MD changes strongly correlate with poorer performance in cognitive tests (Chen et al., 2018). Interestingly, decreases in FA and increases in MD have also been observed in WM that appears normal in T_1 and T_2 weighted MRI images (Zhou et al., 2011). A follow up analysis from a subset of centres with dMRI capability in the LADIS study revealed that diffusion changes in normal appearing WM were better predictors of cognitive decline than the degree of WM hyperintensity or lesion load (Jokinen et al., 2013).

The diffusion tensor model can also create 3D reconstructions of prominent WM tracts. Known as tractography, this technique can help visualize specific tract integrity and identify regions for further analysis. Patients diagnosed with VCI exhibit decreases in FA in the superior longitudinal fasciculus and this predicted executive function scores (Biesbroek et al., 2017). Another study reported that FA and MD of 18 different WM tracts were related to cognitive domains associated with VCI (Biesbroek et al., 2017).

1.2.3. Connectomics and graph theory

Structural connectivity analysis from dMRI data has been proposed as a way to examine the integrity of the entire brain network. The structural connectome refers to a map of all the brain connections (Bullmore and Sporns, 2009; Fornito et al., 2016; Sotiropoulos and Zalesky, 2017). The nodes and edges are the foundation of any connectomics network. A node usually represents an area/location in the brain, and this can range from the microscopic

(e.g. individual neuron) to the macroscopic level (e.g. brain regions) (Figure 1.6), whilst an edge refers to the potential connection between two respective nodes. This can also be represented at the microscopic level via neuronal tracing, or at the macroscopic level via WM tractography generated through dMRI. The adjacency matrix is a common format used to visually represent structural connectomes. Nodes are defined as a columns/rows along each axis, and edges display a colour that corresponds to the strength of the FA value between the nodes (Figure 1.6).

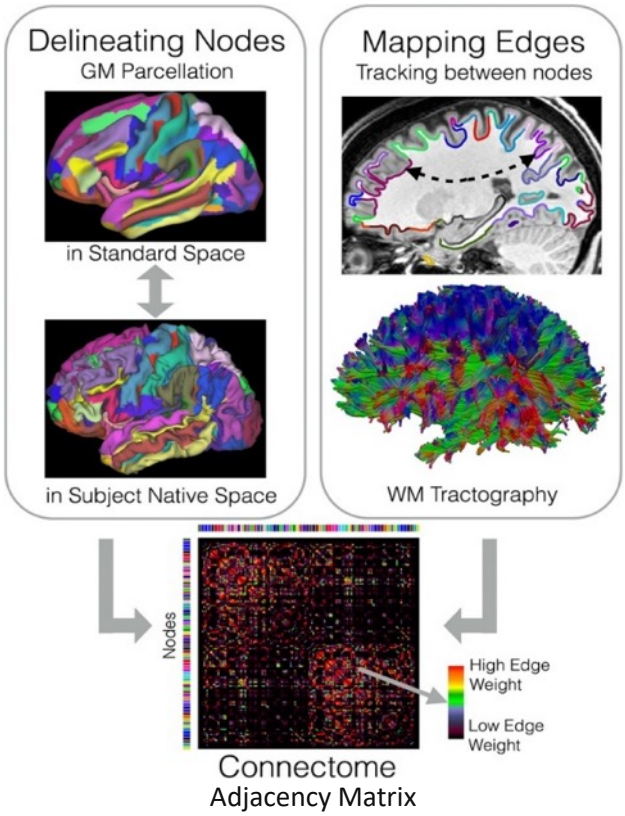


Figure 1. 6. Example process of constructing a structural connectome in the human. The brain is parcellated into regions (nodes) and data can be transformed between a standard and individual subject space (left column). Edges quantify the connection between nodes (right column) based on tractography. This information is used to construct an adjacency matrix in which the weight of the edges is colour coded. Figure taken from (Sotiropoulos and Zalesky, 2017).

Adjacency matrices can also be probed to provide quantifiable measures of overall network characteristics. Widely referred to as graph theory, this type of analysis uses mathematics to estimate network features that are thought to be biologically meaningful and allow for straightforward comparisons between populations. Global efficiency (average shortest path

length between all pairs of nodes) is used as a surrogate of the overall ability of the brain to integrate information (Rubinov and Sporns, 2010). Global efficiency is a measure of information integration. Graph theory can also provide measures that assess how well a network can run specific types of processing based on the strength of connections between smaller groups of structures; these are measures of segregation (Rubinov and Sporns, 2010).

Brain networks tend to possess a characteristic termed small worldness. First modelled by Watts and Strogatz (1998), brain networks generally exhibit short/low path lengths between nodes (global efficiency), coupled with a high clustering of connections between particular groups of nodes (clustering coefficient) (Figure 1.7). Whilst in comparison, a regular lattice-like network exhibits a similar high clustering but is generally less efficient at passing information between distant nodes, as a result of only possessing connections to neighbouring nodes (high path length). Interestingly, when re-wiring a small proportion of paths in a regular lattice-like network to create direct shortcuts to distant nodes, reductions in the average path length can be achieved, whilst in contrast still preserving the high clustering of the network. This efficient connectivity (low path length) coupled with highly specialised grouping (high clustering) is an iconic pattern of small worldness. However, it is possible that the re-wiring of too many paths can reduce this high clustering representative of specialised network grouping, and consequently produce a more random network shape, possessing a short average path length and low clustering.

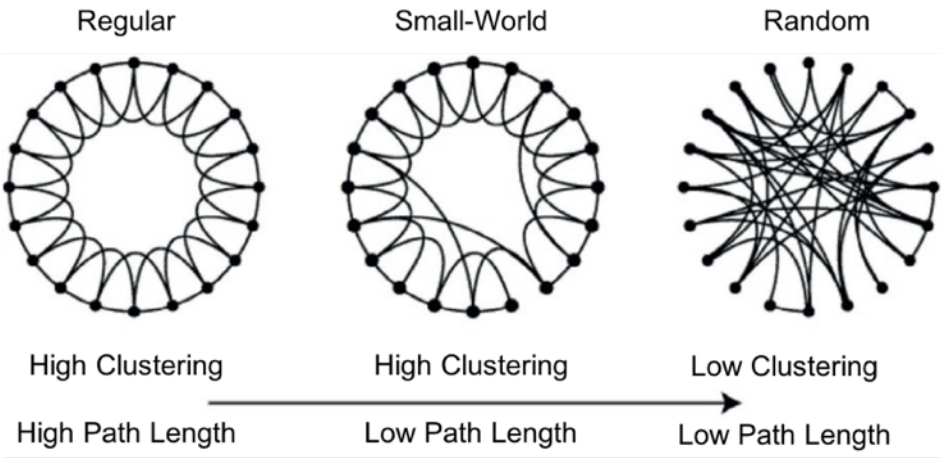


Figure 1. 7. Circular graph illustrating the Watts and Strogatz model for small worldness. In the regular network (left), each node (black dot) is connected via an edge (line) to neighbouring nodes. This results in a high clustering coefficient and a high average path length. The random network (right) exhibits a short average path length, but low clustering specialised processing. Small world-ness (middle) preserves the high clustering present in the regular network as well as the short average path length in the random network. Figure modified from (Watts and Strogatz, 1998).

1.2.4. Structural connectivity in VCI

Using graph theory on reconstructed dMRI structural connectomes is emerging as a promising tool to reveal brain network disconnection in patients with VCI. The St George's Cognition and Neuroimaging in Stroke Study (SCANS), reported widespread decreases in global efficiency in patients with evidence of WM change (n=115) when compared to healthy controls (n=50) (Lawrence et al., 2014): there was also a decrease in local efficiency (Lawrence et al., 2014). While global efficiency measures the shortest average inverse path length between all nodes, local efficiency is calculated specifically for each node and also represents a measure of segregation (Rubinov and Sporns, 2010). Both global and local efficiency were good predictors of poor processing speed and executive function in SCANS (Lawrence et al., 2014). Analysis of a sub-set of patients that underwent a 5-year follow up revealed that the degree of decline in global efficiency was highly associated with conversion to dementia (Lawrence et al., 2018). The Radboud University Nijmegen Diffusion Tensor and Magnetic Resonance Cohort (RUN DMC) followed patients with WM hyperintensities for 6 years. Reduced global efficiency was observed at baseline in patients that went on to develop dementia (Tuladhar et al., 2016).

Similar reductions in global and local efficiency from dMRI have been reported for patients with cerebral amyloid angiopathy (Reijmer et al., 2015), whereas standard small worldness was present in healthy controls. Interestingly, another study in patients with WM change revealed increases in measures of network segregation, specifically clustering coefficient, transitivity and modularity (Kim et al., 2015). Transitivity measures the prevalence of triangles (three inter-connected nodes) normalised across all nodes (Watts and Strogatz, 1998). Whilst modularity is calculated by dividing the network into sub-networks that maximize the number of within sub-network links and minimize the number of between sub-network connections.

Structural connectivity represents the physical arrangement of WM. However, graph theory can also be applied to connectivity data obtained from other MRI methods like functional MRI (fMRI). This can give further insight into how pathology affects structure in conjunction with the function of a network.

1.2.5. Principles of rs-fMRI

Spontaneous fluctuations in the blood oxygen level dependant (BOLD) signal (the oxygenation status of haemoglobin) is considered an indirect measure of neuronal activity (Logothetis, 2008). It is assumed that distinctive anatomical brain regions that exhibit synchronous BOLD activity during rest (resting state or rs-fMRI) are likely connected. A seed-based approach defines a particular region of the brain and looks for additional voxels that exhibit the same patterns of signal fluctuation. Alternatively, independent component analysis (ICA) has been described as a data driven approach that identifies statistically independent temporal and spatial patterns of BOLD signal variation from the data (Chen et al., 2020).

Patterns of predominantly low frequency BOLD (<0.1Hz) synchronicity were first reported in 1995 (Biswal et al., 1995). These activity patterns are robust and evident throughout a range of neuroimaging techniques, such as electroencephalography (Laufs, 2010; Pizoli et al., 2011), magnetoencephalography (Allen et al., 2011), and positron emission tomography (Shulman et al., 1997). These patterns of activity are broadly termed resting-state networks (RSN) (Figure 1.8) and are rapidly evolving into a major field of investigation.

The default mode network (DMN) is the most widely studied RSN. It is composed of the ventral and dorsal medial prefrontal cortices (associated with emotional state and self-referential judgment, respectively) (Gusnard et al., 2001; Simpson et al., 2001), the posterior precuneus, and the lateral parietal cortex (affiliated with memory recollection) (Shannon et al., 2013). Homologous versions of the DMN are evident across a wide range of mammalian species (Buzsaki et al., 2013).

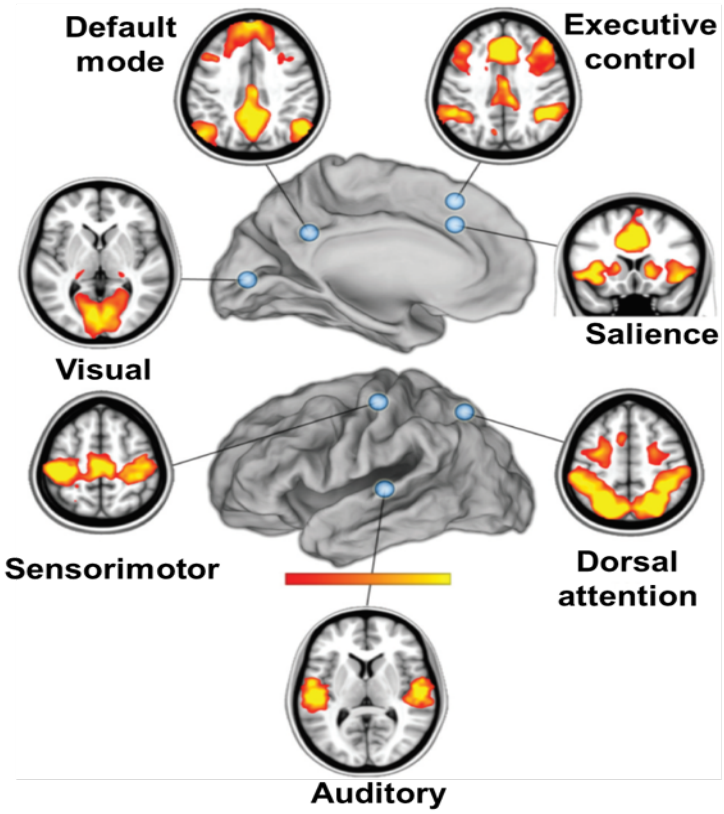


Figure 1. 8. Illustrates the different RSNs in humans derived from BOLD imaging. The centre images are 3D representations of the midline and lateral cortical surface of the brain. Figure from (Raichle, 2015).

1.2.6. Functional connectivity in VCI

There is emerging evidence that functional connectivity is altered in patients with evidence of WM hyperintensities. While these patients exhibit a predictable DMN, they show decreased functional connectivity in the anterior cingulate, medial frontal gyrus, and caudate when compared to age matched controls (Sun et al., 2011). This suggests breakdown of the cortical – subcortical circuitry. Additionally, increased activity was observed in the posterior cingulate that the authors attributed to compensatory mechanisms. In another study, hypoconnectivity in the ventral medial prefrontal cortex was also observed and highly correlated with the degree of WM lesions (Schaefer et al., 2014).

As is the case with dMRI, there is the expectation that brain networks derived from rs-fMRI measurements will exhibit small worldness. Indeed, when graph theory was applied in patients with WM hyperintensities, decreased global and local efficiency and clustering coefficients were reported (Yu et al., 2015). The decreased clustering coefficient was

correlated with reduced cognitive function. Another study reported an increase in shortest average path length (decreased global efficiency) and an increase in modularity in patients with WM hyperintensities compared to healthy controls (Yi et al., 2015). This study also identified 5 RSNs (motor and somatosensory, default mode, frontoparietal, visual processing, and auditory). Four of the RSNs were similar between groups, but the frontoparietal network (executive control) was split into more distinctive activity components in the patients with WM hyperintensities. This suggests increased segregation of this network, and likely explains the increase in modularity. Similar decreases in global efficiency were observed in the hypoperfused hemisphere of patients with unilateral carotid stenosis (Chang et al., 2016). A recent multi-centre study compared several types of functional connectivity analysis and determined that graph theory was the only method robust enough to consistently distinguish patients with frontotemporal dementia from controls across sites, scanners, and analysis protocols (Sedeno et al., 2017).

It is time consuming and costly to follow patient cohorts across several years in order to monitor conversion to dementia and confirm the validity of the imaging biomarker. Animal models may expedite this process and provide knowledge regarding mechanisms of disease progression that could be amenable to treatment.

1.3. Animal models of VCI

Animal models offer mechanistic insight into disease, they also provide opportunities to validate potential biomarkers, and test therapeutic interventions (e.g. optimal dosing, safety profiles) (Madigan et al., 2016; Hainsworth et al., 2017). Animal models can encompass early initiating factors to advanced stages of pathology, and while no animal model has replicated the complete repertoire of VCI, numerous rodent models emulate different features of the disease (Gooch and Wilcock, 2016; Yang et al., 2016).

1.3.1. Bilateral common carotid artery occlusion

One of the most extensively studied rodent models of VCI based on cerebral hypoperfusion is bilateral common carotid artery occlusion (BCCAO) in the rat (Madigan et al., 2016; Yang et al., 2016). A 70% reduction in cerebral blood flow (CBF) is evident following carotid ligation, which recovers to 30-40% of baseline within 30 days (Tomimoto et al., 2003). After 7 days, CBF reductions are approximately 35% and 26% lower in the cortex and

hippocampus, respectively (Neto et al., 2005). BCCAO can produce blood brain barrier (BBB) breakdown and accumulation of matrix metalloproteinases as early as 3 hours post occlusion (Ueno et al., 2002; Sood et al., 2009), and thickening and fibrosis of capillary walls at 12 weeks (Farkas et al., 2007). Though rodents have less WM than humans, the BCCAO model is capable of producing WM damage and cognitive deficits (Gooch and Wilcock, 2016) such as impaired spatial memory in the radial arm and Morris water mazes as early as 7 days post-surgery (Sarti et al., 2002; Farkas et al., 2007; Jiwa et al., 2010).

1.3.2. Bilateral carotid artery stenosis

Mouse models are desirable due to the accessibility of transgenics. In mice, the BCCAO procedure would be fatal due to an incomplete Circle of Willis that results in poor collateral vascular coverage, therefore, the bilateral carotid artery stenosis (BCAS) model was proposed. This involves winding microcoils around each of the common carotid arteries to artificially induce stenosis (Shibata et al., 2004) (Figure 1.9).

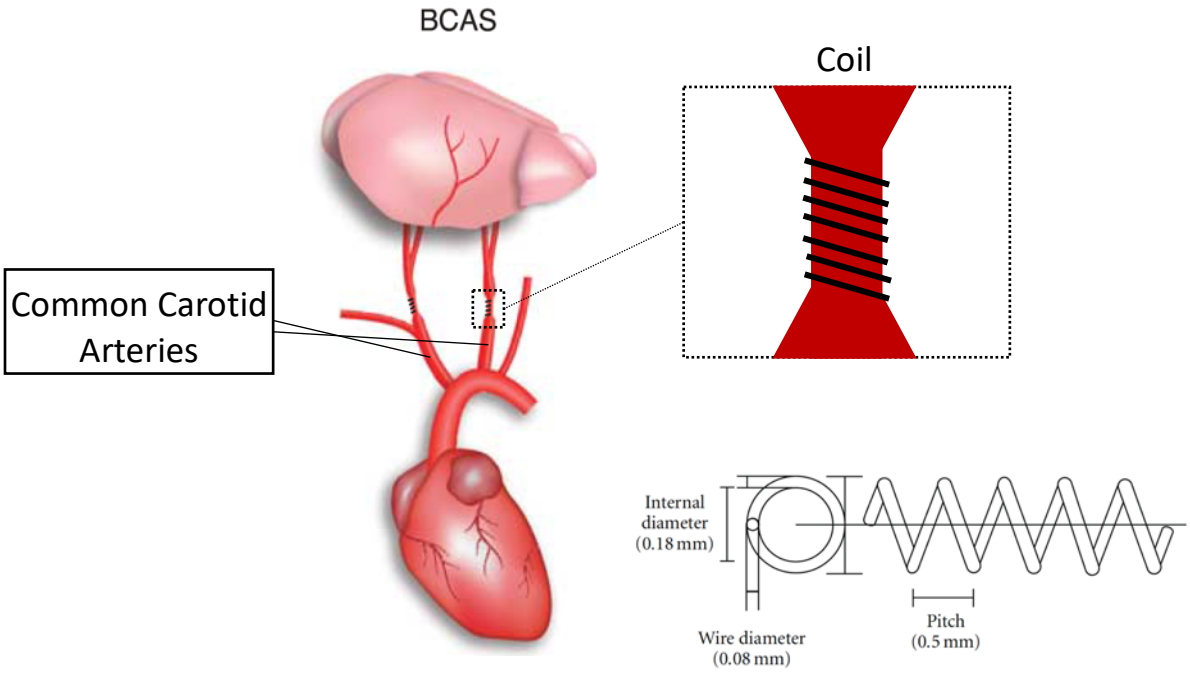


Figure 1. 9. Simplified diagram of the BCAS procedure in the mouse. Microcoils are placed around the common carotid arteries and this reduces blood flow to the brain. Modified from (Shibata et al., 2004; Ihara and Tomimoto, 2011; Bink et al., 2013).

The diameter of the microcoil fundamentally determines the severity of CBF decrease. Small microcoils (0.16 mm in diameter) produced severe reductions in CBF (~50%) but were associated with high mortality rates (~75%) (Shibata et al., 2004). Larger 0.18 mm diameter microcoils were associated with CBF decreases of 30% from baseline that recovered after a month and resulted in lower mortality rates (~15%). The 0.18 mm microcoils are the most widely used in the literature. In another study, these microcoils produced a reduction in CBF to 62% of baseline 2hrs after BCAS that recovered to 80% within a month (Nishio et al., 2010). MRI based assessment of CBF, reported a decrease of more than half immediately after surgery (4hrs), that recovered to almost baseline by 25 days (Fuchtemeier et al., 2015). When the same group employed the smaller microcoils (0.16mm) implanted with a 24 hour delay, reductions in CBF of 40% of baseline were observed at 1-day post-surgery, with an approximate recovery to 75% after 4 weeks (Boehm-Sturm et al., 2017).

BCAS hypoperfusion induces spatial working memory impairments. This has been reported in the radial arm maze that requires mice to retrieve food from 8 arms of a star shaped maze (Shibata et al., 2007; Nishio et al., 2010; Hase et al., 2018b). BCAS mice made significantly more visits into previously entered arms and fewer differing arm choices (Shibata et al., 2007; Nishio et al., 2010; Coltman et al., 2011; Patel et al., 2017; Hase et al., 2018b). Interestingly, comparable paradigms in the Morris water maze have failed to reveal spatial memory deficits in BCAS mice (Coltman et al., 2011; Fuchtemeier et al., 2015). Although cognitive tests associated with executive functions have not been examined in the BCAS model, BCAS mice tend to display reduced alternation behaviours in the Y maze (Maki et al., 2011; Hase et al., 2018a). This suggests a reduced desire to explore novel environments. BCAS mice also displayed impaired novel object recognition, suggestive of breakdown of the connections between the hippocampus and perirhinal and prefrontal cortices (Tsai et al., 2015; Patel et al., 2017). However, other groups have failed to observe any novel object recognition deficits (Boehm-Sturm et al., 2017).

Although early BCAS publications reported WM rarefaction and gliosis (Shibata et al., 2004; Shibata et al., 2007), subsequent studies have reported a more subtle WM pathology. For example, breakdown of myelin was implied due to small accumulations of myelin associated glycoprotein and degraded myelin basic protein in the white matter (Coltman et al., 2011; Holland et al., 2011; Reimer et al., 2011). Myelin biproducts were also found in conjunction with accumulations of extracellular amyloid precursor protein (indicative of axonal damage).

Oligodendrocyte precursors are also depleted in the BCAS model, though the pool was restored within a month (McQueen et al., 2014). Many groups have also reported increased microglia activity in the WM of BCAS mice (Washida et al., 2010; Coltman et al., 2011; Hase et al., 2017), suggesting an inflammatory phenotype that is closely linked to hypoxia (reviewed in (Duncombe et al., 2017)).

Several groups have investigated potential therapeutic agents in the BCAS model. Treatments have generally fallen into the categories of vasodilator, vasoprotective agents (Maki et al., 2011; Kitamura et al., 2017), targets of the renin angiotensin system (Dong et al., 2011; Maki et al., 2011; Fuchtemeier et al., 2015; Iwanami et al., 2015), free radical scavengers (Miyamoto et al., 2013; Seo et al., 2013), or anti-inflammatories (Manouchehrian et al., 2015; Chen et al., 2016; Toyama et al., 2018). Cilostazol is a vasodilator that did not prevent WM damage in BCAS mice, but slightly improved working memory at 3-months post-surgery (Kitamura et al., 2017). In addition, Maki et al. (2011) provided evidence that adrenomedullin facilitated the restoration of cerebral haemodynamics and reduced spatial memory deficits 1m post-surgery. The angiotensin II type I receptor antagonist telmisartan reduced demyelination and inflammation (Washida et al., 2010). The same was reported with another angiotensin II type I receptor antagonist called aliskiren (Dong et al., 2011). Inversely, angiotensin II type 2 receptor stimulation with azilsartan and C21 prevented deficits in spatial memory in the water maze (Iwanami et al., 2015). However, no beneficial effects of C21 were observed in a similar study by our group (Fuchtemeier et al., 2015). Free radical scavengers have also prevented WM degeneration in the BCAS model, potentially by protecting oligodendrocyte precursors (Seo et al., 2013).

1.4. Neuroimaging in the animal model

Given that the BCAS model produces WM damage, an area of interest has been to use dMRI to non-invasively characterize these changes. The first paper to report decreases in FA, specifically localised these reductions in the corpus callosum, internal capsule, and optic tract around 1m post-surgery, without changes in MD (Holland et al., 2011). Axonal damage and myelin bi-products were also observed post-mortem in the WM of BCAS mice. A follow up study at a more prolonged 6-month post-surgical time point confirmed these findings (Holland et al., 2015). Interestingly, a similar study by our group observed no changes in FA in major WM areas at 11, 17- or 25-days post-surgery (Fuchtemeier et al., 2015). Although

small increases in MD and RD were observed, suggesting possible cellular breakdown and demyelination, this was accompanied by a slight increase in AD.

Using slightly smaller microcoils (0.17 mm), another group reported decreases in FA paired with increases in RD in the corpus callosum, and internal and external capsule (Saggu et al., 2016) at 6-weeks post-surgery. A slight decrease in AD was also observed in the internal and external capsule. This was ameliorated in hypoperfused mice with astrocytic knockdown of the pro-inflammatory transcription factor NK-kB. A study from our group using the smallest reported diameter (0.16 mm) of non-magnetic microcoils found no differences in FA, MD, RD or AD in any WM structures at 5 and 7-weeks post-surgery (Boehm-Sturm et al., 2017). This was also the first study to attempt tractography. WM reconstructions illustrated smaller, less dense, and incomplete corpus callosums in the BCAS mice (Figure 1.10). However, it should be noted that the dMRI data in this study was acquired *in vivo*, and some spurious tracts were identified.

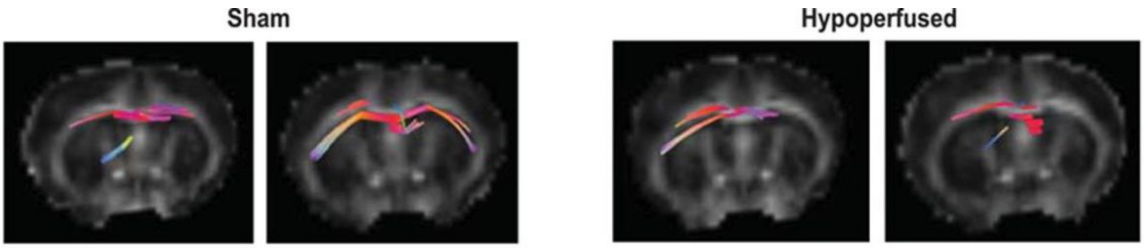


Figure 1. 10. Illustrative reconstructions of the corpus callosum from 2 sham and hypoperfused mice. Taken from (Boehm-Sturm et al., 2017).

Image registration was performed to the MRM NetAt mouse free brain template and atlas (Ma et al., 2008) in order to carry out the first graph theoretical analysis in the BCAS model. Although global efficiency was not significantly different between the BCAS and sham groups, BCAS mice displayed reduced modularity, indicating fewer distinctive sub-networks of structures. They also displayed increased clustering and transitivity, suggesting a potential strengthening of connections within localised sub-networks. Furthermore, global and local efficiency and degrees were effective at correctly predicting the group allocation of the mice, again highlighting the predictive capabilities of graph theory.

1.5. Structural connectivity in the mouse brain

Structural connectivity analysis in rodent brain images is lagging compared to human research. The size of the mouse brain necessitates high spatial resolution, and the hardware capabilities to achieve this with sufficient signal to noise ratio are not standard. As such, a large proportion of structural connectivity research is performed on *ex vivo* brains. Ultimately this allows longer scan times that are less susceptible to distortion, eliminates movement artefacts, and offers more options for contrast agents (Calabrese et al., 2015).

In order to test whether the mouse structural connectome generated by dMRI tractography is accurate, it has been compared to the large scale, high resolution Allen Mouse Brain Connectivity Atlas (AMCA, http://connectivity.brain-map.org/). This dataset contains an expansive map of 1772 neural tracing experiments in the mouse brain (Oh et al., 2014). There was up to 90% similarity between AMCA and dMRI tractography connectivity methods (Chen et al., 2015). It is important to note that this was only possible via optimization of the dMRI parameters combined with a mid-range atlas parcellation (96 regions). Calabrese et al. (2015) attempted the same analysis with a probabilistic tractography algorithm that is sensitive to the distribution of anisotropy within each voxel (Behrens et al., 2007). Compared to deterministic tractography that generates a principal direction of diffusion for each voxel, probabilistic tractography was almost indistinguishable from AMCA with a 99% correlation. Similarly, this was only present with a low level of atlas parcellation (13 regions). There was only 71% similarity for a medium number of structures and 42% similarity with all of the structures. Both AMCA and dMRI tractography structural connectomes have been reported to possess high clustering and short path lengths typical of small world-ness (Chen et al., 2014).

Despite the fact that there are relatively few papers that examine a dMRI based mouse structural connectome, graph theory has shown promise as a good indicator of age (Ingalhalikar et al., 2015). Global efficiency and modularity increase during development, stabilise around 20 days of age, and begin to decline after 80 days of age. Another paper examined changes in structural connectivity in the cuprizone (CUPR) mouse model of demyelination (Hubner et al., 2017). Reductions in FA were observed in CUPR mice along with reductions in fibre density and fewer longer distance tracts. The CUPR mice also exhibited a substantively reduced structural connectome (Figure 1.11).

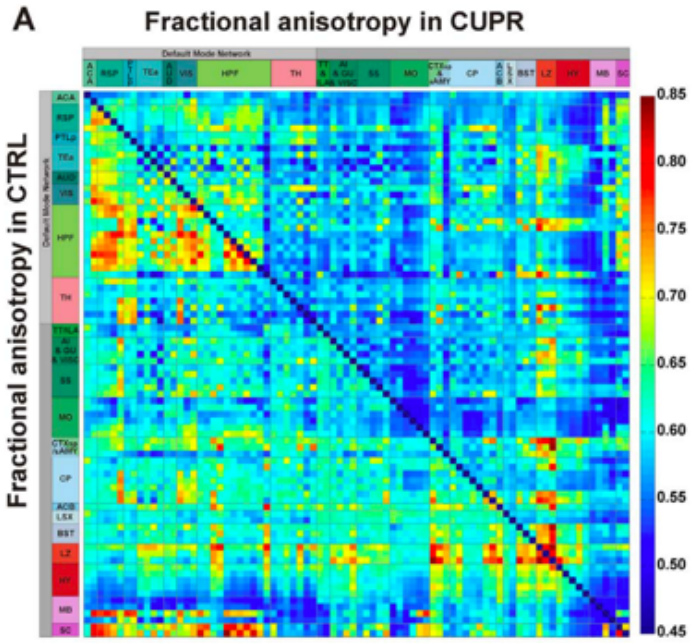


Figure 1. 11. Structural connectome in control (CTRL) and cuprizone (CUPR) treated mice with demyelination. CUPR mice exhibit reduced FA in most regions of the brain, particularly among cortical regions connected to the hippocampus in which the strongest FA was observed in CTRL mice. (ACA - anterior cingulate area, RSP - retrosplenial area, PTLp - periaqueductal grey, TeA - temporal association area, AUD - auditory area, VIS - visual area, HPF - hippocampal formation, TH - thalamus). Figure modified from (Hubner et al., 2017).

Interestingly, the same study also performed rs-fMRI experiments in the CUPR mice. When structural and functional connectivity was compared across the same brain regions, CUPR mice exhibited reduced functional connectivity between the retrosplenial cortices, hippocampal formation and thalamus. These regions were suggested to be the mouse DMN.

Measuring both structural and functional connectivity provides information regarding both the physical alterations in a brain network with disease, but also insight into how this affects function.

1.6. Functional connectivity in the mouse brain

In contrast to rodent brain dMRI connectivity analysis, functional connectivity studies have exploded in the last 10 years (Gorges et al., 2017). The added difficulty of shimming and distortion due to the small size of the mouse brain means that the first report of rs-fMRI in mice was only in 2011. The authors used ICA to identify a large, unified component of

connectivity across the mouse cortex (Jonckers et al., 2011). There is some degree of preconception required for ICA; the experimenter must decide whether to guide the analysis to search for a specific number of activity components. The authors of the first mouse rs-fMRI paper had selected 15 components on the basis of previous experiments in rats. However, when 40 components were selected, more specific cortical regions were identified and the most prominent components were in the motor, sensory and auditory cortices. A subsequent study compared 40 and 100 component ICA and additional, smaller unilateral components were observed when dimensionality was set to 100 (Mechling et al., 2014). These experiments were performed with sedation using the alpha 2 adrenergic agonist medetomidine that has vasoconstrictive effects (Fukuda et al., 2013). Unfortunately, the requirement of sedation and/or anaesthesia to reduce stress and movement influence neural activity, CBF and subsequently BOLD. Furthermore, physiological parameters such as heart rate and respiration can vary depending on the type of anaesthesia/sedation and further influence the BOLD response.

Isoflurane is the most commonly employed anaesthetic for rodent laboratory procedures. It will reduce neuronal activity, but it has also been shown to increase vasodilation (Constantinides et al., 2011). Using low levels of isoflurane, seed based analysis of the medial and lateral cortices displayed the first evidence of the DMN in the mouse (Guilfoyle et al., 2013). Dorsal medial cortical activity extended in a rostral caudal direction. Variations in functional connectivity were subsequently investigated using four different anaesthetic/sedation compounds: medetomidine, isoflurane, propofol and urethane (Grandjean et al., 2014a). Seed based analysis using components identified from ICA revealed little differences among the tested agents when the data was regressed. When the data was un-regressed, medetomidine and isoflurane produced the strongest bilateral cortical and subcortical functional connectivity; medetomidine resulted in slightly weaker inter-cortical connectivity but greater cortical connectivity to striatal regions. Isoflurane and propofol generated strong thalamo-cortical connectivity. Comparable results (primarily unilateral activation) were subsequently reported for isoflurane when compared to urethane and alpha chloralose (Jonckers et al., 2014). In addition to comparing a range of anaesthetics, a group of non-anaesthetised awake mice were also analysed. Following from previous acclimatisation training protocols for MRI used in rats (King et al., 2005), although the interhemispheric connectivity was generally increased for awake compared to anaesthetised mice, there was also a strong increase in variability as mice did not respond to the training as

successfully as previous rat cohorts. For example, stress levels over the acclimatisation period did not reduce as they did previously in rats, therefore increased breathing rates during scanning were evident. This ultimately led to only a proportion (n=5) of the awake mice being recorded with adequate results, furthermore it opens to several more questions on whether the mouse is resting or preforming a task. Overall, the authors concluded that the non-anaesthetised awake procedure was not best suited in mice (Jonckers et al., 2014).

Several studies have attempted to characterize the mouse DMN. Also using isoflurane, the mouse dorsal medial DMN (orbital, cingulate and parietal cortices) was identified when the retrosplenial cortex was used as a seed (Stafford et al., 2014). This DMN was found to possess a strong structural concordance to the AMCA, and was similar to the DMN in primates and humans. The same DMN pattern was observed under medetomidine sedation when the prelimbic cortex was seeded, as well as with ICA in which negative-correlations were also noticed in the parietal cortex (Sforazzini et al., 2014); this group has extensively reviewed the rodent DMN in comparison to primates and humans (Gozzi and Schwarz, 2016). A similar experiment used medetomidine and a processing pipeline that was trained to automatically detect noise and BOLD signal during ICA (Zerbi et al., 2015). The resulting DMN is depicted in Figure 1.12 and is similar to the previous report.

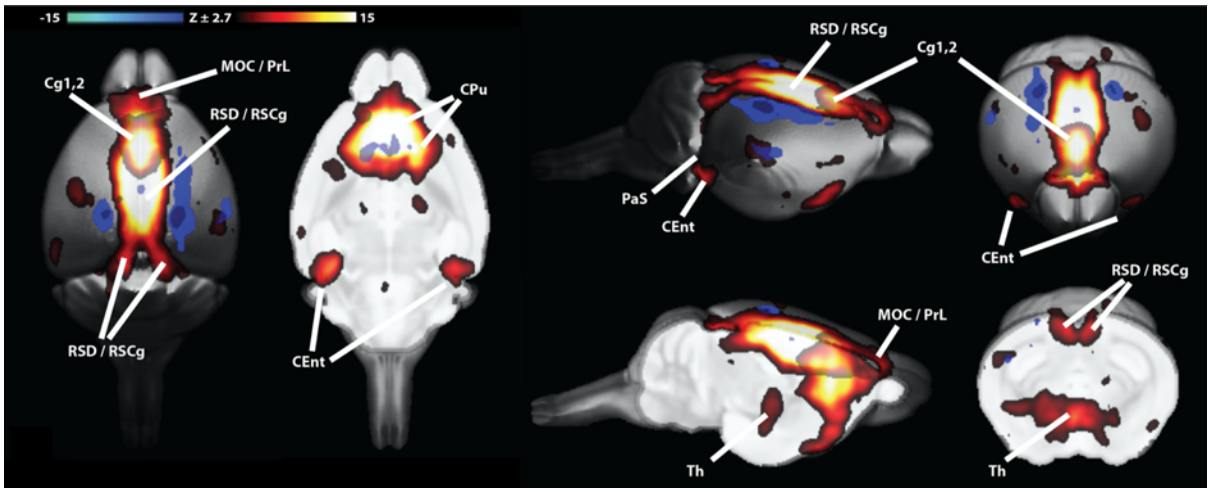


Figure 1. 12. Illustration of the mouse DMN; cingulate, orbitofrontal, retrosplenial, and posterior temporal association cortices, and thalamus. (CEnt - caudomedial entorhinal cortex, Cg1 and Cg2 - cingulate cortices, CPu - caudate putamen, MEnt - medial entorhinal cortex, MOC - medial orbital cortex, PaS - parasubiculum, PrL - prelimbic cortex, RSD and RSCg - retrosplenial dysgranular and granular cortices, Th – thalamus). Taken from (Zerbi et al., 2015).

This paper was also the first to begin to describe additional sub-networks, or RSNs, of bilateral connectivity including sensory, limbic, basal ganglia, and cerebellar sub-networks. The sub-networks were further supported through hierarchical clustering of the activity components according to the strength of the correlation coefficient (Figure 1.13).

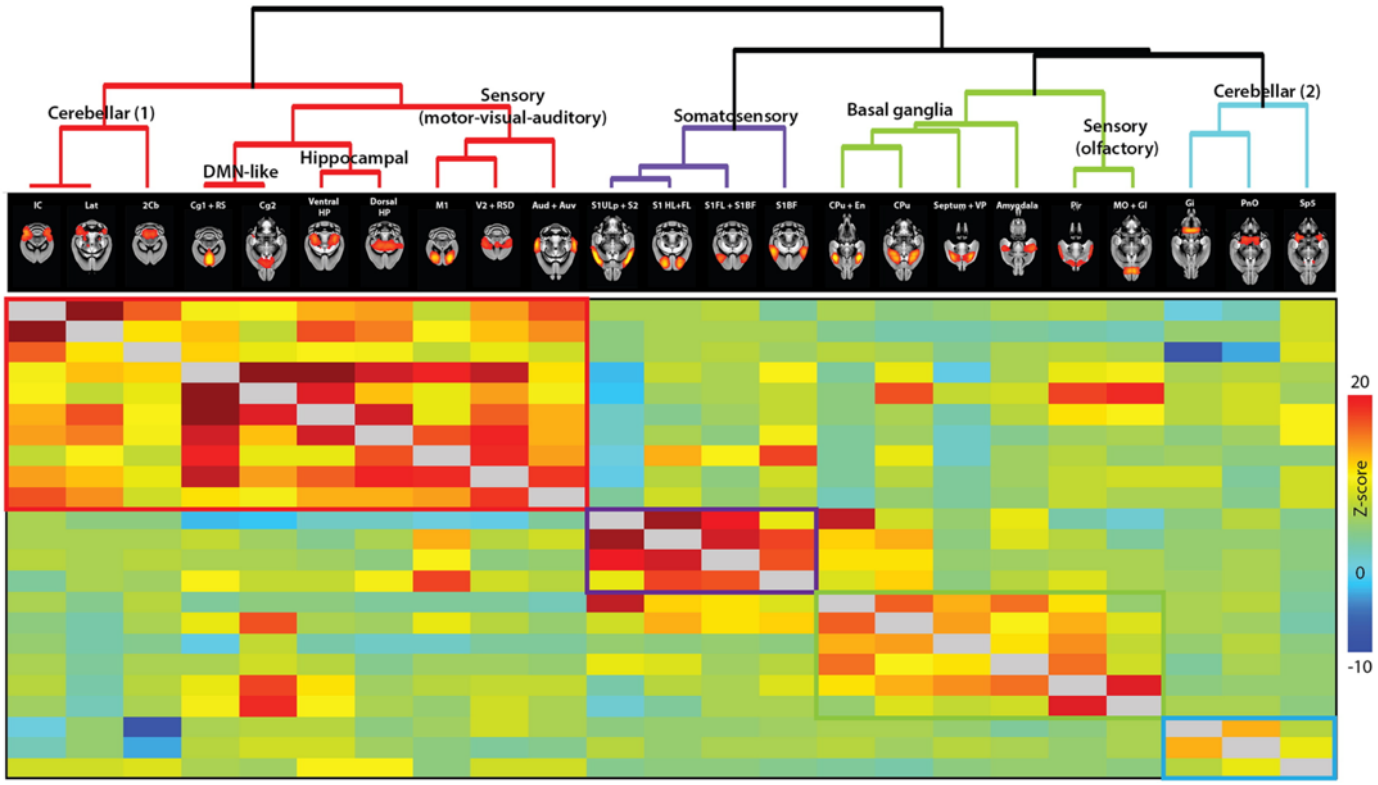


Figure 1. 13. A hierarchical matrix of a mouse functional connectome in which components that are more closely correlated are clustered into four main RSNs: cerebellar, DMN, hippocampal and sensory (red), somatosensory (purple), basal ganglia (green), and cerebellar (blue). Note: the strength of the correlations between each component is depicted in the hierarchical matrix by the scale bar. Figure taken from (Zerbi et al., 2015).

The field then moved towards identification of RSNs. One study attempted to classify components into hubs (Liska et al., 2015) and several nodes were described as integrators, meaning that they were highly connected, and could leave the network vulnerable should damage occur. The integrator nodes included the hippocampus, thalamus, basal forebrain, ventral midbrain, and lateral cortical regions. After the DMN, the connectivity strength of the lateral cortical regions and basal forebrain hubs was highest. Other RSNs that have been

reported include a large, bilateral sensorimotor network that includes activity in the sensory and motor cortices, an autonomic network consisting of the hypothalamus and midbrain, and a salience network including the sensory, auditory, insular and temporal association cortices (Bajic et al., 2017). This expanded to include several cortical networks, as well as striatal and thalamic and hippocampal networks (Grandjean et al., 2017a) (Figure 1.14).

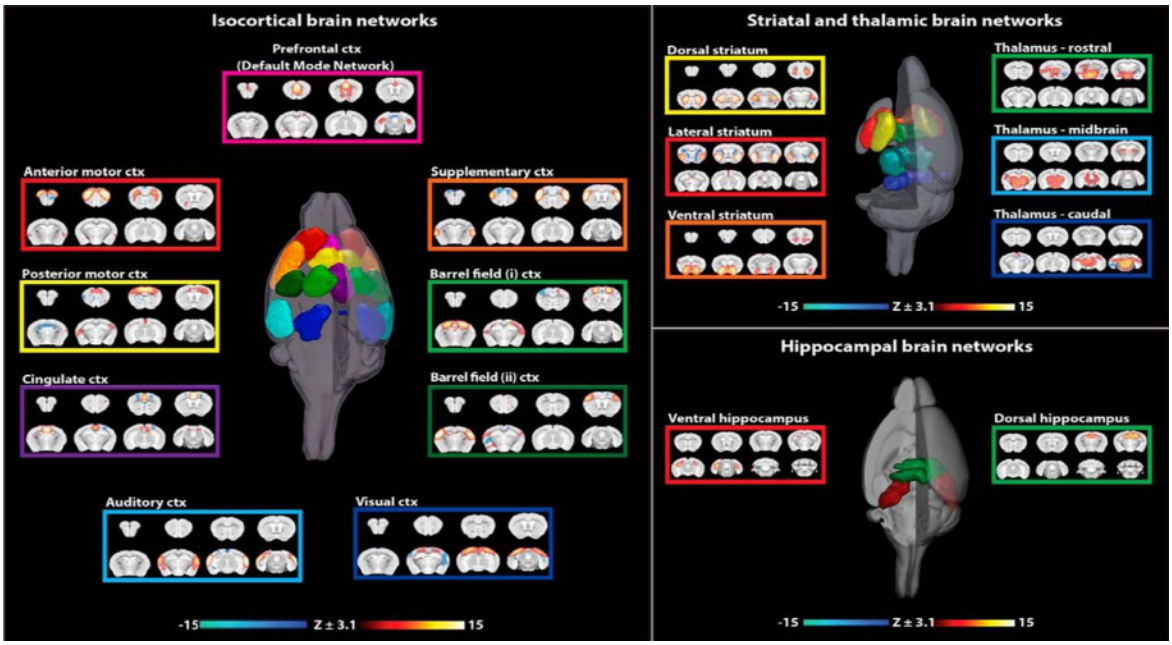


Figure 1. 14. Illustrates an overview of the range of RSNs in the mouse. Abbreviations: ctx- cortex. Taken from (Grandjean et al., 2017a).

In addition, this study compared the functional connectivity results to structural connectivity patterns in the AMCA. There was a general similarity between structural and functional connectivity matrices when approximately 238 seeds were used to analyse the rs-fMRI data from the 254 possible Allen injection sites. Cortical, hippocampal and striatal regions were the most highly correlated between the 2 analyses. A prominent example of structural and functional connectivity overlap was the primary somatosensory, motor and anterior cingulate cortices (Figure 1.15). Many regions exhibited strong bilateral (homotopic) structural and functional connectivity. Interestingly, structural connectivity was high in the thalamus, whereas cortico-thalamic pathways were underrepresented through rs-fMRI. On the other hand, functional connectivity between the hippocampus and distant regions like the retrosplenial, cingulate, entorhinal and perirhinal cortices was high, whereas AMCA injection

sites in the dentate gyrus only revealed confined structural connectivity within the region of the hippocampus (Grandjean et al., 2017a).

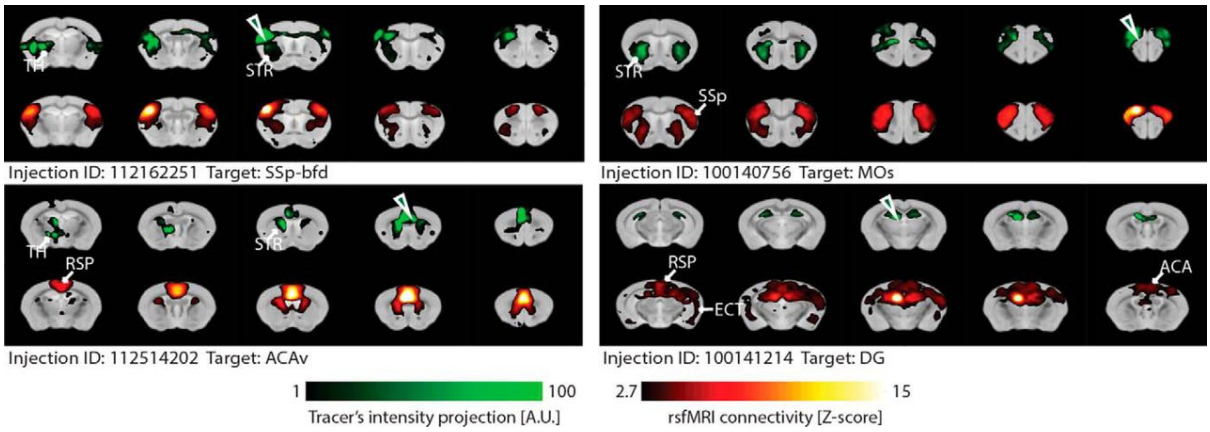


Figure 1. 15. Illustration of the comparison of structural (green) and functional (orange) connectivity in four regions of interest; primary somatosensory area (top left), motor area (top right), anterior cingulate area (bottom left), and dentate gyrus (bottom right). Each injection/seed site is highlighted with a white arrow. (TH – thalamus, STR – striatum, SSp – primary somatosensory area, RSP – retrosplenial cortex, ECT – ectorhinal cortex, ACA – anterior cingulate area). Figure taken from (Grandjean et al., 2017a).

Recent research investigated reproducibility among a range of datasets from 15 different centres (Grandjean et al., 2020). De-noising and motion correction strategies resulted in comparable specific BOLD signal, but different degrees of spurious signal. Nevertheless, despite substantive differences in animal preparation and scan parameters, seed-based analysis from the anterior cingulate revealed a consistent DMN across 70% of the datasets. ICA across the data also revealed several bilateral cortical activity components as well as some prominent sub-cortical components (thalamus, caudate putamen, nucleus accumbens and hippocampus). Not surprisingly, non-sedated mice showed higher overall functional connectivity, followed by a combination of isoflurane and medetomidine. Overall, respiration condition did not influence signal, neither did field strength, though access to a cryocoil was an advantage.

A few groups have examined functional connectivity change using rs-fMRI in transgenic mice. The ArcAß mice model Alzheimer's disease and begin to show amyloid build up by 6 months. Wild-type mice exhibit strong functional connectivity, particularly among cortical components, starting around 5 months of age. This was overall much weaker in the ArcAß mice with substantive decline starting around 19 months of age (Grandjean et al., 2014b).

Mice with deletion of the mu opioid receptor gene exhibited normal structural connectivity and no widespread changes in functional connectivity, seed-based analysis from the activity components associated with pain processing revealed reorganization (Mechling et al., 2016). Specifically, wild-type mice displayed more positive correlations among pain network structures: the habenula, prefrontal cortex, nucleus accumbens, thalamus and peri-aqueductal gray, ventral tegmental area, which is indicative of the reward circuitry.

Utilizing MRI methods to generate and analyse structural and functional connectomes in models of disease susceptible to network damage can offer promising discoveries in terms of pathological profiling.

1.7. Thesis Aims

Development of better experimental animal models and translational neuroimaging methods were declared top research priorities for VCI during the Alzheimer's Disease-Related Dementias Summit 2016 (Corriveau et al., 2016; Hainsworth et al., 2017). The ability to generate and analyse structural and functional network profiles in mouse models could help identify susceptible brain regions, develop and validate neuroimaging biomarkers for early identification, allow testing of therapeutic agents and provide valuable insight into disease mechanisms. The primary aim of this thesis is to develop an automated processing pipeline incorporating recent advances in data processing to both improve and standardise mouse pre-clinical imaging. The secondary aim is to identify neuroimaging biomarkers of dMRI and rs-fMRI in the prominent BCAS mouse model of VCI.

Chapter 2. General Methods

The data pre-processing and automated pipelines described in this chapter were used throughout the thesis. The accompanying scripts are in the Appendix A.

2.1. Data pre-processing

Data pre-processing generally encompasses data conversion, orientation confirmation, standard template creation, image registration and correcting for potential signal bias.

2.1.1. Data conversion

Converting rodent data from the native MRI scanner ParaVision (version 6.3) format (Bruker, Ettlingen, Germany) into the most widely used file type Neuroimaging Informatics Technology Initiative (NIFTI) was performed for rs-fMRI data using Bru2nii (https://github.com/neurolabusc/Bru2Nii), or the Python (version 3.8.1) tool Bruker2nifti (https://github.com/SebastianoF/bruker2nifti) (Ferraris et al., 2017) for dMRI data.

2.1.2. Orientation confirmation

The anatomical orientation was checked (anterior-posterior, superior-inferior, medial-lateral). When incorrect, orientation was adjusted using a combination of tools (fslorient, fslswapdim) available from the Oxford Centre for Functional Magnetic Resonance Imaging of the Brain (FMRIB) Software Library (FSL) (Smith et al., 2004b; Woolrich et al., 2009; Jenkinson et al., 2012). FSL was used extensively for much of the data processing. The FSL NIFTI viewer (FSLeyes) was used to visualize all results.

2.1.3. Structural template creation

A subject derived structural template (average of all individual subject T_2 images) was created using Advanced Normalization Tools (ANTs) version 2.2.0 (https://github.com/ANTsX/ANTs) (Avants et al., 2011). The antsMultivariateTemplateConstruction2 tool averaged all of the high-resolution structural images acquired throughout each study (Figure 2.1).

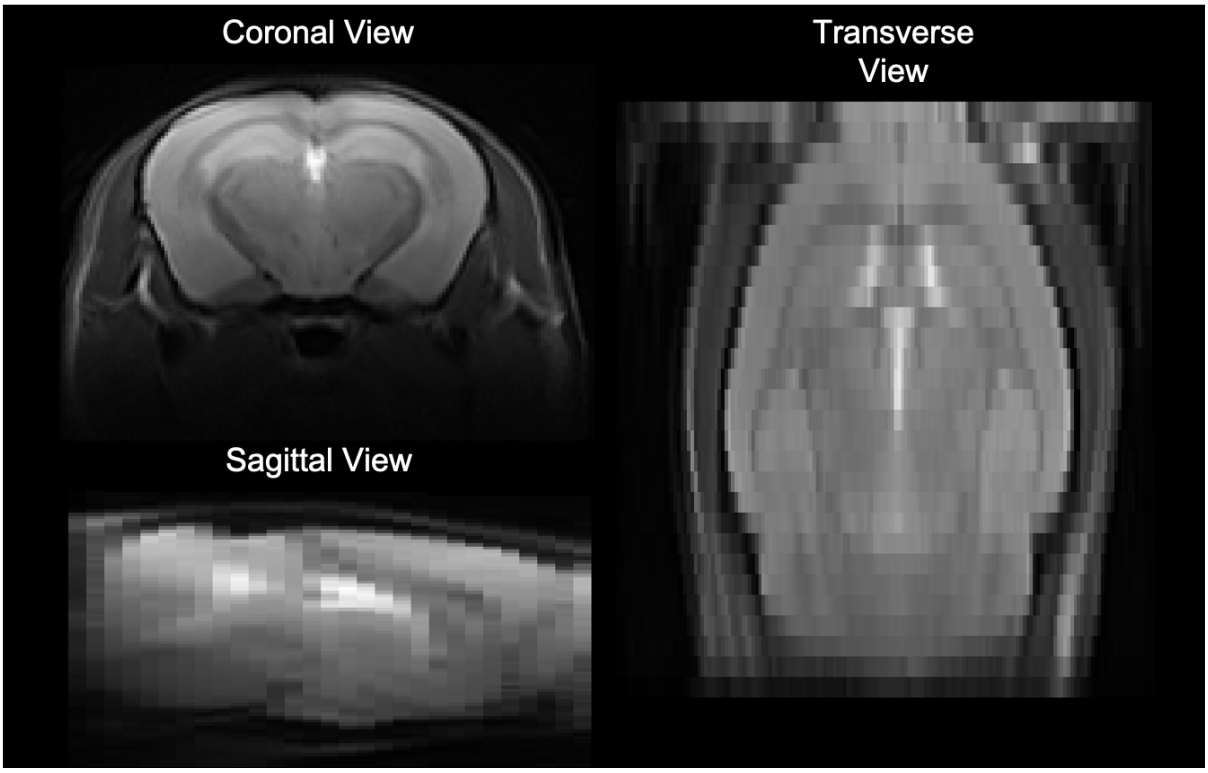


Figure 2. 1. The structural mouse brain T_2 template generated from all of the individual mouse T_2 images.

2.1.4. Bias correction

Surface coils create a hyperintense signal bias that tapers off inferiorly as the distance from the surface coil is increased. The ANTs nonparametric nonuniform intensity normalization algorithm (N4BiasFieldCorrection) was used to homogenize signal intensity (Tustison et al., 2010). The signal intensity histogram of the image is first modelled to a Gaussian distribution. Then a B-spline model was used to sample signal intensity values at regularly spaced intervals throughout the histogram to determine the bias. The data was spatially smoothed according to the B-spline model of bias (Figure 2.2).

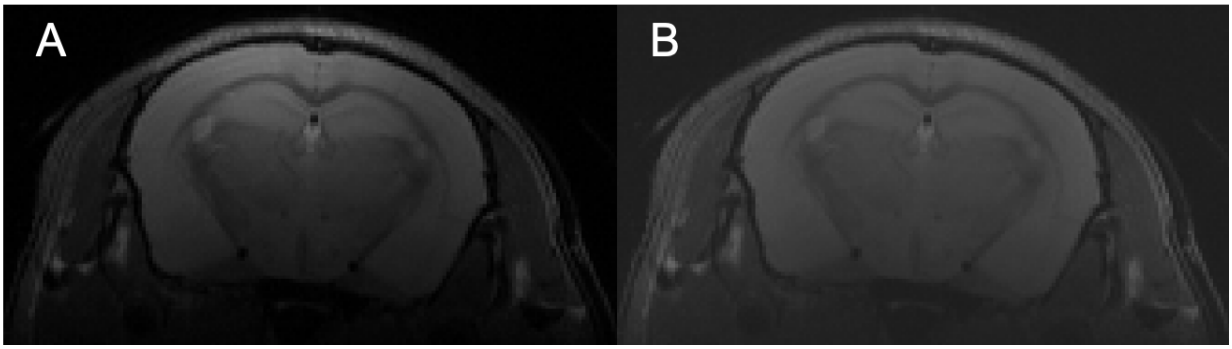


Figure 2. 2. Coronal views of a non-bias corrected (A) and a bias corrected (B) T_2-weighted image.

2.2. rs-fMRI pipeline

An overview of the rs-fMRI pipeline is displayed in Figure 2.3.

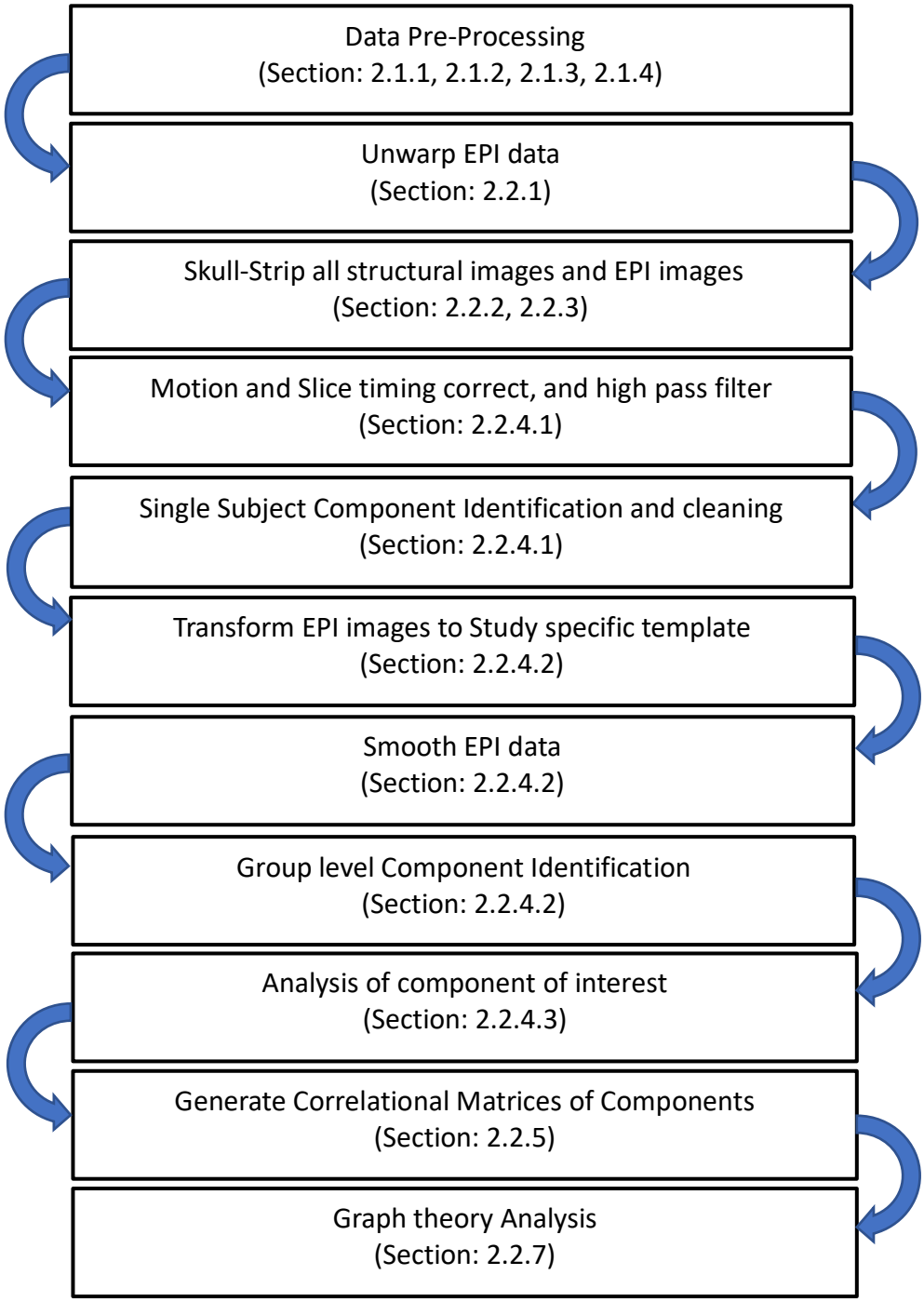


Figure 2. 3. Flow chart of the rs-fMRI pipeline. Each box displays the process and the corresponding command line tool.

2.2.1. Correcting for image distortion

Gradient echo (GE), echo-planar imaging (EPI) is the most prominent acquisition method for rs-fMRI, due to the high temporal resolution that enables capture of physiological processes. One drawback of this technique is the susceptibility to image distortions as a result of magnetic field inhomogeneities. This can often be prominent at tissue interfaces. There are several FSL methods available to correct the images for distortions. A map of the magnetic field (measured in Hertz (Hz)) was converted into radians per second (rad/s) and non-brain tissue removed using (fsl_prepare_fieldmap). Subsequently, boundary-based registration and unwarping using (epi_reg) that focuses on the WM (generally more robust to scanning artefacts) (Greve and Fischl, 2009) was employed.

2.2.2. Structural image registration and skull stripping

The antsRegistrationSyN.sh tool was used to register the average T_2 template (produced in section 2.1.3) to AMCA's MRI template and accompanying atlas. Due to comparable contrast, AMCA's WM and grey matter masks, excluding the CSF, were used to bring the T_2 template into Allen space. CSF exclusion during registration was necessary due to opposing tissue contrasts between the T_2 and AMCA templates for (Figure 2.4).

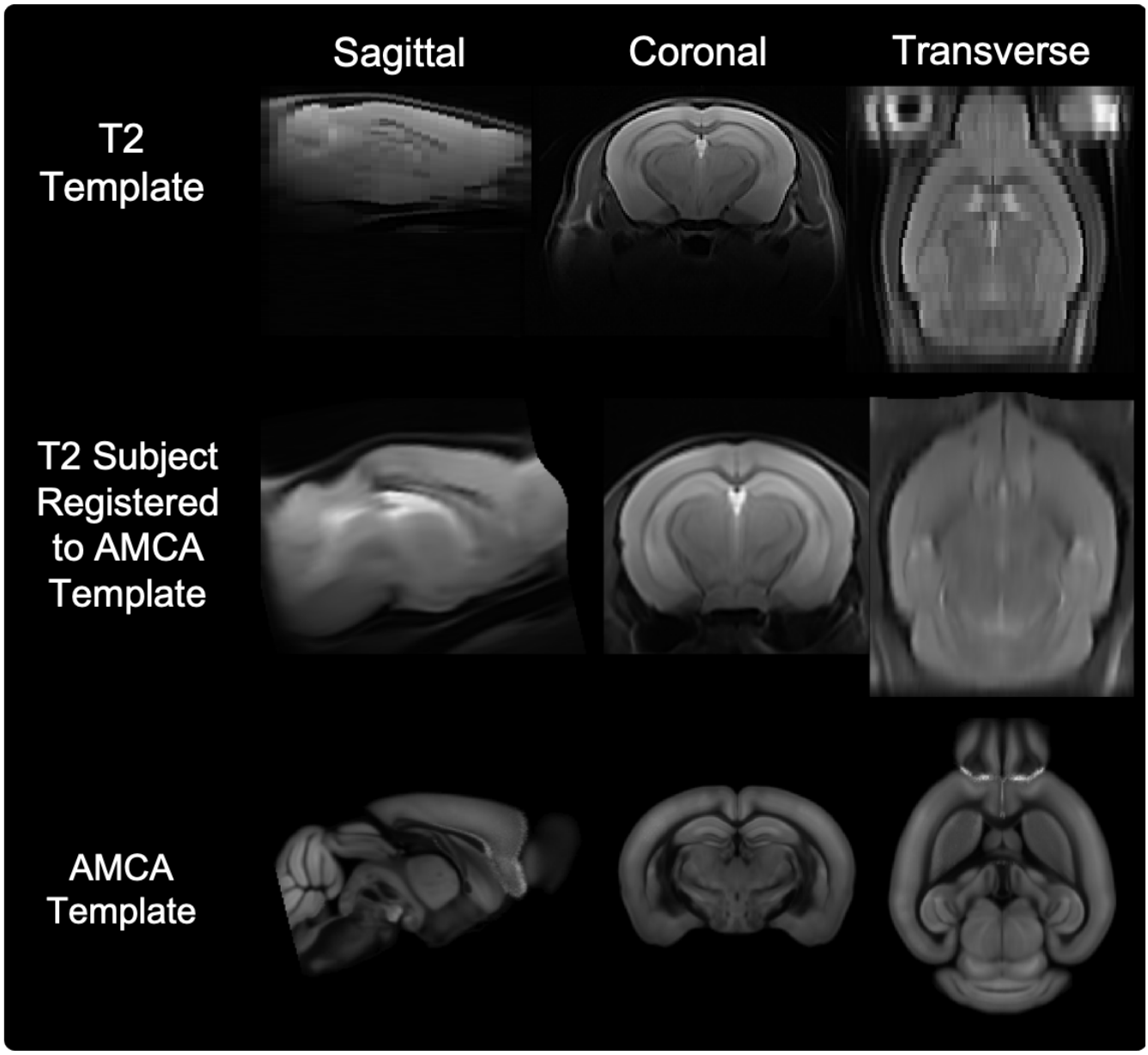


Figure 2. 4. The average T_2 template (from Figure 2.1) registered to AMCA's template.

The individual subject T_2 images were then registered to the subject derived average structural T_2 template using the same tool.

The antsApplyTransforms tool is able to make use of transformation files generated from previous image registrations. It was used to bring the AMCA whole brain mask first into the average T_2 template space (using the inverse transformation from section 2.2.2), and then into

each individual subject T_2 space. The AMCA mask was then used to remove all non-brain tissue (skull strip) from the structural T_2 images through multiplication with the fslmaths tool (Figure 2.5).

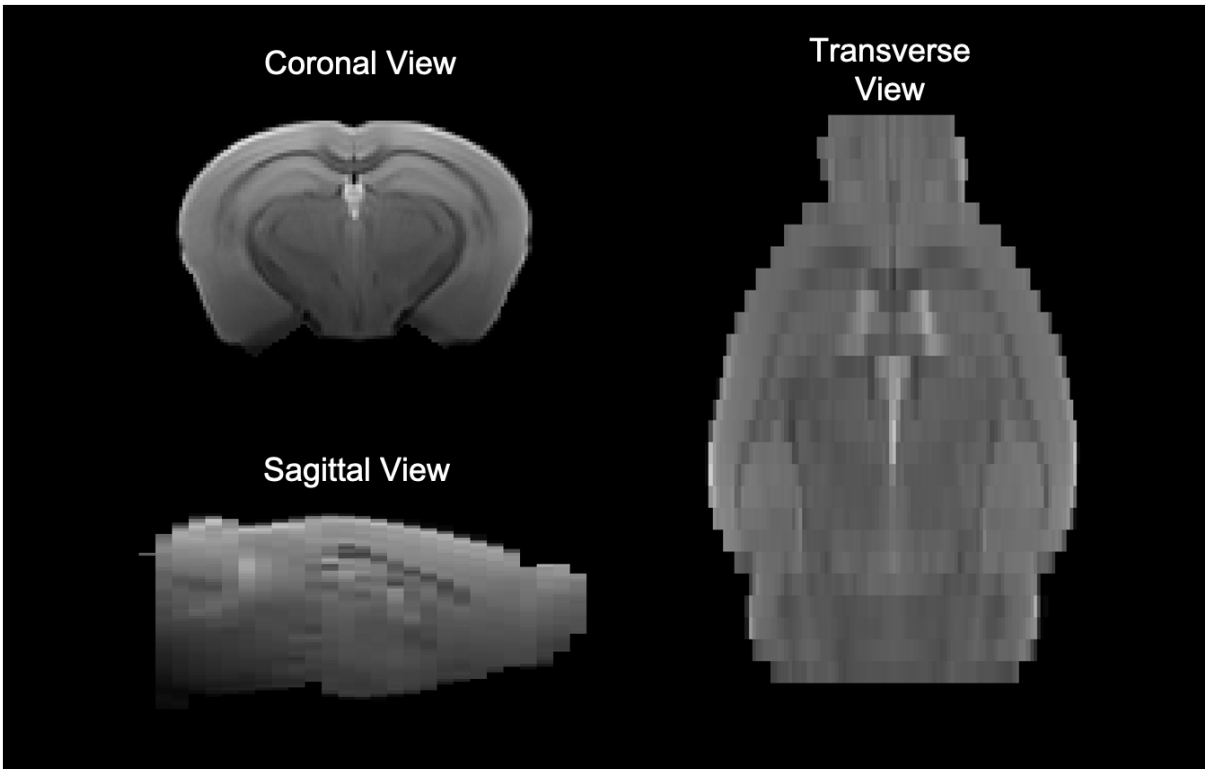


Figure 2. 5. Skull stripped average T_2 weighted study derived template.

2.2.3. Functional image registration and skull stripping

A similar process was applied to the rs-fMRI images with slight modifications. As the rs-fMRI data contained a time course (each image slice was acquired with several repetitions), it was not possible to directly transform the AMCA mask into this space. The fslroi tool was used to remove the time component from the rs-fMRI data by extracting the first repetition from each timeseries (Figure 2.6).

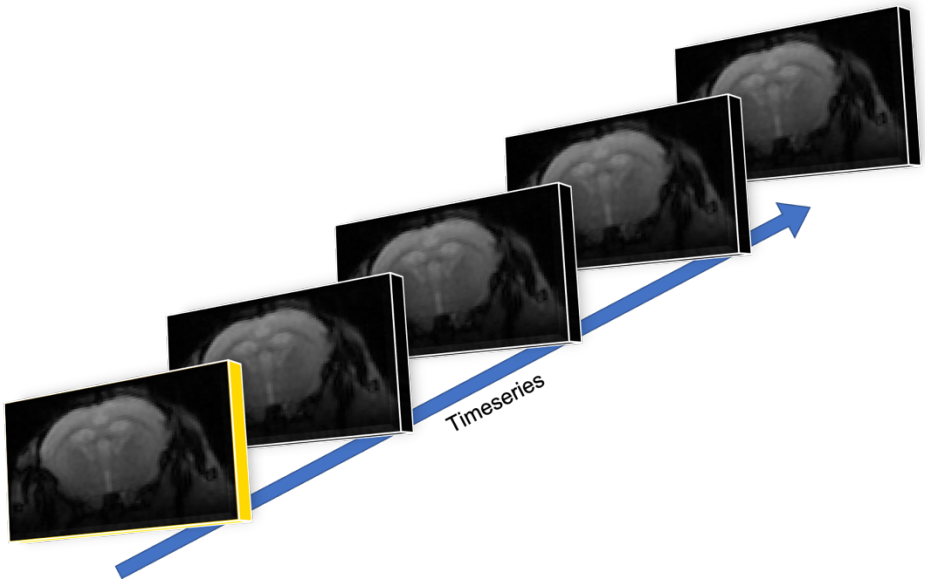


Figure 2. 6. Illustration of the time course of one tissue slice from a rs-fMRI dataset. The first repetition (highlighted) was extracted for each tissue slice.

The antsApplyTransforms tool used the transformation files generated when the AMCA whole brain mask was brought into individual subject T_2 space, and further bring the mask into each individual subject rs-fMRI space. This tool also changed the mask voxel resolution to match the rs-fMRI data.

The fslmaths tool was then used for skull stripping and the same process was applied to the complete rs-fMRI time course for every subject (Figure 2.7).

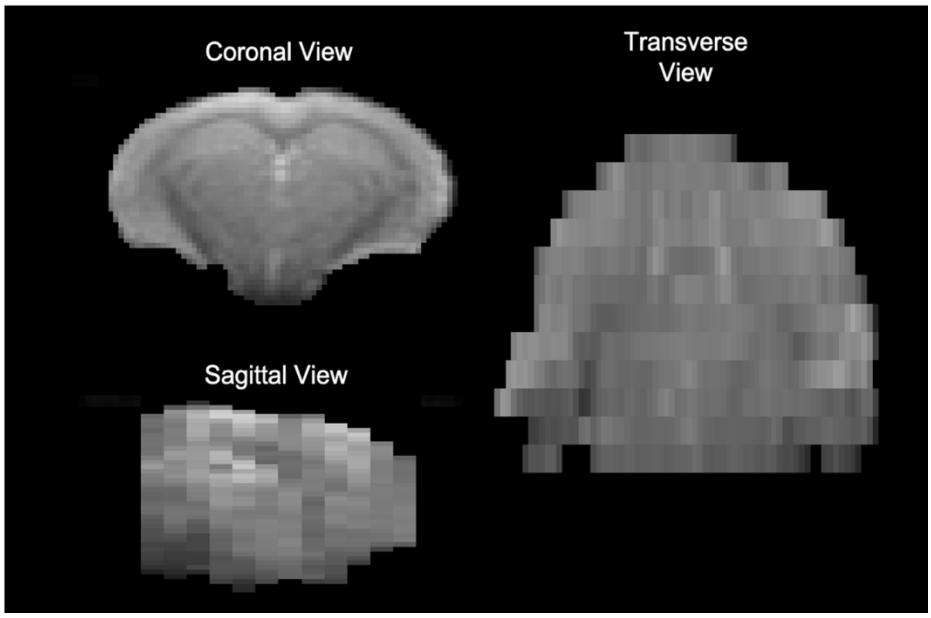


Figure 2. 7. Skull stripped rs-fMRI data.

Alignment of the individual subject rs-fMRI data sets was achieved using the antsRegistrationSyN.sh tool with rigid and affine registration. This was performed for the skull stripped data in which the time course was removed. Subsequently, the antsApplyTransforms tool was used to apply the same registration to the rs-fMRI images with the time course using a nearest neighbour interpolation to reduce excessive blurring and preserve voxel information.

2.2.4. Independent component analysis

2.2.4.1. Removing noise at the single subject level

FSL's ICA tool MELODIC was used to apply a high pass frequency filter to the rs-fMRI data (fslmaths: 0.01Hz) as neural derived BOLD signal is generally predominant at frequencies no lower than 0.01Hz. The MCFLIRT tool removed sources of motion throughout each scan (cardiac, respiratory, scanner vibration) (Jenkinson et al., 2002). The slicetimer tool was employed to amend timing deviations as a result of slice-dependant delays during the collection of each individual slice for an image. Without this correction method certain slices can be temporally out of sync, affecting the quality of components. For example, when data was collected using an interleaved order (e.g. 1, 3, 5… 2, 4, 6…), all odd slices were collected before the even slices. This results in a temporal delay between the first and last slice. The slicetimer tool implements a temporal shift by reversing the temporal delay of the collection order, helping to improve temporal estimation between voxels within each slice during statistical analysis. MELODIC automatically determined the number of independent signal components at the level of each individual subject (Beckmann and Smith, 2004).

The resulting motion correction was manually checked, images were excluded if there was > 0.005° or 0.02mm of translation or rotation, respectively, in any direction. Subsequently, each component was manually inspected and classified as either BOLD signal or noise (Griffanti et al., 2017). For a component to be classified as BOLD signal it must have predicted 1.5-3% of signal variance, was predominantly low frequency (0-0.1Hz) in the power spectrum, exhibited no major spikes in the signal time course (motion), and was not located in a major vessel or ventricle (Figure 2.8). This procedure resulted in removal of approximately 70-80% of the components in each subject but was necessary to increase the sensitivity to BOLD signal for analysis.

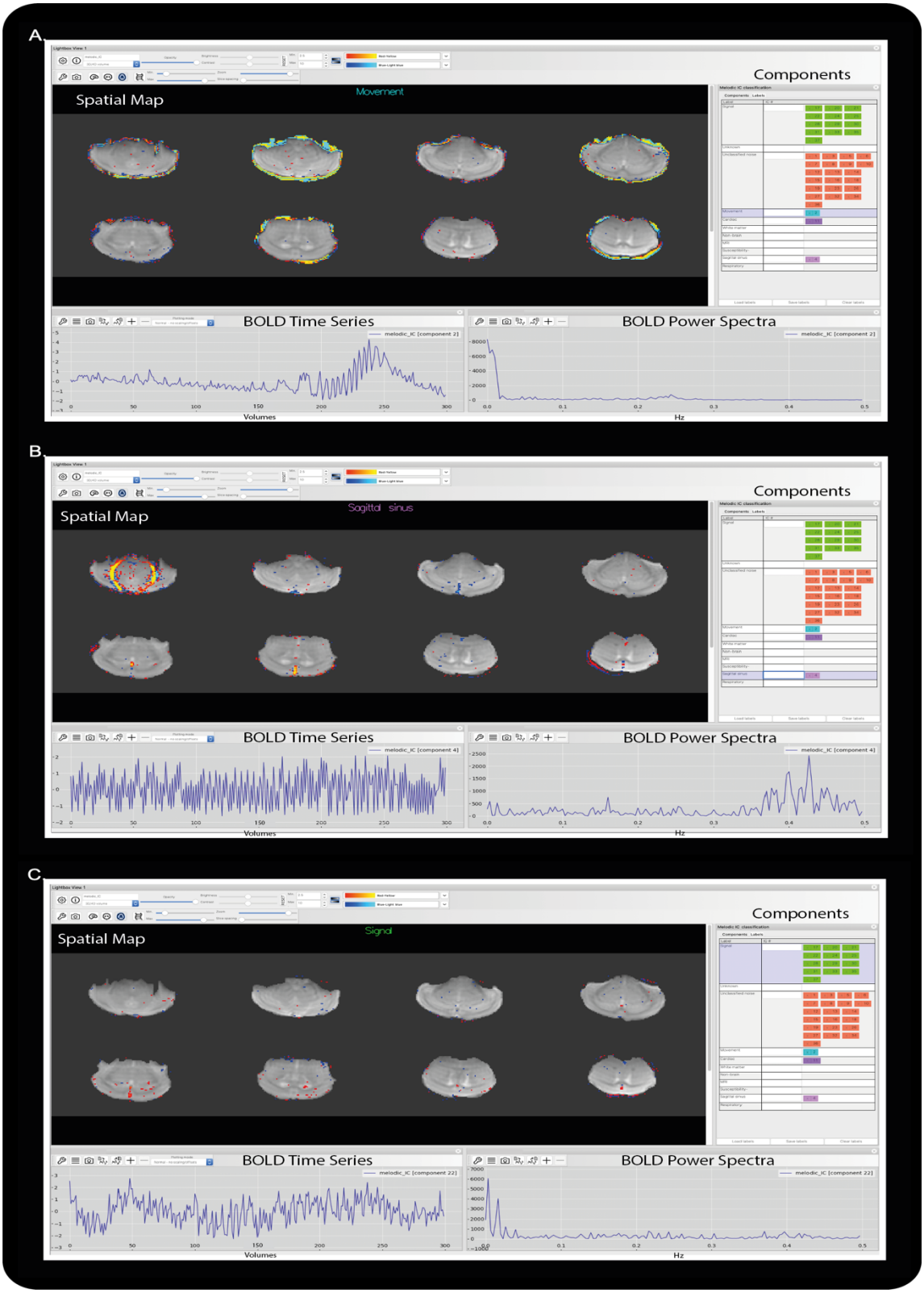


Figure 2. 8. Classification of noise and signal in an individual mouse. A) Signal is located around the edge of the brain, there is a major spike in the time course (lower left), and position in the power spectrum is quite low (lower right); this was classified as motion. B) Signal is located in a major vessel (sagittal sinus vein) and in the CSF. The signal time course (lower left) appears normal, but the position within the power spectrum (lower right) is quite high. C) BOLD derived signal with a stable time course and appropriate position in the power spectrum.

2.2.4.2. Group level independent component analysis

EPI images were aligned into the common template space using the transformation files generated from the registration stages (selecting nearest neighbour interpolation option). Spatial smoothing was performed on data after noise was removed, and the size of the smoothing kernel was determined via the full width at half maximum (FWHM) of a Gaussian distribution (0.7mm) (Bajic et al., 2017) with FSL's FEAT tool.

MELODIC was again used to temporally concatenate all the subjects (multi session option) and to automatically determine the number of independent signal components at the level of the group. The same criteria employed in 2.2.4.1 was used to classify components as BOLD signal or noise.

2.2.4.3. Dual regression

FSL's permutation analysis tool dual regression (Beckmann et al., 2009; Nickerson et al., 2017) was used to probe the resulting group level components for relationships across space and time.

General linear models were designed (using glm gui) for each experiment to compare data to a specified number of random comparisons. These random comparisons, otherwise known as permutations, control the lowest potential p-value that can be resolved. For example, the lowest possible p-value when running 500 permutations is p=0.002, whereas it is p=0.0002 with 5000. Higher numbers of permutations do not increase the chance of finding effects, but rather increase the confidence of a p-value. Sample size and study design usually determines the optimum number of permutations; the default 5000 was chosen.

The general linear model regressed the BOLD time series for each individual subject's components, as well as the corresponding spatial maps for each component, against the group. Voxelwise testing was subsequently used to probe for statistical differences, and all comparisons were corrected with Bonferonni (0.05/number of comparisons) (Figure 2.9).

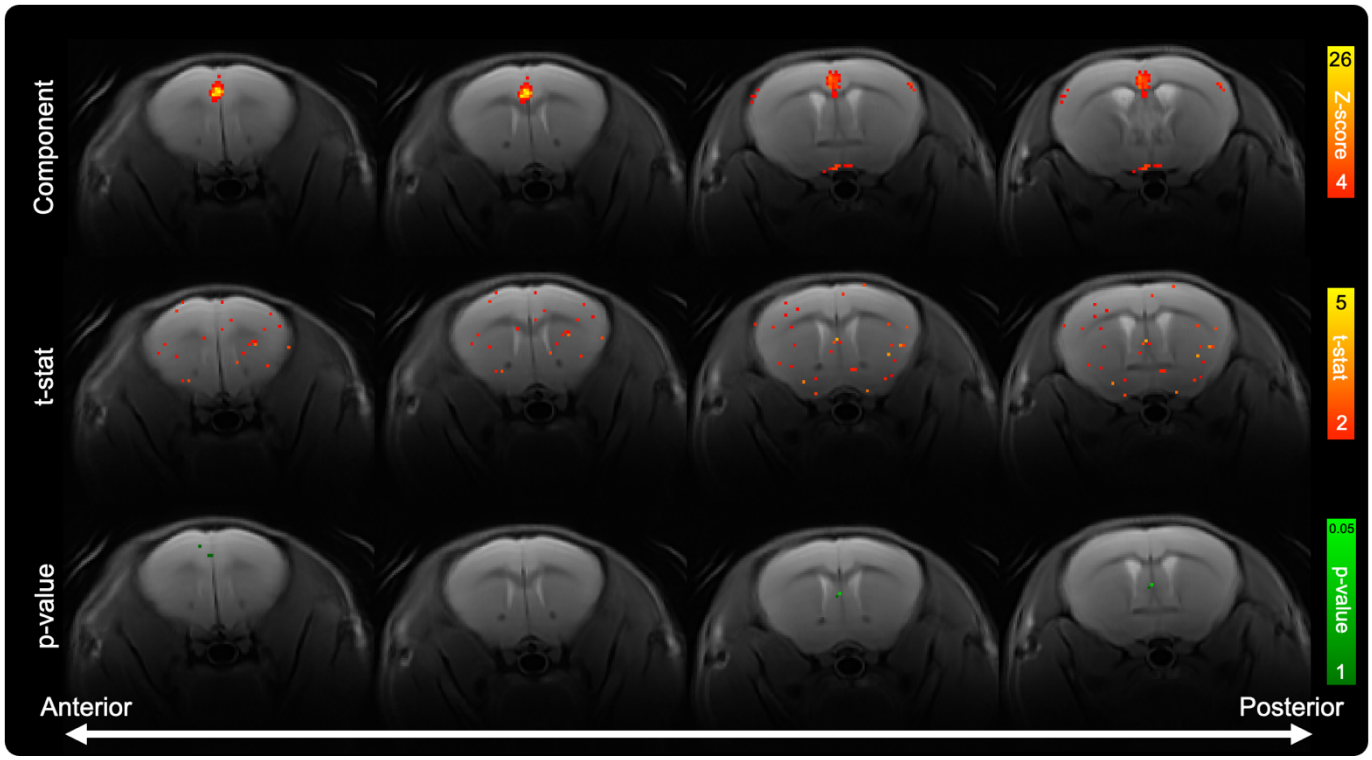


Figure 2. 9. Example of an output from a dual regression. (Top) A BOLD signal component is overlaid onto the T_2-weighted subject template. (Middle) The t-stat displays voxels throughout the brain that are highly correlated with the component. (Bottom) The p-value displays whether the correlation was significantly different in each voxel between groups, according to the design of the general linear model.

2.2.5. Hierarchical network analysis

Qualitative analysis of the components was also performed. The Matlab (version R2018a) toolbox FSLNets (version 0.6) (Smith et al., 2013) investigated the correlations between all components and generated large scale connectivity matrices that were organized in a hierarchical fashion (the activity components that were most highly correlated were clustered together) (Figure 2.10). Matrices were produced only for positive and negative correlations. FSLNets was also used to manipulate the matrices.

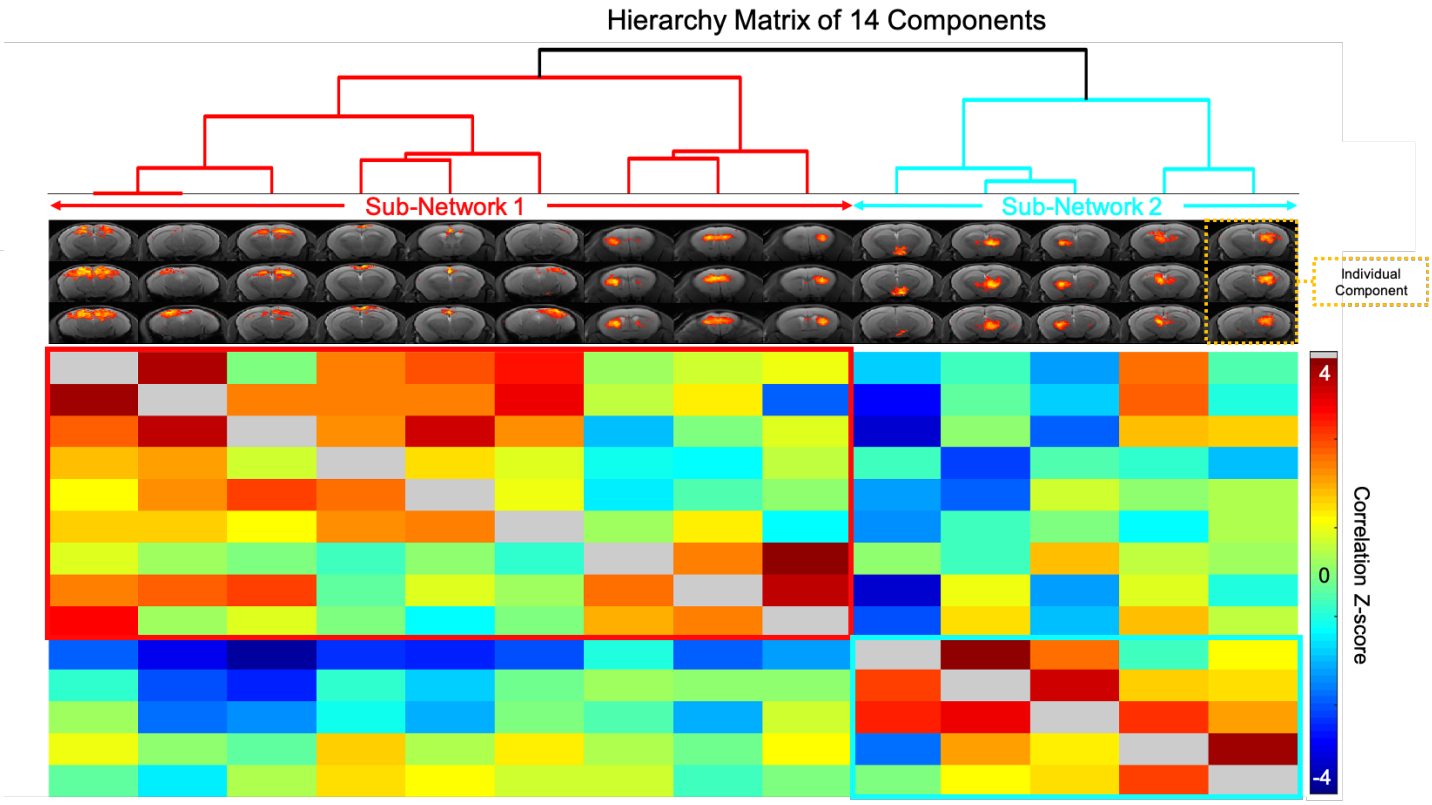


Figure 2. 10. Hierarchical connectivity matrix of 14 components. Each component is positioned adjacent to components in which the time courses are highly correlated (scale bar indicates the strength of the correlation). There are two distinctive sub-networks of clustered components (red = 1 and blue = 2).

2.2.5.1. Connectivity images

For visualization of sub-networks, three-dimensional glass brains were produced (Figure 2.11A). The fslmaths tool was used to group Allen regions into major brain structures of anatomical interest (e.g., whole brain, ventricles and hippocampus). ITK-SNAP (version 3.6.0, http://www.itksnap.org/pmwiki/pmwiki.php) was used to segment major brain structures into 3D surface projections.

ParaView (version 5.6.0, https://www.paraview.org/) was used to visualize the 3D surface projections. To import individual activity components, FSL was used to display the local maxima and eliminate voxels that were not part of the component. Subsequently, fslmaths was used to binarize the local maxima into a mask and the surface projection was prepared as per above with ITK-SNAP. Once the surface projections were imported into ParaView, they could be displayed as spheres and connecting lines were added manually, and colour coded to display the correlations between the components (Figure 2.11B).

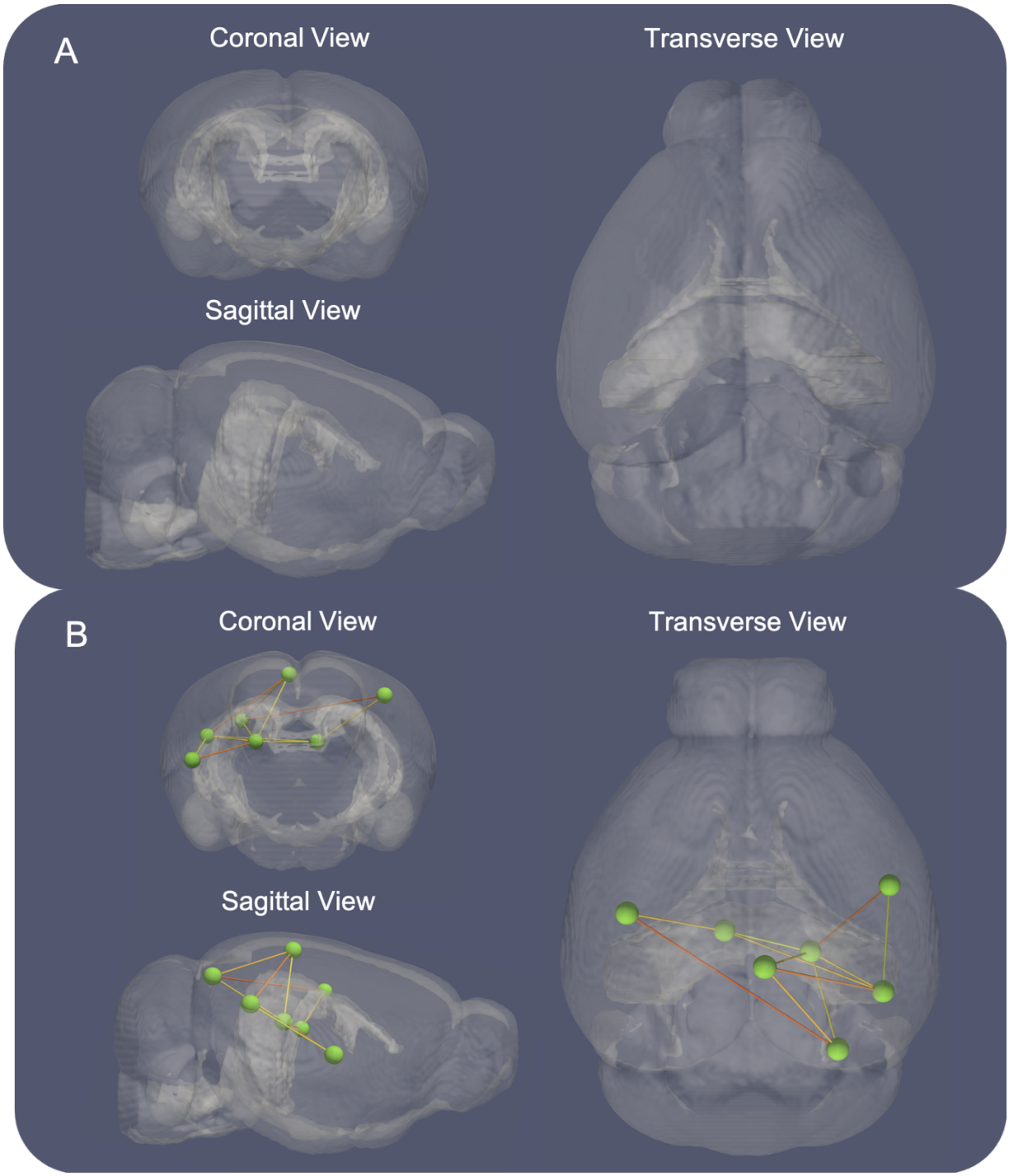


Figure 2. 11. A) The AMCA rendered into a 3D surface projection with the hippocampus and ventricles included to aid as a reference. B) Spheres represent activity components, while the connecting lines represent the correlation between the components. Note: Activity components are colour coded according to a hierarchical sub-network, and correlations are colour coded as per Figure 2.10.

2.2.6. Seed based analysis

A hypothesis driven approach was also used to investigate correlations among activity components in pre-determined regions of interest. The fslsplit tool was used to generate individual image files for each component. As per section 2.2.5.1, masks of components of interest were generated with fslmaths, and the general linear model was used for a voxelwise comparison of the component of interest to the other voxels in the brain.

2.2.7. Graph theory

Network features were quantitatively calculated with the Matlab (version R2018a) Brain Connectivity Toolbox (Rubinov and Sporns, 2010) (https://sites.google.com/site/bctnet/). A proportional threshold was used to preserve the strongest correlations (range 10 - 90%) within a connectivity matrix, whilst maintaining density (keeps the same number of connections across groups). The resulting matrices were examined to determine which proportional threshold provided the highest small world-ness value. The proportional threshold was then applied to matrices generated from each individual subject. Subsequently, global efficiency, modularity and transitivity were calculated for each subject, as well as local efficiency for each component for each subject. Network characteristics were analysed for group differences using SPSS (version 26).

2.3. dMRI pipeline

An overview of the dMRI pipeline is displayed in Figure 2.12.

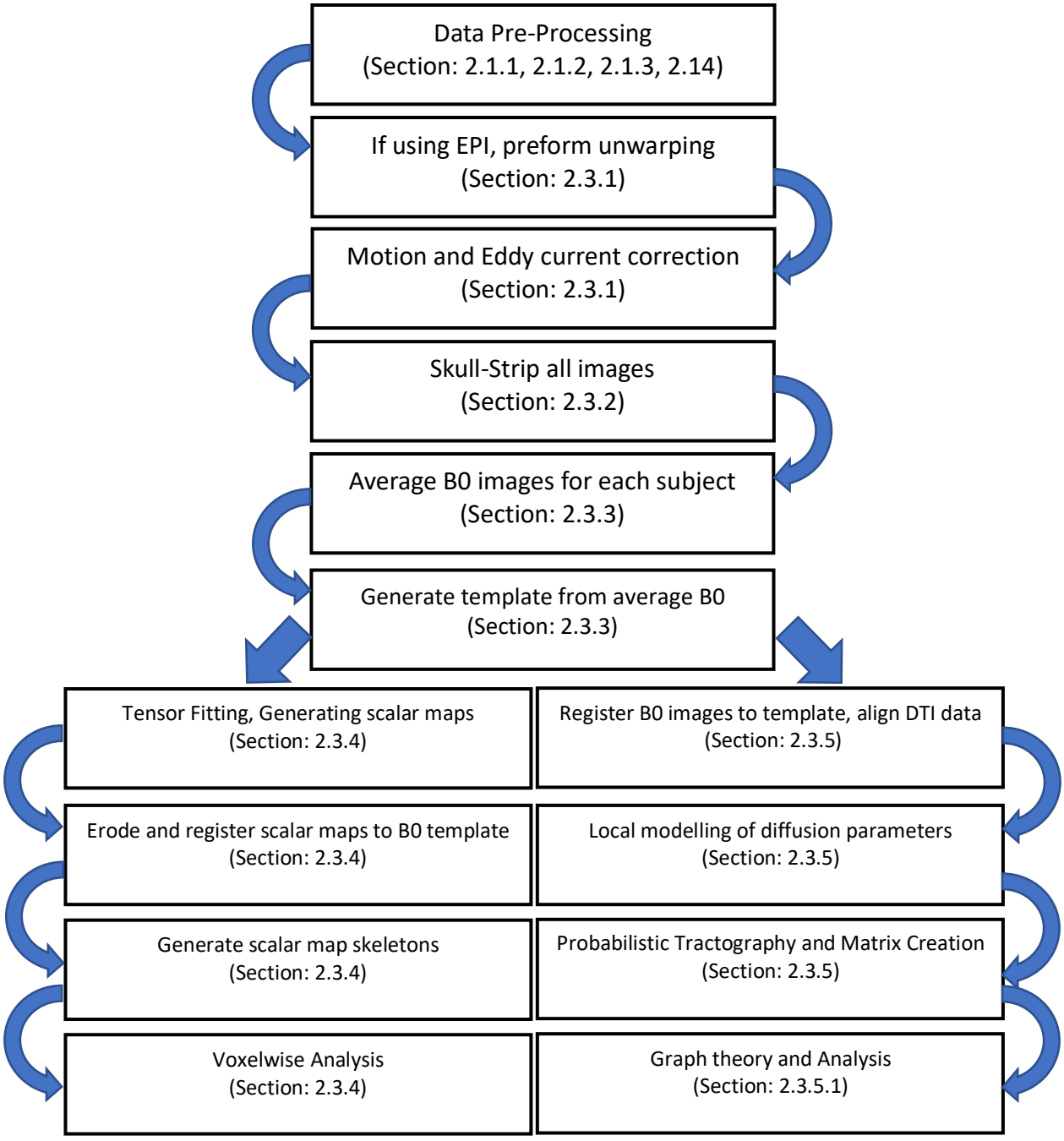


Figure 2. 12. Flow chart of the dMRI pipeline. Each box displays the process and the corresponding command line tool.

2.3.1. Correcting for image distortion

As is the case with the rs-fMRI data, dMRI data is acquired using EPI, therefore image distortions need to be corrected. In addition, the intensive use of gradients induces eddy current distortions that can result in blurring and ghosting artefacts. FSL's TOPUP tool (Smith et al., 2004a) requires two non-diffusion weighted images with opposing phase-encoding directions. Originally described by Andersson and colleagues (2003), the distortion differences between the two images can be used to calculate a susceptibility induced off-resonance field that can be used for correction. Subsequently, remaining motion and eddy current artefacts can be corrected with the eddy tool (Andersson and Sotiropoulos, 2016).

2.3.2. Skull stripping

Once image distortions were corrected, skull stripping was performed with the AMCA brain masks using the transformation files produced in sections 2.2.2 and 2.2.3.

2.3.3. Template creation and image registration

An EPI template of all subjects was prepared from the non-diffusion weighted (B0) images. These images were extracted from individual subject 4D dMRI data sets using fslroi, and averaged using fslmaths. Results were inspected, as blurring could indicate failure of image distortion correction (motion or magnetic field drift). The antsMultivariateTemplateConstruction2 was used to average each subject's B0 images into a study template (Figure 2.13).

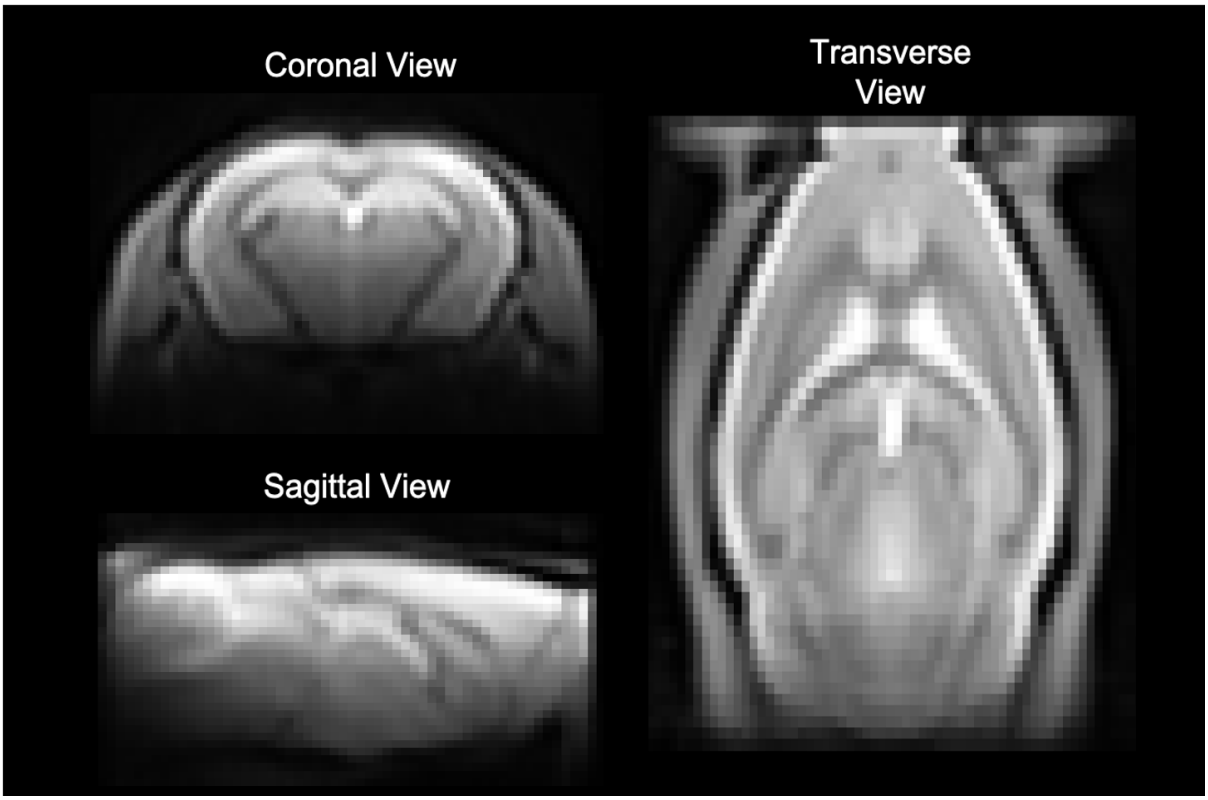


Figure 2. 13. Average B0 study derived template.

The antsRegistrationSyN.sh tool was then used to register the individual subject B0 images to the averaged B0 template. Subsequently, the antsApplyTransforms tool applied the transformation files to each subject's original 4D dataset with the nearest neighbour interpolation option.

2.3.4. Tract based spatial statistics

Scalar maps (FA, AD, MD, and RD) were calculated by fitting each voxel to a diffusion tensor using FSL's DTIFIT (Figure 2.14).

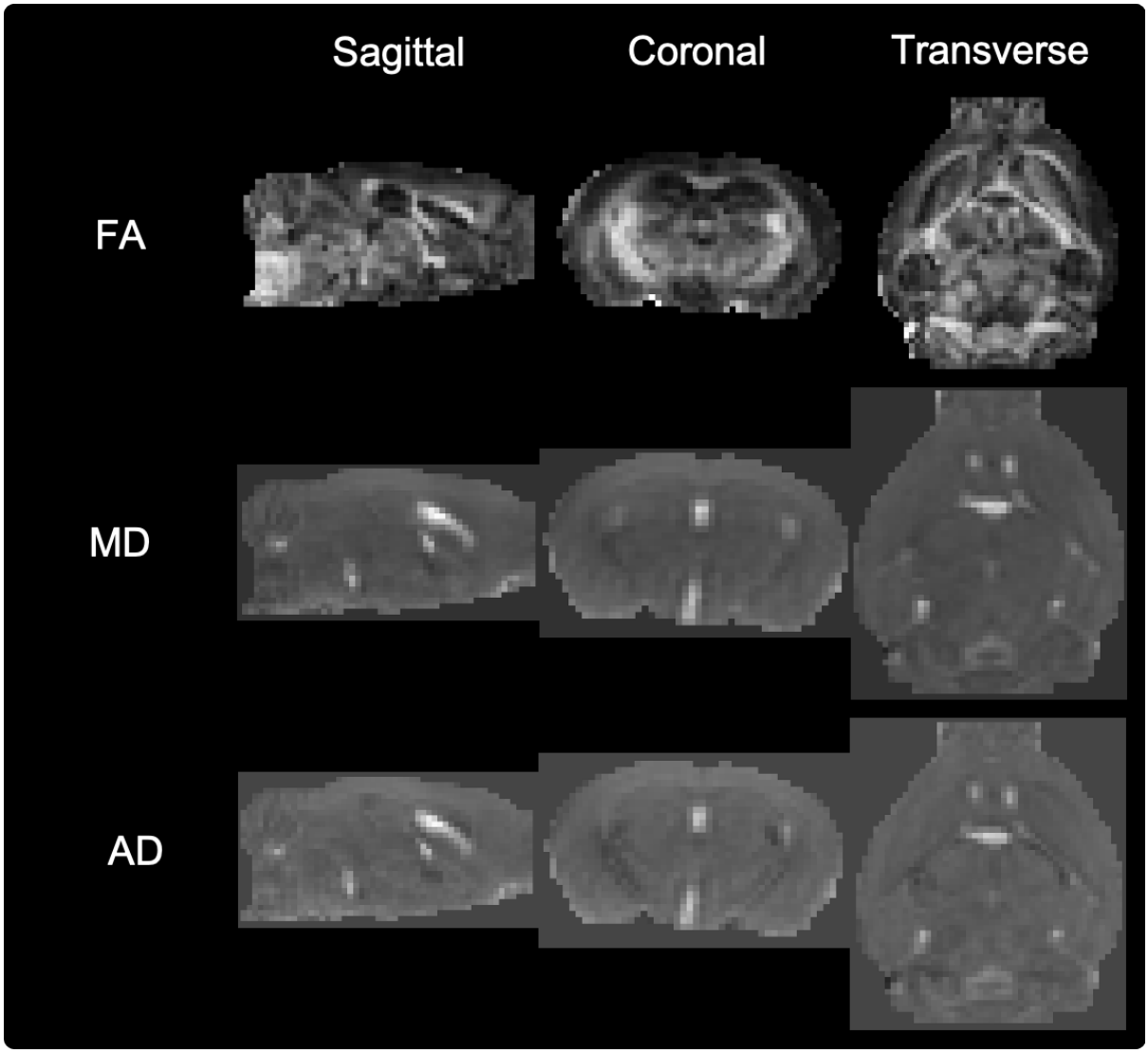


Figure 2. 14. Representative scalar maps from an individual subject.

Tract base spatial statistics (TBSS) from the FSL toolbox (Smith et al., 2006) was used to remove brain surface edges, align scalar maps, threshold and lastly generate a group based FA skeleton for voxelwise comparisons. For the first stage, the highly variable voxels of the brain surface were eroded, and end slices were removed to provide distinctive borders while reducing variability. Non-linear registration was used to align all the individual subject FA maps. Since rodents have less WM than humans, FA maps can be difficult to register. In this situation, the antsApplyTransforms tool was used to assist with FA alignment by taking advantage of the transformation files produced when individual data sets were registered to the average B0 template. All the registered FA maps were used to generate a mean group FA

map. Then the mean FA map had a threshold of 0.4 applied to remove non-WM voxels and generate a mean group FA skeleton (Figure 2.15).

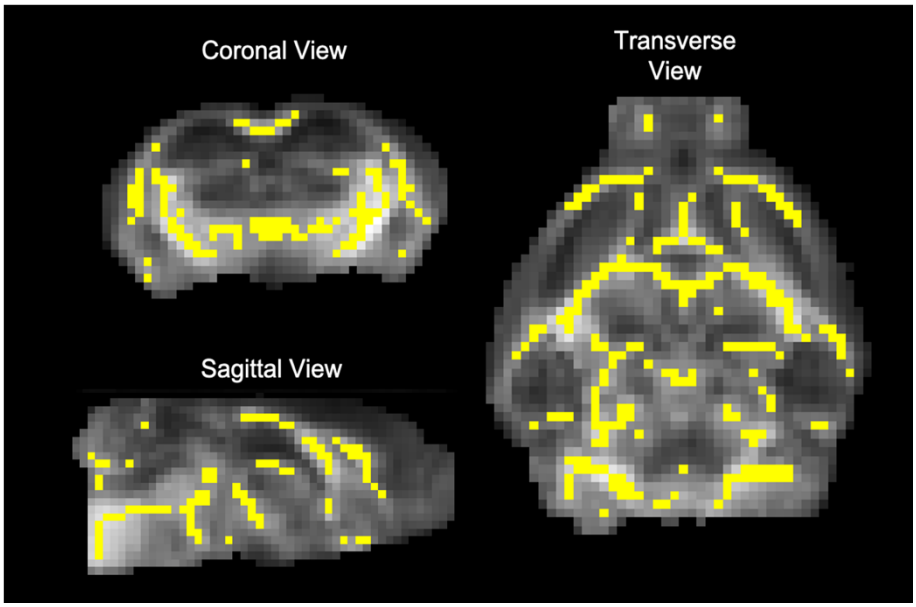


Figure 2. 15. The FA skeleton average generated from all subject FA images is displayed in yellow. Areas with a high FA value are highlighted in yellow on a background FA map average.

A general linear model was designed (glm gui) to specify group and voxelwise comparisons for the scalar maps using FSL's randomise tool (Winkler et al., 2014) (Figure 2.16).

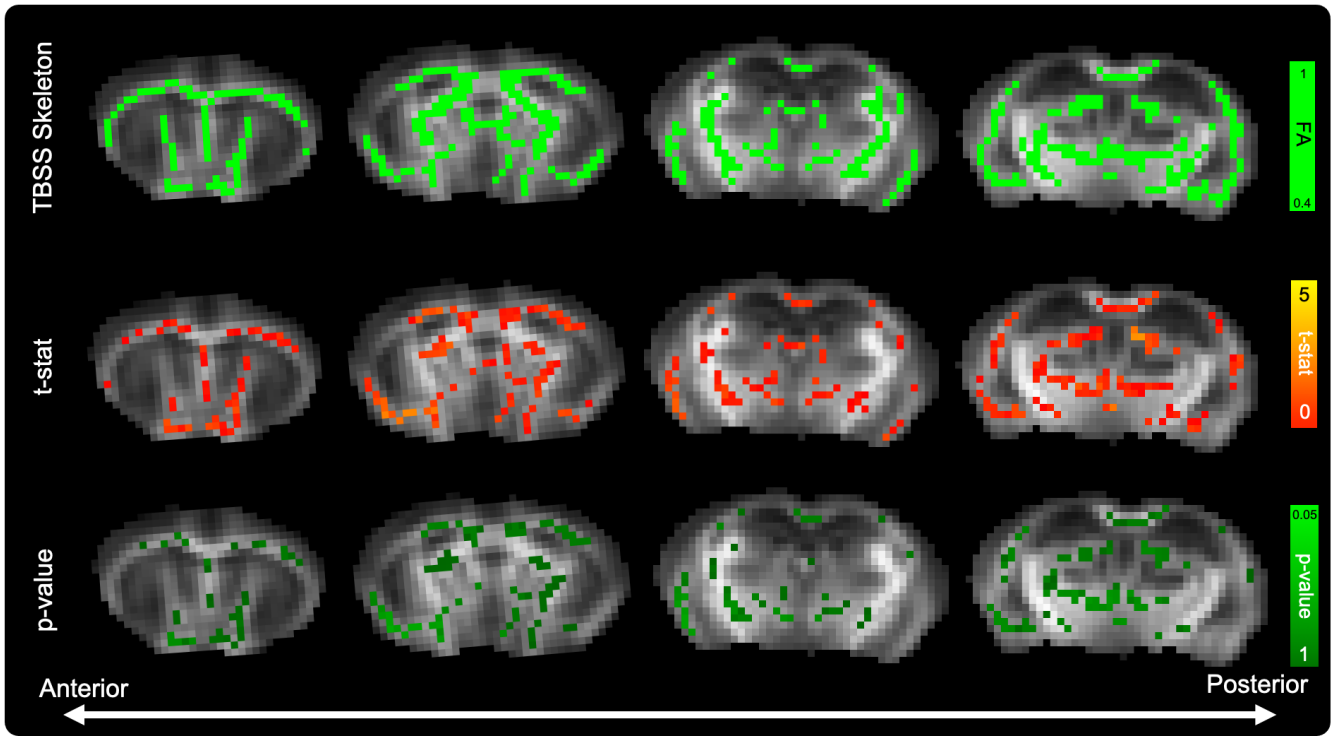


Figure 2. 16. Voxelwise comparisons of FA values between groups. (Top) TBSS skeleton with the strongest FA values used for the analysis overlaid onto the average FA skeleton. (Middle) The t-stat displays voxels throughout the brain that have a different FA values between groups. (Bottom) The p-value displays whether the t-stat difference was significantly different in each voxel, according to the design of the general linear model.

2.3.5. Probabilistic tractography

Using the transformation files generated from registration of individual B0 images to the B0 template, and a nearest neighbour interpolation, all the raw 4D dMRI data was registered into the same space. FSL's Bedpostx tool (Jbabdi et al., 2012) was used to fit a probabilistic diffusion model to each voxel. The model estimates all potential fibre orientations and calculates the possibility for error. Subsequently, FSL's probtrackx2 was used to run probabilistic tractography (with the network option) on the output of Bedpostx for each subject. This generated a connectivity matrix for each subject that quantified the number of fibres between each structure. Connection weights of all structural matrices were $\log_{10}$ scaled (Oh et al., 2014) (Figure 2.17).



Figure 2. 17. Structural connectivity matrix from an individual sham subject's dMRI dataset. Regions determined by the AMCA atlas.

2.3.5.1. Graph theory

All graph theory procedures were performed as described in section 2.2.7, except directional based variations were used instead of the non-directional equivalent.

Chapter 3. Development of the data processing pipeline for evaluation of structural and functional connectivity in the mouse

3.1. Introduction

Some of the most widely used and gold standard MRI processing software tools designed for humans are included in FSL (Smith et al., 2004a; Woolrich et al., 2009; Jenkinson et al., 2012). Overall, FSL offers the most extensive package in terms of data pre-processing and analysis. Our initial aim was to adapt FSL tools for rodent data, but this was not always straightforward. Certain stages of the pipeline were more effectively achieved with other data software packages. For example, ANTs (Avants et al., 2011) generally offered greater performance and adaptability after visual inspection compared to FSL for bias correction and registration in the mouse. It was better able to account for differing tissue contrasts between *in vivo* MRI scans and the *ex vivo* histological template. Other steps had to be re-worked completely, for example, skull stripping to remove non-brain tissue was achieved by optimizing a series of registrations and transformations. The preclinical functional and structural processing pipeline overviewed in Chapter 2 was therefore developed from adapting and testing a series of software packages, tools, and options. This chapter explains the processes employed and the reasoning behind the choices that resulted in the pipeline described in Chapter 2. The Results and Discussion sections are therefore combined.

3.2. Results and Discussion

3.2.1. Data pre-processing

3.2.1.1. Data conversion

Bru2nii (https://github.com/neurolabusc/Bru2Nii) was used to convert the rs-fMRI scans into NIFTI format. However, for conversion of the dMRI data, it did not automatically extract the b-vector and b-value information required for processing. Although this information can be extracted manually from the corresponding method text file, this can be time consuming and challenging for non-expert users without ParaVision methods file expertise. The Bruker2nifti package (https://github.com/SebastianoF/bruker2nifti) (Ferraris et al., 2017) was able to convert the dMRI scans whilst being able to automatically extract the b-vector and b-value information into corresponding text files. However, Bruker2nifti has the drawback that anatomical orientation information can be lost, particularly for data acquired with earlier versions of ParaVision.

3.2.1.2. Orientation confirmation

When it was necessary to adjust anatomical orientation of dMRI data, distinguishing between left and right was difficult due to the anatomical symmetry of the brain. A workaround was established by inputting the dMRI data into FSL's DTIFIT immediately after NIFTI conversion to view the primary diffusion direction (labelled V1). Ideally, the primary diffusion direction should align with the major WM tracts (Figure 3.1).

It is recommended to use a marker of left and right during scanning that is easily distinguishable when viewing. Certain groups developed more sophisticated markers that can be simply made for preclinical models, with screws that can be inserted into the skull to provide an accurate reference point (Glud et al., 2017). Tools have also been created in the AFNI software package (Cox, 1996) to solve potential lateral flip discrepancies between structural and corresponding functional human scans using a cost function analysis between the two images.

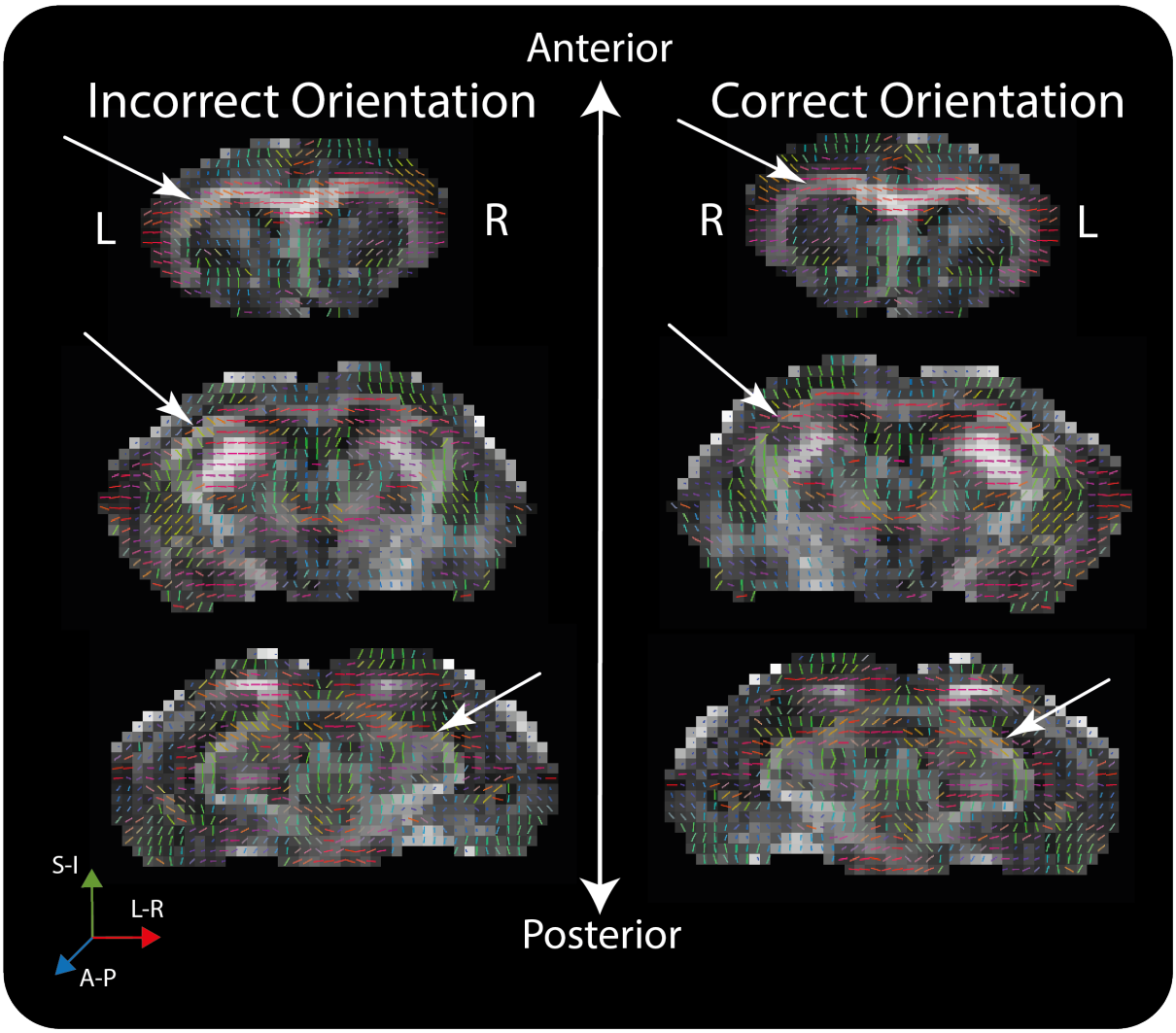


Figure 3. 1. Comparison of anatomical orientation differences between flipped left and right images. Primary diffusion directions are overlaid as coloured ellipse in each voxel of the FA scalar map. (Left) Incomplete corpus callosum demonstrates the anatomical orientation is incorrect between left and right as shown at each arrowhead. (Right) Complete corpus callosum demonstrates the anatomical orientation is correct between left and right again highlighted by corresponding arrowheads, therefore we concluded the right panel to be correct.

3.2.1.3. Bias correction

Low-frequency signal bias can affect image quality particularly if surface coils were used in the scanning setup. This can result in a smooth decrease of signal intensity in relation to the increased spatial distance from the coil. A range of tools have been developed to correct this bias field; FSL has the FMRIB's Automated Segmentation Tool (FAST), and we tested its effectiveness against ANTs N4BiasFieldCorrection (Tustison et al., 2010). Previous comparisons between these prominent bias correction strategies in clinical T_1 and T_2 weighted scans that included white matter hyperintensities (WMH) and stroke lesions reported better performance and consistency using FAST compared to N4BiasFieldCorrection (Valdes Hernandez Mdel et al., 2016). Displaying fewer distortions of hyperintensities in each image, however the quality of tissue segmentation, especially of pathology such as WMH was a determining factor in the quality of the bias correction in FAST. To our knowledge no comparisons have been done at the preclinical level between FAST and ANTs, therefore we ran a simple comparison within our data for each subject. Overall from visual inspection, we discovered that N4BiasFieldCorrection was better at identifying the source of bias in the rodent compared to FAST. The N4BiasFieldCorrection determined the signal intensity bias was most closely aligned to the superior aspect of the brain where the surface coil was placed, whereas FAST did not locate this bias (Figure 3.2). After bias correction with N4BiasFieldCorrection, tissue contrasts were more uniform throughout the image and this resulted in improved registration to the template.

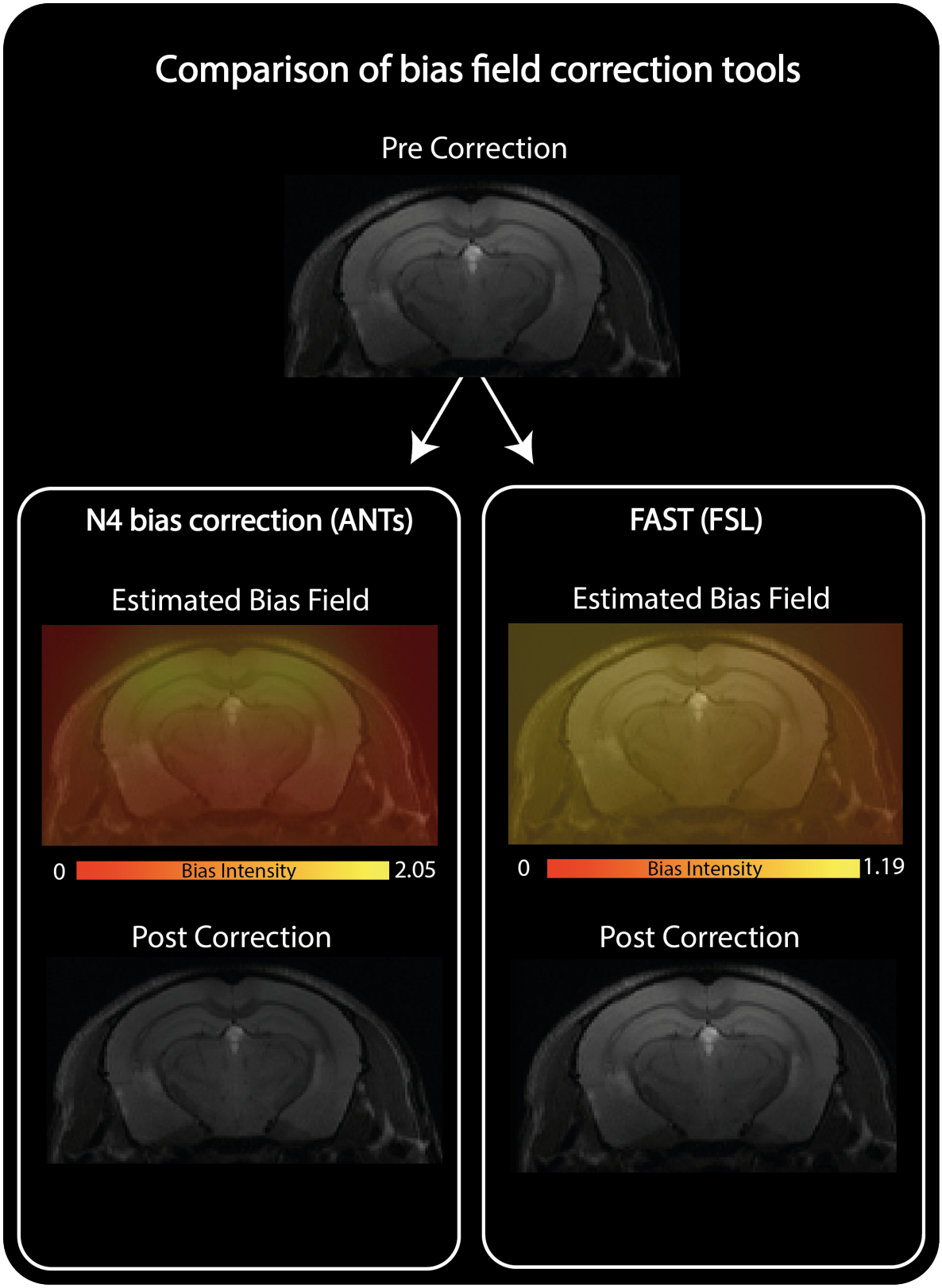


Figure 3. 2. Comparison of two different bias field correction tools (ANTs vs FSL) on a T_2 structural scan. Bias intensity determined by each tool is overlaid as a colour map. (Left) N4BiasFieldCorrection was more effective in locating the signal bias induced by the surface coil and resulted in a more homogenous image. (Right) FAST was less effective at determining the bias, and the corrected images still displayed a strong superior to inferior signal intensity bias.

3.2.2. rs-fMRI pipeline

3.2.2.1. Structural image registration and skull stripping

Registration is necessary for image analysis (e.g., voxelwise analysis, atlas parcellation) as correct alignment of all subjects can remove the variability in head anatomy and scanning position that might otherwise make the image analysis invalid. Linear registration is commonly used to align anatomy within subjects across different types of images. Rigid registration (6 degrees) uses rotation and translation across three directions (x, y and z) and the affine approach (12 degrees) builds on this by incorporating additional scaling and shearing in the three directions. Non-linear registration uses a higher level of elasticity through employing far more degrees of freedom and is usually effective when registering subjects that have slight variations in anatomical structure and with different levels of image distortion. We compared ANTs versatile linear and non-linear registration tool (antsRegistration.SyN) and FMRIB's Linear Image Registration Tool (FLIRT) and FMRIB's Non-linear Image Registration Tool (FNIRT). From visual inspection, both ANTS and FLIRT performed equally well with both outputs being identical for linear affine registration of structural images within and among subjects.

However at the non-linear level, slight differences were noticeable. It is generally recommended before FNIRT to have FLIRT to run previously on the dataset, and the additional FNIRT process resulted in much more substantive smoothing of structural images (Figure 3.3). In addition, all scans had to be scaled to up by a factor of 10, which in turn deleted anatomical orientation information. ANTs registration tools did not require scaling the data, smoothing was much less pronounced, and there was a slightly better alignment of WM regions (Figure 3.3).



Figure 3. 3. Comparison between registration techniques for an individual T_2 weighted scan to the subject derived structural template. (Left) FLIRT + FNIRT non-linear registration of an individual structural scan to the subject derived structural template (Middle). (Right) ANTs registration of the same subject to the template.

Registration of the *in-vivo* T_2 weighted MRI scans to the AMCA template was problematic due to the differences in tissue contrast and anatomical structure. The AMCA template was generated via serial two-photon (STP) tomography (Oh et al., 2014) using *ex-vivo* post-fixed brains removed from the skull. This difference in the imaging method, in addition to the non-uniform structural shrinkage of the brain as a result of *ex-vivo* fixation (de Guzman et al., 2016), meant not only tissue contrasts differed, but the possibility that fixation induced morphological differences in anatomy (Lerch et al., 2012). Without a suitable registration to the AMCA template, this atlas would be unable to be used for analysis. The solution to the problem of differing tissue contrasts, was to use a WM and grey matter tissue mask that excluded CSF of the AMCA template. This subsequent mask was input into the registration script, allowing CSF regions to be ignored during registration. Overall, using a grey matter

and WM mask was the simplest solution that did not involve altering the AMCA template directly.

Although employing the WM and grey matter mask excluded CSF, there were still misalignments when individual subject scans were registered to AMCA. This was due to the extreme non-linear warping required to shape an *in-vivo* brain to the *ex-vivo* AMCA brain. When investigating the misalignment of the non-linear registration, this was a result of weak WM and grey matter contrasts within individual subject scans. In an attempt to correct for poor tissue contrasts randomly present at the individual level, an average template of all the structural T_2 weighted images was created using the template creator provided in the ANTs toolbox (antsMultivariateTemplateConstruction2.sh). Registering this subject structural average template to the AMCA template resulted in the greatest alignment (Figure 3.4). Overall the ANTs registration tool (antsRegistration.SyN) (Avants et al., 2011) performed the greatest non-linear registration. FNIRT did not offer a comparable solution as images non-linear alignment was slightly reduced and images had to be scaled by a factor of 10. Subsequently, the corresponding AMCA atlas and masks could be transported to the average template space by applying inverse executions of the transformation files using additional ANTS tools (antsApplyTransforms). An identical approach was then used to move scans through different spaces (Figure 3.4).

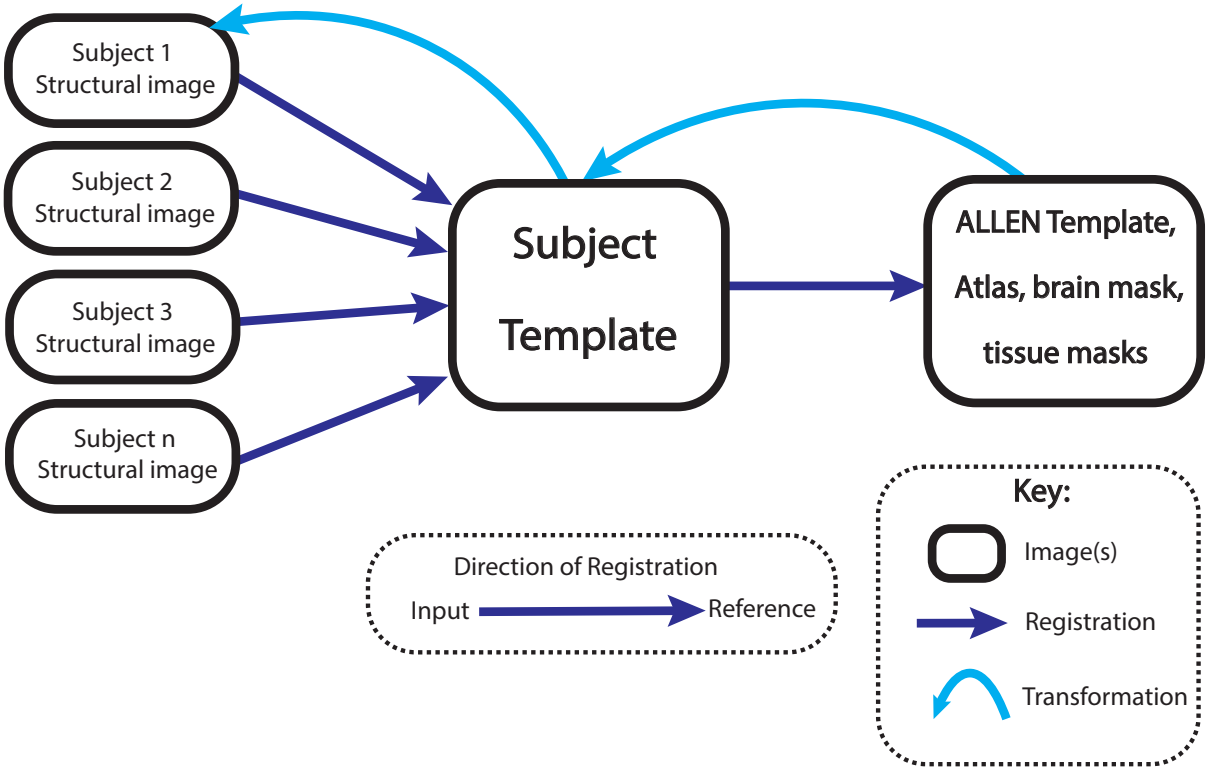


Figure 3. 4. Flow chart of the indirect registration method developed for the processing pipeline. The average T_2 template was registered to the AMCA template, and the inverse process was used to bring the AMCA template and atlases back into the T_2 template space. The same strategy was used to bring individual subject images into template space and vice versa.

The indirect two-step process displayed in Figure 3.4 drastically improved alignment compared to classic registration methods involving the direct registration of each individual subject straight to the AMCA template, comparable outputs are shown in Figure 3.5.

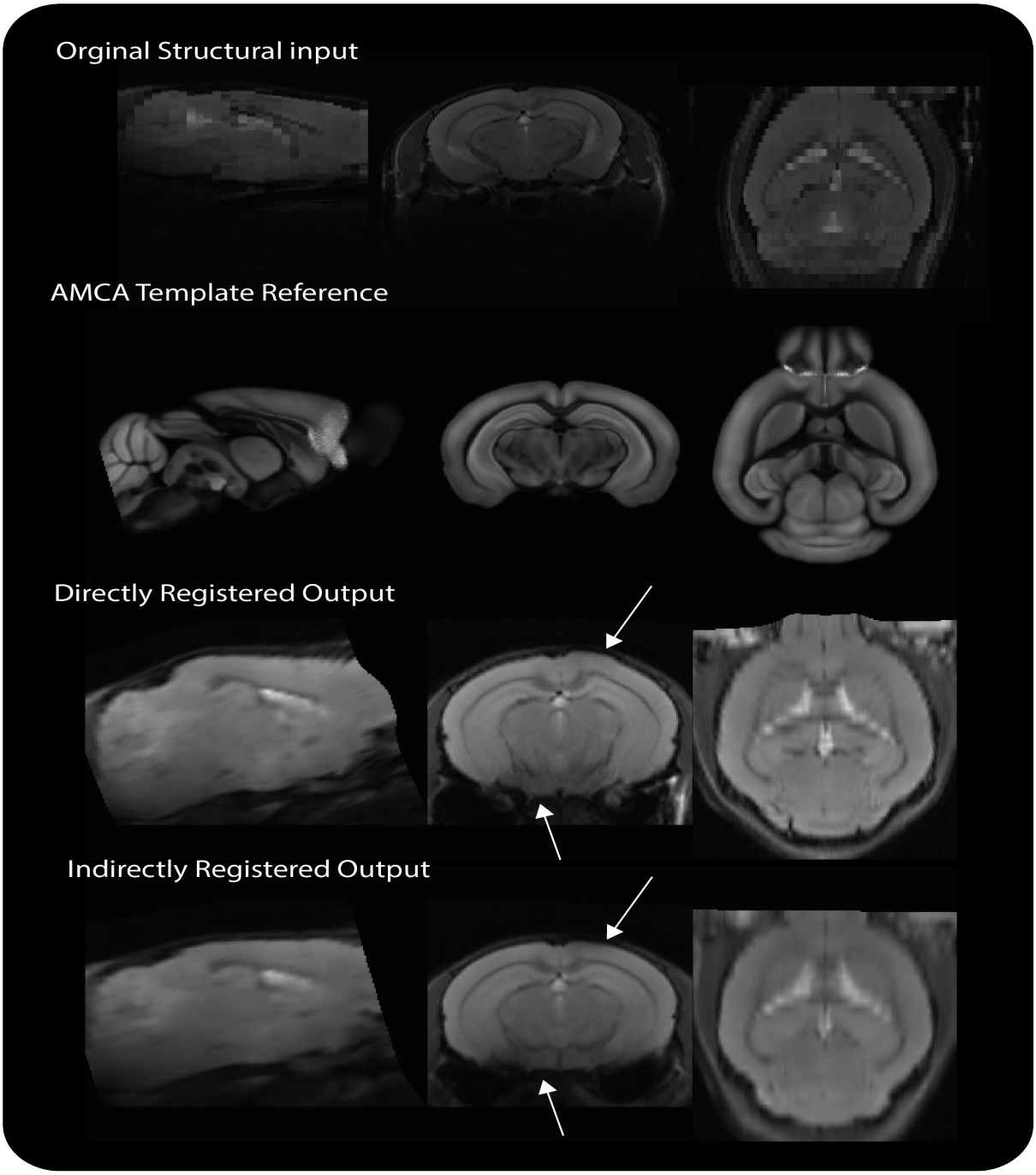


Figure 3. 5. Comparison of registration methods. Three views of an individual structural scan and the AMCA template. The directly registered output is the result of the individual subject registration to the AMCA template. The indirect registered output was created from initially registering the subject specific template to the AMCA template, and then registering individual scans to the subject specific template space and then using the transformation files from the initial subject-AMCA template registration to move each subject into AMCA space. When visually investigating the outputs, we determined the indirect method had greater alignments with the AMCA atlas (areas of improvements highlighted by white arrows).

Using the indirect two step transformation strategy, the AMCA whole brain mask was transformed into individual subject space and used for skull stripping.

Using the two step transformation strategy, the whole brain mask provided a visually superior skull stripping mask compared to FSL's Brain Extraction Tool (BET) (Figure 3.6). Since BET is designed for human data, we also compared the rodent adaptation of BET termed rodent BET (rBET). Although rBET did offer an improvement, the processing pipeline using the two-step transformation strategy did provide a superior skull stripping mask, particularly at the most anterior and posterior brain regions (Figure 3.7).

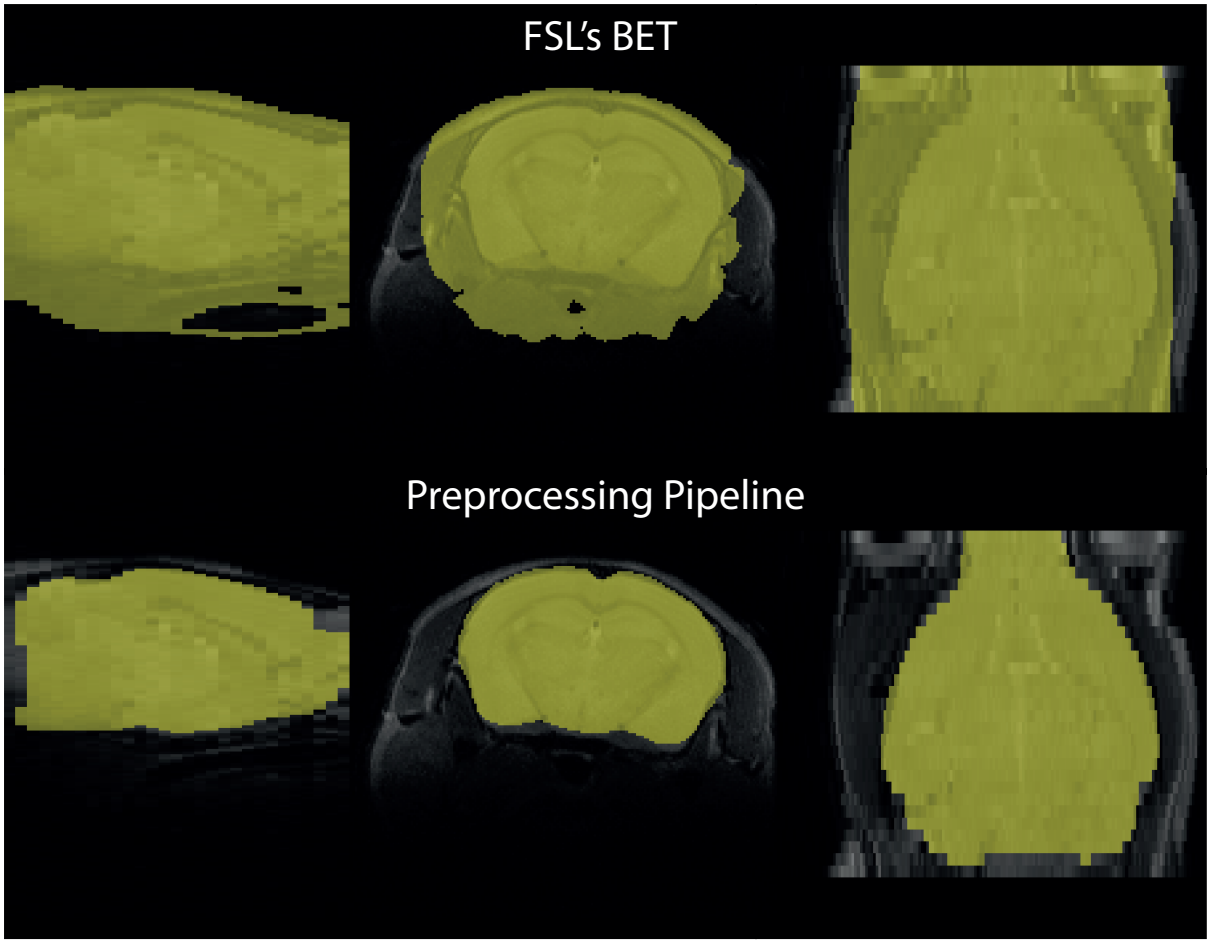


Figure 3. 6. Comparison of skull stripping methods. Skull-stripping mask (yellow) for FSL's BET (Top) and the method resulting from indirect registration protocols (Bottom).



Figure 3. 7. Illustration comparison of the output skull-stripping mask (highlighted in yellow) from both rodent adapted BET and the mask derived from the processing pipeline for a single T_2 weighted image. Each of the 3 comparisons is displaying different positions, primarily coronal anterior through to posterior positions. The view of each image is shown within every box as a coronal, transverse, and sagittal view, with the processing pipeline output on the top of each section and rodent BET in each bottom section. White arrows highlight the improvements in the differentiation of brain to non-brain tissue that concluded our decision to choose the processing pipeline method.

3.2.2.2. Functional image registration and skull stripping

Skull stripping was repeated for the functional images using the AMCA mask that was transformed into individual subject T_2 space.

Using the individual transformation files from the two step process to bring the functional images into the average T_2 template space posed a challenge. In particular, the rigid rotation caused a strong shearing in some of the thick slices (Figure 3.8).

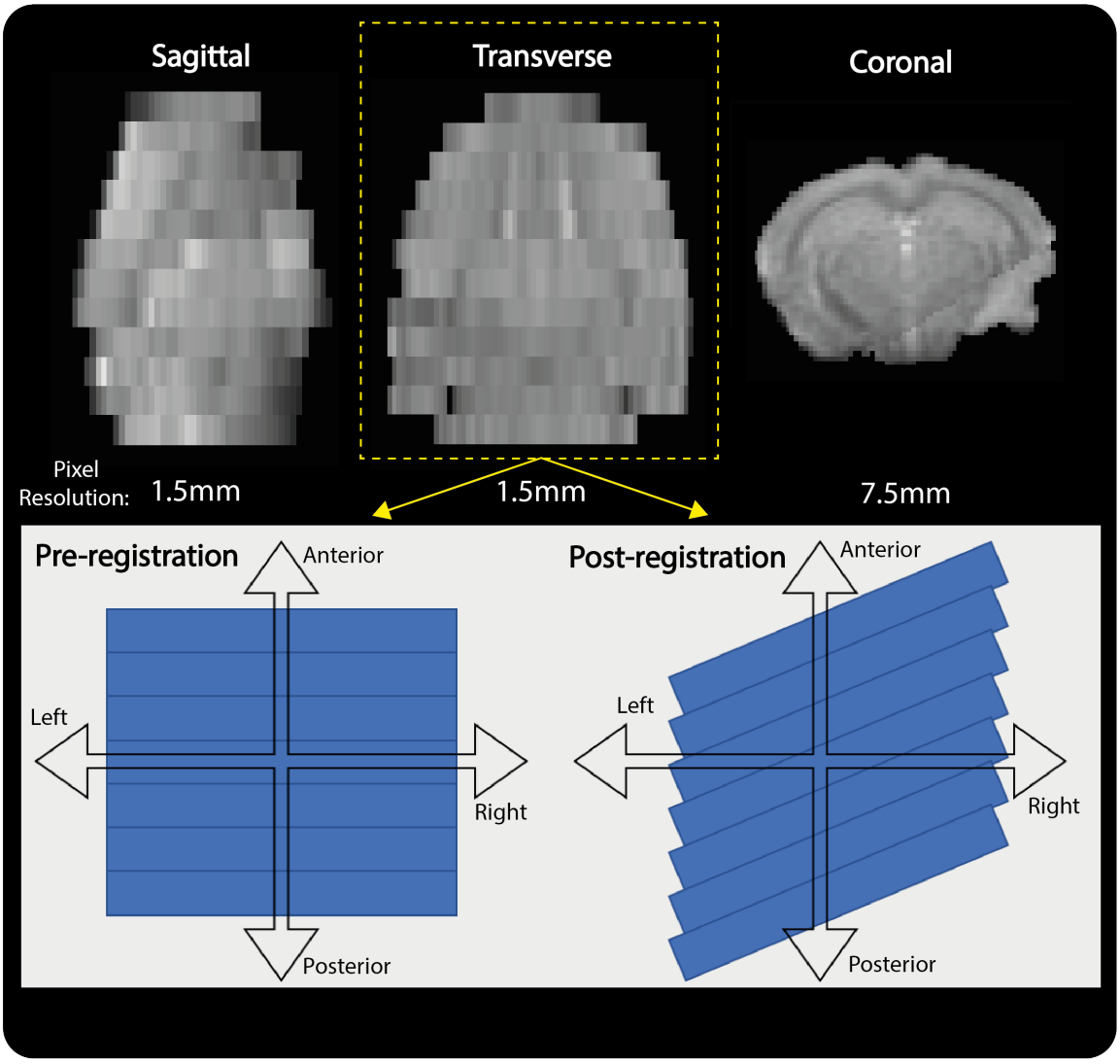


Figure 3. 8. Illustration of the slicing when rotational transformation from structural images was applied to the functional data. Shearing is most obvious in the coronal plane in which structures were prone to be cut out.

As it was still necessary to accurately align all the subjects for the rs-fMRI analysis, all the structural T_2 scans were registered to a single subject's rs-fMRI scan. Applying the corresponding transformation files to an individual subject rather than the subject structural template substantially reduced the shearing between slices in addition to keeping good alignment (Figure 3.9).

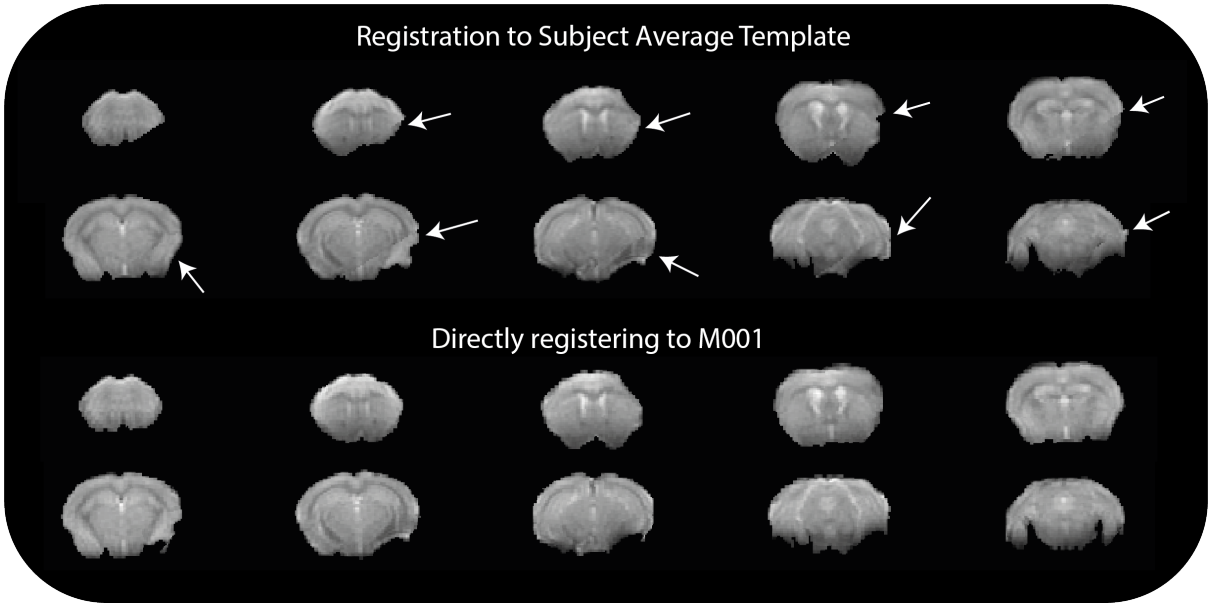


Figure 3. 9. Example displaying the comparisons of shearing generated by linear a registration (affine) of the functional rs-fMRI data as a result of rotational transformations. Shearing is most visible as lines through coronal slices when individual rs-fMRI images were registered to the average structural template. Shearing was improved by registering the structural images to an individual rs-fMRI data set (M001).

3.2.2.3. Determining motion

The first step towards manual classification of noise is to correct for potential motion throughout the timeseries. FSL's motion correction tool MCFLIRT (Jenkinson et al., 2002) reduces motion throughout a selected timeseries by performing a linear rigid registration (6 degrees of freedom) to realign all the volumes to a selected reference volume. The default reference is set to the middle volume of the timeseries. Once all volumes are aligned to the reference volume, MCFLIRT will output a report of the translational and rotational displacement (Figure 3.10). This motion report can help further understand the source of motion through displaying the intensity and frequency of displacement relative to the previous and overall timeseries volumes. Two common motion sources identified in this sample was a sharp sudden spike possibly from twitching, and a small consistent motion derived from a probable cardiac pulse (Figure 3.10, M018 estimated rotational motion) (Bajic et al., 2017). Sometimes long gradual displacements in a certain direction can also be present in certain subjects, this however can indicate possible signal drift as a result of the scanning hardware rather than the subject.

Although MCFLIRT corrected a large proportion of subjects, certain subjects still possessed considerable amounts of motion, whereby the majority of these displacements were driven by cardiac sources (weak consistent pulses throughout the timeseries). These remaining motion artefacts were removed during the single subject ICA cleaning process, using the MCFLIRT motion report as a reference. Similarities between the motion report and component timeseries in the MELODIC view can help identify a particular component as noise (component timeseries shown in Figure 3.12) (Griffanti et al., 2017). Whilst none of our subjects required removal of volumes in their timeseries, if a particular subject did display high amounts displacement, then removal may have to be considered. Removal can apply to either a single volume or a small subsection of scans that induce high amount of motion they prevent the output of clean signal components in the ICA cleaning process. This begins with identifying the selected volume, certain FSL command line tools such as 'fsl_motion_outliers' can be particularly useful in identifying large motion outlier volumes. After identification, the subsequent volume(s) are inspected by eye and then removed from the timeseries ('fsl_split' and 'fsl_merge' were used for this). Since all subjects require the same number of volumes in a timeseries for group-ICA, the missing scans should not be simply left out, the scan prior and post of the removed volume can be averaged together to

generate a fill-in volume for the timeseries. If a large proportion of the volumes in a subjects timeseries were affected by high motion, whereby no clear signal could be detected in the subsequent single subject ICA, then the worst-case scenario would be to remove the subject altogether.

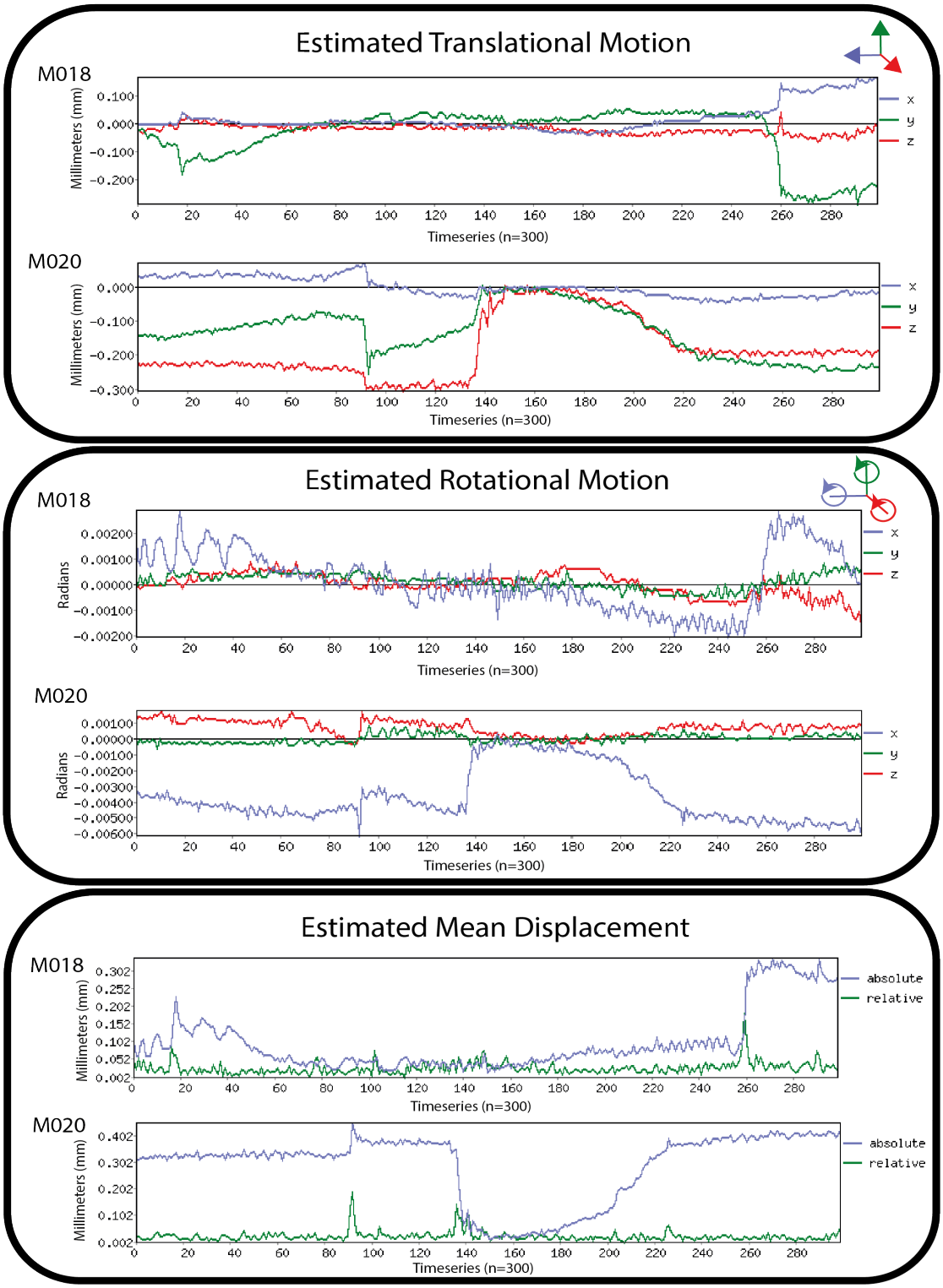


Figure 3. 10. Output from the FSL motion correction tool (MCFLIRT) (Jenkinson et al., 2002) from a subject with relatively little (M018) and high motion (M020). (Top, Estimated Translational Motion) Illustrates the translational motion from 3 degrees of freedom (x, y, z). (Middle, Estimated Rotational Motion) Illustrates the rotational degrees of freedom; roll, pitch, and yaw (respectively to the x, y, z axis). (Bottom, Estimated Mean Displacement) Illustrates the overall displacement throughout the whole scan within the subject timeseries absolute and relative to each previous scan. Scans had a repetition time of 1 second, therefore overall timeseries was 300 seconds (5 minutes) in total.

3.2.2.4. Removing noise at the single subject level

As a significant proportion of rs-fMRI data is generally contaminated with noise, the images first undergo cleaning at the level of the individual subject. High-pass filtering helps to remove a noise below the neurally driven BOLD threshold of 0.01Hz, but multiband and physiological artefacts still reside between 0.01 – 0.1Hz. Noise is classified at the single subject level depending on 3 major factors: spatial mapping, the oscillation pattern of the signal throughout the timeseries, and the power spectral density (Griffanti et al., 2017). Examination of these factors is often performed with automated methods that have been fine-tuned for use with human data and have not been modified for use in rodents. For example, the AROMA tool (https://github.com/maartenmennes/ICA-AROMA) or FSL's FIX tool, which uses a cluster of pre-evaluated manual training classifiers, preferably from the same study. Particularly for FSL's FIX, this process teaches the machine learning program in which it can accurately classify components in an automated fashion (Salimi-Khorshidi et al., 2014). Alternatively, classification of noise is a manual process that is time-consuming and requires a high level of expertise. To our knowledge, no previous research has been published recommending how to identify noise in this way in the mouse. We took guidance from Bajic and colleagues (2017) and incorporated knowledge from methods traditionally applied to human data.

3.2.2.4.1. Spatial mapping

Of the 3 major factors that identify whether a specific component is neurally generated, spatial mapping is considered the driving determinant (Griffanti et al., 2017). Generally, neural driven BOLD signal should cluster in grey matter regions. While we did observe this in the mouse (Figure 3.11, top), the clusters were more often scattered (Figure 3.11, bottom), which is somewhat expected as the data had not been smoothed at this stage. The scattered clusters were usually associated with a singular anatomical region rather than prominent RSNs, like the DMN, that can be observed at the single subject level in the human. The scattered clusters were included even though they often contained additional noise. Signal generated through physiological noise has been proposed to appear as a random spread of small clusters in WM, CSF, and blood vessels. We did not observe clustering in the white matter in the mice, but there was occasionally signal located in the CSF, or associated with major vessels like the Circle of Willis or the sagittal sinus. These clusters were occasionally

contaminated by motion such as CSF or vessel pulsation. We found that noise generated through motion was a very common finding, otherwise mentioned as a 'halo' around the brain (Shirer et al., 2015), this motion artifact was easily identified as a crescent and/or circular shape around or at least located at one edge of the brain. (Figure 3.11, middle).

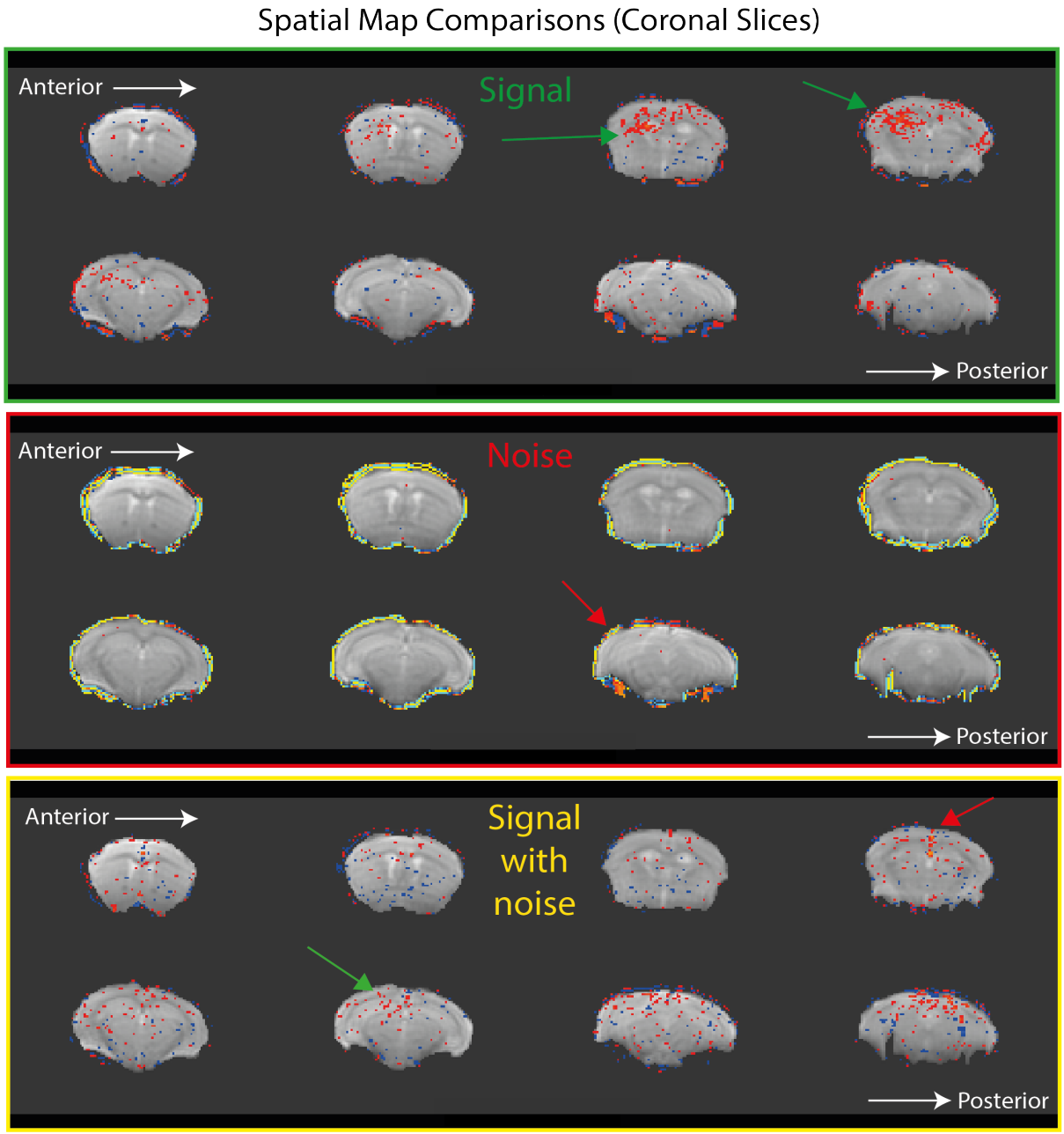


Figure 3. 11. Spatial maps displaying the variability among components from a single subject. Coronal slices are displayed anterior (top left) to posterior (bottom right). (Top, green highlight) Displays an example of neural driven signal clustering in grey matter (hippocampus predominantly). (Middle, red highlight) Example of motion, the signal is located outside of the brain. (Bottom, yellow highlight) Illustrates the most common type of component with a mixture of signal with low levels of clustering in grey matter regions. Green arrows indicate neurally driven signal and red arrows point to signal driven by noise.

3.2.2.4.2. Timeseries

The second major factor accounted to classify a certain component as BOLD or artifact was its associated signal throughout the time course. To be labelled as BOLD signal, a consistent oscillation pattern with no sudden jumps (Figure 3.12, top) was required. The presence of sudden jumps in this pattern was a sure indicator of motion (Figure 3.12, middle). To further confirm potential motion, the MCFLIRT motion report was used as reference to support suspected removal; as sudden jumps in the component timeseries in the MELODIC view would otherwise be positioned at the same volume in the MCFLIRT motion report.

The most common observed timeseries of a component labelled as BOLD signal in our sample was not completely consistent. Whereas the majority of these signal components did have some consistent oscillating patterns, they also possessed the occasional large, intermittent peaks associated with motion (Figure 3.12, bottom). These components were still labelled as BOLD signal however, as a component with some element of signal is advised to be kept rather than regressed out, as such a small proportion of the overall signal is BOLD driven (Griffanti et al., 2017). Arguably, including only the perfect components could generate cleaner components at the group level, but it is possible such components may not reflect functional connectivity at the whole brain level, but rather a small proportion of incomplete RSNs less affected by noise artifacts. Lastly it is possible for non-random artifacts (i.e. from cardiac sources) that may have been labelled as BOLD signal previously in the single subject ICA, to instead cluster with similar noise to form a single complete noise artifacts at the group level. In the current sample, 19 of the original 59 from the group ICA seemed to be complete noise and were subsequently removed.

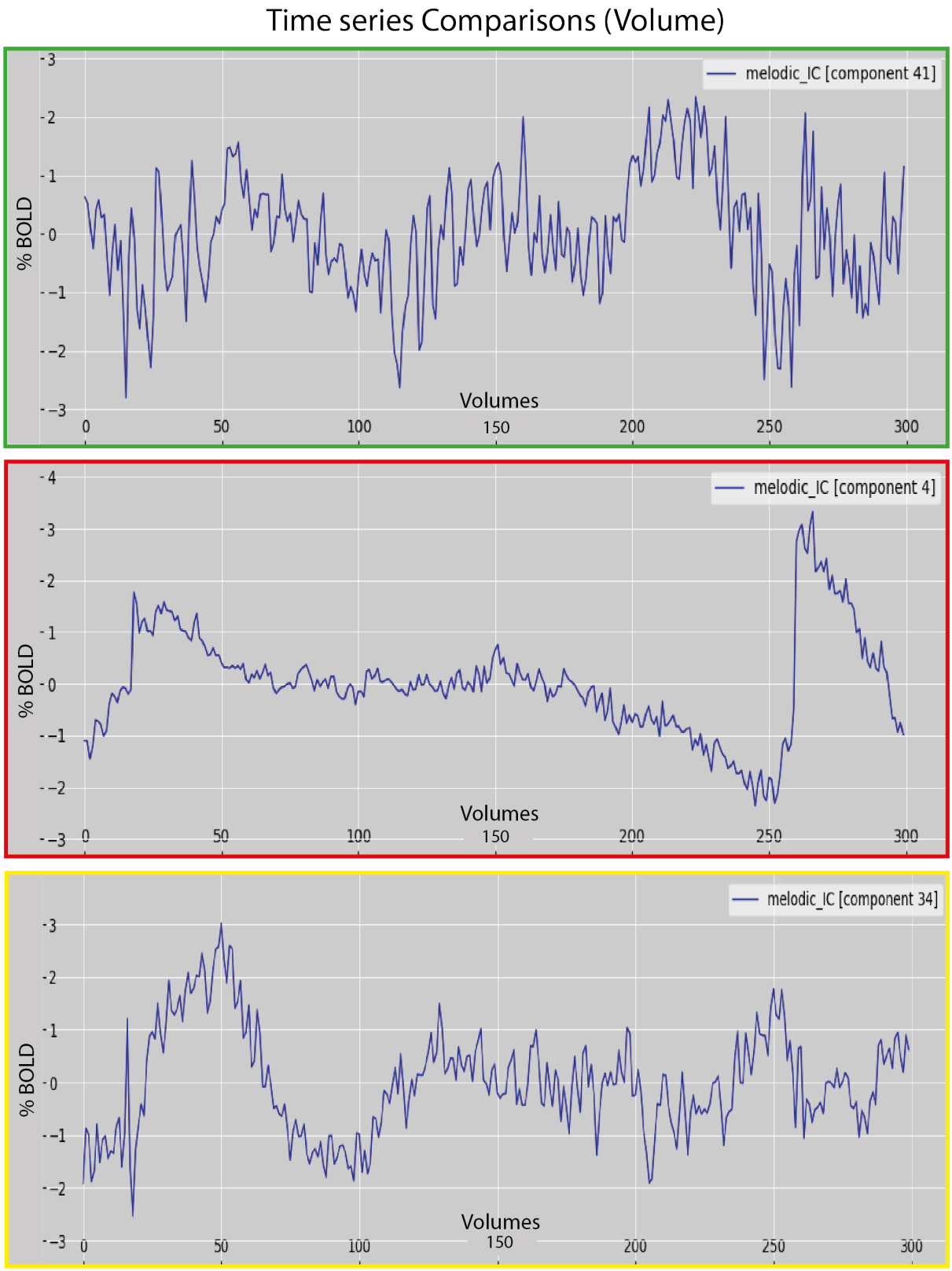


Figure 3. 12. Comparisons of 3 different component timeseries generated through single subject ICA. Signal intensity is displayed as a function of the number of repetitions. (Top, green highlight) A consistent oscillation pattern throughout the timeseries. (Middle, red highlight) A timeseries that was associated with noise due to motion indicated by the sudden increase in signal around 250 repetitions. (Bottom, yellow highlight) A component timeseries that had traces of signal and evidence of noise elements.

3.2.2.4.3. Power spectral density

As neurally driven BOLD signal should be located between 0.01 and 0.1Hz, at least one strong peak should be located in this range (Griffanti et al., 2017). There were indeed instances where a clear, singular peak was identified in the accepted range (Figure 3.13, top). Components were firmly classified as noise when there were no peaks in the accepted range but rather within the higher frequencies (Figure 3.13, middle). However, with the mice, the most typical scenario was a combination of BOLD signal and noise in which the majority of the signal was located within the correct range, but there were often multiple peaks (Figure 3.13, bottom). These components were included for further analysis.

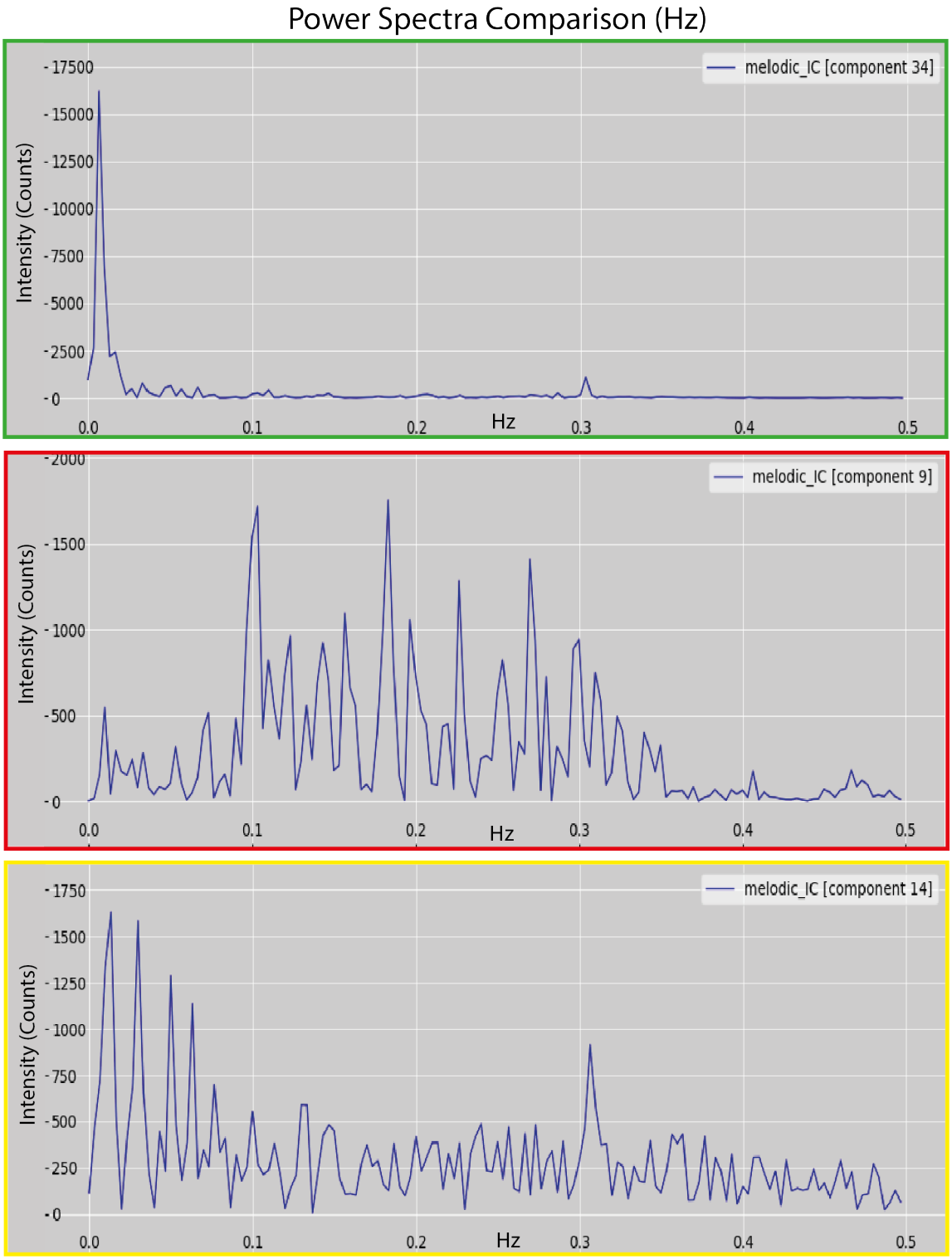


Figure 3. 13. Comparison of 3 different component power spectra generated through single subject ICA. Signal intensity is displayed as a function of frequency. (Top, green highlight) Spectra clearly indicative of a neurally driven component, with a singular peak between 0.01 and 0.1 Hz. (Middle, red highlight) Clear noise component with frequencies residing in the middle of the frequency ranges. (Lower, yellow highlight) The majority of the signal components also contained aspects of noise, with several peaks located at the lower end of the spectra.

3.2.2.5. Group level independent component analysis

After registration and spatial smoothing, the group level ICA was performed on the entire cohort of animals. First however, a decision needed to be made on what group of subjects to perform group level ICA on. For example, performing the analysis on only a control group would generate components that are unaffected by the treatment/condition of interest; this might be closer to average healthy mouse RSNs. This offers an advantage of generating more complete RSNs and easier interpretation if there are large differences between the groups. However, separating groups can also result in less sensitivity and therefore statistical power to detect differences in component strength. In contrast, performing the analysis on the entire cohort provides greater sensitivity when comparing components that exist in both groups (hybrid maps), however certain RSNs maybe incomplete from including the clinical group also (Bijsterbosch et al., 2017). The option to derive group-ICA maps from the whole study sample or just the control group is dependent on the sample size and study question. For example, the clinical and sham groups may require to be used to reduce variance if the individual groups are too small. Moreover group-ICAs generated by Werner and colleagues (2014), calculated group-ICA through both clinical and control samples. As a result, RSNs like the DMN network appeared split into two separate networks, however specific cortical and sub-cortical components such as the cingulate, supplementary motor area, medial and lateral prefrontal cortex were still individually sensitive enough to detect changes, but not as one complete network. In contrast, research comparing network differences between chronic pain conditions and healthy controls used a set of group-ICA components that were generated from a previous healthy cohort (Baliki et al., 2014). These included; DMN, salience, sensorimotor, frontoparietal and visual networks. Directly comparing these RSNs, group differences in chronic pain was specific to the DMN. The decision to include a particular clinical group or timepoint is dependent on the research question and group size. If the investigation is more exploratory or low group size, then sensitivity maybe more important and both groups should be used. Otherwise if comparing a specified complete RSN is critical, then generating normal components that more accurately reflect healthy RSNs from baseline data or control group would be recommended.

Previous mouse rs-fMRI research has shown a high variability in component dimensionality. It is possible to select the ideal number of components you would like the analysis to detect, and this has ranged from 15 (Sforazzini et al., 2014), to 30 (Zerbi et al., 2015), to 70 (Bukhari et al., 2017) and 100 components (Sethi et al., 2017). Therefore, to assess an optimal parcellation for our data, we ran three different group-level MELODICs; one with 15 (Figure 3.14), another with 30 (Figure 3.15) components, and a data driven approach that automatically generated an optimal number of components through estimations of the predictable amount of variance that can be explained from the data quality (Figure 3.16). Following Bajic and colleagues (2017), we assessed whether the components resembled distinct RSNs. However unlike widespread RSNs that output in human ICA (Baliki et al., 2014; Werner et al., 2014), none of the individual components in any of the three varying ICA dimensionalities resembled known or previously reported RSNs.

Two commonly reported mouse RSNs, homologous to the human and primate are the DMN and salience networks. These RSNs have been primarily identified through a hypothesis driven method known as seed-analysis. This method essentially displays the whole brain correlations of one or more specific anatomical regions. For example, seed-analysis at the retrosplenial cortex, a region regarded as a central node of the mouse DMN analogue (Zerbi et al., 2015; Grandjean et al., 2017b), displayed a wide range of positive correlations. These regions included the; cingulate, ventral hippocampus, temporal, prefrontal and orbito-frontal cortices (Sforazzini et al., 2014), regions similar to other rodent RSNs (Lu et al., 2012). In contrast, the components output from the ICA of the exact same data, displayed the bilateral regions of the DMN split into individual components. Similarly, a second major network identified as the mouse salience analogue has been described when bilateral seeds placed in the anterior insular regions showed high correlations to; dorsal anterior cingulate, ventral striatum and nucleus accumbens (Sforazzini et al., 2014). Again, this pattern displays similarities to the salience network counterpart of the human and primate (Di Martino et al., 2008; Ham et al., 2013).

In the mouse, none of these network analogues discovered through seed-analysis have yet to be identified as complete as a single component using data driven ICA (Zerbi et al., 2015; Bukhari et al., 2017; Bukhari et al., 2018), or has been labelled as the DMN but only consists of certain nodes of the mouse DMN (Grandjean et al., 2017b). However, one potential solution to still view large whole brain mouse RSNs through ICA is to cluster highly

correlating component timeseries together and then investigate each sub cluster. Widely known as a hierarchy matrix, it was first used in the mouse ICA by Zerbi and colleagues (2015), allowing the investigation of whole brain interactions between components and identifying possible large scale RSNs.

The components generated from the current sample differed slightly depending on the dimensionality selected. Group-ICA maps from the 15 dimensionality displayed a strong bilaterality, resembling part similarity to ICA-maps of the same dimensionality (Sforazzini et al., 2014). A large proportion of the ICA-maps, however, were difficult to anatomically define due to a lack of clustering and high scattering of signal (Figure 3.14, components; 7, 10, 11, 12). At the 30 dimensionality (Figure 3.15), some ICA-maps became more anatomically distinct, whilst maintaining a certain amount of bilaterality. Although a large proportion of components were not as anatomically clear, and bilateral compared to similar research at the same dimensionality (Zerbi et al., 2015), it is possible that these differences could be explained as result of differences in anaesthesia. Whilst still unsure, we ran an ICA using an automatically determined dimensionality. A total of 59 components were generated, which, overall displayed the strongest anatomical distinct signal components (Figure 3.16). This change could have been as a result of the higher dimensionality, parcellating elements of noise from signal components. Though majority of components were still unilateral, we decided the more anatomically distinct and cleaner components was more favourable for stronger interpretations of components during analysis.

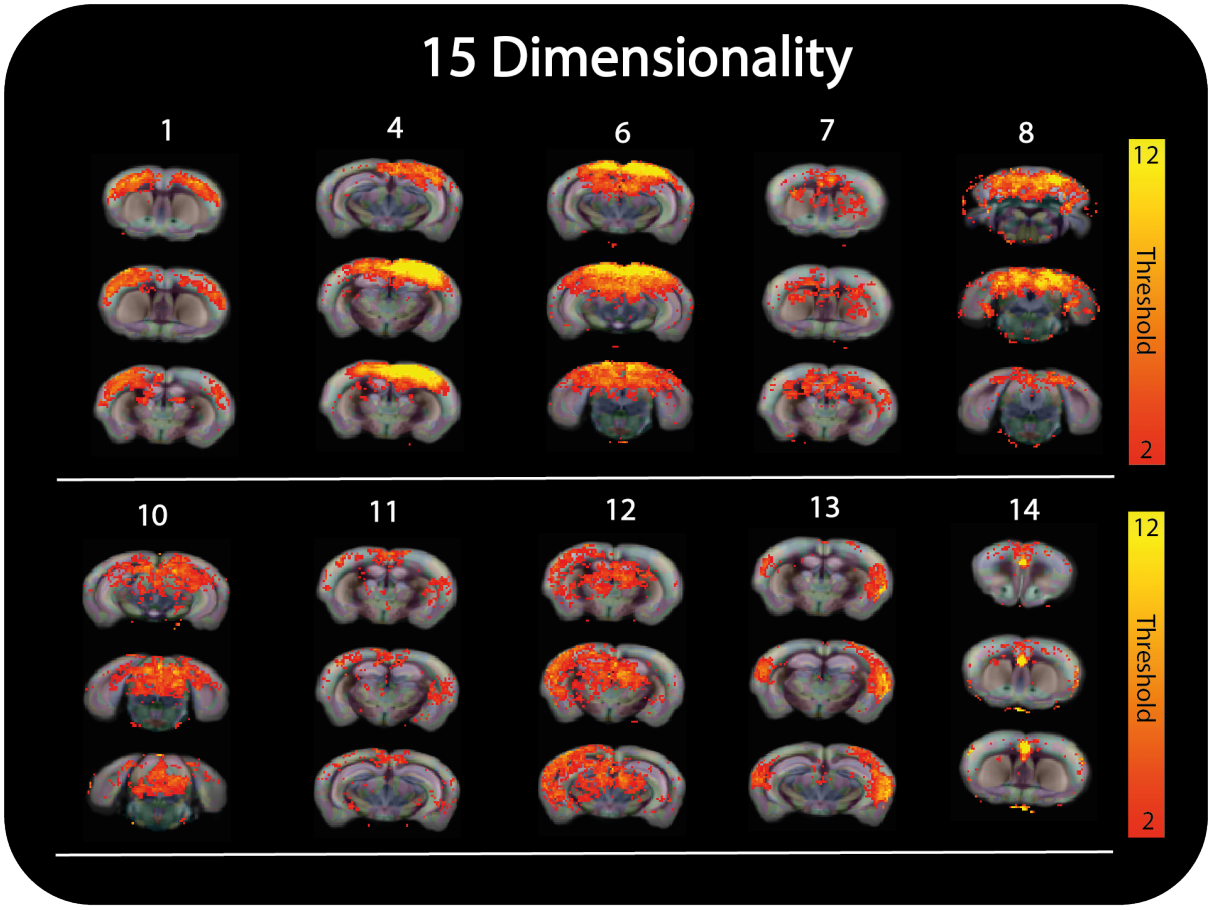


Figure 3. 14. Neural driven components from a 15-dimensionality option. Ten of the resulting components are overlaid on 3 coronal slices from the AMCA template and transparent atlas background. Although majority of the components are bilateral, a large proportion (6, 7, 10, 12) cover the majority of the brain, making it difficult to distinguish between anatomical regions. Note: scale bars refer to the z score threshold.

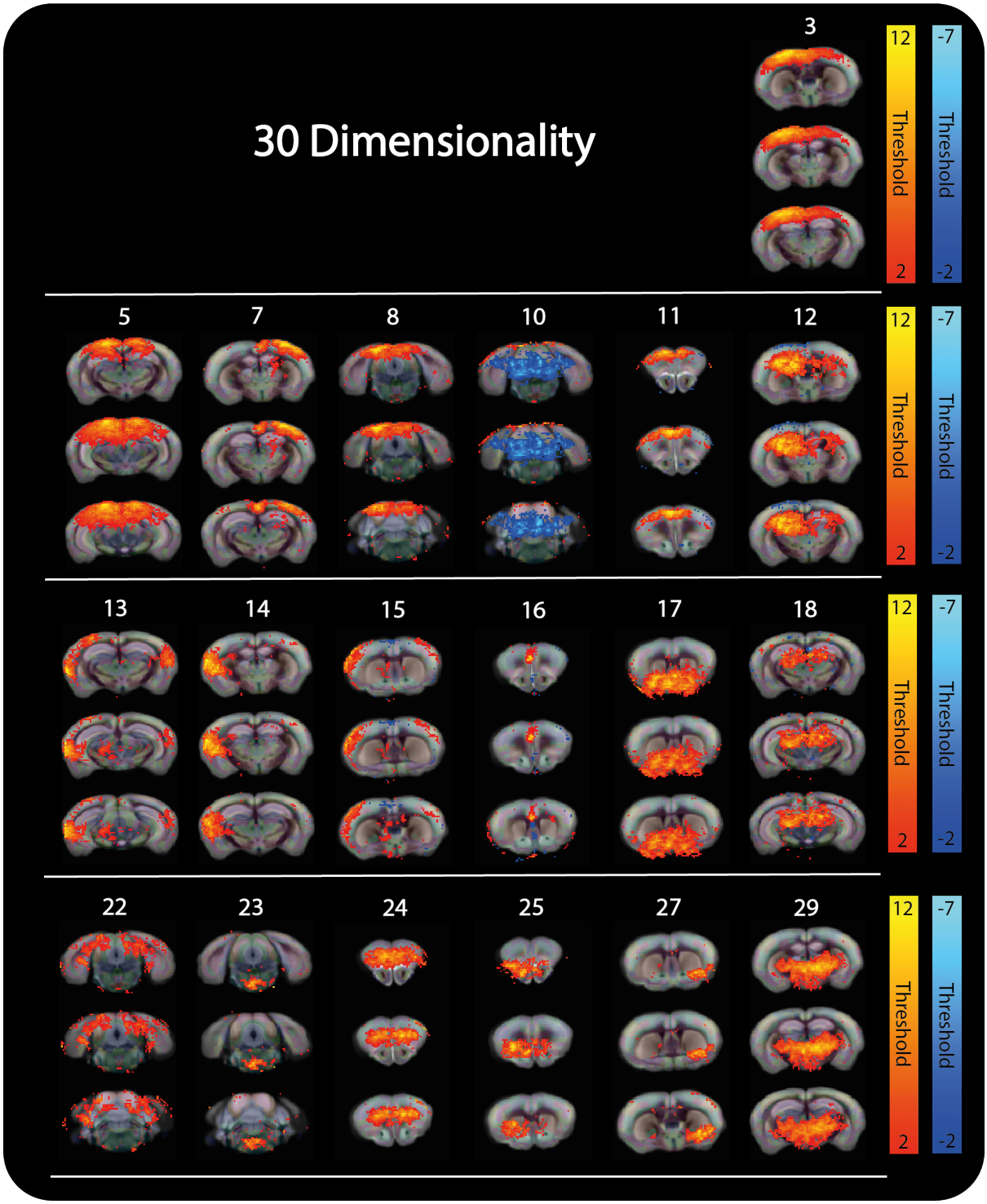


Figure 3. 15. Neural driven components from a 30-dimensionality option. Nineteen of the resulting components are overlaid on 3 coronal slices from the AMCA template and transparent atlas background. Components are parcellated into more distinct anatomical regions. Negative z-score thresholds were included at this dimensionality option as a neurally driven component consisting of primarily negative BOLD signal was output (component 10). Note: scale bars refer to the z score threshold.

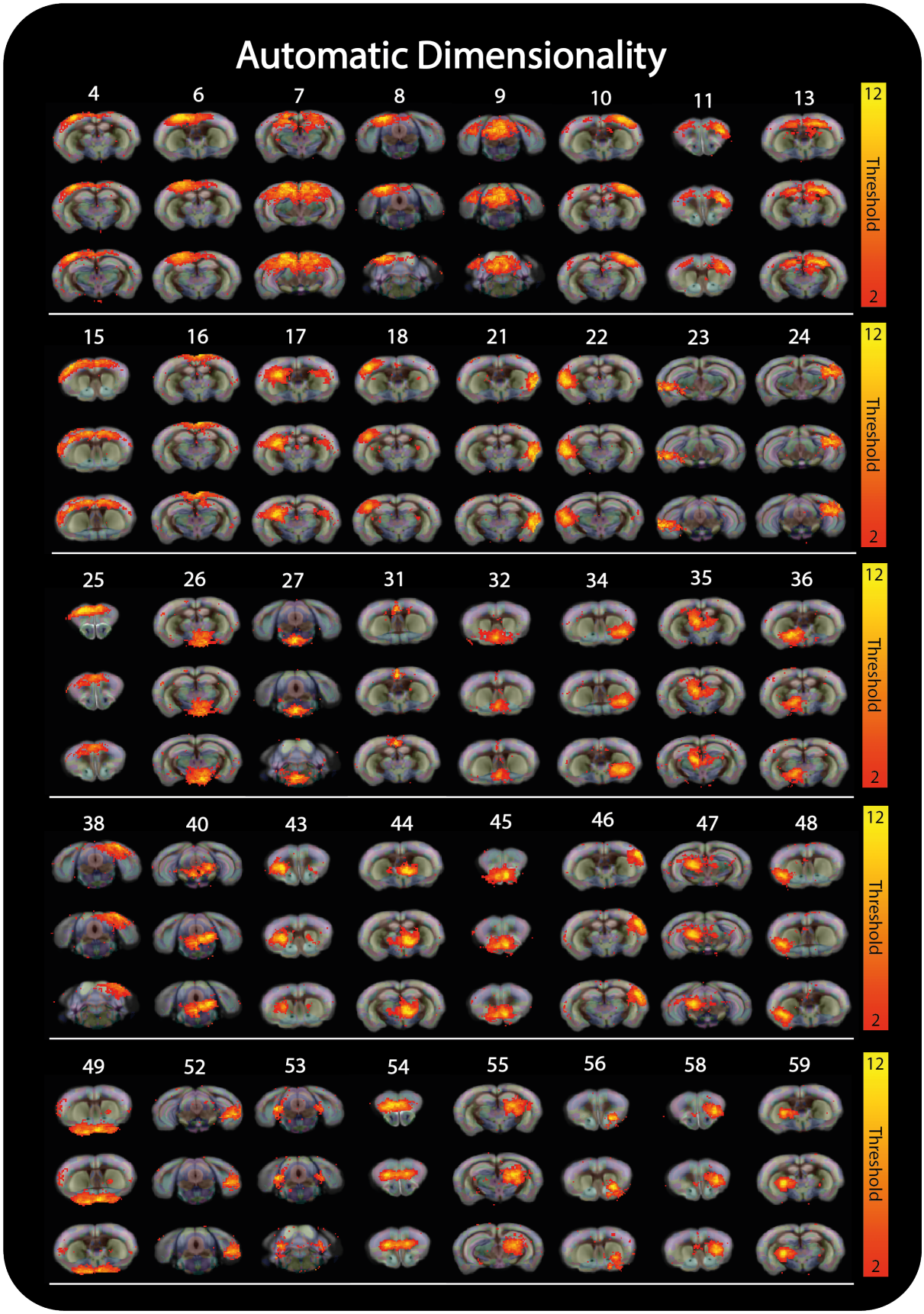


Figure 3. 16. Neural driven components from an automatic dimensionality option. Forty of the resulting components are overlaid on 3 coronal slices from the AMCA template and transparent atlas background. Note: scale bars refer to the z score threshold.

3.2.2.6. Hierarchical network analysis

Although a great deal of noise was removed at the single subject level ICA, there was still some noise driven components that were clearly visible in the power spectra at the group level (Figure 3.17).

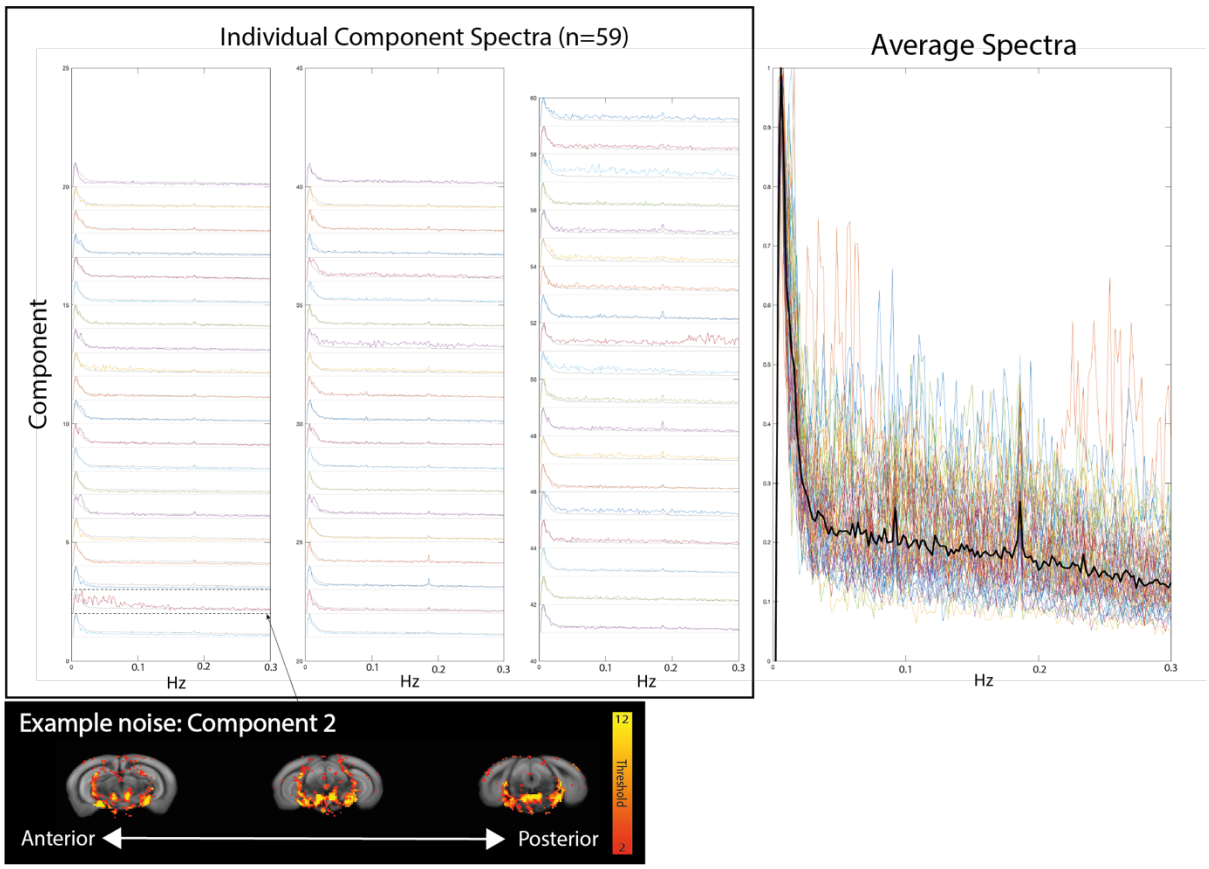


Figure 3. 17. Power spectra for a series of components. (Left) Individual component power spectra are displayed alongside a spatial map of an example of a noise component that is suggestive of CSF. Note: scale bars refer to the z score threshold. (Right) Combined power spectra for each component with the average indicted by a black line.

We investigated two strategies to remove noise components during FSLnets: aggressive (removes suspected noise components and their associated variance found in the timeseries) and unaggressive (just removes suspected noise component) component removal. Similar to single subject ICA cleaning used previously and similar ICA studies (Zerbi et al., 2015), after comparing the average Hz spectra of both techniques (Figure 3.18), the non-aggressive removal was chosen. This was the most effective as the average timeseries kept a more preferred power spectra peak that is indicative of neurally driven BOLD. Overall, we were surprised to learn that additional removal of the variance associated with artefactual components worsened the spectral distribution of the data for the remaining clean components.

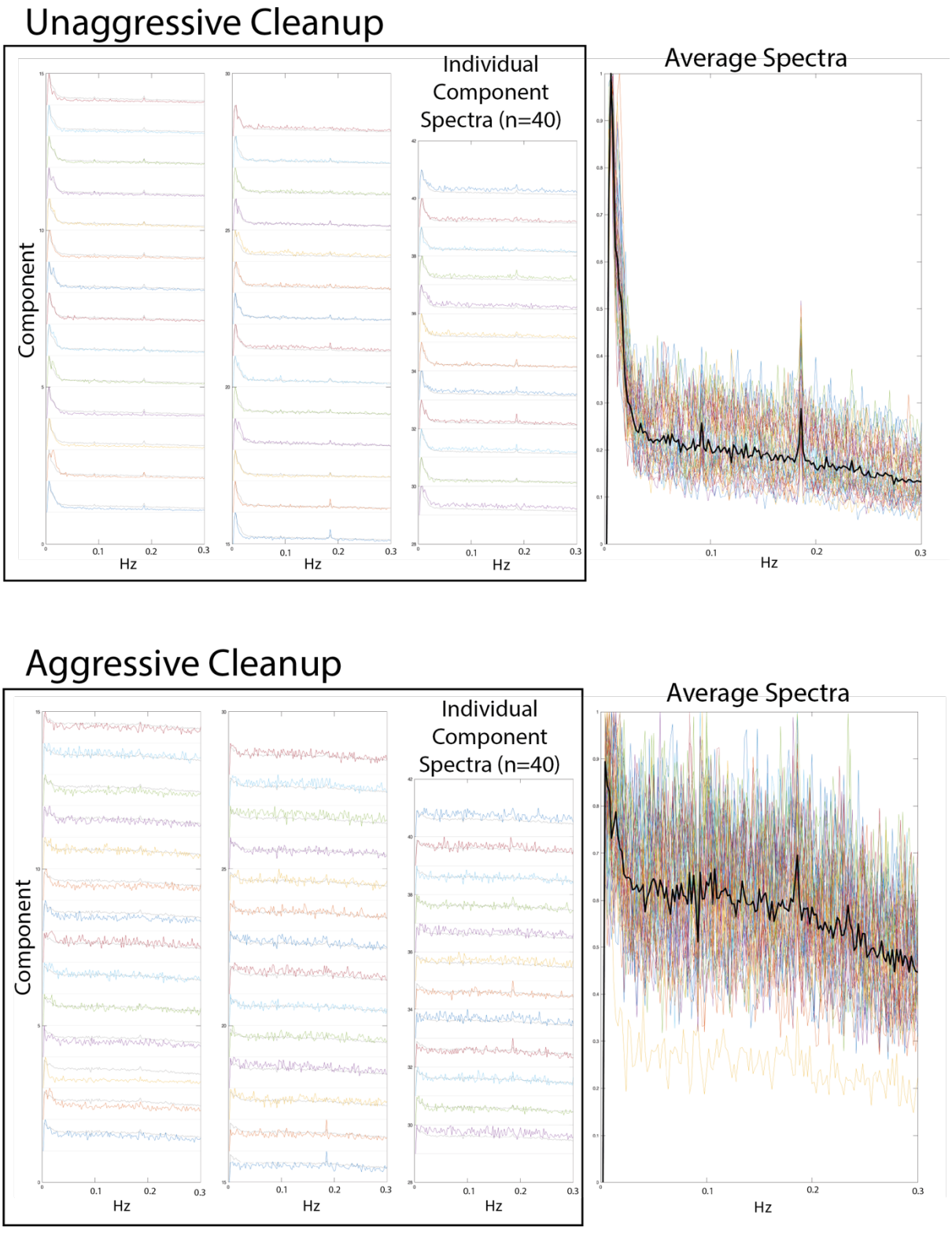


Figure 3. 18. Comparison of aggressive and unaggressive clean up strategies. (Top) The average spectra resulting from unaggressive clean up that included removal of the variance associated with the timeseries. (Bottom) The average spectra resulting from unaggressive clean up that included removal of the variance associated with the timeseries.

Another option to take into consideration when constructing connectivity matrices, is how to estimate connectivity. Whilst there are a large range of methods (e.g., Bayes nets, Granger causality, coherence, Patel's conditional dependence) two of the simplest and most widely used techniques are the partial and full correlation coefficients. Whilst the partial correlation coefficient is just reporting the direct relationships between two nodes, for example the direct relationship of node A and B, the full correlation coefficient instead calculates the direct and indirect relationships between nodes, for example the relationship between node A and B whilst considering the interactions of additional nodes such as C (Bijsterbosch et al., 2017). Comparisons of hierarchical clustering using full and partial correlation coefficients are displayed on Figure 3.18. Clear clusters of highly correlated and anti-correlated components are visible when full correlations were used, and the clusters were composed of meaningful regions in terms of underlying anatomical connectivity. When partial correlations were employed, investigating the more direct relationships between nodes, no meaningful clusters of highly correlated structures were observed.

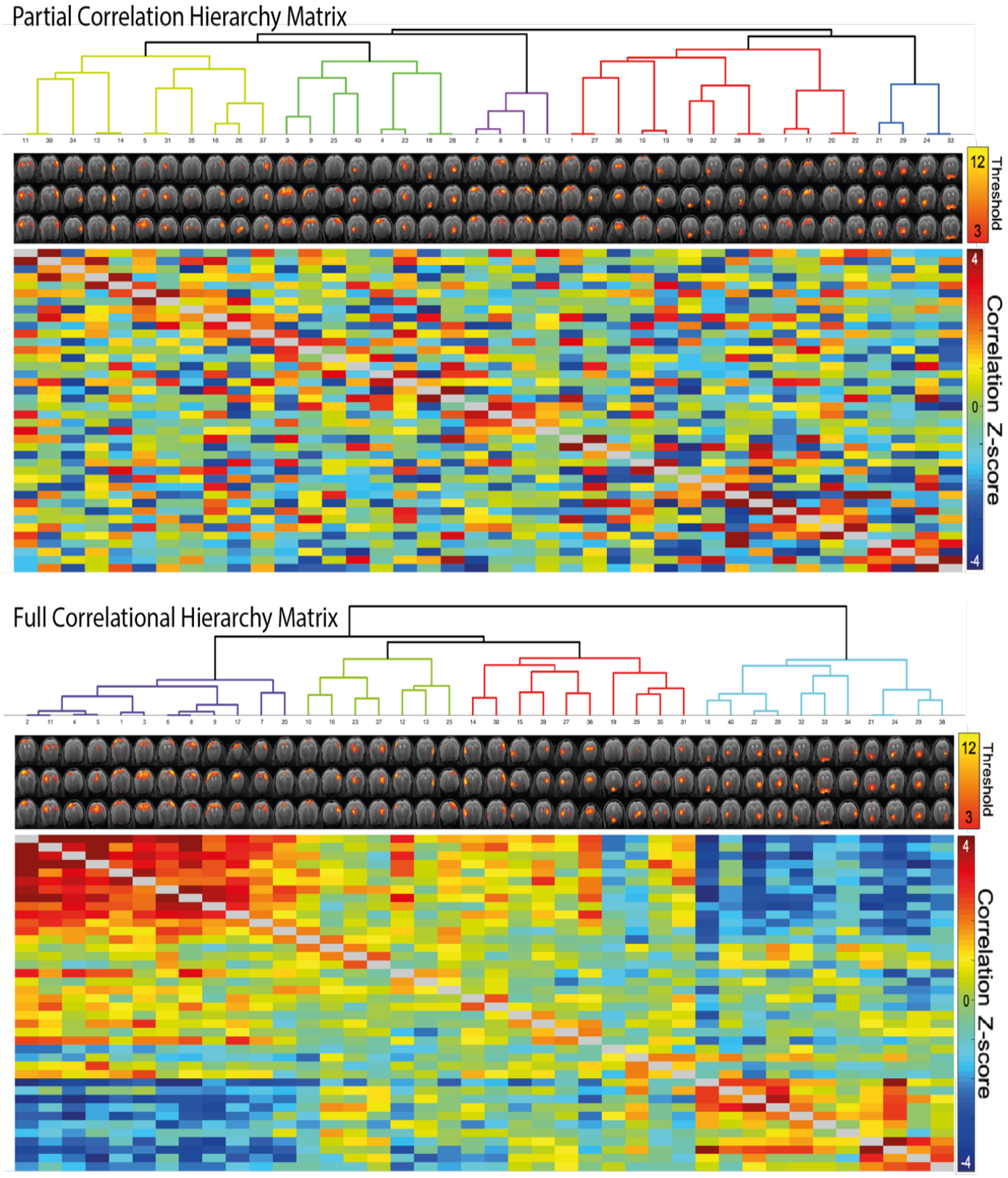


Figure 3. 19. Comparisons of partial and full correlational coefficient hierarchical clustering. (Top) Hierarchy matrix with edges representing the partial correlational coefficient. (Bottom) A hierarchy matrix with edges representing the full correlational coefficient. Note: scale bars refer to the z score threshold and the strength of the z correlation.

3.2.2.7. Connectivity images

In order to maintain spatial accuracy of the components when being displayed in three dimensional glass brains, we modified a pipeline originally described in (Madan, 2015). This pipeline determined the location of the maximum signal from the spatial map for each component, which avoided manual placement based on anatomical interpretation of the signal location. When the component was bilateral, two maximum locations were determined. This process is displayed in Figure 3.20.

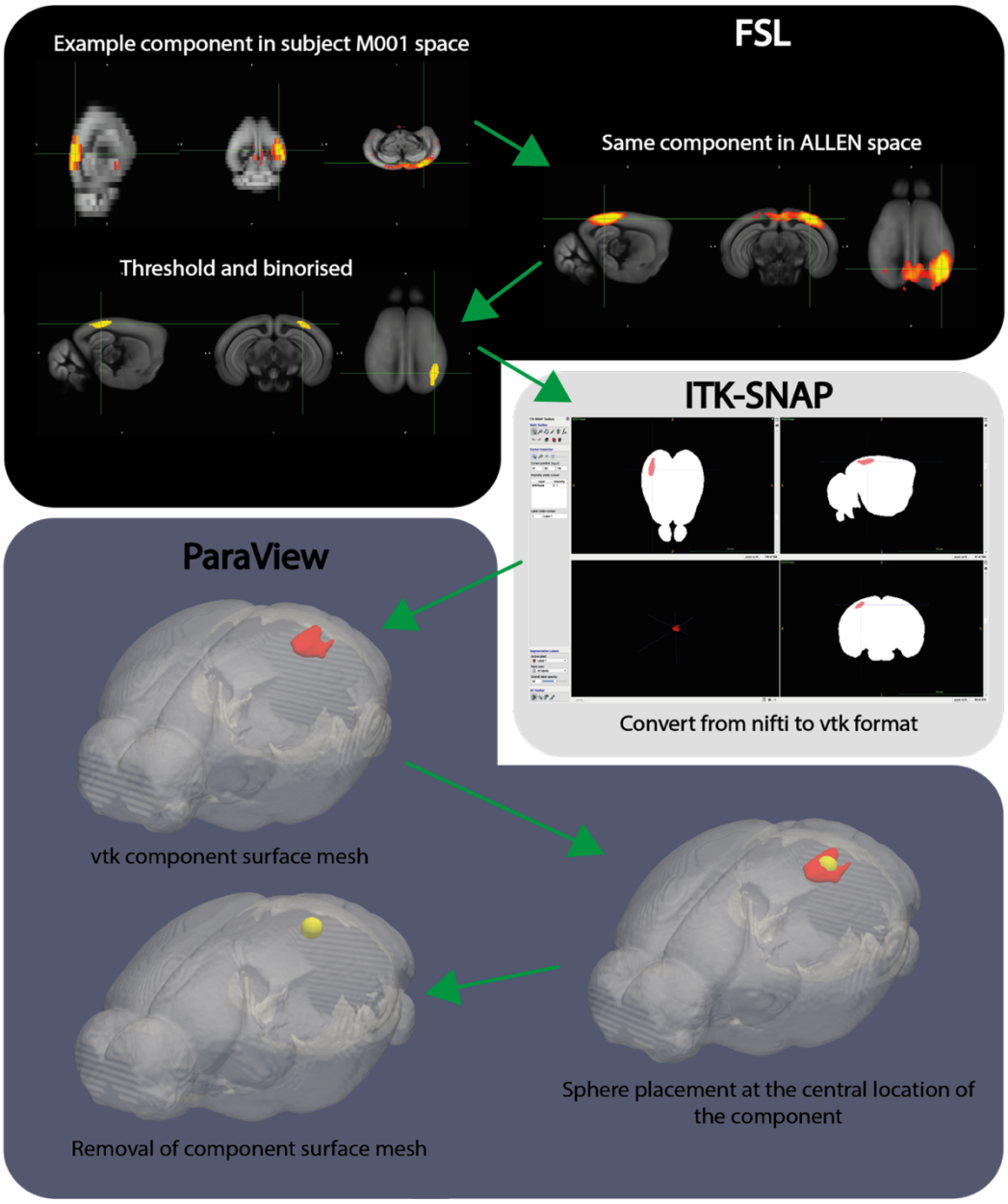


Figure 3. 20. Pipeline overview of converting a component into a three-dimensional spherical representation, modified from (Madan, 2015).

3.2.2.8. Graph theory

Thresholding is generally required to perform graph theory, removing potential false-positive random connections and thereby increasing sensitivity to potential true network changes. One simple and widely used technique is a global threshold, which removes any correlation strengths (edges) below a certain defined value. This cut-off value can be determined by a meaningful statistical analysis, such as removing certain nodes based on a significant alpha statistic from a one-sample t-test of an average matrix. Contrastingly a threshold can be determined via a more generic value of network topology such as using a particular graph theory statistic (Fornito et al., 2016). Whilst easy to employ, global thresholds may result in the exclusion of connections and affect the network density (overall number of edges/connections) disproportionately between groups. For example, if one particular group is associated with average lower connectivity strength (i.e., a pathological group), more edges will be removed as a result of global thresholding. Generating differences in network density that might inflate a potential a false-positive in graph theory values sensitive to density differences (Fornito et al., 2016). When applying a global absolute threshold across all the data, differences in network density was evident, with a reduction in network density in the hypoperfusion group (Figure 3.21).

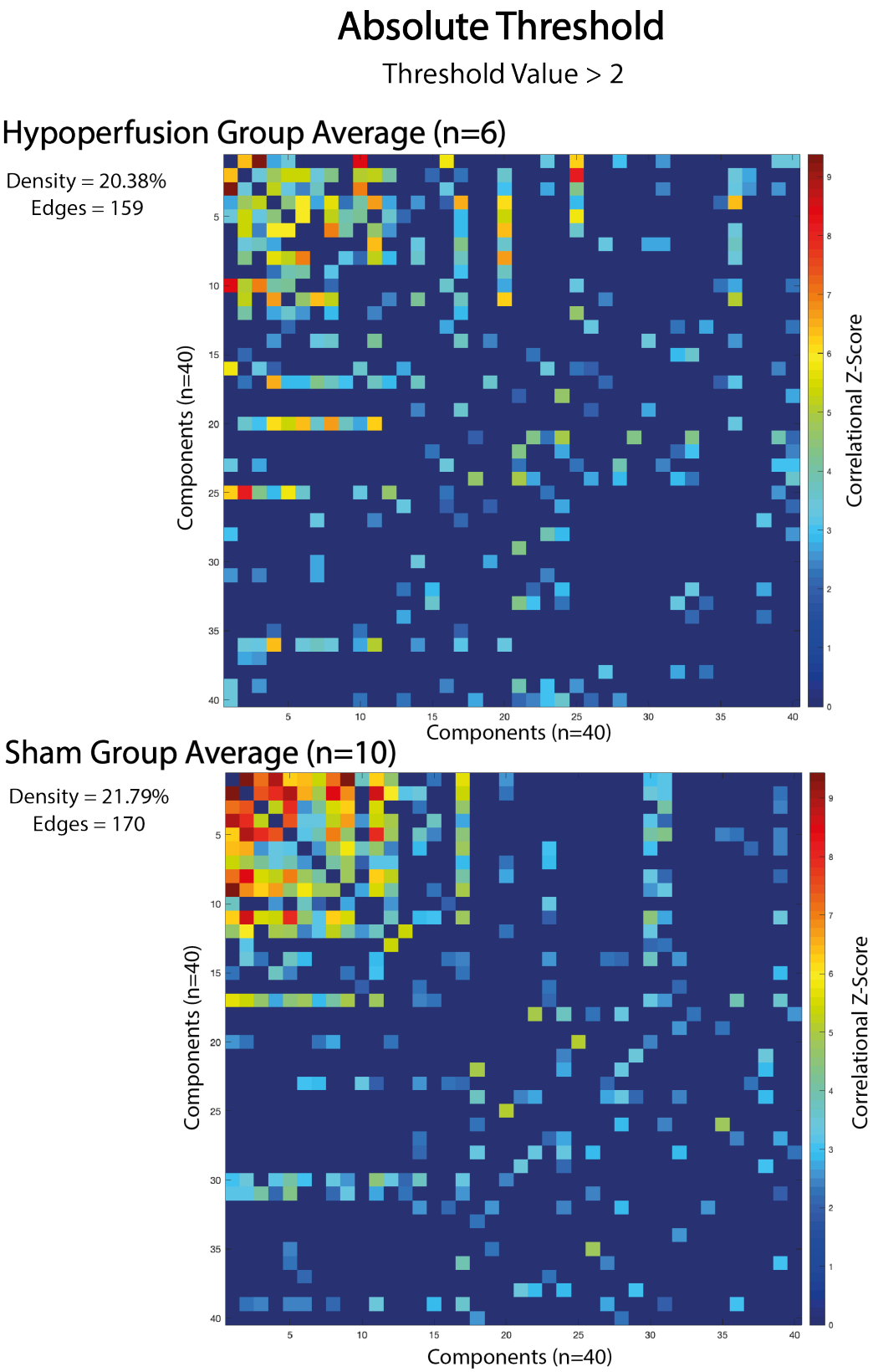


Figure 3. 21. Differences in network density between groups when a global absolute threshold is used. Connections below a strength of 2 were removed. (Top) The hypoperfusion group lost 11 more edges than the sham group (Bottom). Note: scale bars refer to the z score threshold and the strength of the correlation.

An alternative method involves using a proportional threshold that is based on the network density rather than an absolute value. For instance, a threshold that would preserve 40% of the strongest connections would be applied differently between groups, but network density and topology would be maintained across groups graph theory. Selecting a high proportional threshold could not only remove true connections but also could fragment the network if the connections were critical. In contrast, a low proportional threshold will leave too many weak or spurious connections and add additional randomness to the network (Fornito et al., 2016).

We tested whether small worldness could help determine the optimal proportional threshold (Watts and Strogatz, 1998). Generally, a high small-world topology will include a low average pathlength and a high clustering coefficient. Small worldness can therefore be calculated and it is also sensitive to network randomness; it will be zero if paths are too fragmented and key nodes become disconnected from the network (Watts and Strogatz, 1998) (Figure 3.22). We determined that a proportional threshold that results in the highest small worldness value was ideal for all groups.

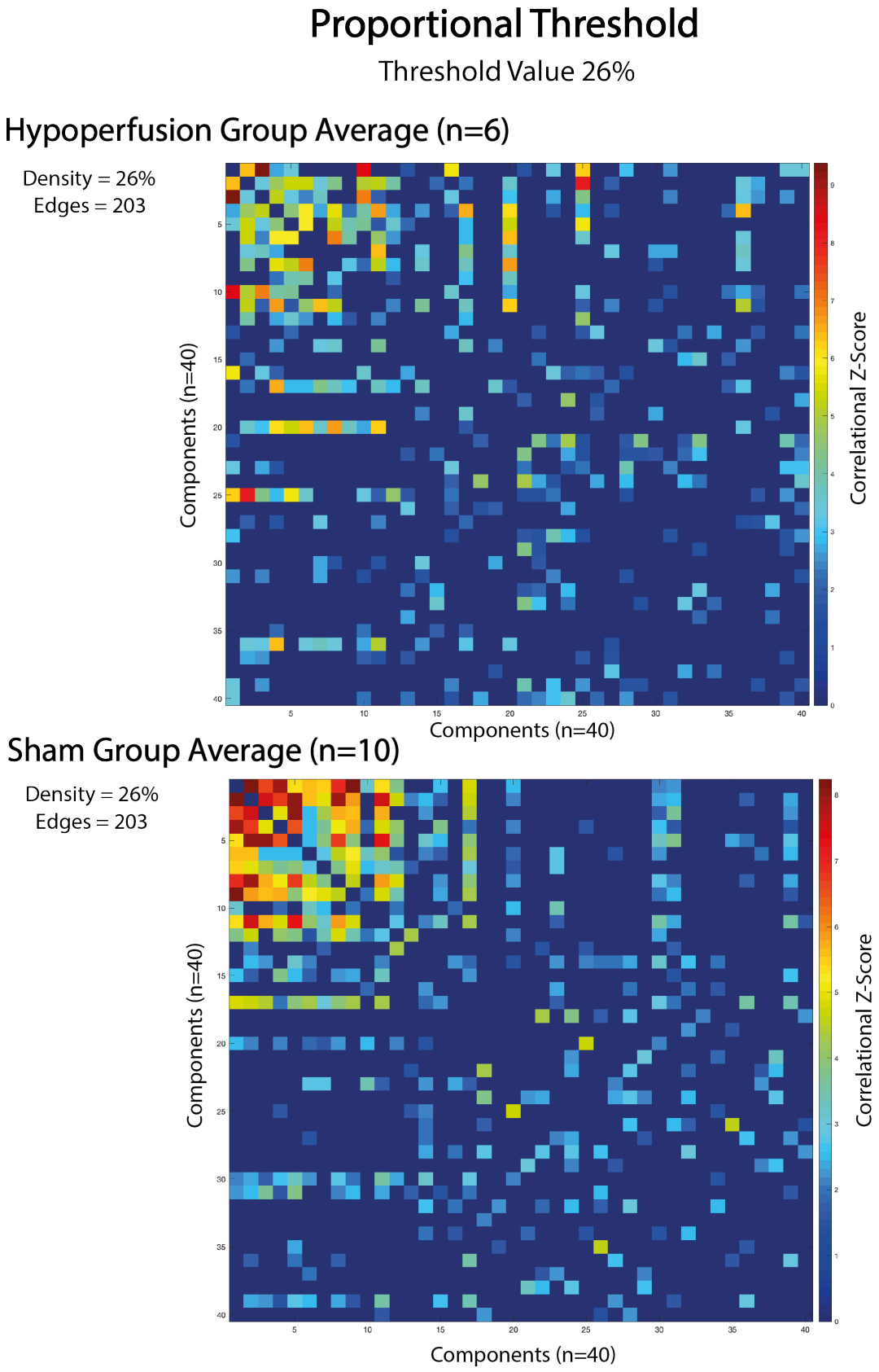


Figure 3. 22. Comparison of the network density between groups when using a proportional threshold. The 26% of the strongest correlational z-scores are kept for each matrix, preserving the density and therefore the network topology between the hypoperfusion (top) and the sham group (bottom).

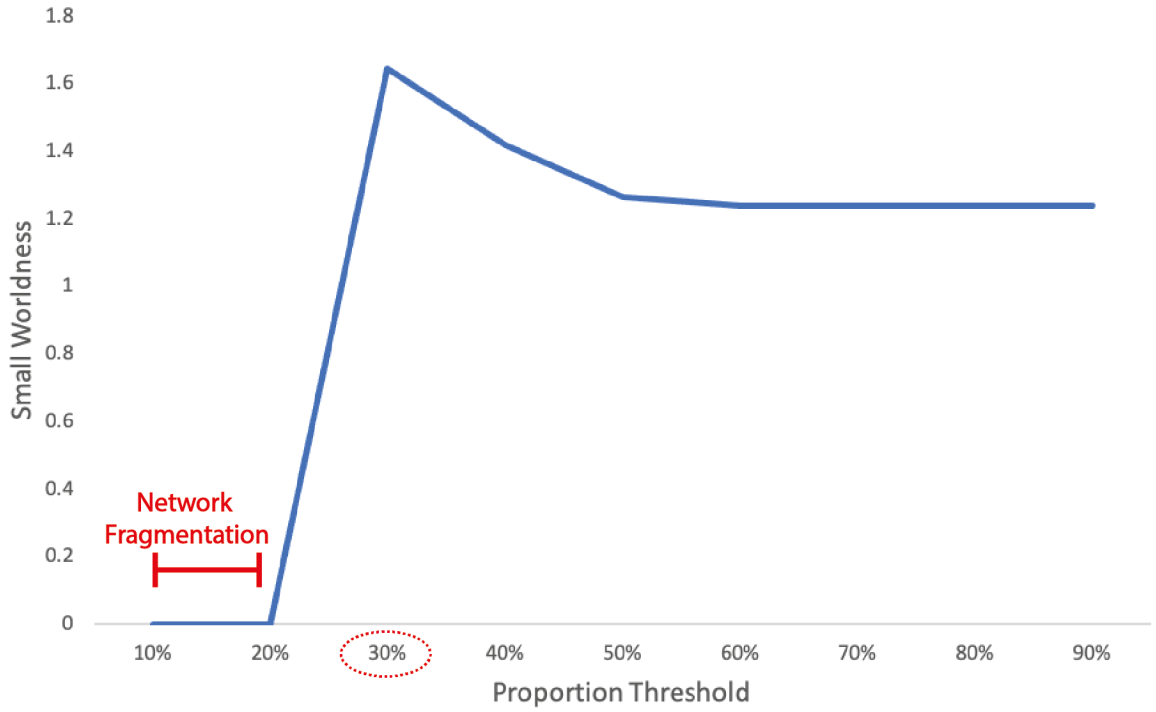


Figure 3. 23. Small worldness as a function of proportional threshold. (Top) Small worldness values are maximal when between 20-30% of the strongest connections are preserved.

3.2.3. dMRI pipeline

3.2.3.1. Template creation and image registration

The two-step registration method established to bring structural T_2 data in and out of AMCA space did not translate well to the rs-fMRI or dMRI data. When individual subject dMRI was registered to the T_2-weighted subject template via the transformations of the corresponding T_2-weighted structural image to the T_2-weighted subject template, significant misalignments were observed (Figure 3.24). This could possibly be due to movement between acquisition of the dMRI and structural T_2-weighted images and/or from resolution differences (the structural T_2-weighted images were not isotropic). The dMRI data also exhibited substantial warping, particularly in the posterior slices. Therefore, a method was developed to improve registration. A subject derived B0 template (the image in which no diffusion gradient was applied) was prepared from extracted B0 images from each subject. As each subject had multiple B0 volumes, this resulted in high quality template construction.
Subsequently, each of the subject B0 images was registered to the B0 template, and registration was dramatically improved (Figure 3.24). Since the B0 images have the same contrast as the structural T_2-weighted scans, the AMCA template and atlas could be registered directly into the B0 space using the corresponding T_2 transformation files.

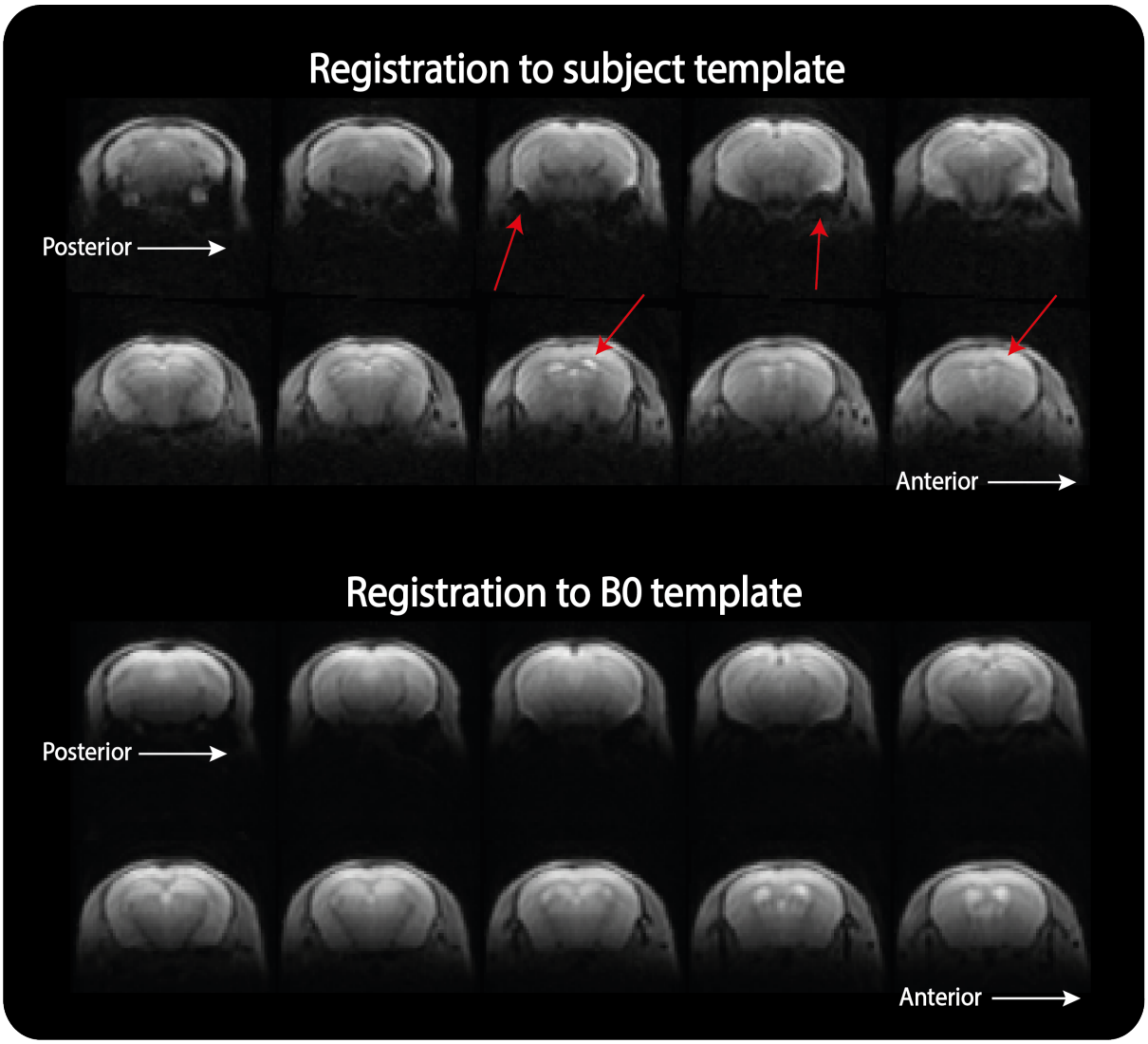


Figure 3. 24. Registration comparisons between using individual B0 or T_2 weighted images to each corresponding template. (Top) Coronal slices display a T_2 weighted image that was aligned with the T_2 weighted subject template (red arrows display warping and misalignments in the B0 image). (Bottom) Corresponding coronal slices display a B0 image that was aligned with the B0 template.

3.2.3.2. Tract based spatial statistics

The non-linear registration step performed by FSL's TBSS script had to be reworked for the rodent as it made use of FLIRT and FNIRT, which required scaling up the mouse data. Figure 3.25 illustrates a brief overview of the changes to the TBSS script. ANTs registration tools were used instead of FLIRT and FNIRT, which included the transformation files produced from B0 registrations. Another script was prepared to ensure the naming of the registration outputs was consistent so the last TBSS processing stage would work.

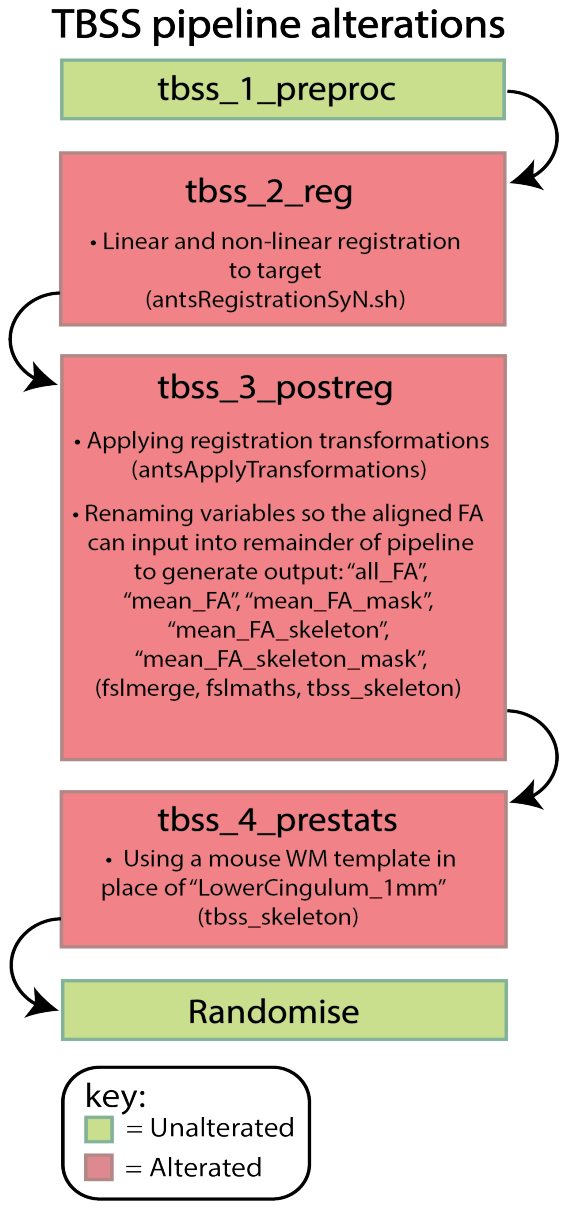


Figure 3. 25. Flow chart overview of the adjustment of the TBSS scripts. Altered scripts are highlighted in red. Note: associated scripts are included in the appendix A.

3.2.3.3. Probabilistic tractography

After running probabilistic tractography, output streamlines for individual subjects were inspected for a coherent layout of streamline directions in relation to the anatomical WM tracts (Figure 3.26).

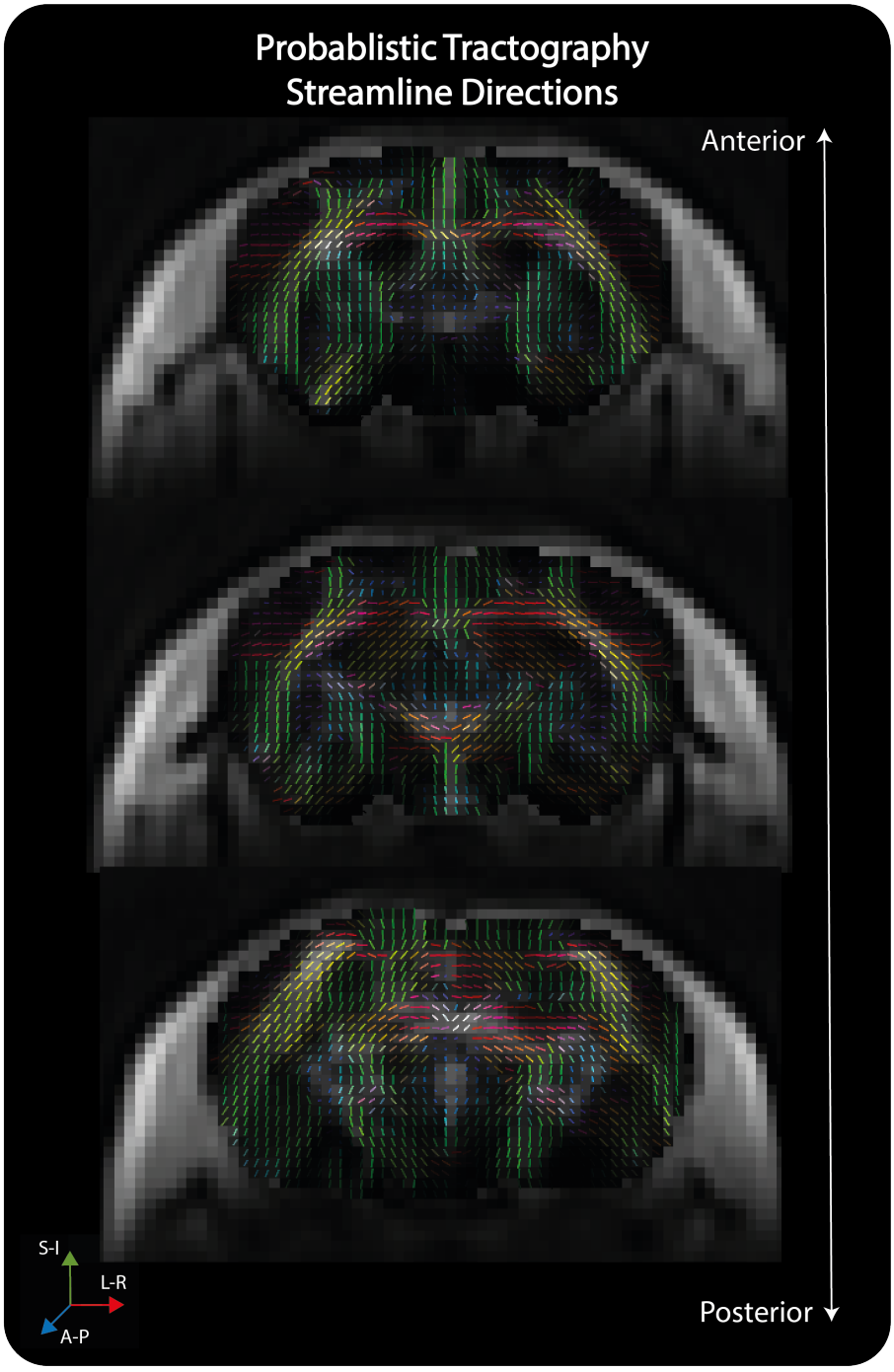


Figure 3. 26. Coronal display of primary diffusion directions employed throughout probabilistic tractography. Primary diffusion directions are overlaid as coloured ellipses in each voxel of the FA template.

The AMCA atlas contains 1199 regions, which is anticipated as it was generated from microscopic data. Only 681 regions still remained after the down sampling required to register AMCA to the B0 template. Structural connectivity matrices produced across the 681 regions were not normally distributed. Furthermore, there was a drop off in connectivity as distance from the seed increased. This results in a connectivity matrix that was difficult to visualise as the connection strengths spanned such a large range, furthermore the majority of these strengths were located very closely together (Figure 3.27). A typical method to correct for this is to apply a $\log_{10}$ scaling factor to the connectome. This has already been reported in primates (Ercsey-Ravasz et al., 2013) and mice (Calabrese et al., 2015) tractography research. Figure 3.28 displays the same connectivity matrix and histogram after applying a $\log_{10}$ transformation. Relative connectivity strengths were more easily viewed, and the histogram displayed a more appropriate distribution.

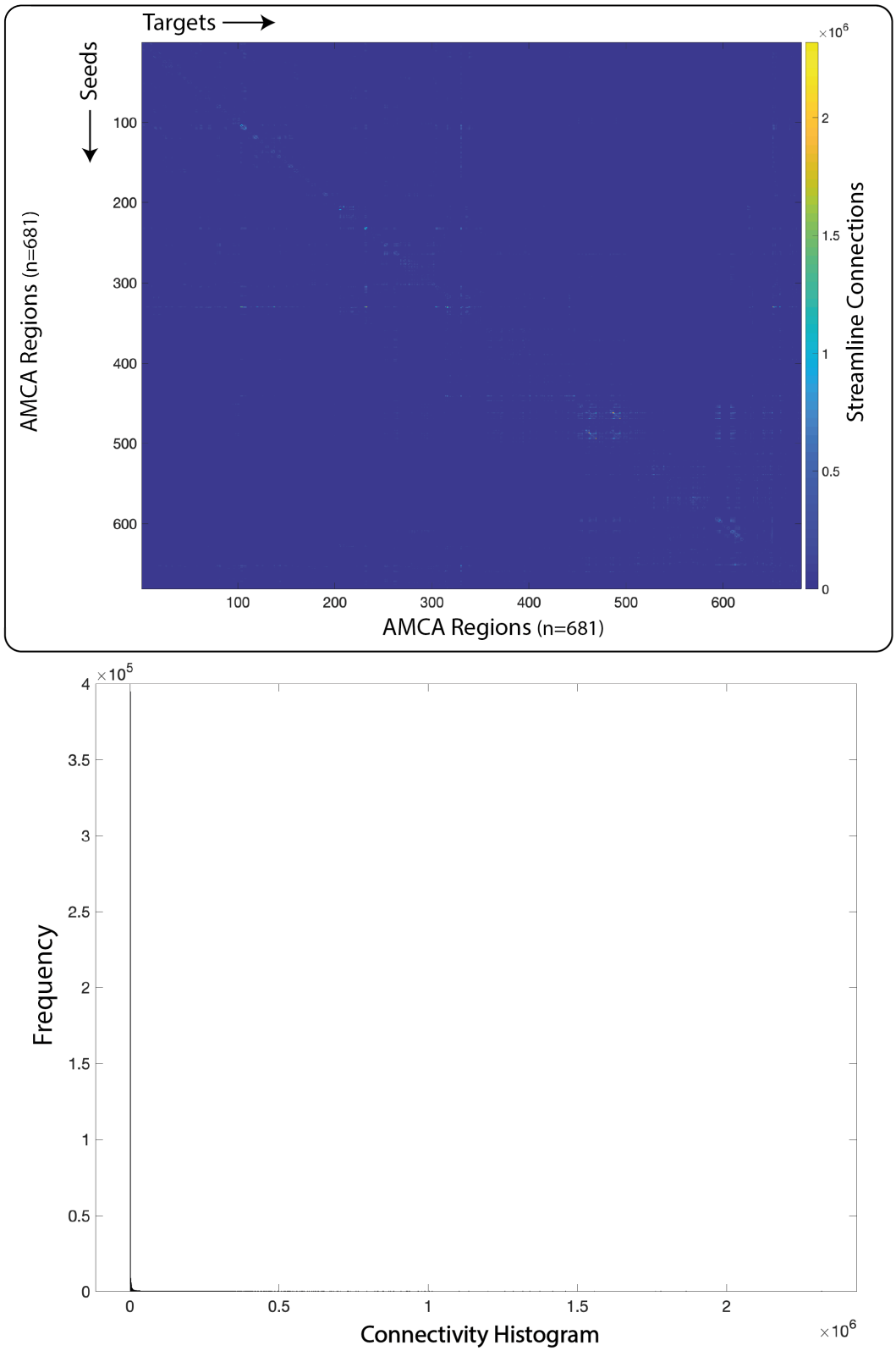


Figure 3. 27. Structural connectivity matrix and corresponding connectivity histogram of an individual subject. (Top) Probabilistic tractography structural connectivity dMRI matrix generated from 691 AMCA regions. Note: scale bar reflects the number of connectivity streamlines. (Bottom) Associated histogram of the range and frequency of connection strengths within the connectivity matrix.

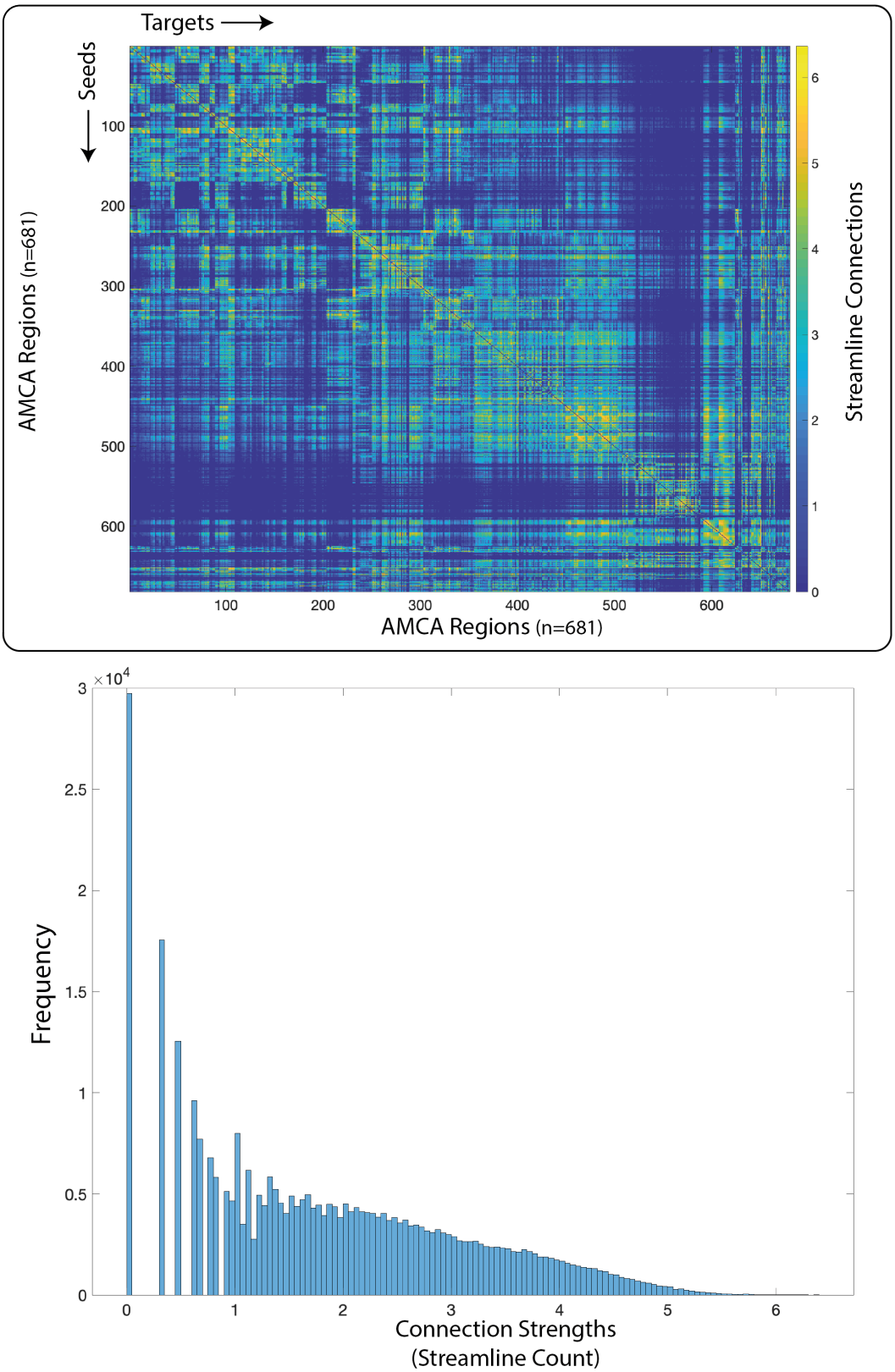


Figure 3. 28. Structural connectivity matrix and corresponding connectivity histogram of an individual subject scaled by a factor of Log_{10}. (Top) Probabilistic tractography structural connectivity dMRI matrix generated from 691 AMCA regions. Note: scale bar reflects the number of connectivity streamlines. (Bottom) Associated histogram of the range and frequency of connection strengths within the connectivity matrix. Seeds (y-axis) reference to tract begging and targets (x-axis) reference associated ends.

We identified 32 key parent regions in the 681 region AMCA atlas and amalgamated the structures that comprised them to reduce dimensionality. Some naming changes were made to parent regions and associated hierarchies (Figure 3.30).

Subsequently, a modified AMCA atlas was built that amalgamated regions into only the corresponding parent regions (32 in total). For example, multiple cortical layers were amalgamated into a signal cortical region. This gave more focus at the macroscale, helping to analyse at the whole brain level, rather than at the mesoscale cortical layer. Both atlases are depicted in Figure 3.29.

Overall, 681 AMCA atlas regions survived the re-sampling into dMRI B0 template space. AMCA was called in the probtrackx2 command line, optimised for graphical unit processing (Hernandez-Fernandez et al., 2019) with the network option.

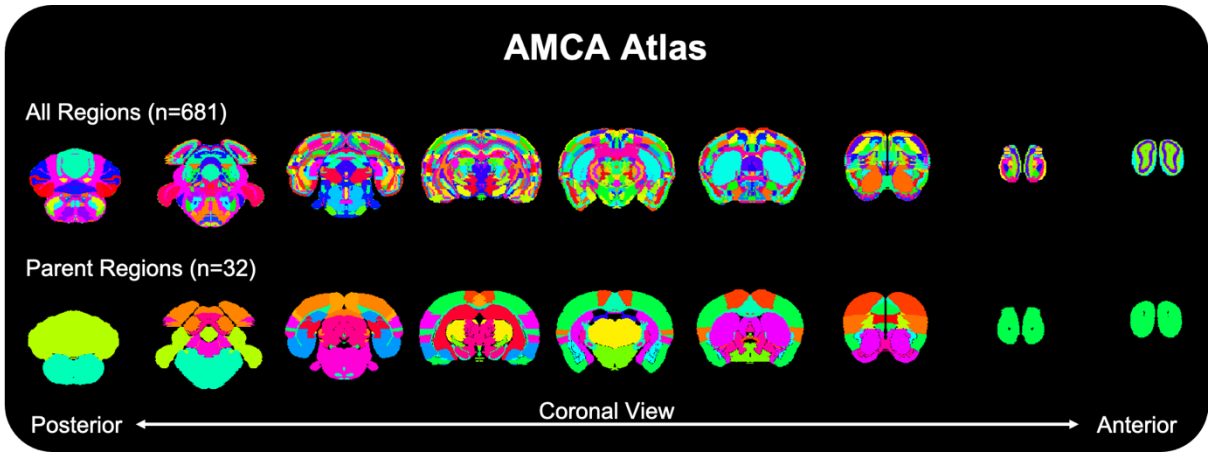


Figure 3. 29. AMCA atlases with different regional dimensionality. (Top) the AMCA atlas with 681 regions and the in-house generated equivalent parent atlas containing 32 regions (bottom).

Full AMCA (n=681)

Hierarchy	Parent
Isocortex	Agranular_Insular_Area
Isocortex	Anterior_Cingulate_Area
Isocortex	Dorsal_Auditory_Area
Isocortex	Primary_Auditory_Area
Isocortex	Ventral_Auditory_Area
Isocortex	Ectorhinal_Area
Isocortex	Gustatory_Areas
Isocortex	Infralimbic_Area
Isocortex	Orbital_Area
Isocortex	Perirhinal_Area
Isocortex	Posterior_Parietal_Association_Area
Isocortex	Prelimbic_Area
Isocortex	Retrosplenial_Area
Isocortex	Somatomotor
Isocortex	Somatosensory
Isocortex	Temporal_Association_Area
Isocortex	Visceral_Area
Isocortex	Visual_Areas
Olfactory	Olfactory_Areas
Hippocampal_Formation	Hippocampal_Region
Hippocampal_Formation	Retrohippocampal_Region
Cortical_Subplate	Cortical_Subplate
Cerebral_Nuclei	Pallidum
Cerebral_Nuclei	Striatum
Brain_Stem	Thalamus
Brain_Stem	Hypothalamus
Brain_Stem	Midbrain_Sensory
Brain_Stem	Midbrain_Motor
Brain_Stem	Midbrain_Behavioral
Brain_Stem	Pons
Brain_Stem	Medulla
Cerebellum	Cerebellum
White_Matter	White_Matter

Parent AMCA (n=32)

Hierarchy	Parent	Sub regions (n=681)
Isocortex	Insular_Cortex	12
Isocortex	Anterior_Cingulate_Area	9
Isocortex	Auditory_Area	21
Isocortex	Ectorhinal_Area	5
Isocortex	Frontal_Association_Area	6
Isocortex	Infralimbic_Area	6
Isocortex	Orbital_Area	13
Isocortex	Perirhinal_Area	5
Isocortex	Posterior_Parietal_Visual_Association_Area	7
Isocortex	Prelimbic_Area	5
Isocortex	Retrospenial_Area	14
Isocortex	Motor	7
Isocortex	Somatosensory	48
Isocortex	Temporal_Association_Area	6
Isocortex	Visual_Areas	34
Hippocampal_Formation	Retrohippocampal_Region	36
Hippocampal_Formation	Hippocampal_Region	17
Cerebral_Nuclei	Striatum	26
Cerebral_Nuclei	Pallidum	16
Midbrain	Midbrain_Superior_Colliculus	9
Midbrain	Midbrain_Motor	25
Midbrain	Midbrain_Behavioural_State	25
Interbrain (diencephalon)	Thalamus	45
Interbrain (diencephalon)	Hypothalamus	49
Hindbrain	Pons	47
Hindbrain	Medulla	46
Cerebellum	Cerebellum	36
Olfactory	Olfactory	47
Cortical_Subplate	Cortical_Subplate	10
Lateral_Forebrain_Bundle_System	Corpus callosum	25
Lateral_Forebrain_Bundle_System	Corticospinal tract	18
Medial_Forebrain_Bundle_System	Fornix	6

Figure 3. 30. Adaptation of the AMCA atlas to reduce the number of regions. (Left) Parent regions and associated hierarchies of the AMCA atlas with 681 regions. (Right) Parent region changes following amalgamation of children regions into the 32 parent regions.

Chapter 4. Structural and functional network changes in a mouse model of vascular cognitive impairment.

4.1. Introduction

WM hyperintensity progression observed on conventional T_2-weighted MRI has been widely identified as the strongest predictor of cognitive decline that subsequently resulted in vascular dementia from multicentre longitudinal collaborations (LADIS, 2011). The majority of these hyperintensities were located in periventricular WM regions in addition to the corona radiata and centrum semiovale. Subsequent continuing research in the LADIS sample investigated these findings further in WM hyperintensities using dMRI techniques in order to quantify tissue microstructure. Independent of WM hyperintensity volume, lacunes and brain atrophy, the strongest predictor of cognitive decline in VCI related tasks was MD. Furthermore, diffusivity measures of tissue appearing normal in the T_2-weighted structural images had a greater predictability of cognitive decline compared to hyperintense tissue (Jokinen et al., 2013). This suggested that WM hyperintensities widely associated with VCI, could just be the surface of cerebrovascular pathology detectable by MRI. Similar large-scale studies (SCANS) have further helped support the sensitivity of dMRI scalar measures to cerebrovascular pathology than WM hyperintensity load, in addition to comparing dMRI scalar variables. These studies not only discovered MD and FA as strong predictors of executive dysfunction, but RD as the strongest predictive variable in contrast to AD (Lawrence et al., 2013). Employing more refined techniques of voxelwise dMRI scalar comparisons with TBSS, all WM regions were compared with cognitive performance in different longitudinal multi-centre cohort (RUN-DMC). Corresponding to previous findings, dMRI scalars FA and MD were strongly associated with cognitive performance, particularly in the genu and splenium areas of the corpus callosum. In addition, the cingulum bundle was the greatest predictor of verbal memory, whilst frontal WM was the greatest predictor of psychomotor speed (Tuladhar et al., 2015).

In an attempt to further investigate the subtle WM changes in dMRI data, subsequent research has henceforth examined structural network connectivity changes in connectomes generated through tractography. This not only offers direct comparison of connectivity between specified regions in modelled WM tracts (Liu et al., 2017) but also allows the

exploratory investigation of structural network and topology through graph theoretical measures. For instance graph theory measures in structural dMRI networks, has allowed groups to identify global efficiency (associated as a marker of the overall ability for brain network to share information quickly) as a powerful predictive biomarker of decline in cognitive function (Lawrence et al., 2014; Tuladhar et al., 2016). In addition to structural connectivity, MRI techniques investigating functional connectomes (rs-fMRI) have reported reductions in global efficiency with patients with WM hyperintensities (Yu et al., 2015), and in the hypoperfused hemisphere of patients with unilateral carotid stenosis (Chang et al., 2016).

Whilst clinical imaging of longitudinal multicentre cohorts like LADIS, SCANS and RUN-DMC provide a window into pathophysiology, these large-scale longitudinal studies can be time consuming and expensive. Furthermore, with the exception CASADIL, VCI cohorts generally have a large variability and comorbidity of cerebrovascular disease (Jokinen et al., 2013; Skrobot et al., 2018). Ultimately, this can make it difficult to classify the specific roles certain cerebrovascular diseases play in pathology and cognitive deficits. Animal models offers the ability to explore the role of specific cerebrovascular risk factors on pathology and cognition, while being cost and time effective (Jiwa et al., 2010).

The BCAS mouse model recapitulates features of VCI such as white matter damage and cognitive deficits. Early imaging experiments in the BCAS model suggest WM damage through decreases in FA (Holland et al., 2011; Holland et al., 2015; Saggu et al., 2016). Our research group was the first to attempt to examine structural connectivity with dMRI (Boehm-Sturm et al., 2017). While there were no significant differences in global efficiency between sham and hypoperfused mice, it did remain a good predictor as, together with local efficiency, it was accurately able to predict group allocation. Significant differences between sham and hypoperfused mice were present in measures of network segregation, which represent the ability of the brain to perform specialised processing within distinctive hubs of well-organized structures. There was a significant decrease in modularity and a significant increase in transitivity in the hypoperfused animals. Modularity reports on the number and size of hubs, whereas transitivity measures the fraction of triangle connections (triplets) of a given network. This suggested that, while the network ability to share information efficiently was preserved, there was a deterioration in specialised hubs that was accompanied by a compensatory increase in smaller clusters (Boehm-Sturm et al., 2017). We further sought to

complement this data with an understanding of functional connectivity change using rs-fMRI. We also wished to improve our dMRI data processing pipeline. The analysis pipeline created and evaluated for both rs-fMRI and dMRI data was presented in detail throughout Chapters 2 and 3. The purpose of the present study was to apply this analysis to a group of sham and BCAS mice at chronic timepoints (3 and 6 months).

4.2. Methods

4.2.1. Experimental design

All of the following procedures were given approval by the Landesamt für Gesundheit und Soziales and conformed to the German Animal Welfare Act and institutional guidelines. Twenty-one male C57/BL6J mice (8 weeks of age, Charles River, Germany) were housed in an environment in which temperature (22±2°C), humidity (55±10%) and light cycles (12/12-hour light/dark) were strictly controlled.

Global cerebral hypoperfusion was induced using specialised, non-magnetic, surgical grade microcoils (Shannon Coiled Springs Microcoil, Limerick, Ireland). Microcoils (160µm inner diameter) were placed around both carotid arteries that were exposed through a midline incision in the neck. Muscles and glands were guided into the original position and wounds sutured with local anaesthetic prior to recovery. Bilateral implantation was separated by a 24-hour interval. Sham subjects underwent the same procedure, however, a larger non-constricting microcoil (500µm inner diameter) was placed instead. Group sizes were; sham (n=10) and hypoperfused (n=11). Animals were euthanised at 6-month post-surgery. A timeline of the study is depicted in Figure 4.1.

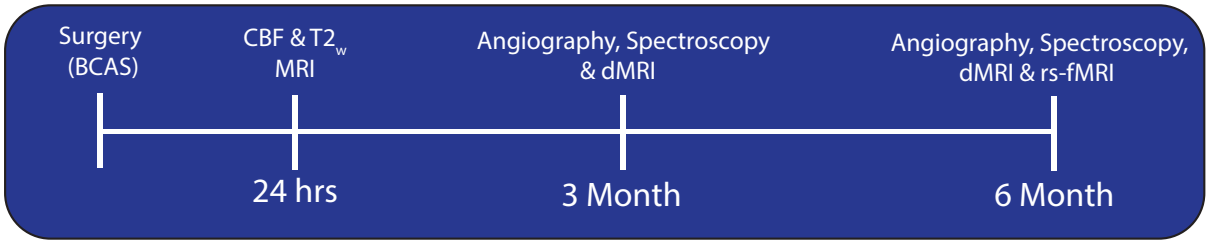


Figure 4. 1. Timeline of experimental design. BCAS surgery was performed and scanning was conducted at 24hrs, and 3- and 6-months post-surgery.

4.2.2. MRI hardware and acquisition

Scanning was performed on a 7T system (Bruker BioSpin, Germany) under isoflurane anaesthesia and temperature and respiration were monitored remotely with MRI compatible equipment (SA Instruments, USA).

T_2 weighted imaging was performed with a mouse quadrature surface coil (Bruker BioSpin, Germany) and Paravision 5.0 software using a rapid acquisition relaxation enhancement (RARE) sequence (TR/ΔTE/TEeff: 3100/11/33ms, RARE factor: 8, 32 consecutive slices, slice thickness: 0.45mm, FOV: 16.2mm^2, resolution: 100 μm^2, averages: 2, acquisition time: 2min 4s). A fast alternating inversion recovery (FAIR) sequence was used for CBF (TR/TE: 12 000/35.9ms, 16 TIs: 35-1500ms, FOV: 25.6mm^2). Time of flight angiography was acquired with a 20mm diameter quadrature volume coil (RAPID Biomedical, Germany) (TR/TE: 15/2.5ms, FOV: 25mm^3).

The dMRI and rs-fMRI were acquired with a cryogenically cooled transmit/receive surface coil and Paravision 6.0 software (Bruker BioSpin, Ettlingen, Germany). The dMRI scan was an isotropic EPI diffusion tensor imaging (DTI) sequence, comprising 5 b0 images and 126 gradient directions (TR/TE: 7500/18ms, 4 segments, 2 b values (0 and 1000 s/mm^2), gradient duration (δ): 2.5ms, gradient separation (Δ): 8.1ms, 58 consecutive slices, FOV: 16.2 mm^2, acquisition matrix 72 x 48 enlarged by partial fourier transformation to 72 x 72, resolution: 225 μm^3, acquisition time: 1 h 5 min). The rs-fMRI was a T_2* weighted EPI sequence (TR/TE: 1000/10ms, 300 repetitions, FOV: 19.2 x 12mm, 12 slices, slice thickness: 0.75mm, resolution: 150μm, acquisition time: 5min).

4.2.3. Processing of MRI data

4.2.3.1. CBF

CBF maps were calculated via the T_1 method, and processing of rs-fMRI and dMRI was performed as described in Chapter 2 with the following exceptions.

4.2.3.2. rs-fMRI

Image distortion correction was not performed since the field map was collected prior to shimming. Components generated from MELODIC (Beckmann and Smith, 2004) were created from an average of all subjects (n= 16). Three different component dimensionalities were selected, these were set to 15, 30 and an automatic number of components (principal component analysis chose the number of components based on a predictable amount of variance that can be explained according to the data quality) and were each tested.

For the dual regression, a hypothesis driven approach was used to focus on regions predicted to be most affected by hypoperfusion: the hippocampus and visual cortex as well as highly connected areas such as the retrosplenial cortex, hypothalamus, and thalamus. We also were interested in regions associated in the mouse DMN; therefore, the caudate and prefrontal cortex were additional regions of interest. All p-values in the resulting clusters were Bonferroni corrected.

For seed based analysis, masks were generated from individual components or from AMCA.

4.2.3.3. dMRI

No correction for EPI distortions could be performed as the fieldmaps collected were taken prior to shimming, making them invalid for distortion correction. For TBSS, WM skeletons were generated for each timepoint (3 and 6 months) (Figure 4.2).

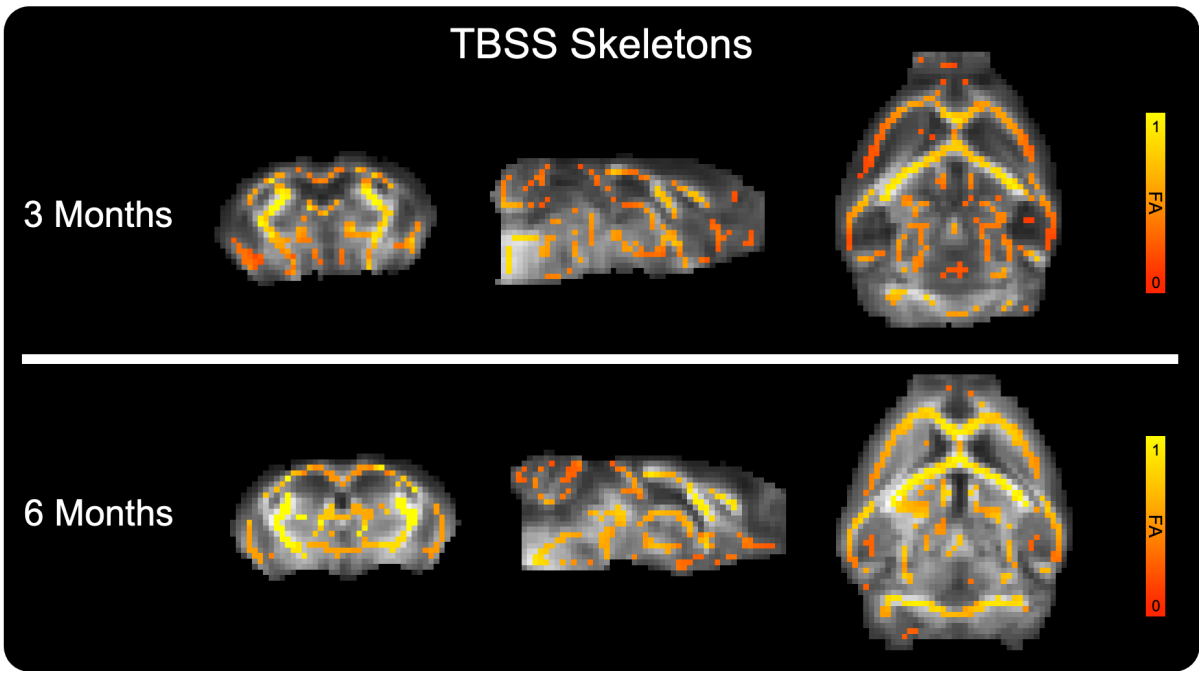


Figure 4. 2. WM skeletons for TBSS analysis. WM skeletons for each timepoint (3 and 6 months (n=16). Note: the scale bar depicts the FA value.

Overall, 681 AMCA atlas regions survived the re-sampling into dMRI B0 template space. AMCA was called in the probtrackx2 command line, optimised for graphical unit processing (Hernandez-Fernandez et al., 2019) with the network option.

Subsequently, a modified AMCA atlas was built that amalgamated regions into only the corresponding parent regions (32 in total). For example, cortical layers were amalgamated into a signal cortical region. This gave more focus at the macroscale whole brain level, rather than at the mesoscale cortical layer level. Both atlases are depicted in Figure 4.3.

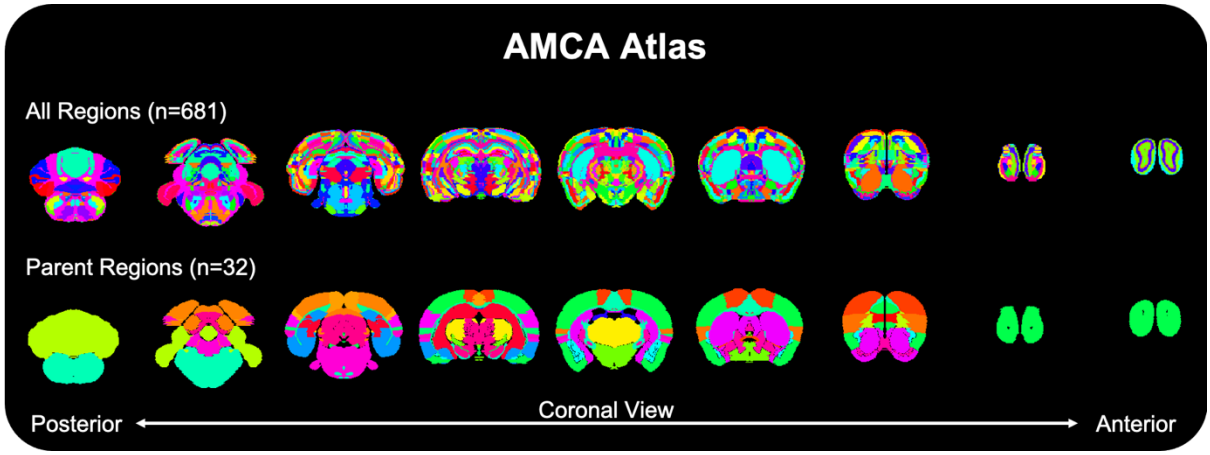


Figure 4. 3. AMCA atlases with different regional dimensionality. (Top) the AMCA atlas with 681 regions and the in-house generated equivalent parent atlas containing 32 regions (bottom).

4.2.4. Statistical Analysis

Data was analysed with the SPSS statistical package (version 26) and testing for normality was performed using a Kolmogorov-Smirnov test. A series of un-paired t-tests was used to compare individual components between groups, and false discovery rate was used for multiple comparison corrections. All graph theory values between groups were assessed with t-tests or appropriate analysis of variance (ANOVA) (2 or 3 way, or repeated measures), or the equivalent non-parametric tests.

4.3. Results

There was high mortality in the hypoperfused group: two animals within 48hrs, and a further three at 9, 28, and 32d post-surgery, respectively. Final group sizes were sham (n=10) and hypoperfused (n=6).

4.3.1. CBF

Throughout all timepoints CBF remained stable in shams. In contrast, the hypoperfused group had the strongest CBF reduction at the 24-hour post-surgical timepoint that recovered over time (time: $F(2,26)= 5.2$, $p= 0.01$, group: $F(1,13)= 133.9$, $p< 0.01$, interaction: $F(2,26)= 7.9$, $p< 0.01$) (Figure 4.4). The strongest CBF recovery was observed between the 3- and 6-month timepoints.

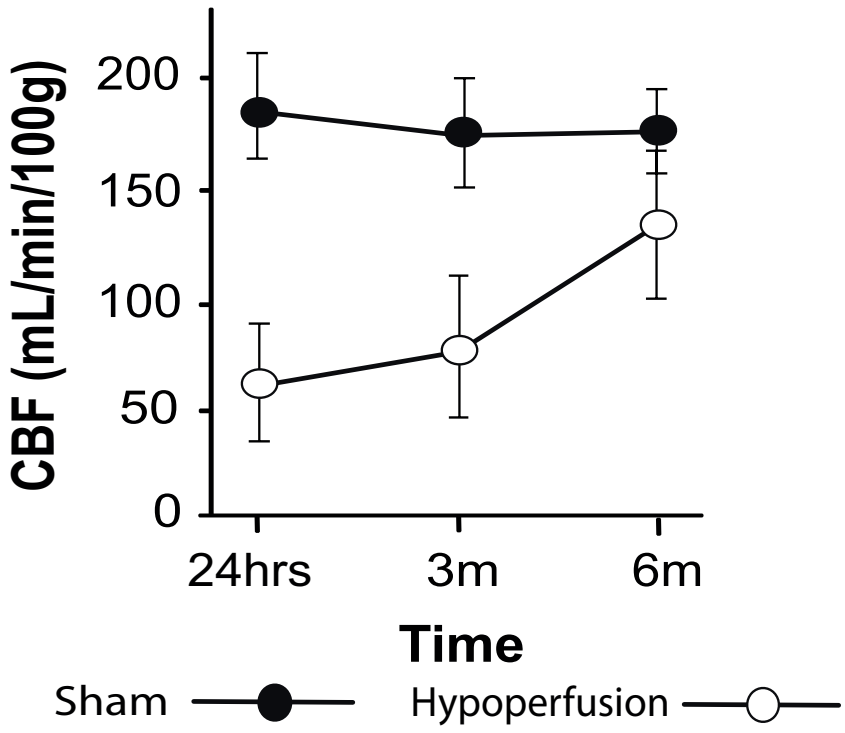


Figure 4. 4. CBF over 6 months in sham (n= 10) and hypoperfused (n= 6) mice.

4.3.2. rs-fMRI

4.3.2.1. Independent component analysis

As we were unsure about the optimal number of components, ICA was run with 15, 30 and an automatic option (Figure 4.5).

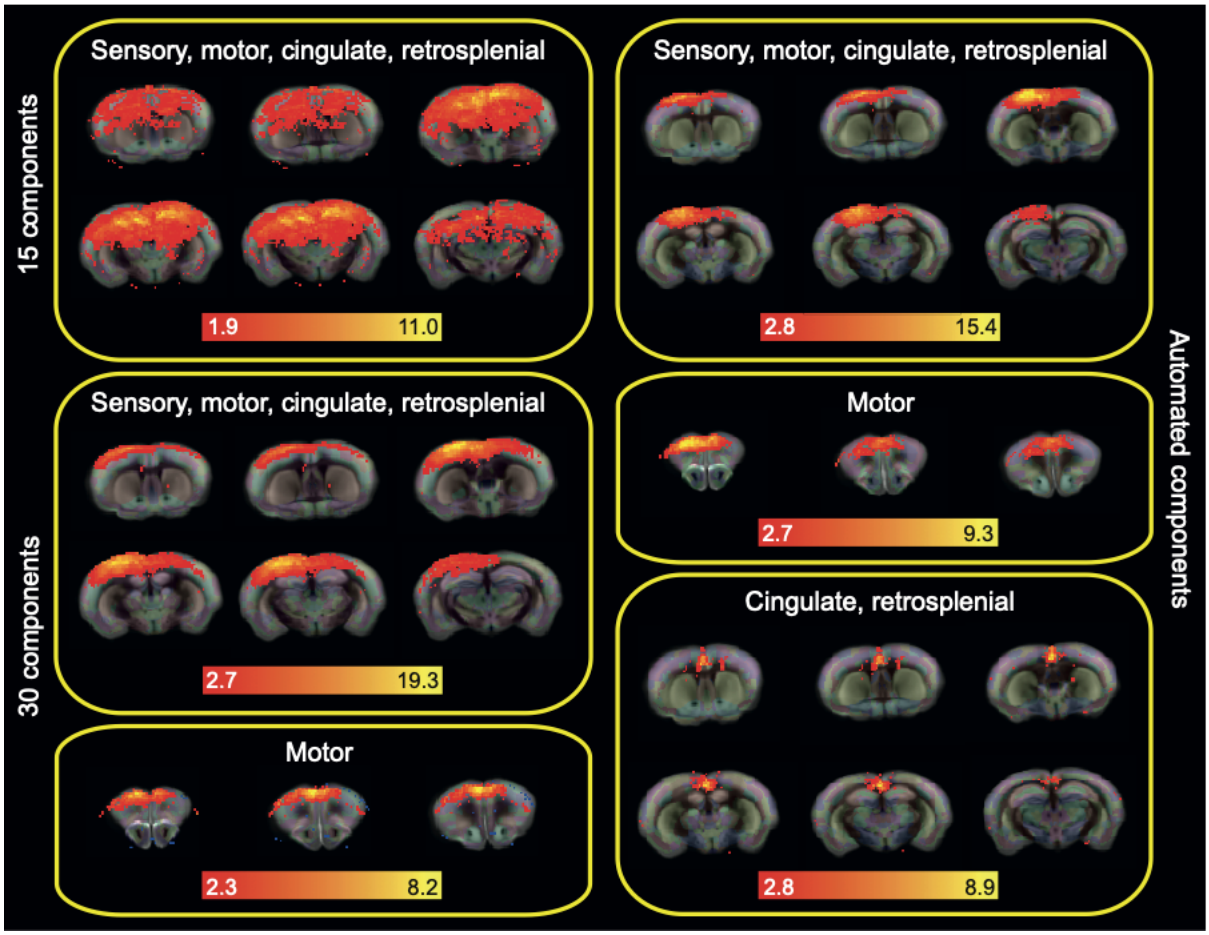


Figure 4. 5. Variation in the dimensionality estimation for selected components. Similar components were selected in the illustration, displaying the difference between the; 15 (top left), 30 (left middle and bottom), and an automatically determined number of components (59) (right). With a dimensionality set at 15, the component spans the sensory, motor, cingulate, and retrosplenial cortices. Whereas at 30 (bottom left and middle right, respectively), a motor cluster is depicted separate to the sensory regions. In contrast in the automated dimensionality (middle right), alongside the additional components in the 30 option, separate components in the cingulate and retrosplenial cortices are detected. Note: Components are overlaid onto AMCA and scale bars correspond to the z-score.

From the automated approach, 59 distinctive activity components were present across all subjects (n=16), and 40 of these were classified as primarily neurally driven BOLD signal. The 40 components are depicted in Figure 4.6. Subsequently, hierarchical analysis identified 4 highly correlated clusters of components (Figure 4.6). The most prominent cluster was composed of components in the sensory, motor and visual cortices as well as the cingulate and retrosplenial cortices. There were also sub-cortical components linked to the sensorimotor (dorsolateral caudate and peri-aqueductal gray) and visual systems (hippocampus, superior colliculus, retrosplenial and visual cortices) (Figure 4.6: purple). This cluster was anti-correlated with a cluster composed of limbic structures (thalamus, hypothalamus, nucleus accumbens, ventral pallidum and preoptic area) (Figure 4.6: blue).

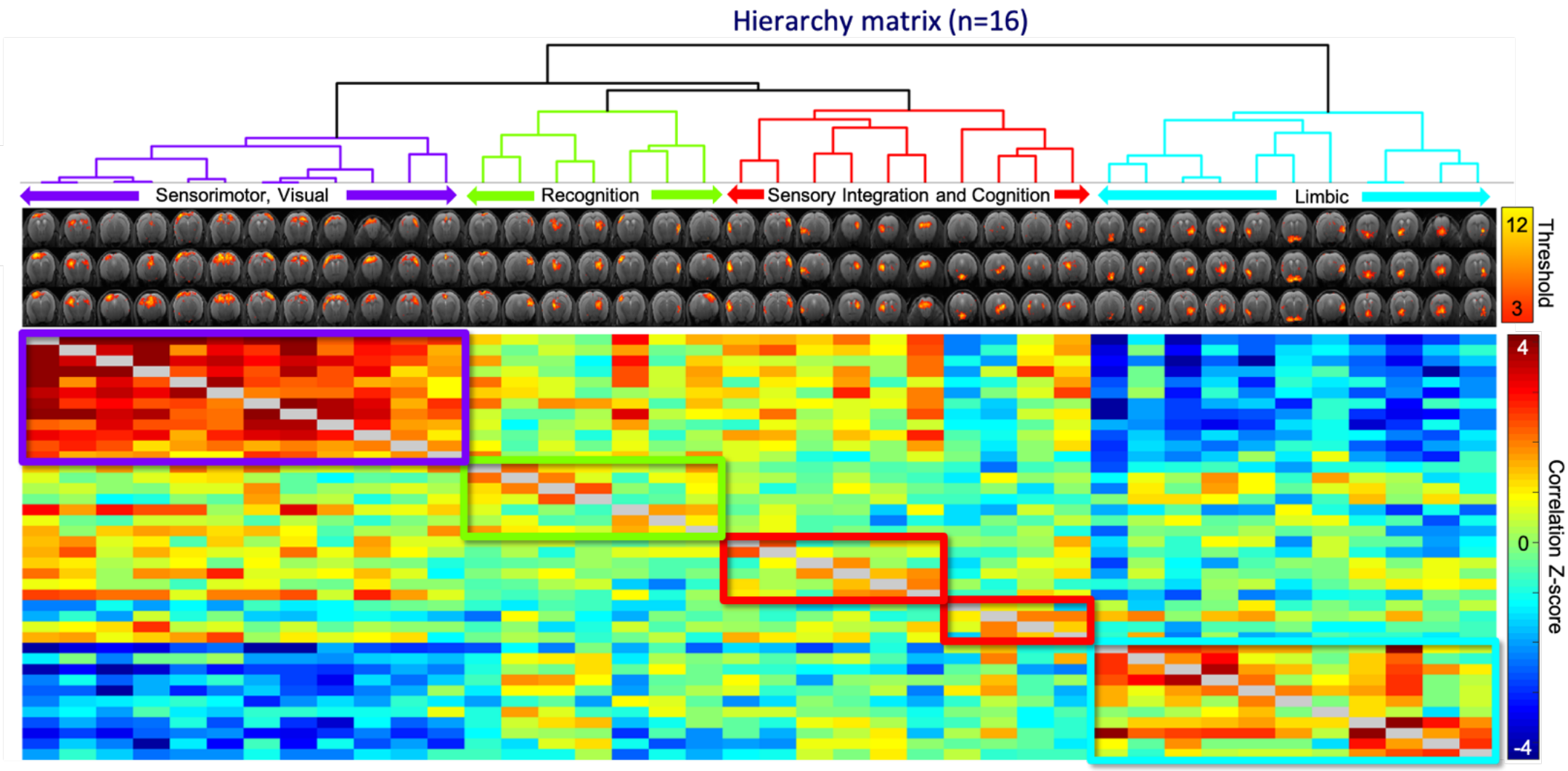


Figure 4. 6. Hierarchy matrix displaying highly correlated clusters of components. Each neurally driven component (n=40) is overlaid onto 3 T_2 weighted images organized into columns (anterior to posterior). The clusters are color coded (purple: sensorimotor and visual, green: recognition, red: sensory integration and cognition, and blue: limbic). The matrix displays the correlations between all components. Note: scale bars refer to the z score threshold and the strength of the z correlation.

The clusters are further displayed with individual components in Figures 4.7 - 4.8.

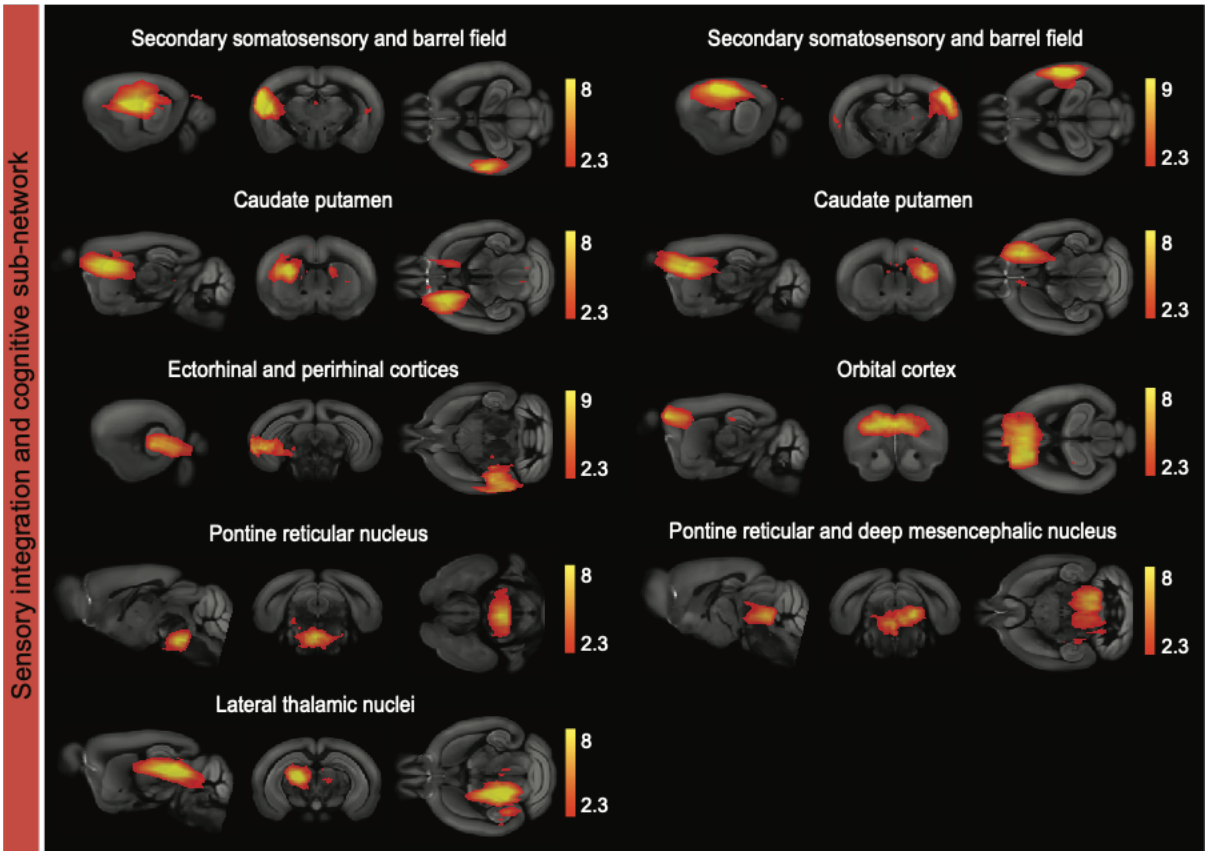


Figure 4. 7. Spatial maps of sensorimotor, visual, and limbic component clusters. The sensorimotor, visual (purple) contains 12 and the limbic (blue) cluster contains 11 independent activity components that are highly correlated. These clusters were negatively correlated with each other. Note: Components are overlaid onto AMBA template and scale bars correspond to the z score.

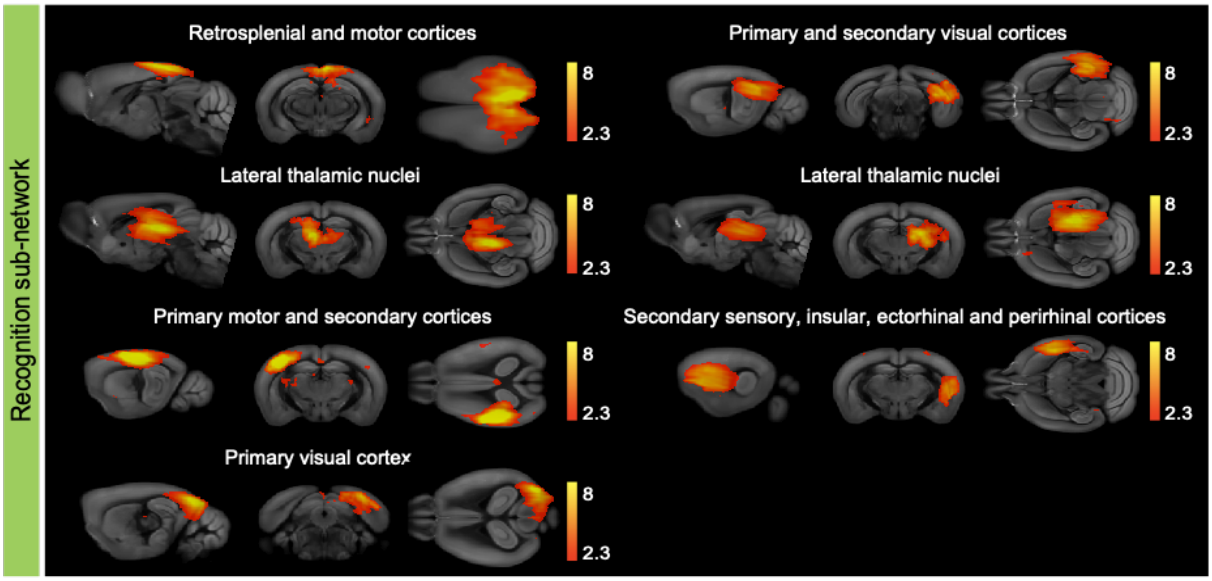


Figure 4. 8. Spatial maps of recognition, sensory integration, and cognition component clusters. Recognition (green) contains 7 and the sensory integration and cognition (red) cluster contains 9 independent activity components of high inter correlation. Note: Components are overlaid onto AMBA template and scale bars correspond to the z score.

From viewing the clusters in the hierarchy matrix (Figure 4.6), we were interested in speculating the potential functional nature of these highly correlated regions. Two component groupings of functional interest were the recognition (Figure 4.8) and sensory association and cognition clusters (Figure 4.7), respectively highlighted in green and red in the hierarchy matrix (Figure 4.6). The green cluster (Figure 4.8) primarily consisted of components located in cortical (retrosplenial, visual and sensorimotor) and lateral thalamic areas, this prompted a potential link to recognition (Figure 4.8). As the retrosplenial cortex has been found to possess reciprocal connections with sensory, motor and visual cortices in addition to the anterolateral thalamus. Previously reviewed in (Seabrook et al., 2017; Mitchell et al., 2018), this network pattern has been suggested to engage in the integration of information, specifically in spatial navigation (learning location and recognizing landmarks). Furthermore reciprocal connections are also present in the visual cortices and lateral thalamic nuclei (Shibata et al., 2004).

The sensory integration and cognition cluster shown in red on the hierarchy matrix (Figure 4.6) was subsequently labelled as a result of component regions located in the secondary somatosensory and prefrontal cortices (containing the anterior cingulate). This combination of highly correlated regions could be a resulting factor of the reciprocal connections between the secondary somatosensory and the prefrontal cortices. Through further investigation, the secondary somatosensory has been suggested to play a major integrative role in sensory information processing, while the prefrontal cortices have been implicated in behavior modulation and performance adjustment (Laubach et al., 2018). Additional regions included in the cluster were the caudate and features of the midbrain and pons. This grouping could be a result of the projections from the prefrontal cortex to the medial caudate associated with sensory and cognitive processes (Voorn et al., 2004). In contrast to the caudate, the functional association of the pontine tegmental area and deep mesencephalic nucleus has been associated with sleep and consciousness. As a network, these regions receive striatal input that could play a role in perception, vigilance and awareness linked to cognitive basal ganglia behaviors (Rodríguez et al., 2001).

The four hierarchical clusters are further displayed in a three-dimensional view of the brain in Figure 4.9.

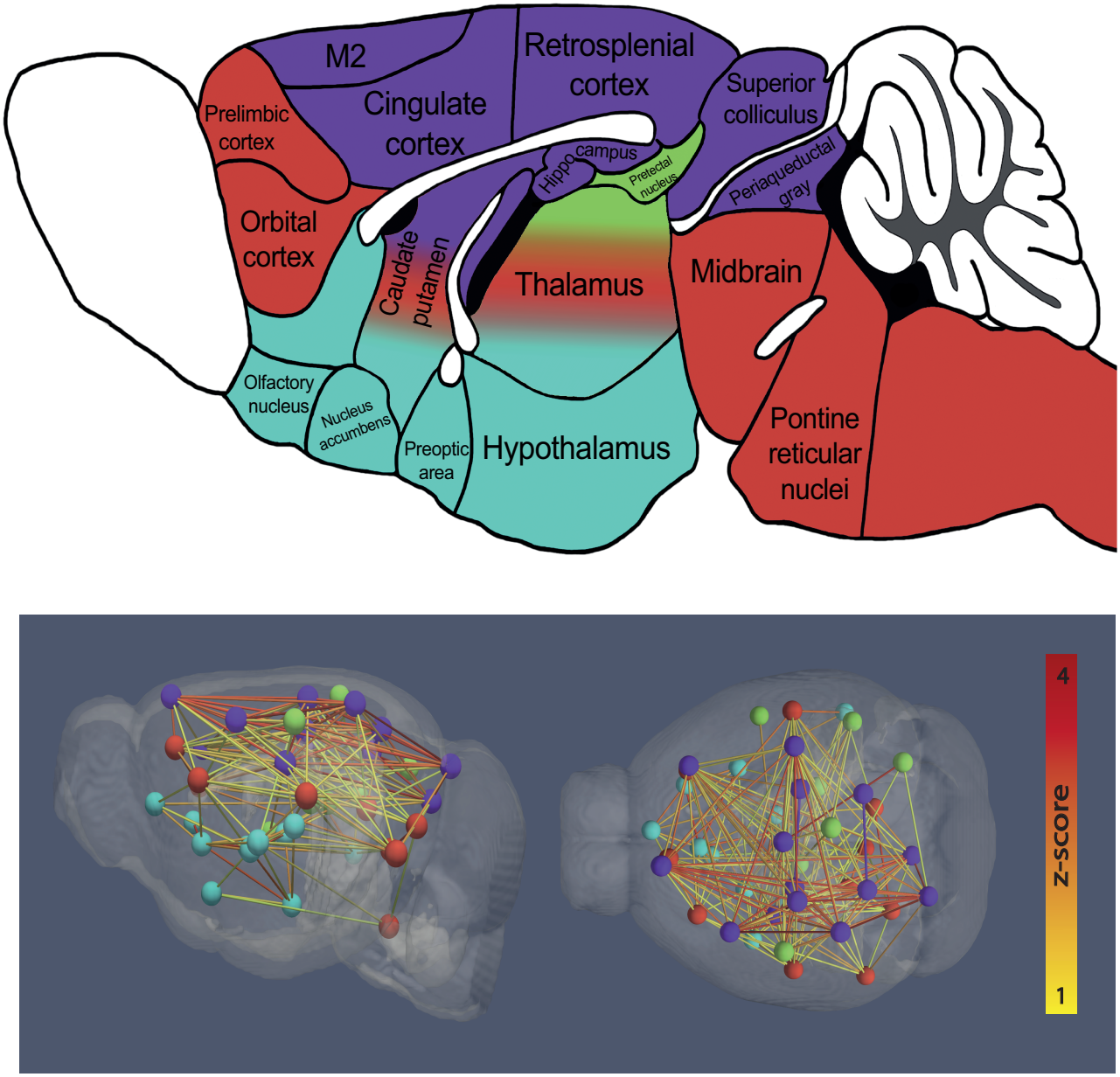


Figure 4. 9. Hierarchical clusters resulting from independent component analysis. (Top) Sagittal cartoon of the mouse brain (Paxinos and Franklin, 2019) colour coded according to the clusters displayed in the hierarchy matrix. (Bottom) Sagittal and superior views of a transparent mouse brain with the four colour coded clusters. Note: spheres represent the components and connecting lines indicate the correlation strength.

4.3.2.2. Qualitative network differences between groups

Connectomes emphasizing group network differences are displayed in Figure 4.10. Visual inspection of the three-dimensional glass brain connectomes was unremarkable. However, when the clusters were displayed individually, there was a large reduction in correlational strengths in the sensorimotor and visual cluster in the hypoperfused group. The limbic cluster appeared similar between groups. Similar patterns are observed in the circular views of the connectomes, with a reduction of correlational R-value strength between nodes within the sensorimotor and visual cluster for the hypoperfused group. Another noticeable difference in the hypoperfused group was a reduced correlational strength between the orbital frontal node and the sensorimotor, visual node clusters. In contrast, a clear increase in correlational strength was visible in the hypoperfused group, specifically between the sensorimotor, visual cluster and the insular node located in the recognition cluster (Figure, 4.10).

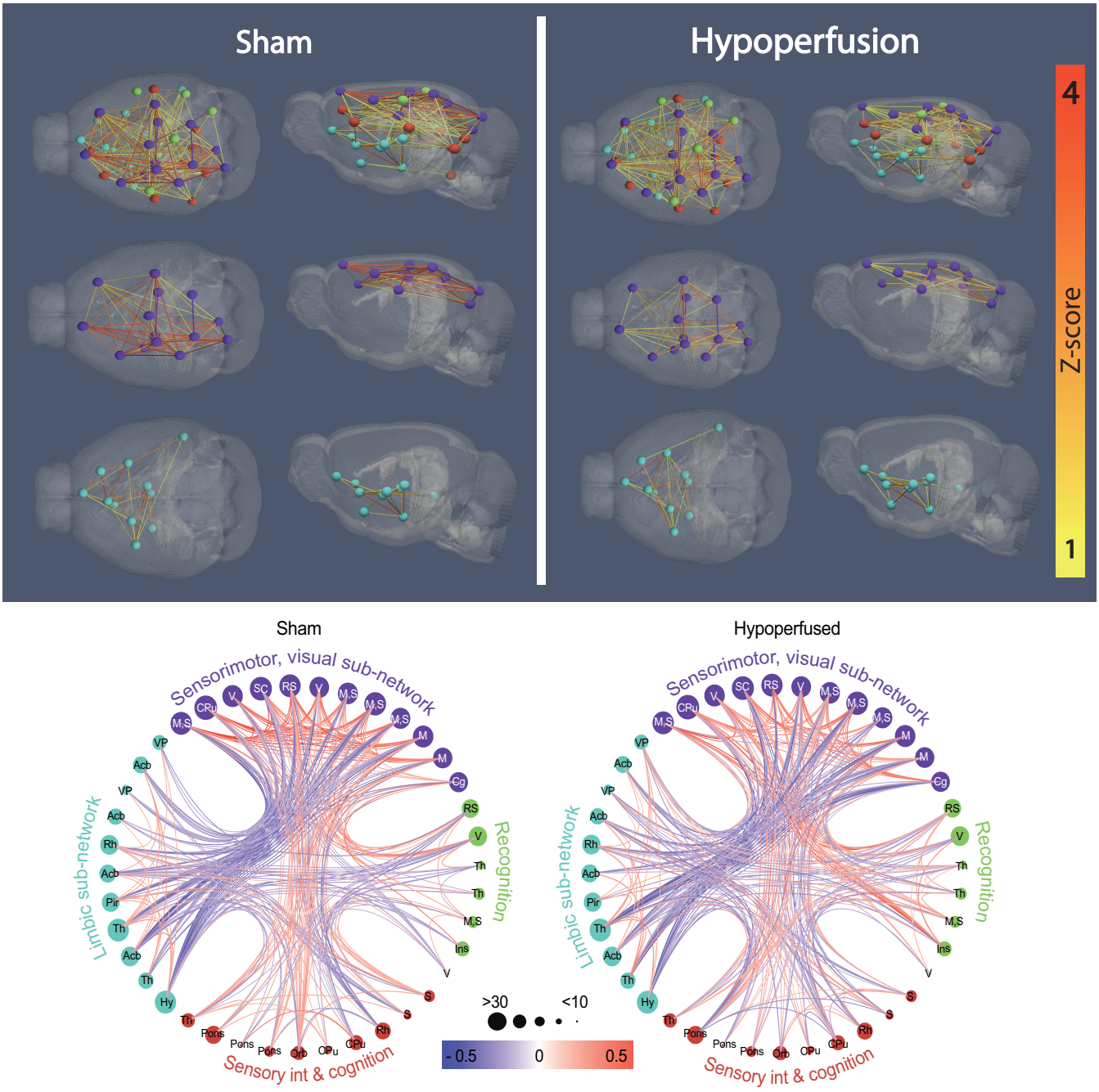


Figure 4. 10. Functional connectomes of sham and hypoperfused animals. (Top image) (Upper row) Saggital (left facing) and transverse (superior facing) glass brain connectomes of all clusters for the sham (n= 10) and hypoperfused (n= 6) between groups. (Top image) (Middle and bottom row) Same group specific views, but only of specific clusters; sensorimotor, visual cluster displayed in purple and the limbic cluster in blue. (Bottom image) Circular views of the connectomes displaying the four clusters. Each individual circle represents a specific component. Circle size dictates the overall number of connections and the scale bar represents the correlation strength (r value). Abbreviations: motor (M), sensory (S), visual (V), retrosplenial (RS), cingulate (C), frontal association (FrA), rhinal (Rh), and prefrontal (Pf) cortices, superior colliculus (SC), thalamus (Th), caudate putamen (CPu), hypothalamus (Hy), nucleus accumbens (Acb), pre-optic nuclei (POpt), olfactory nucleus (Olf), Insular (Ins).

To further investigate group comparisons, differences in correlational strength was calculated to allow a semi-quantification of the functional connectome (Figure 4.11). Confirming the observations mentioned above, the sham group had stronger increases in positive correlations within the sensorimotor and visual cluster. In comparison the hypoperfused group had stronger positive correlational values between the sensorimotor, visual and the limbic clusters compared to shams. In a similar fashion, the hypoperfused group showed stronger correlational values between the sensorimotor, visual and recognition clusters. The strongest differences for negative correlations were between the sensorimotor, visual, and sensory integration and cognition clusters.

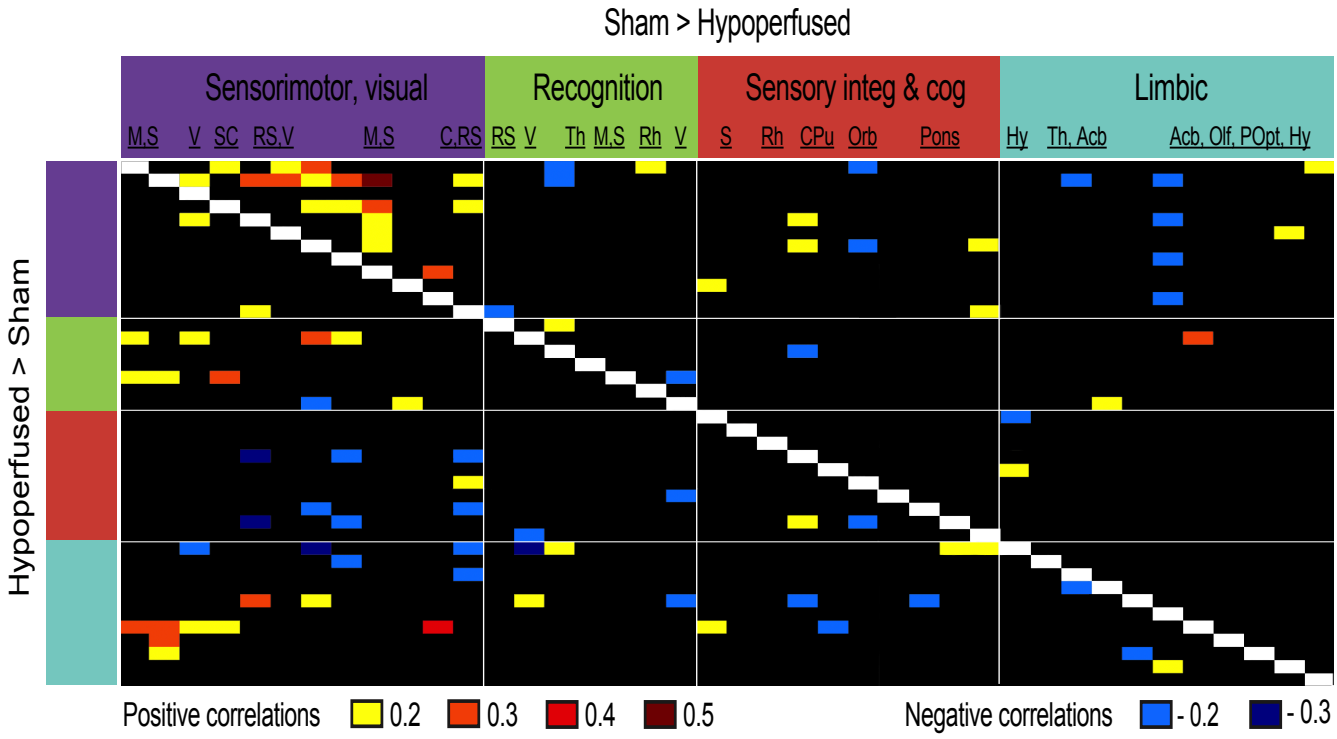


Figure 4. 11. Semi-quantification of functional connectivity strength between sham and hypoperfused animals. Connectivity matrix displaying the strength of the correlation differences between groups (top indicates stronger correlations in shams and bottom stronger correlations in the hypoperfused group). Abbreviations: motor (M), sensory (S), visual (V), retrosplenial (RS), cingulate (C), frontal association (FrA), rhinal (Rh), and prefrontal (Pf) cortices, superior colliculus (SC), thalamus (Th), caudate putamen (CPu), hypothalamus (Hy), nucleus accumbens (Acb), pre-optic nuclei (POpt), olfactory nucleus (Olf). Note: scale bars refer to the strength of the correlation differences between groups.

4.3.2.3. Dual Regression

Dual-regression analysis was performed for 14 components of interest (Figure 4.12). Component selection was primarily based on regions associated with the behaviour impairments commonly showcased in this model.

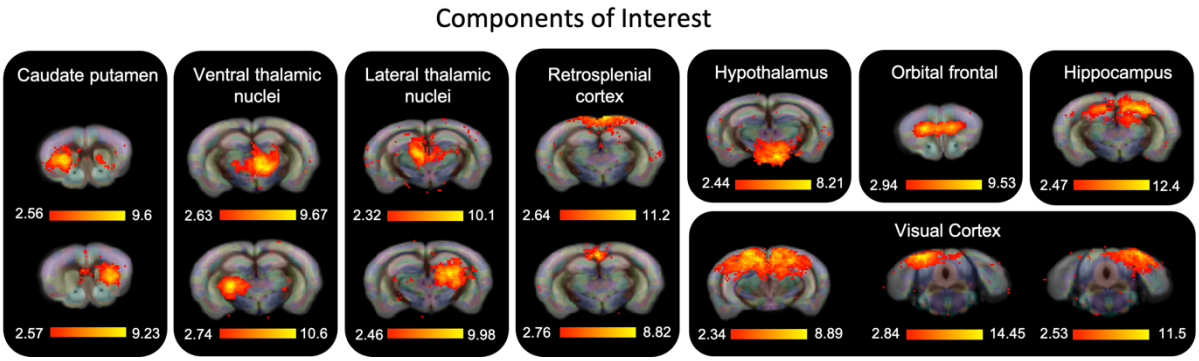


Figure 4. 12. Hypothesis driven analysis of 14 components of interest. Each component is overlaid on AMCA template and atlas. Note: scale bars correspond to the z score.

Following dual regression and voxelwise testing of the resulting spatial maps, three components had clusters of voxels in which the null hypothesis was rejected. These components were the hippocampus, and visual and retrosplenial cortices, though these differences did not remain significant after correcting for multiple comparisons.

In order to investigate statistical group differences of the timeseries correlations between all 40 components, connectivity matrices were generated for the positive only correlations (Figure 4.13). Generally, the first 17 components (majority of them in the sensorimotor, visual cluster) showed the strongest group differences, with correlational values reduced in the hypoperfused animals. No significant group differences were reported for correlational strengths between the 40 components after multiple comparison corrections (false discovery rate).

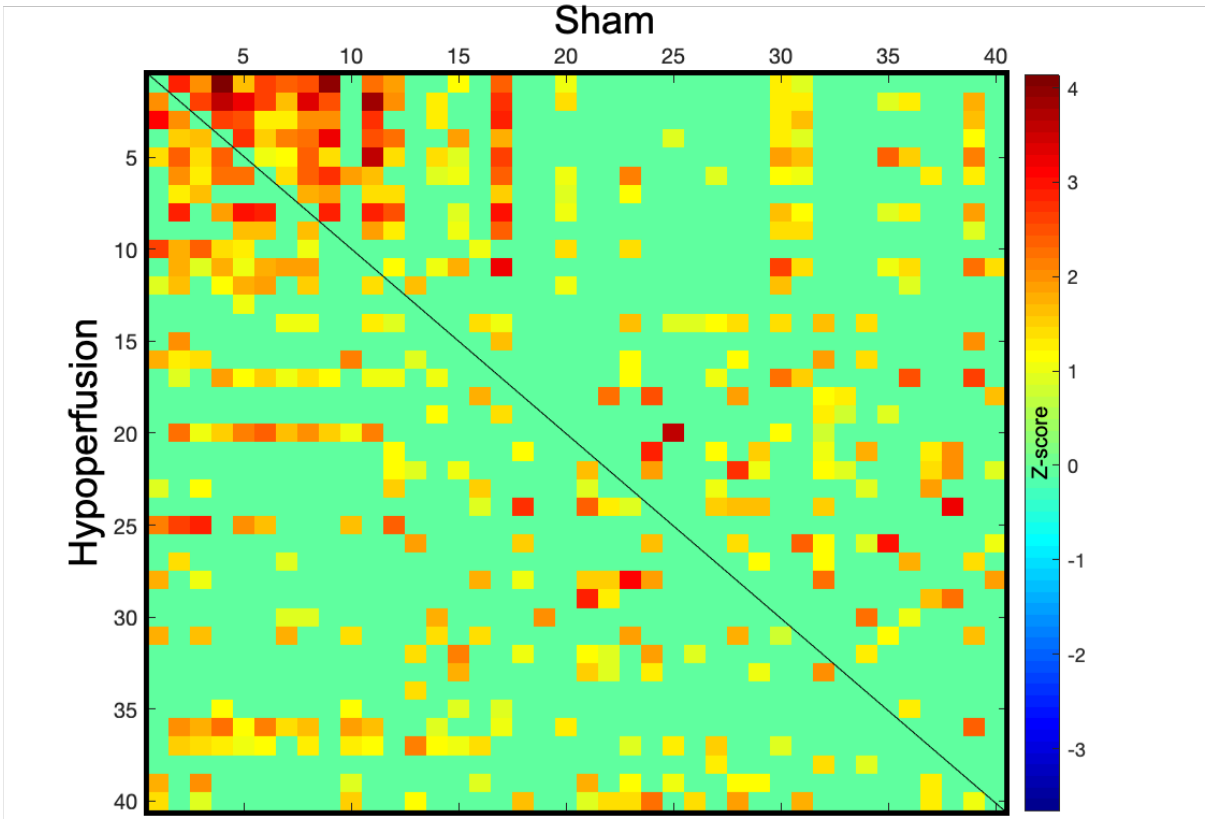


Figure 4. 13. Functional connectivity strength for activity components in sham and hypoperfused groups. Positive only correlational matrix comparing the sham (n=10) (upper diagonal) and hypoperfused (n=6) (lower diagonal) groups. Note: scale bars refer to the z score threshold.

4.3.2.4. Default mode network

Seed analysis from the cingulate revealed that shams showed high correlations between the cingulate and retrosplenial, motor and somatosensory cortices and thalamus. The hypoperfused group displayed very little correlational activity (Figure 4.14).

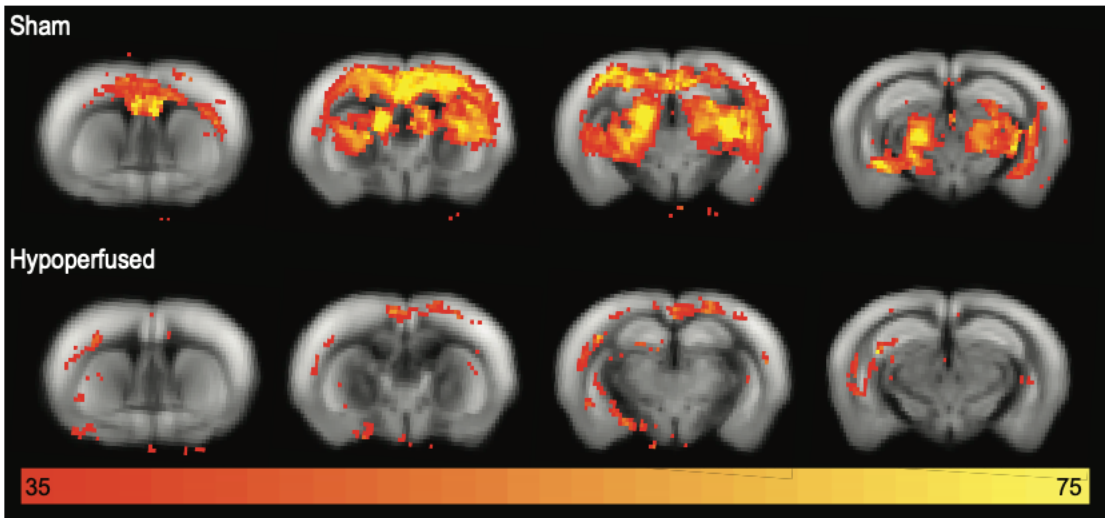


Figure 4. 14. The default mode network is reduced in hypoperfused mice. Cingulate seeding produced a strong, primarily cortical, rostral-caudal midline activity pattern (rodent default mode network) in the sham animals that was markedly reduced in the hypoperfused group. Note: Components are overlaid onto AMCA and scale bars correspond to the z score.

4.3.2.5. Graph Theory

As shown in Figure 4.15, there was no significant difference between sham and hypoperfused mice for the graph theory parameter of global efficiency (U= 26.0, p= 0.71).

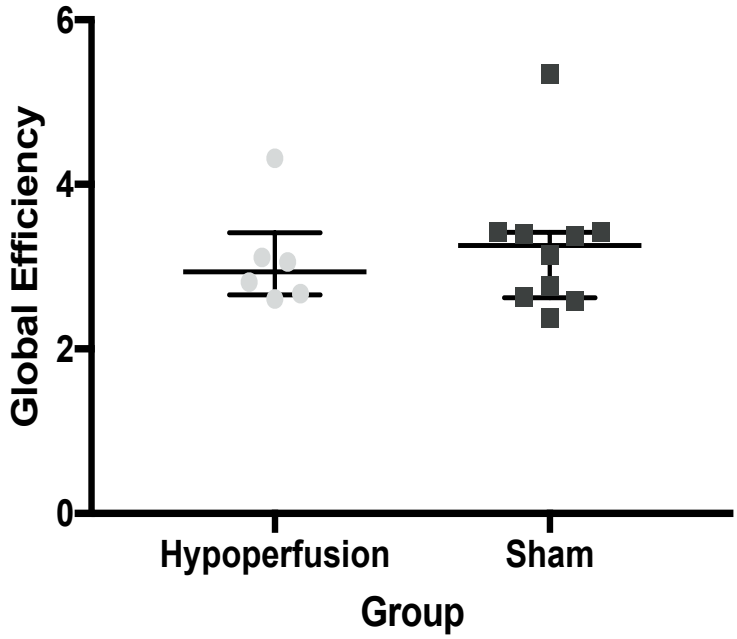


Figure 4. 15. No differences in global efficiency between sham and hypoperfused mice. Global efficiency (median ±interquartile range) for each group: sham (n= 10) and hypoperfused (n= 6).

Local efficiency was examined for each individual component, a main effect of group F(1, 14)= 0.4, p< .03, η_p^2 = 0.25 was reported for local efficiency. In general, local efficiency values were lower for most components in the hypoperfused group (Figure 4.16). There was also a main effect of component F(39, 546)= 2.688, p< .001, η_p^2 = 0.16; there was no main effect for the interaction between group and component F(39, 546)= 0.884, p= 0.67, η_p^2 = 0.06.

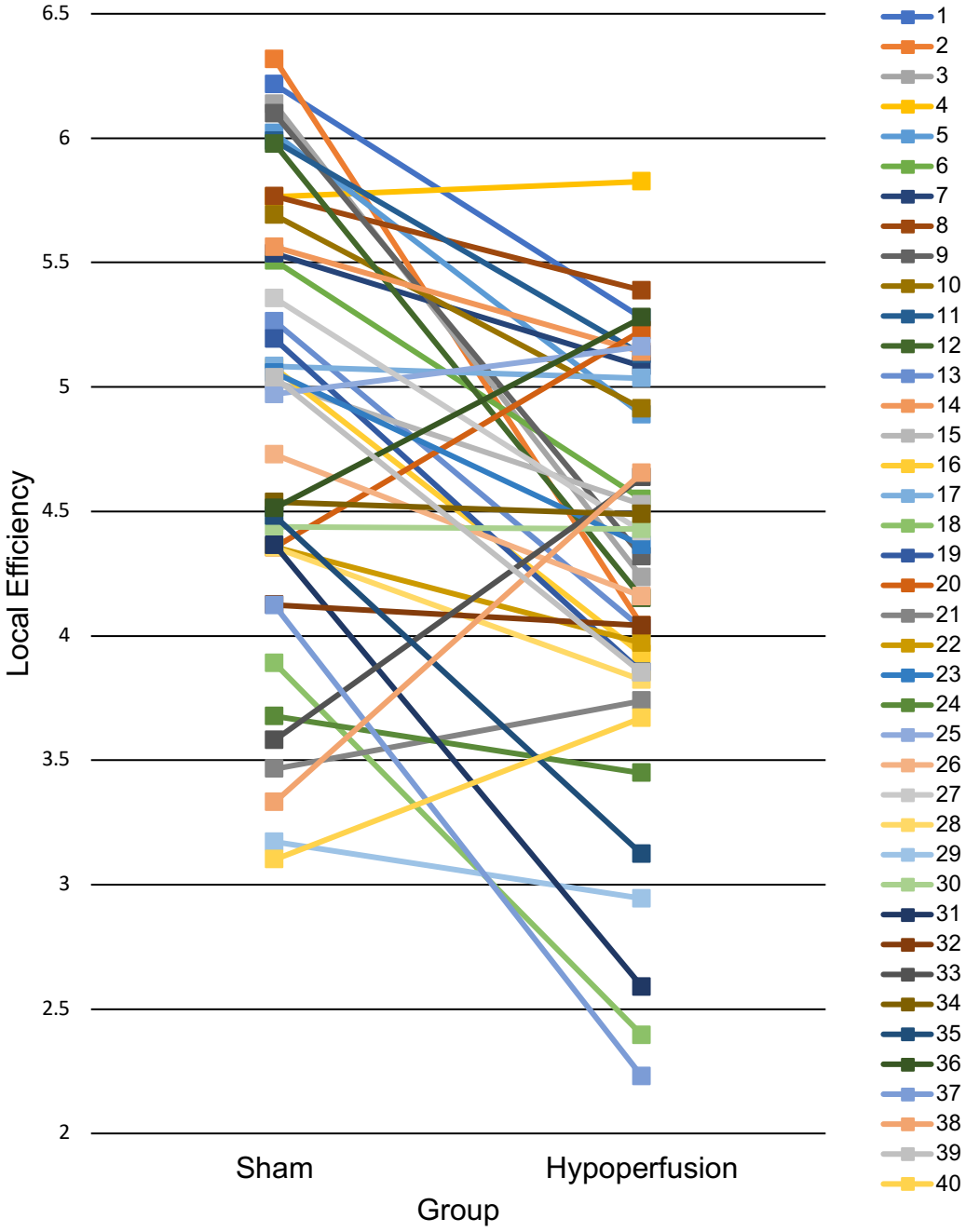


Figure 4. 16. Local efficiency interaction between sham and hypoperfused animals. Local efficiency for all components (n= 40) in each group: sham (n= 10) and hypoperfused (n= 6).

Figure 4.17 depicts the segregation measures transitivity and modularity, and there were no significant differences between sham and hypoperfused animals for either measure: transitivity (U= 16.0, p= 0.15) or modularity (t(14)= 0.19, p= 0.85).

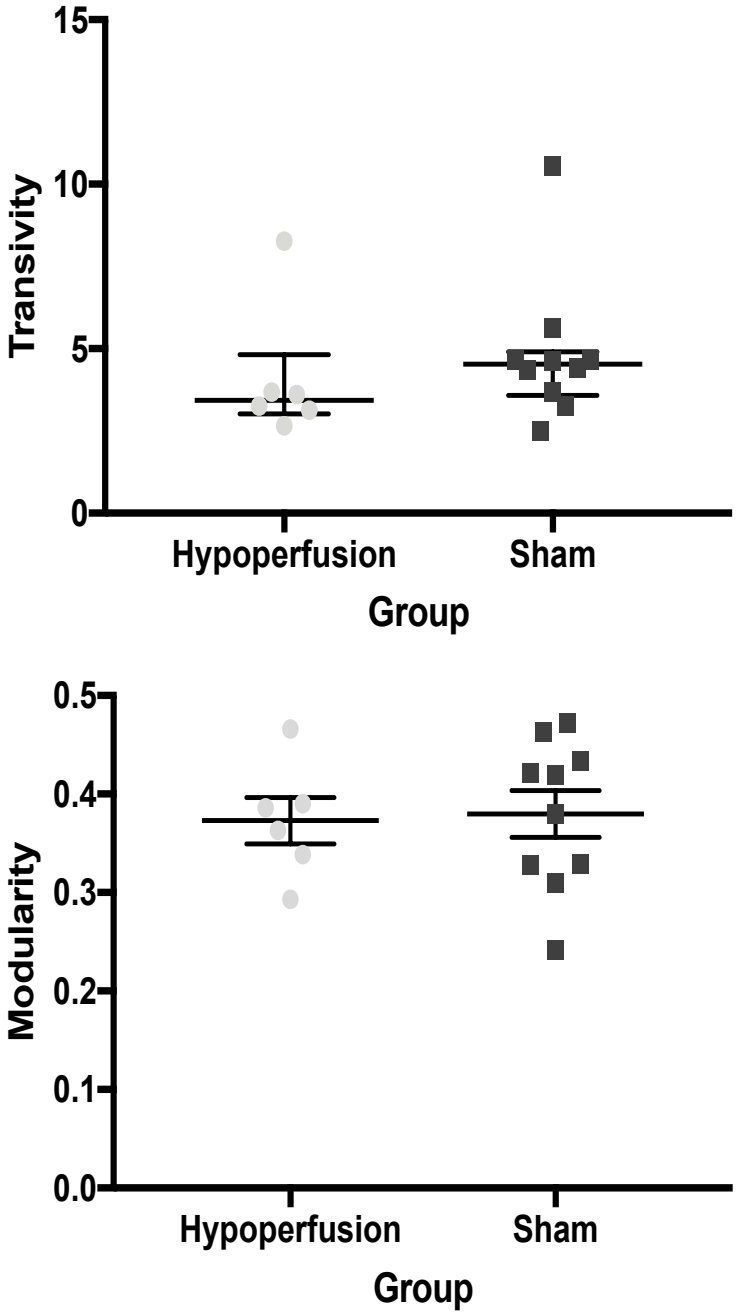


Figure 4. 17. No differences in transitivity or modularity between sham and hypoperfused mice. (Top) Transitivity and (Bottom) modularity (median ±interquartile range) in each group: sham (n= 10) and hypoperfused (n= 6).

4.3.3. dMRI

4.3.3.1. TBSS

Voxelwise comparisons for differences in FA between sham and hypoperfused WM for the 3- and 6-month timepoints are displayed in Figures 4.18 and 4.19, respectively.

For the 3-month timepoint, voxels having stronger FA in the hypoperfused group compared to the sham group are displayed in Figure 4.18. From visual inspection, the hypoperfusion group had higher FA generally in the corpus callosum and anterior commissure, whereas the shams had displayed increased FA predominantly in the fimbria and posterior regions such as the periaqueductal grey and lateral lemniscus.

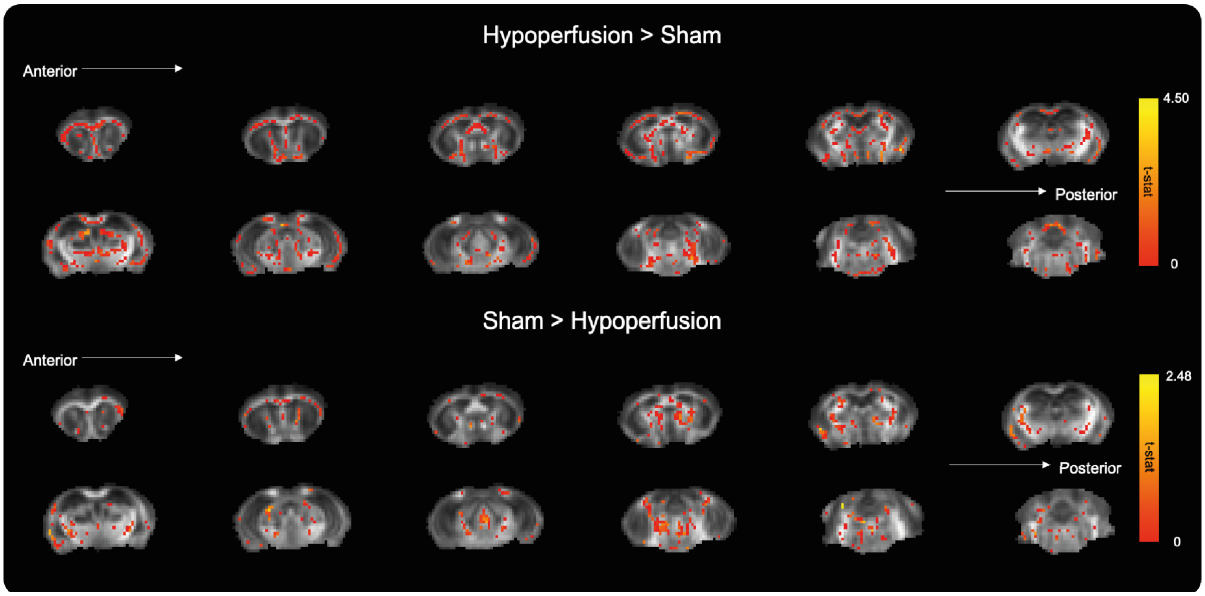


Figure 4. 18. Spatial map differences in FA between sham and hypoperfused mice. Coronal views of the voxels in which FA is higher in the sham (n=10), and higher in the hypoperfused (n=6) group at the 3-month timepoint. Note: scale bar corresponds to the t-statistic.

For the later 6-month timepoint, while the hypoperfused group had higher FA in the fimbria and the posterior forceps subsection of the corpus callosum. In contrast, the hypoperfusion group showed strong reductions in FA in the corpus callosum specifically on the right side in addition to the internal capsule compared to shams.

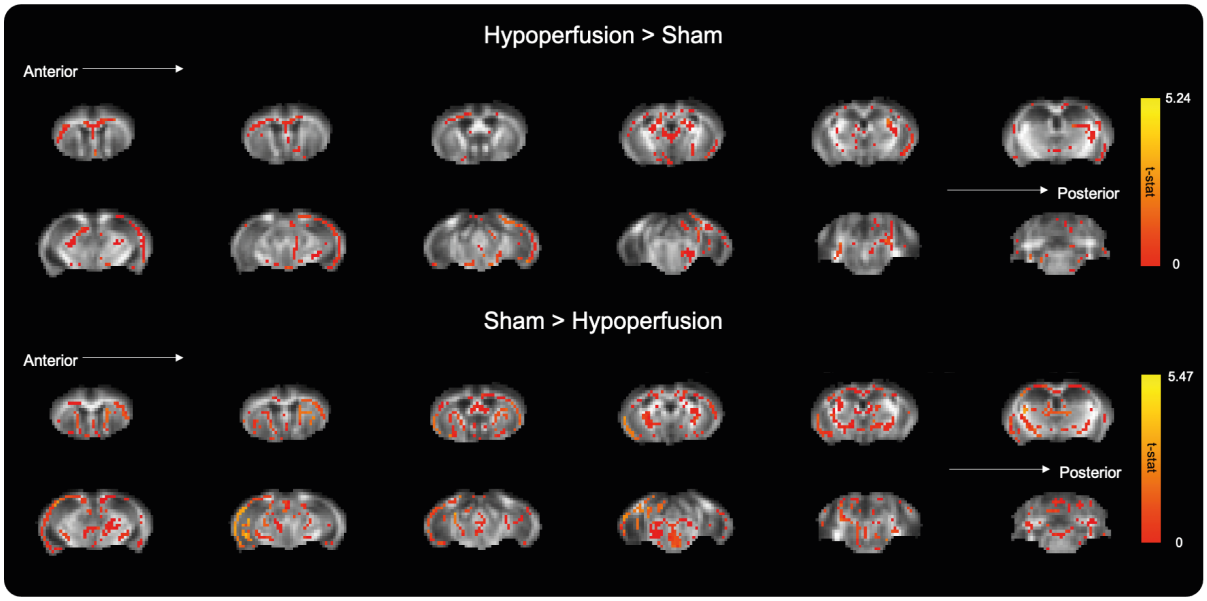


Figure 4. 19. Spatial map differences in FA between sham and hypoperfused mice. Coronal views of the voxels in which FA is higher in the sham (n=10), and higher in the hypoperfused (n=6) group at the 6-month timepoint. Note: scale bar corresponds to the t-statistic.

Follow up statistical analysis of the voxelwise comparisons between groups (hypoperfused, sham) for each timepoint (3- and 6-months) revealed none of these differences illustrated in Figure 4.18 and 4.19 achieved significance at either timepoint. Prior to multiple comparison correction, the 3-month timepoint still showed no significant voxelwise differences between groups. At the 6-month timepoint, the largest reductions in FA for the hypoperfusion group compared to shams was displayed in the right corpus callosum and internal capsule (Figure 4.20). These differences were unable to maintain significance however after family-wise error rate correction for multiple comparisons.

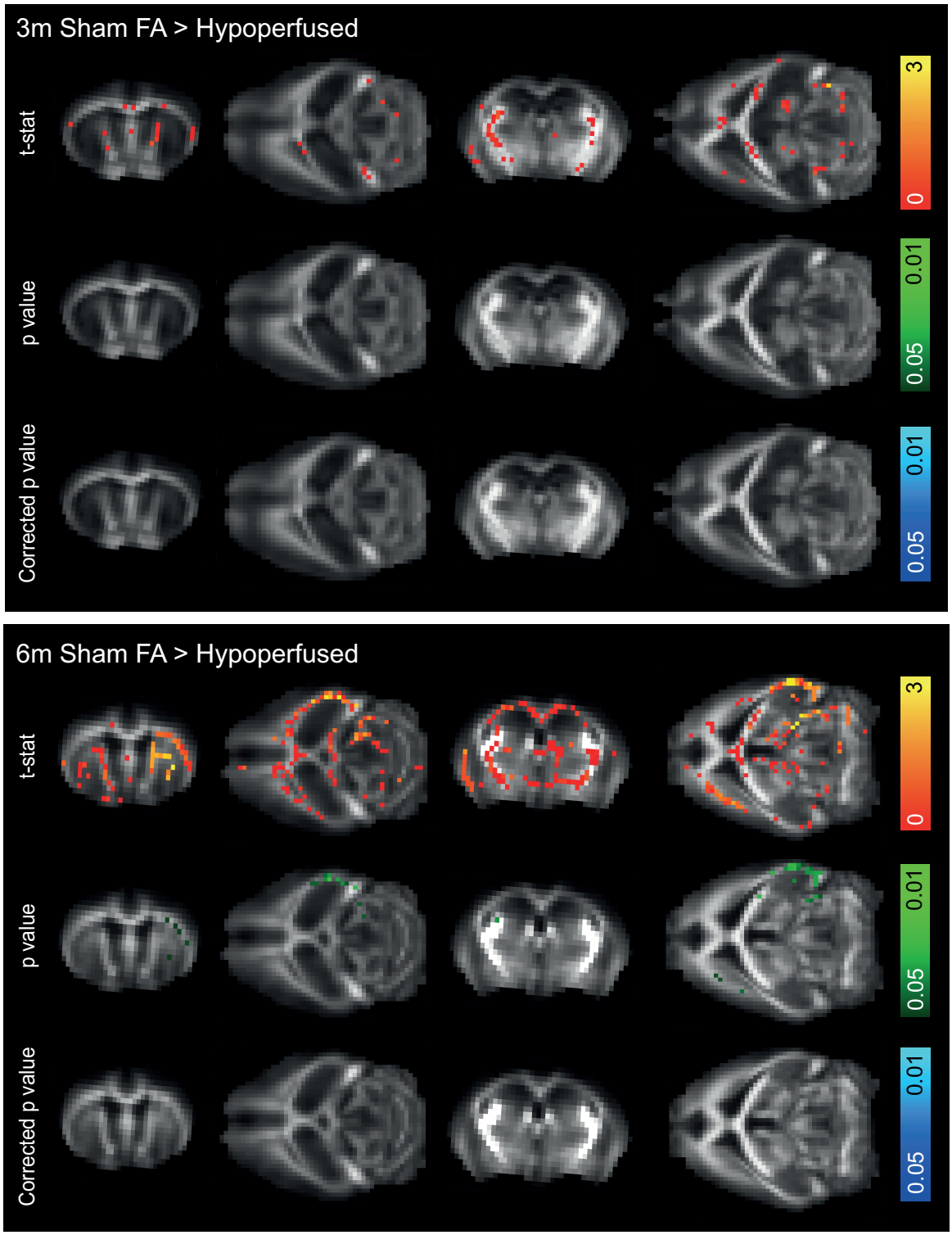


Figure 4. 20. White matter is only subtly affected by hypoperfusion. Sham animals exhibited higher FA values in many white matter voxels at both 3 and 6m. Note: orange scale bar represents the t-statistic, green scale bar represents the p value, and blue scale bar represents the corrected p-value overlaid onto the mean FA map from all mice at each timepoint.

4.3.3.2. Tractography

Probabilistic tractography produced structural connectivity matrices for both groups are displayed at all timepoints in Figures 4.21 and 4.22. As expected, the AMCA regions (n= 681) generally had increased structural connectivity to regions within the same parent region in the atlas hierarchy. In terms of interconnectivity between other parent regions, the white matter areas had the largest interconnectivity to all other regions as predicted. While in contrast the medulla had reduced interconnectivity to all other regions except the pons and cerebellum. The AMCA partitions the midbrain regions into three functional categories; sensory, motor and behavioural. All of these sub-regions had high connectivity to each other in addition to the cerebellum. Cortical regions broadly showed high connectivity to specific neighbouring regions with the somatosensory areas showing the highest spread of cortical connectivity. Overall from visual inspection, no noticeable differences were present between groups at each timepoint. From all the regions in the AMCA atlas (n= 681), the caudate had the highest connectivity, however after further investigation the caudate also was the largest region with the most seed regions. In comparison to the average number of seeds per region (M= 48.21, SD= 81.73), the caudate far excelled the number of seeds (n= 1377) in total. After further inspection of the AMCA atlas, while the majority of regions were broken down to a mesoscale parcellation, other areas like the caudate were at a macroscale level (atlas comparison illustrated in Figure 4.3). In order to better control the scale of parcellation and reduce seed variance, we adapted the AMCA atlas (n= 681) into an AMCA parent atlas (n= 32) that was parcellated via the parent hierarchy of each associated region (Figure 4.23).

After viewing the parent matrices (Figure 4.23), although a similar pattern of connectivity to the full AMCA matrix was present, generalised segregated groupings between cortical regions and a combination of the midbrain, deception and brain stem was noticeable. While white matter and cerebellar regions displayed high interconnectivity between all regions similar to the full AMCA matrices (Figure 4.21 and 4.22), the hippocampal and striatal regions also displayed similar regional interconnectivity. The frontal association area (FrA in Figure 4.23) had noticeability reduced connectivity compared to the other regions, although this area still had reduced amounts of seeds (n=3) compared to the average (M= 968.69) due to its size. Again, similar to the AMCA matrix (n=681) no noticeable group differences were present at either timepoint.

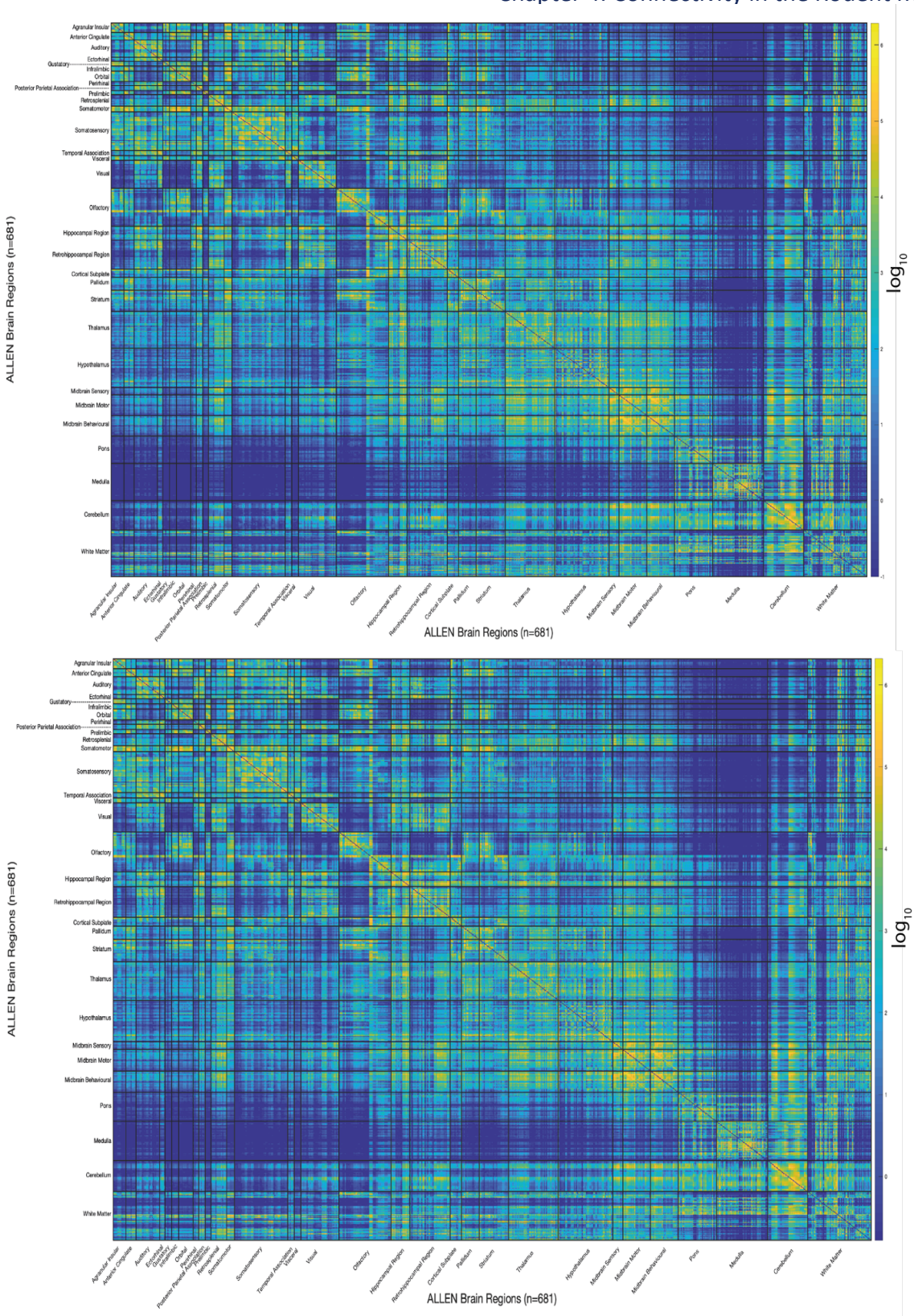


Figure 4. 21. Structural connectivity at the 3-month timepoint for the sham (top) and hypoperfusion (bottom) group. Each matrix illustrates the number of connective streamlines calculated through probabilistic tractography between all of the AMCA regions (n=681). Note: scale bar reflects the number of connectivity streamlines scaled by a factor of $\log_{10}$.

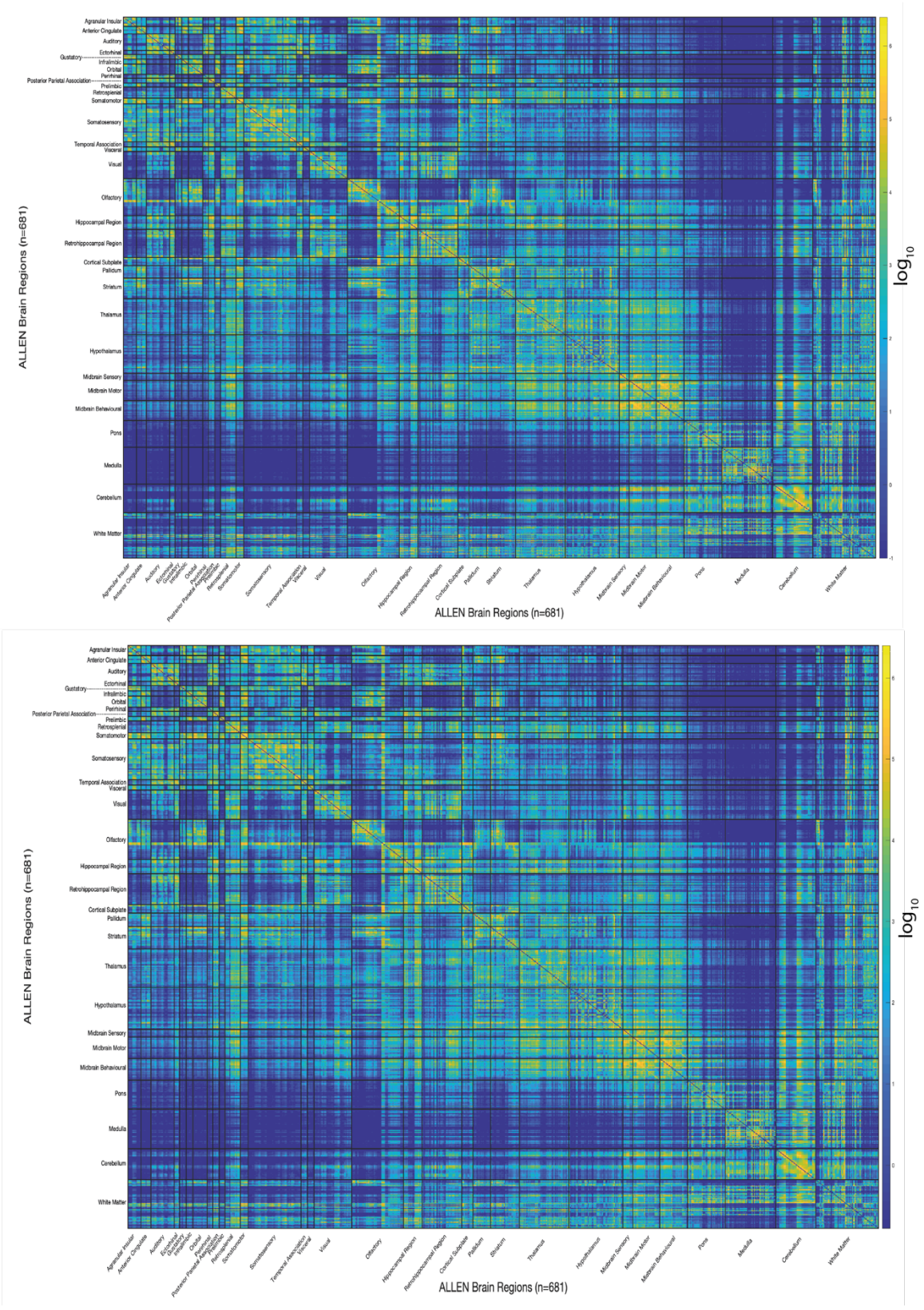


Figure 4. 22. Structural connectivity at the 6-month timepoint for the sham (top) and hypoperfusion (bottom) group. Each matrix illustrates the number of connective streamlines calculated through probabilistic tractography between all of the AMCA regions (n=681). Note: scale bar reflects the number of connectivity streamlines scaled by a factor of $\log_{10}$.

Similar connectivity matrices are displayed for the AMCA parent atlas in Figure 4.23.

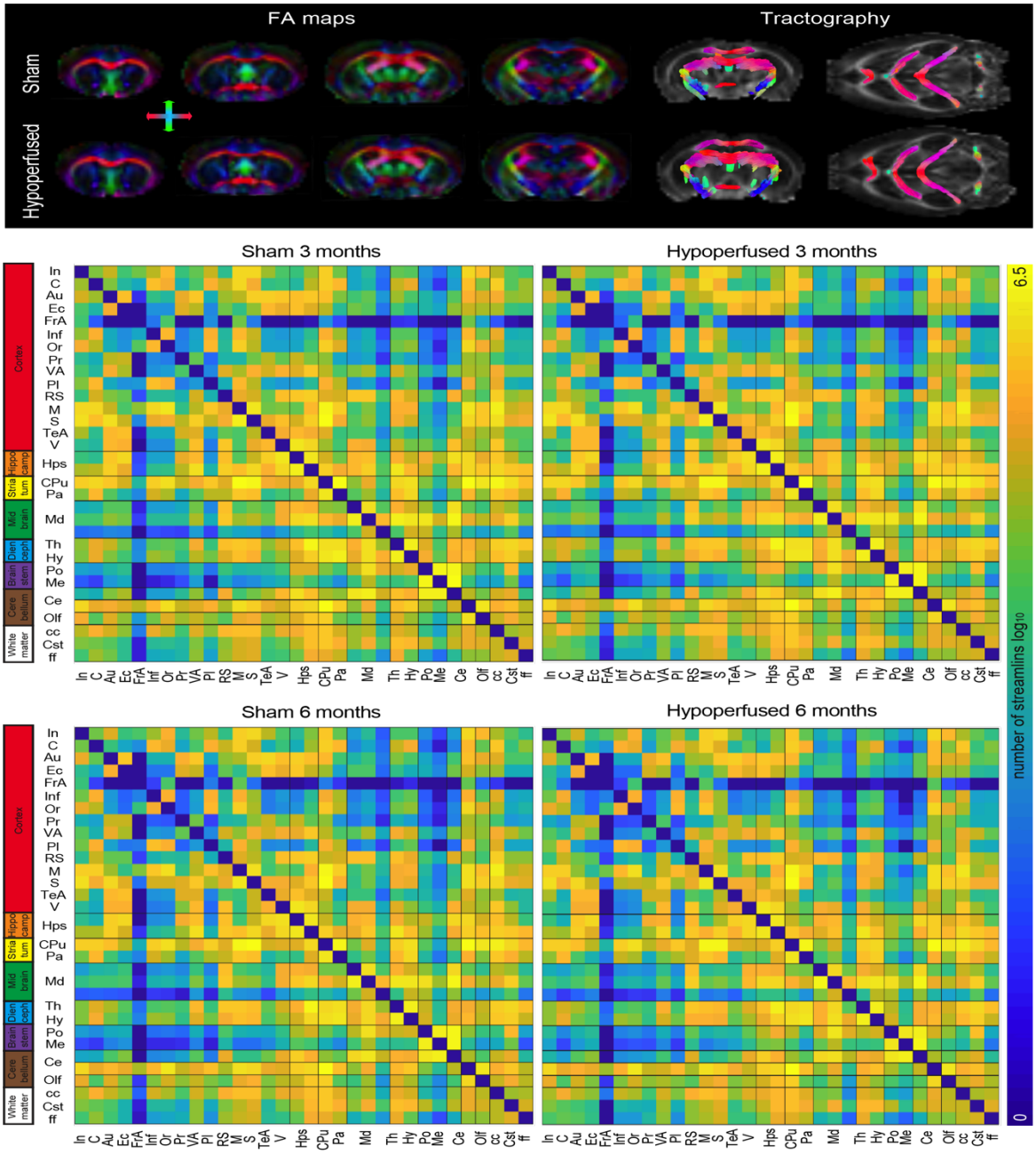


Figure 4. 23. Structural connectivity is intact in hypoperfused mice at both timepoints. Fractional anisotropy (FA) maps and white matter reconstructions from representative sham and hypoperfused animals. Note: Direction is indicated by color. Structural connectivity matrices from 32 seeded parent regions are displayed for sham and hypoperfused mice at 3 and 6m. Note: scale bar corresponds to edge weighting: the number of streamlines between each region. Abbreviations: insular (In), cingulate (C), auditory (Au), ectorhinal (Ec), frontal association (FrA), infralimbic (Inf), orbital (Or), perirhinal (Pr), visual association (VA), prelimbic (Pl), retrosplenial (RS), motor (M), sensory (S), temporal association (TeA), and visual (V) cortices, hippocampus (Hps), caudate putamen (CPu), ventral pallidum (Pa), midbrain (Md), thalamus (Th), hypothalamus (Hy), pons (Po), medulla (Me), cerebellum (Ce), olfactory region (Olf), corpus callosum (cc), corticospinal tract (Cst), fornix (ff).

4.3.3.3. Graph theory

For graph theory measures of integration, no significant main effects were reported for global efficiency for timepoint $F(1, 14) = 0.25$, $p = 0.63$ or group $F(1,14) = 0.61$, $p = 0.45$, and the interaction between timepoint and group was also insignificant $F(1,14) = 0.03$, $p = 0.88$ (Figure 4.24).

However, for local efficiency, a significant main effect of timepoint $F(1,510) = 13.17$, $p<.001$, $\eta_p^2 = 0.03$ was observed; there was a slight reduction in local efficacy at 6-months ($M = 0.70$, $SE = 0.01$) compared to 3-month ($M = 0.71$, $SD = 0.01$). However no significant main effect was reported for group $F(1, 510) = 0.23$, $p = 0.64$, and there was no interaction between timepoint and group $F(1,510) = 1.01$, $p = 0.32$. A significant interaction was present between region, group and timepoint $F(31,434) = 1.9$, $p =.003$, $\eta_p^2 = 0.12$. Follow up t-tests before correction for multiple comparisons, revealed significant group differences at the visual association area both at the 3-month $t(14) = -2.5$, $p = 0.02$ and 6-month $t(14) = -3.8$, $p = .002$ timepoints. This effect was similarly reported in the midbrain at the 3-month $t(14) = -2.3$, $p = 0.04$ and 6-month $t(14) = -3.0$, $p = 0.01$ timepoints. Furthermore, significant differences were only seen at the 6-month timepoint for the corticospinal tract $t(14) = -2.7$, $p = 0.02$, cerebellum $t(14) = -2.4$, $p = 0.03$, and auditory cortex $t(14) = 2.2$, $p = 0.04$. After correction for multiple comparisons using a false discovery rate (FDR), the visual association area at the 6-month timepoint was the only comparison that remained significant $t(14) = -3.8$, $p = 0.05$ after multiple comparison corrections between the hypoperfusion ($M = 0.70$, $SD = 0.16$) and sham ($M = 0.68$, $SD = 0.01$) groups.

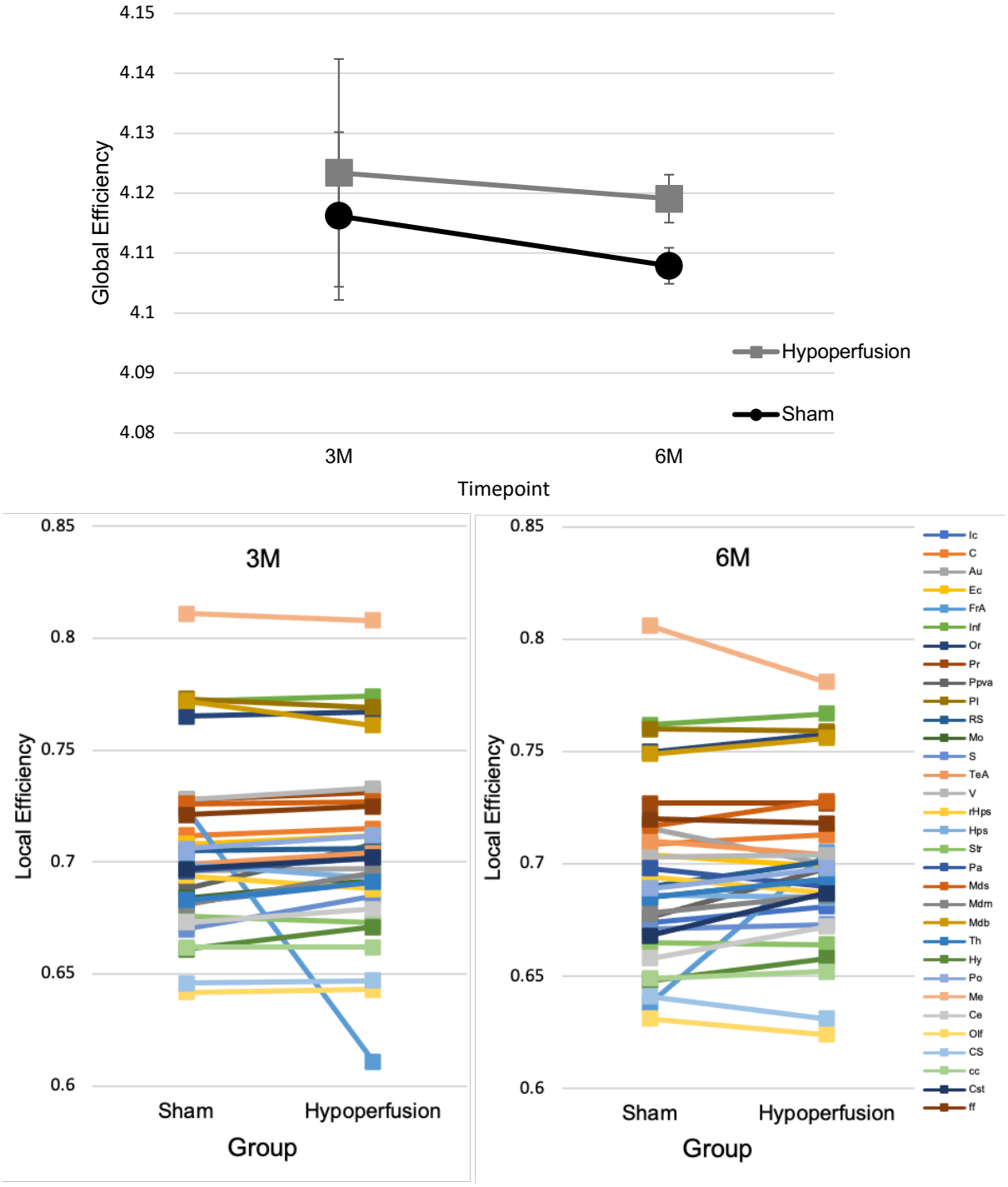


Figure 4. 24. Integration graph theory values (global and local efficiency) for dMRI at 3- and 6-months. (Top) Global efficiency (mean ± SE) for sham (n=10) and hypoperfused (n=6) groups. (Bottom) Local efficiency (mean) for all 32 AMCA parent regions in both groups at 3 and 6 months. Abbreviations: cingulate (C), auditory (Au), ectorhinal (Ec), frontal association (FrA), infralimbic (Inf), orbital (Or), perirhinal (Pr), prelimbic (Pl), retrosplenial (RS), motor (M), sensory (S), temporal association (TeA), and visual (V) cortices, hippocampus (Hps), retrohippocampal (rHps), ventral pallidum (Pa), midbrain behavioral (Mdb), midbrain superior colliculus (Mds), midbrain motor (Mdm), Striatum (Str), thalamus (Th), hypothalamus (Hy), pons (Po), medulla (Me), cerebellum (Ce), olfactory region (Olf), corpus callosum (cc), corticospinal tract (Cst), fornix (ff), internal capsule (Ic), posterior parietal visual association (Ppva), Cortical Subplate (CS).

For graph theory measures of segregation, no significant main effects for modularity were reported for timepoint $F(1,14) = 2.92$, $p = 0.11$, or group $F(1,14) = 2.63$, $p = 0.13$, or the interaction $F(1,14) = 0.02$, $p = 0.89$. For transitivity, a significant main effect was observed for timepoint $F(1,14) = 20.44$, $p < .001$, and there was a decrease in values at 6 months ($M = 0.58$, $SE = 0.01$) compared to 3 months ($M = 0.59$, $SE = 0.01$). However, there was no main effect of group $F(1,14) = 0.79$, $p = 0.39$, or an interaction between timepoint and group $F(1,14) = 0.01$, $p = 0.94$.

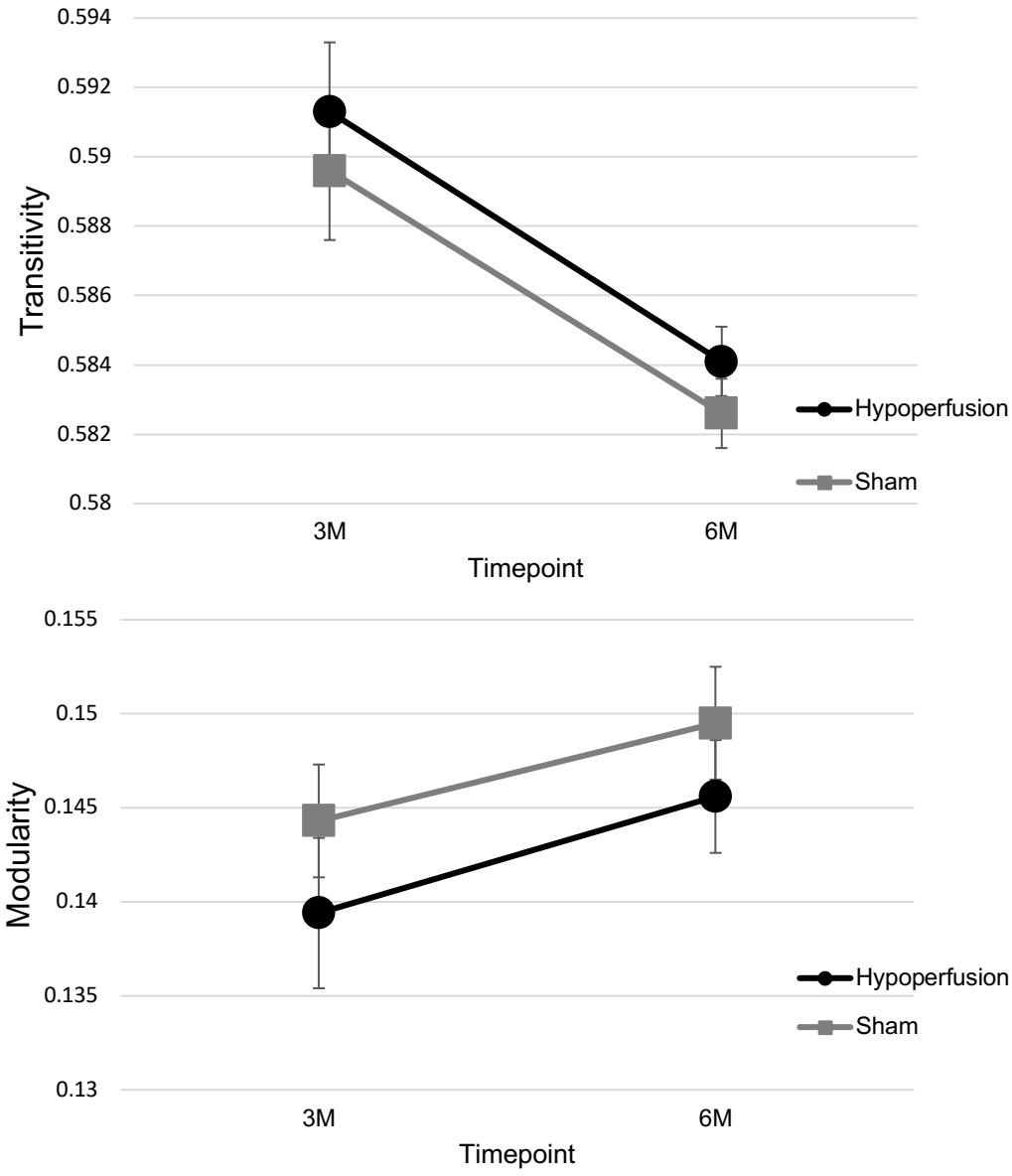


Figure 4. 25. Segregation graph theory measures for dMRI structural connectivity data. (Top) Transitivity and (Bottom) modularity (mean ± SE) for sham (n=10) and hypoperfused (n=6) mice at 3 and 6 months.

4.4. Discussion

To our knowledge, this was the first attempt to classify functional and structural network changes at chronic timepoints (3- and 6-months) in an acute BCAS mouse model (160μm coils). In line with previous findings, the restricting microcoils demonstrated a sharp reduction of blood flow compared to the non-restricting sham group. Throughout the later timepoints, a recovery of CBF was evident with a return close to sham levels. This decrease in CBF supports the effectiveness of a microcoil at this size, in addition this sharp initial reduction could link to the high mortality evident in this type of model. Even when adding a 24-hr gap between each microcoil placement, a mortality rate of nearly a half was still present in the condition group, implicating the severity of this model. Throughout the duration, a recovery of CBF was evident in the condition group, almost returning back to the sham levels. This chronic return to normal levels supports the capability for the mouse brain to restore CBF overtime that corresponds in the same microcoil size at shorter timepoints (Boehm-Sturm et al., 2017) and for similar microcoil sizes (0.18mm) (Shibata et al., 2004; Nishio et al., 2010; Fuchtemeier et al., 2015).

Data investigating functional connectivity was collected only at the 6-month timepoint. Whilst we were able to detect anatomically relevant resting-state networks within the mouse, the dual-regression analysis reported none of the components of interest (n=14) were significantly different as a result of hypoperfusion. From visual appearance, timeseries correlation strength between all components (n=40) did appear reduced in the hypoperfusion group. In addition, seed analysis of the cingulate appeared to show weaker correlations in neighbouring regions in the hypoperfused group. Statistical analysis, however, revealed the only group differences for direct comparisons of correlational interactions between all component timeseries was at the local connectivity level (local efficiency), although this group effect did not interact with a specific arrangement of components. No significant group differences were reported for any other measures of global network connectivity (global efficacy) or sub-network arrangement (transivity and modularity). Measures of structural connectivity were taken at two timepoints (3- and 6-months). Although TBSS analysis, showed stronger differences at the 6-month timepoint, no significant group differences were reported for voxelwise comparisons of FA. After generating a model of structural connectivity using probabilistic tractography with the dMRI data, analysis of the same measures of network integration and segregation previously used in the functional graphs

revealed no significant group change for all graph theory measures or associated group interactions. A significant interaction was present however for group, timepoint and region for measures of local efficiency. After post-hoc investigation, only the visual association area showed significant reduction in local efficacy at the 6-month timepoint for the hypoperfusion group after correction for multiple comparisons. This decrease in structural connectivity observed specifically in the visual cortex aligns what was reported in the dual regression in the functional analysis. Although insignificant after multiple comparisons, a visual component showed the strongest ranked differences in the rs-fMRI analysis. Overall, these findings are suggestive that the visual system is vulnerable to chronic hypoperfusion and the effectiveness of using exploratory network techniques to investigate subtle damage in preclinical models.

4.4.1. Functional connectivity network

The 40 neurally driven components generated through ICA and their corresponding hierarchical clustering support the existence of resting-state networks previously seen the mouse (Sforazzini et al., 2014; Stafford et al., 2014; Zerbi et al., 2015; Bukhari et al., 2017; Sethi et al., 2017). The total sum of these components comprised of four major clusters; sensorimotor and visual cluster, recognition memory cluster, sensory integration and cognition cluster, and a limbic cluster. The components generated show a strong correspondence with previous mouse resting-state research. Components located at the cingulate, motor, somatosensory, hippocampus and thalamus show a strong similarity to components previously reported (Sforazzini et al., 2014; Zerbi et al., 2015; Bukhari et al., 2017). Furthermore, previous research employing clustering using a similar hierarchy matrix, displayed familiar component clustering, motor, auditory and visual cortices (Zerbi et al., 2015).

The most obvious differences to previous mouse rs-fMRI research (Grandjean et al., 2014a; Stafford et al., 2014; Zerbi et al., 2015; Bukhari et al., 2017) was that the majority of the components generated were unilateral rather than bilateral. After viewing the hierarchy matrices, unilateral components tended to cluster to their corresponding bilateral components. Several factors could have influenced lack of bilateral components; ICA dimensionality determined automatically might have been set too high at 59. Previous research has widely

varied on a standardised number for ICA dimensionally, with some papers using 30 components (Zerbi et al., 2015), 70 components (Bukhari et al., 2017) and 100 components (Sethi et al., 2017). This variability seen previously in dimensionality selection in mouse ICA influenced our decision to choose the automatic approach. After viewing component comparisons on different dimensionalities within our data and comparing these results to previous research. An ICA dimensionality set to 30 as previously used in Zerbi and colleagues (2015) might have arguably been best for dual-regression analysis. Most bilateral components that contained more complete rodent RSNs were present at the 30 dimensionality, whilst in comparison to the 15 dimensionality components were less anatomically ambiguous due to such large component coverage. Therefore, analysing components containing more complete RSNs, whilst still being anatomically specific, might have reduced the severity of multiple corrections in the dual regression. In addition, the component analysis could have had stronger statistical power as they would contain a more complete network of regions. Another factor that might have affected bilaterality, could have been the anaesthetic used, as isoflurane has been reported to generate weaker cortical and more unilateral components compared to using medetomidine (Grandjean et al., 2014a). More recently Grandjean and colleagues (2020) have identified across a widespan of multi-centre datasets, other major factors affecting functional connectivity in addition to choice of sedation. Overall, the quality of scanning equipment and breathing conditions (mechanical ventilation being gold standard) also heavily affected the sensitivity and specificity of functional connectivity in RSNs such as the DMN.

Regarded as an inferior subsystem of the primate DMN, individual components associated with the mouse “DMN-like” analogue, consist of the cingulate, retrosplenial, medial orbital and parietal regions (Stafford et al., 2014). Although these regions were present in the ICA output, during hierarchical clustering, only the cingulate and retrosplenial components seemed to show a strong timeseries correlations with each other, though both were associated with different sub-networks. As the orbital frontal component displayed strong positive timeseries correlations with the sensorimotor and visual networks, stronger positive correlations with caudate components ultimately grouped the orbital frontal component to the sensory integration and cognition network. This lack of a rodent DMN clustering in components associated with the network could have been the resulting influence from the hypoperfusion group. Due to small group sizes, both groups were used to generate hierarchy matrices. Therefore, if chronic hypoperfusion was affecting rodent DMN connectivity, the

reduced DMN from the hypoperfused group could have affected a DMN-like clustering in the hierarchy matrix. Further investigation using seed analysis on the cingulate, a prominent region in the DMN analogue in the mouse, revealed strong connectivity primarily in cortical, rostral-caudal midline regions. This pattern of functional connectivity associated with the cingulate, strongly corresponds with the DMN connectivity evident between the cingulate, retrosplenial and parietal cortices. In addition to the functional connectivity associated with the primary visual and somatosensory regions implicated only in functional connectivity in the rodent DMN-analogue (Upadhyay et al., 2011; Lu et al., 2012; Stafford et al., 2014). In comparison, this pattern of functional connectivity in the seed analysis was not present in the hypoperfused group. This lack of correlation in the caudate for the seed analysis supports the possibility that the lack of DMN-like clustering in the hierarchy matrix could have been influenced by the hypoperfusion group. For future functional connectivity research, it seems generating component hierarchy matrices specifically from the control group may help identify and compare component clusters and interactions of RSNs to previous research.

Strong negative correlations in the hierarchy matrix were present between the sensorimotor, visual and the limbic networks. Though it is possible that these networks may be functionally connected through opposing timeseries patterns, it is important to note the global signal regression used to generate the functional matrixes can artifactually inflate negative correlations (Murphy and Fox, 2017). Hence, negative correlations were removed during the thresholding before graph theorical analysis.

4.4.2. Functional connectivity differences between sham and hypoperfused mice

From visual appearance, group-based differences in correlational strength vary depending on the network cluster being viewed. The hypoperfusion group had the largest reduction of correlational strength within the sensorimotor and visual network. Whilst a subsequent increased correlational strength was present between inter-network connections of the limbic and sensorimotor clusters. This not only supports a reduction in functional connectivity specifically in the sensorimotor and visual component correlations in chronic hypoperfusion, it also displays an increase in sub-cortical connectivity between the limbic and the sensorimotor and visual clusters, possibly from the resulting reduced connectivity in the

latter. Increased functional connectivity as a suggestive compensatory mechanism has been reported in alternative models of cerebrovascular disease. For example, previous rs-fMRI analysis on a mouse model of mild stroke discovered increased synchronicity of functional connectivity within the sensorimotor regions that continued up to 12-weeks post stroke (Minassian et al., 2020). Whilst in comparison, similar rs-fMRI research investigating a mouse model of severe stroke in the same strain of mouse, reported decreases in functional connectivity strength instead (Green et al., 2018). Suggesting the possibility of a limit to this compensatory mechanism based on the severity of damage. Additionally, though damage was unilateral, changes in functional connectivity was equally affected in both hemispheres and not just on the ischemic side. Demonstrating the sensitivity of functional network change at the global level as a result of localised damage.

For the dual-regression analysis, the components of interest were selected based on previous pathology related to this model. Overall the strongest differences pre-correction was displayed from components located at the hippocampus, retrosplenial and visual cortices. Although significance did not survive multiple comparisons for these components, the locations align with what is known about pathology and deficits in the BCAS model. For example, previous BCAS research reported memory deficits in the water maze and observe atrophy within the hippocampus (Shibata et al., 2007; Boehm-Sturm et al., 2017). Furthermore, previous functional connectivity research has identified the rostro-dorsal section of the hippocampus as the most functionally connected region throughout the mouse brain (Mechling et al., 2014). Playing an important part within the limbic system, it is connected structurally to the cingulate through the Papez circuit in addition to the entorhinal regions (Shah et al., 2012). In accordance with the changes reported from the hippocampus, seeding in the cingulate revealed reduced connectivity in the hypoperfused group. These findings not only highlight memory impairment with regard to the hippocampal component, but also implicate the damage to visual processes, previously noticed with Ihara and Tomimoto (2011) with slight optic nerve rarefaction after 30-days. At a less severe microcoil size (180 μm) to the present study, immunohistochemistry staining reported damage to the optic tract, whilst the major WM regions of the corpus callosum and internal capsule were unscathed at the 6-week timepoint (Sigfridsson et al., 2018). At the same microcoil size, later timepoints in the 16-week post-surgery reported higher WM severity scores in the optic nerve and tract in comparison to shams (Hase et al., 2017).

To our knowledge this was the first time in the BCAS model functional networks were generated from ICA components and analysed with graph theoretical methods. Generally, all networks possessed a combination of high-clustering and low average path length, an arrangement frequently termed as a small-world pattern of connectivity. This is a commonly reported feature of brain networks in humans (Li et al., 2019; Wang et al., 2019) and rodents (Chen et al., 2014). Although these functional networks displayed these features, the only group difference reported from the graph theory measures at the local integration level. Coupled with a non-significant interaction for component, further investigation found this reduction was shared across the majority of components rather than a specific grouping. Furthermore, no significant differences were found after multiple comparisons for comparisons of specific nodes overall, suggesting the possibility that the connective functional topology generally at some local nodes is affected. This reduction, however, is not specific to individual nor a sub-grouping of connections as a result of chronic hypoperfusion. Functional connectivity analysis on transgenic mouse models of Alzheimer's disease have generally reported a decrease in connectivity, with the strongest reductions in the hippocampus and somatosensory regions (Shah et al., 2013). Recent research employing graph theory on functional connectomes in transgenic mouse models have reported no changes for integratory and segregatory measures (modularity, global and local efficiency) (Kesler et al., 2018). Differences were present, however, in a graph theory measure sensitive to reductions located at specific pathways critical to network efficiency. Known as the characteristic path length, this measure is calculated from the average shortest path length connecting all pairs of nodes which is then divided by the mean path of a random network of the same size (Watts and Strogatz, 1998). Higher scores are suggestive to specific disconnections of important nodes, therefore requiring less efficient connections to nodes. For future functional research of the BCAS model, characteristic path length might provide a greater specificity to subtle changes as at the visual level, connectivity seemed to change specifically for individual nodes. Furthermore, it is possible that a lack of statistical power resulting from the small condition group size (n=6) could have influenced the results. As significant voxelwise differences in the dual regression prior to correction of multiple comparisons were mostly a single voxel, this lack of clustering could have been a result of high variability and low statistical power.

4.4.3. Structural connectivity differences between sham and hypoperfused mice

The strongest differences in FA between the hypoperfusion and sham groups was at the 6-month timepoint, driven primarily through reduced FA at the posterior corpus callosum for the hypoperfusion group. Although even the strongest differences were still insignificant after multiple comparison corrections, the same BCAS procedure at earlier timepoints (5-7 weeks) in previous research similarly did not report significance differences for FA values at the voxelwise comparison level. Comparisons of visual tractography, though, did display a less dense corpus callosum in the hypoperfusion group (Boehm-Sturm et al., 2017). Additional BCAS research using a moderate microcoil size (180μm) at the same timepoint (6-month), however, reported significant FA reductions in the corpus callosum in addition to the internal capsule and fimbria (Holland et al., 2015). The same research group reported voxelwise differences in FA for the corpus callosum and internal capsule at the 1-month timepoint (Holland et al., 2011), with similar research displaying FA changes in the same regions in addition to the external capsule (Saggu et al., 2016). The inconsistent results in voxelwise comparisons of DTI scalar variables could be a result of numerus factors. The most obvious potential factor was the sample size of our condition group (n=6) compared to Holland and colleagues in (2011) (n=15) and Holland and colleagues in (2015) (n=21). Furthermore, it is possible that the non-magnetic surgical grade microcoils that we have used in this study and previously (Boehm-Sturm et al., 2017) could be a major factor in the differences evident in the literature. As the same manufactured microcoils (Sawane Spring Co, Shizuoka, Japan) used in Holland and colleagues in (2011) and Holland and colleagues in (2015) showed substantial degradation only after 1-month in comparison to the non-magnetic surgical grade microcoils (Shannon Coiled Springs Microcoil, Limerick, Ireland) used in this study and prior (Supplementory Boehm-Sturm et al., 2017). Lastly, the sham group in previous literature from other research groups (Holland et al., 2011; Holland et al., 2015; Saggu et al., 2016) did not have a non-restricting microcoil placed instead. Therefore, it is possible that the difference reported between groups could of be a result of signal interference from the coil placed in the condition group.

Visual inspections of structural connectivity matrices generated through tractography showed no clear differences between group for either timepoint, in both the full and parent AMCA parcellated matrices. Quantitative analysis of graph theory measures reported no significant differences for group, but timepoint revealed a clear change in the transivity measure of

segregation. An overall decrease in transivity was present in the later timepoint, suggesting a decrease of highly connected triples within the structural network. Visual changes were also present in the other graph theory measure of segregation. Although statistically insignificant, a small increase in modularity was present in the later timepoint. These changes throughout timepoint for segregation align with previous studies on mouse specific ageing and graph theory measures of structural connectivity. Investigations on mouse structural connectomes recorded a logarithmic increase in modularity throughout ageing, this increase, whilst sharp after the early postnatal age of 15 days, levelled off in the later adult age recorded between days 20-80 of age (Ingalhalikar et al., 2015). Since the mice were already past this age in the earliest timepoint, this explains the slight insignificant increase in modularity at the 6-month timepoint. Although Ingalhalikar and colleagues (2015) did not measure transivity, whereas modularity as able to measure larger sub-groups, it is possible this developmental neuronal plasticity and pruning as a reorganisational response to environmental stimulation and behaviour could be continuing at the smaller scale between triplet connections. Overall, the only significant graph theory difference related to group was a measure associated with integration and connectivity at the local level. After further investigation, this interactional significance between group, region and timepoint that remained significant after multiple comparisons was the visual association region at 6-months. A significant increase in local efficiency was interestingly present in the hypoperfused group, suggesting an increase in connectivity is present in the visual association area during the 6-month timepoint in the hypoperfused mice compared shams. Furthermore, this difference in the visual association region aligns with the functional results, implicating that this structural change could be potential compensatory mechanism from the resulting functional damage to the somatosensory and visual cortex in the component analysis. Previous similar increases in local efficiency have been reported for BCAS mice at earlier timepoints, however the subsequent changes to localised nodes were not reported (Boehm-Sturm et al., 2017). Although the resulting functional dual regression analysis similarly showed the strongest non-significant differences in the visual component. This output from the dual regression combined with the structural network analysis does support the visual regions being somewhat sensitive to chronic hypoperfusion.

Previous findings from our research group have indicated group differences in graph theory values at earlier timepoints (5-7 weeks) using the same BCAS model (Boehm-Sturm et al., 2017). More specifically, these group differences were present for local efficiency, transivity

and modularity, with hypoperfusion influencing increases for transivity and local efficiency, whilst decreasing modularity. With regards to structural network connectivity, it is possible that earlier BCAS timepoints, as a result from the sharp CBF reduction initially, show substantial network change that is less diverse at the 3 and 6-month timepoints. Whereby at the chronic 6-month timepoint, this damage is specific to visual regions. Other possibilities for these differences at the earlier timepoints (Boehm-Sturm et al., 2017) to chronic timepoints could be due to the differing methodologies in generating structural connectomes to processing graph theory measures. Boehm-Sturm and colleagues (2017) used a deterministic tractography method that focused on the most prominent streamlines, whilst the probabilistic technique used here also models error in addition to displaying greater tract sensitivity for clinical investigations of Parkinson disease (Petersen et al., 2017; Muller et al., 2018). Another possible explanation for this variability could be due to the lack of thresholding used in previous research (Boehm-Sturm et al., 2017), therefore the influence of weak and spurious connections might have leverage for the differences between groups.

4.4.4. Conclusions

The ability to investigate major WM tracts and functional connective hubs in addition assessing subsequent structural and function network change has been valuable in further understanding the link specific pathology plays in diseases like VCI. In conclusion, these results suggest that specifically at the 3-month BCAS timepoint, no group differences were present for direct regional voxelwise comparisons and structural network topology generated through dMRI. The 6-month timepoint replicated these results at the 3-month except an increase in local connectivity was evident in the visual association area as a result of hypoperfusion. Additionally, no group differences were present for data-driven functional hubs of activity, however weaker local functional connection strengths were present in the hypoperfusion at the 6-month timepoint. Although statistically these changes did not report a specific set of component nodes, a visually noticeable correlational difference was present in the sensorimotor and visual network between groups. Furthermore, the current findings are in concordance to previous research comparing structural (tract-tracing) and functional (rs-fMRI) connectivity (Stafford et al., 2014), displaying a strong correspondence in network topology of small-wordless and graph theory between structural and functional connectomes. From the resulting CBF reduction from the BCAS model, hypoperfusion affected differences

visually and statistically in regions associated with visual processing. Overall, the sensitivity of assessing functional and structural connectivity in unison offers a window into further identifying potential biomarker profiles of disease and has recently been employed in similar preclinical mouse models (Hubner et al., 2017). From these findings, it is suggestive to investigate the behavior and connectivity in visual/sensory areas in addition to hippocampal regions from resulting chronic hypoperfusion.

Chapter 5. Structural and functional network changes in an ovine model of cerebrovascular disease.

5.1. Introduction

Thus far the preclinical pipeline developed to investigate structural and functional connectivity has been able to identify changes in specific circuitry as a result of hypoperfusion. A necessary part of this process was adapting many of the tools originally designed for clinical data. Whilst this pipeline is easily applicable to other rodent models, the ideal scenario of this project is to have the ability to use this pipeline along the entire translational spectrum.

Sheep models are an intermediate large animal that share more anatomical similarities to humans compared to the commonly used preclinical rodent models. The translational advantages of the ovine brain not only include closer similarities in size compared to that of the rodent, but also anatomy; for example, ovine and human brains are both gyrencephalic whilst the rodent is lissencephalic. Furthermore, the ovine brain has a more substantive WM to grey matter ratio compared to that of the rodent. For example, the average WM ratio in mice is approximately 10%, whilst in the ovine brain this percentage is 30%, far closer to the 40-45% evident in humans (Boltze et al., 2017). As a consequence of this greater translational potential, certain research groups have begun to use sheep to model cerebrovascular disease, in particular stroke (Wells et al., 2012). Analysing functional and structural MRI indicators in the sheep could provide greater insight into brain processes in combination with advantages of pathological investigation *ex vivo*. Recent advances have also been made in ovine neuroimaging, particularly with high resolution reconstruction of WM tracts using dMRI (Pieri et al., 2019) in addition to task-based fMRI (Lee et al., 2015). Furthermore, there have been three different ovine MRI atlases developed, providing the potential to construct connectomes (Ella and Keller, 2015; Nitzsche et al., 2015; Liyanage et al., 2016).

For these reasons, testing our pipeline in an ovine model of cerebrovascular disease would represent a significant contribution to the field. Via collaboration, we have access to dMRI and rs-fMRI data collected from an ovine model of middle cerebral artery occlusion (MCAO). Overall, the aim is to adapt the pipeline for use in this intermediate model.

5.2. Methods

5.2.1. Experimental design

Female Murano sheep (n=21), aged 18-24 months, underwent transient right MCAO with reperfusion (Wells et al., 2012). Briefly, sheep were anaesthetised with ketamine and diazepam (100 and 5mg/mL) and maintained with ketamine (4mg/kg/hr) and isoflurane. The MCA was accessed via craniectomy on the edge of the temporal bone, and occluded with a Sugita temporary mini straight aneurysm clip (Mizuho Medical Inc, Japan) for 2-hours until reperfusion. The exposed area was irrigated using saline, preventing the potential drying of the cerebral cortex. The craniectomy was sealed with dental acrylic cement, the wound sealed and animals allowed to recover. Animals were humanely euthanised at approximately 30 days post-surgery.

5.2.2. MRI hardware and acquistion

Scanning was performed on a 3T system (Siemens, Germany) prior to surgery and at 6- and 28-Day post-surgery.

T_1 weighted imaging was performed using a magnetization prepared rapid acquisition gradient echo (MP-RAGE) sequence (TR/TE: 2300/2.58ms: 88 consecutive slices, slice thickness: 900µm, FOV: 166 x 178mm, resolution: 625µm^2, acquisition time: 33.26 seconds). T_2 weighted imaging was performed using a sampling perfection with application-optimized contrasts using different flip angle evolution (SPACE) sequence (TR/TE: 3200/410ms: 96 consecutive slices, slice thickness: 900µm, FOV: 201 x 239mm, resolution 390.6µm^2, acquisition time: 39.94 seconds).

The dMRI scan was an isotropic EPI DTI sequence, comprising 11 b0 images and 524 gradient directions (TR/TE: 3200/101ms, 2 b values (0 and 1000 s/mm^2), FOV: 250 x 155 x 219mm, resolution: 2500mm^3, acquisition time: 1h 16min). The rs-fMRI was a T_2* weighted EPI sequence (TR/TE: 1590 /31ms, 120 repetitions, FOV: 240mm^2, 36 slices, slice thickness: 2.5mm, resolution: 2.04mm^2, acquisition time: 7min).

5.2.3. Processing of MRI data

All data was processed as described in Chapter 2, with the following exceptions.

5.2.3.1. Data pre-processing

5.2.3.1.1. Structural template creation

All subject pre-stroke T_1-weighted structural scans (n=21) were used to generate a study specific T_1 average template. Once created, the study specific template was registered to the T_1-weighted template of the corresponding ovine stereotaxic atlas (Ella et al., 2017). The atlas and associated tissue maps were then transformed into the study template space for analysis.

5.2.3.2. rs-fMRI

5.2.3.2.1. Independent component analysis

The pre-stroke datasets of all subjects (n=21) were used to generate healthy resting state components with the automatic dimensionality option. The automated approach determined 32 resting state components best fit the data.

5.2.3.2.2. Dual regression

Only components that were comprised of primarily neurally driven signal were inputted into the dual regression analysis. In order to derive the directionality of any differences in addition to the significance, the GLM was comprised of 3 separate paired t-tests (Pre vs 6-Day, Pre vs 28-Day, and 6-Day vs 28-Day). Subsequent corrections for multiple comparisons (number of components chosen and number of paired t-tests ran) were performed using Bonferroni.

5.2.3.2.3. Hierarchical network analysis

The correlational strength of each signal component timeseries was compared to every other signal component for each of the 3 timepoints (pre, 6- and 28-Day post stroke) and converted into edges on full correlation z-score matrices. Differences for each individual correlational edge were compared using permutation testing and corrections for multiple comparisons were

adjusted using a family wise error rate (FWE). A Bonferroni correction was applied for the results of each paired t-test.

5.2.3.3. dMRI

5.2.3.3.1 Tract based spatial statistics

Individual WM skeletons were generated for each timepoint. All skeletons showed high similarity (Figure 5.1). The same GLM employed for rs-fMRI was used for TBSS.

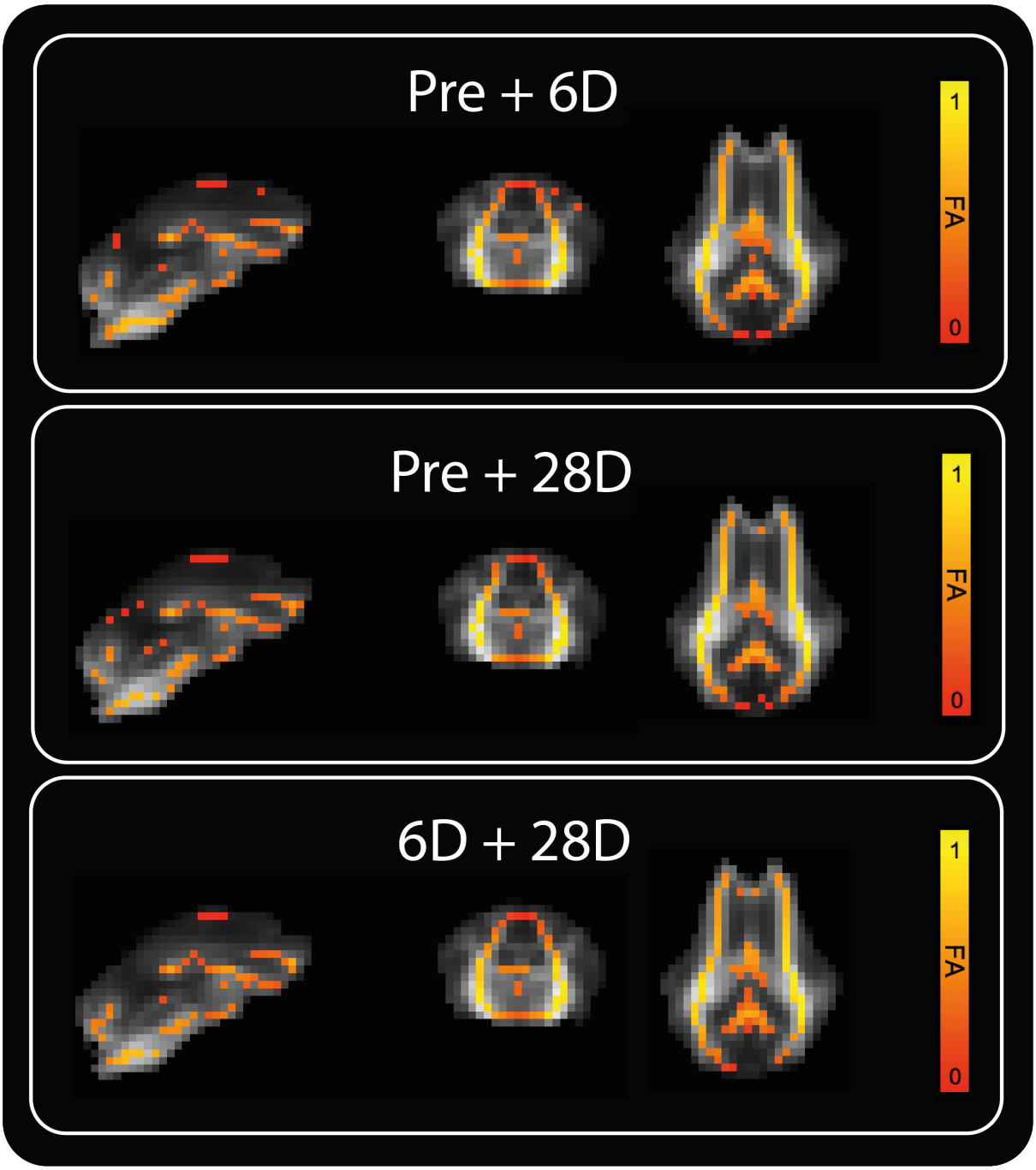


Figure 5. 1. WM skeletons for TBSS analysis. Each box displays regions of average highest FA for the combined groups for each GLM contrast. Note: the scale bar depicts the FA value.

5.2.3.3.2. Deterministic tractography

DSI studio (http://dsi-studio.labsolver.org/) was used to generate deterministic WM tracts for qualitative analysis. This was done prior to registration to help identify WM and qualitative differences (e.g., potential edema) between the different timepoints. Deterministic tracts were generated using FA values, with a minimum threshold of 0.3, an angular threshold of 60 degrees, a step size of 1.25mm, and tract lengths below 10mm and above 300mm were discarded. The tracking algorithm employed the Runge-Kutta fourth order method (RK4), with 1 000 000 randomly placed seeds throughout the brain.

5.2.3.3.3. Probabilistic tractography

The ovine stereotaxic atlas (Ella et al., 2017) was further modified to use unilateral labels (n= 94) rather than the original bilateral cortical and sub-cortical labels (n= 47). This atlas was used to generate the connectivity matrices.

5.2.4. Statistical analysis

Graph theory data was analysed using SPSS (version 26). A Kolmogorov-Smirnov test was run to assess normality. To remain consistent with the design of the GLM, a series of paired t-tests were conducted between the different time points. However, for local efficiency, mixed design repeated measures ANOVAs was used to be able to examine the interactions at the level of individual components. FDR corrections were performed to correct for multiple comparisons.

5.3. Results

5.3.1. rs-fMRI

5.3.1.1. EPI unwarping process

During the EPI unwarping stage, slight alignment issues were noticeable between the functional EPI and structural T_1 weighted images during BBR registration. Investigating this further, we compared the quality of resting state components from data undergoing the EPI unwarping stage, against data skipping the process entirely. In addition to differences in component dimensionality automatically selected in the ICA for unwarped (n= 34) against non-unwarped (n= 32) data, distinctions were also present in the spatial map intensity, variance explained and spectra amplitude of components (Figure 5.2). Overall components generated from skipping the unwarping stage (no unwarp), output a combination of increased intensity of component spatial maps, higher variance explained, and stronger amplitude of the low frequency peak compared to components undergoing EPI unwarping.

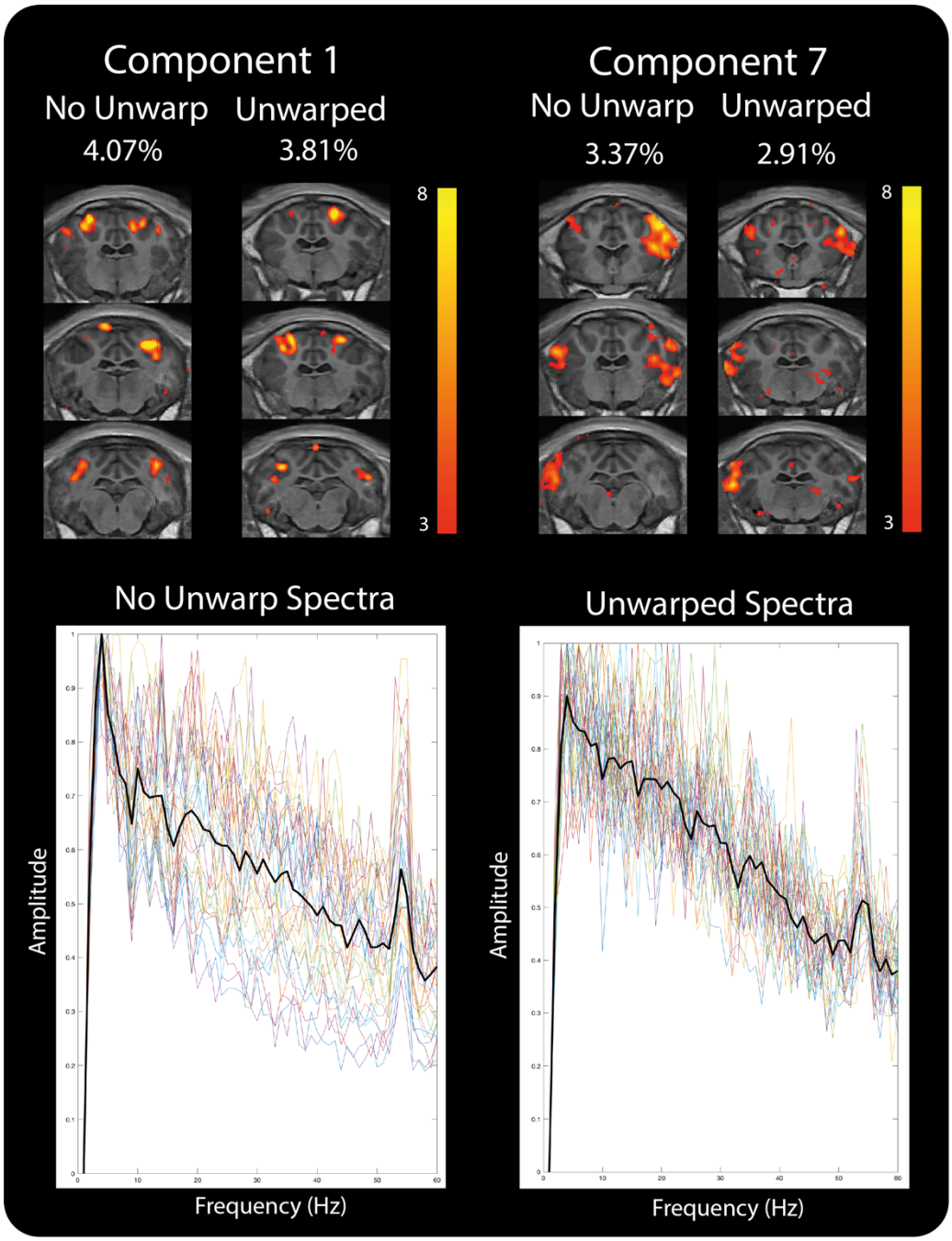


Figure 5. 2. Comparisons between pre-stroke components generated from unwarped data (using epi_reg) or non unwarped data (skipping the process). (Top) Spatial map comparisons of signal ICA components generated with data either undergoing EPI unwarping (unwarped) or skipping the process entirely (no unwarp). Equivalent components from the unwarped dataset were selected against the signal components identified from the no unwarp data. Percentages refer to the percentage of explained variance, output in the MELODIC report for each component. (Bottom) Continuation of the component differences in the spectra output for all components generated in each respective ICA between unwarped and non-unwarped data (black line represents average of all components). Distinctions were evident in the amplitude and shape of the iconic low frequency peak (Hz) of output components.

5.3.1.2. Independent component analysis

The majority of the components identified were not in the brain. A total of 4 components were comprised of neurally driven BOLD signal and located in grey matter areas. Three additional components were a combination of BOLD signal and noise from non-brain regions.

All signal components spanned multiple brain regions across both hemispheres with many similarities among many components (Figures 5.3 - 5.4 and Appendix B). The strongest component (Component 1) predicted 4.07% of the variance and was prominent in the suprasylvius gyrus (SS), which is involved in sensation, as well as the sylvian gyrus (SG) (primary somatosensory region). It also included the ecto- and endolateralis gyri, which correspond to the visual cortex (Appendix B.1). Component 7 predicted 3.37% of the variance and involved the primary somatosensory cortices (SG), the temporal lobe and insular cortices (Appendix B.2). Component 11 predicted 3.12% of the variance and included the majority of the cingulate (C) gyrus as well as the motor regions (pre- and post-cruciate gyri) and the primary somatosensory region (SG). This component may represent the ovine DMN (Figure 5.3 and Appendix B.3).

Of the components that included a mixture of BOLD signal and noise from non-brain areas, Component 13 explained 3.08% of the variance and included the hypothalamus and some adjacent non-brain voxels, as well as the posterior sylvian gyrus and anterior C. Component 20 predicted 2.97% of the variance and included the olfactory bulb and some adjacent non-brain voxels, as well as the anterior C, and the posterior sigmoideus gyrus. Component 22 predicted 2.93% of the variance and included the parahippocampal cortex and some adjacent non-brain voxels, as well as the hippocampus and orbitofrontal gyrus. Component 24 was the most contaminated. It predicted 2.92% of variance and included the right parahippocampal cortex, left orbitofrontal gyrus and somatosensory cortices such as the posterior sygmoideus and SG. These components may represent limbic sub-networks (Figure 5.4, Appendix B.4, B.5, B.6, B.7).

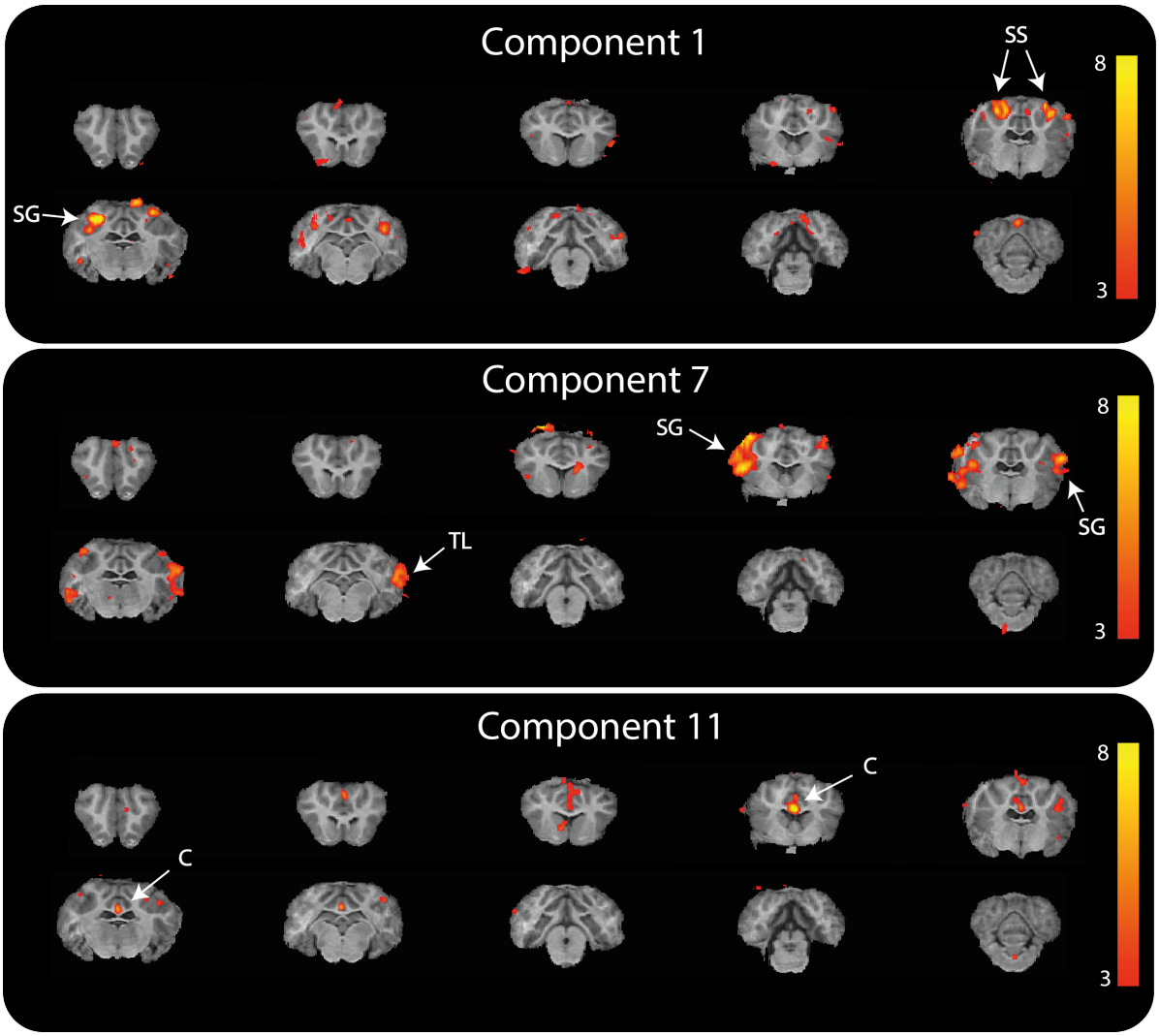


Figure 5. 3. Individual component spatial maps. Components 1 and 7 include sensory and visual and sensory and memory regions, respectively and Component 11 may represent the ovine DMN. Note: Components are overlaid onto the T_1 weighted template from the sheep stereotaxic atlas (Ella et al., 2017) and scale bars correspond to the z-score. Abbreviations: suprasylvius gyrus (SS), sylvian gyrus (SG), temporal lobe (TL), cingulate gyrus (C).

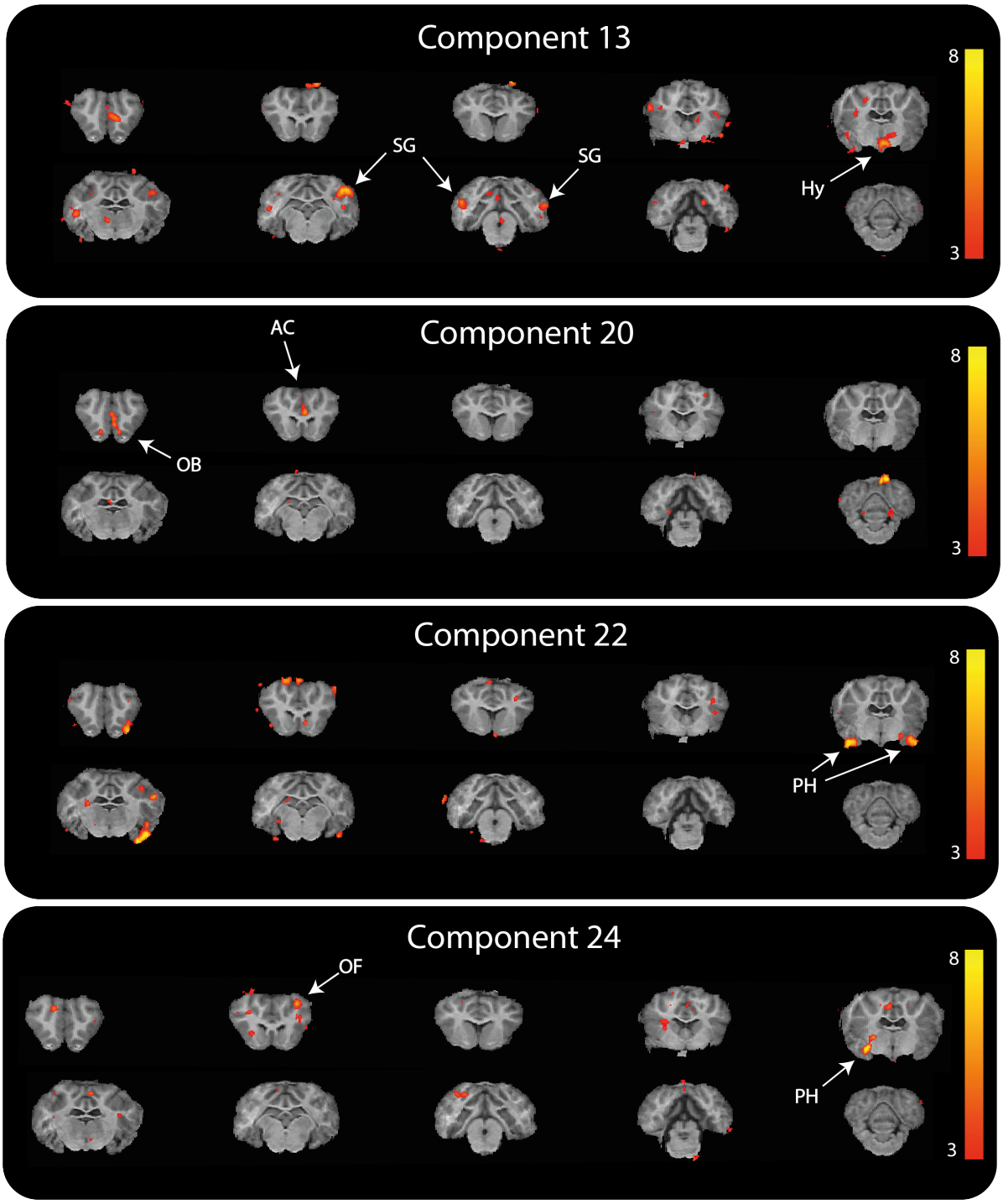


Figure 5. 4. Individual component spatial maps. Components 13, 20, 22, and 24 include several limbic regions. Note: Components are overlaid onto the T_1 weighted template images from the sheep stereotaxic atlas (Ella et al., 2017) and scale bars correspond to the z-score. Abbreviations: sylvian gyrus (SG), hypothalamus (Hy), orbitofrontal (OB), anterior cingulate (AC), parahippocampal (PH), olfactory bulb (OF).

Hierarchical clustering of all signal components prior to stroke revealed that all component time series were highly correlated (Figure 5.5). Two separate clusters were present: one cluster contained Components 1, 11, 20, and 22, and was primarily driven by the SS, C, olfactory bulb, C and parahippocampal gyri (blue cluster, Figure 5.5). The second cluster (red cluster, Figure 5.5) contained Components 7, 13, and 24 and was primarily driven by the bilateral SG, hypothalamus, and right parahippocampal gyrus.

5.3.1.3. Qualitative network comparisons between timepoints

Initial comparisons between the pre-stroke and post-stroke timepoints revealed a widespread correlational increase among component timeseries at both post-stroke timepoints compared to the pre-stroke timepoint (displayed in Figure 5.6 and 5.7). This was similar across both clusters.

More subtle changes were present between the post stroke timepoints. Increased correlational strengths were evident in the majority of edges connected to the right hypothalamus (rHy) at the 6-day compared to 28-Day post stroke. In contrast, increased correlations were present between the majority of the components and the suprasylvius gyrus (SS) at the 28-Day timepoint.

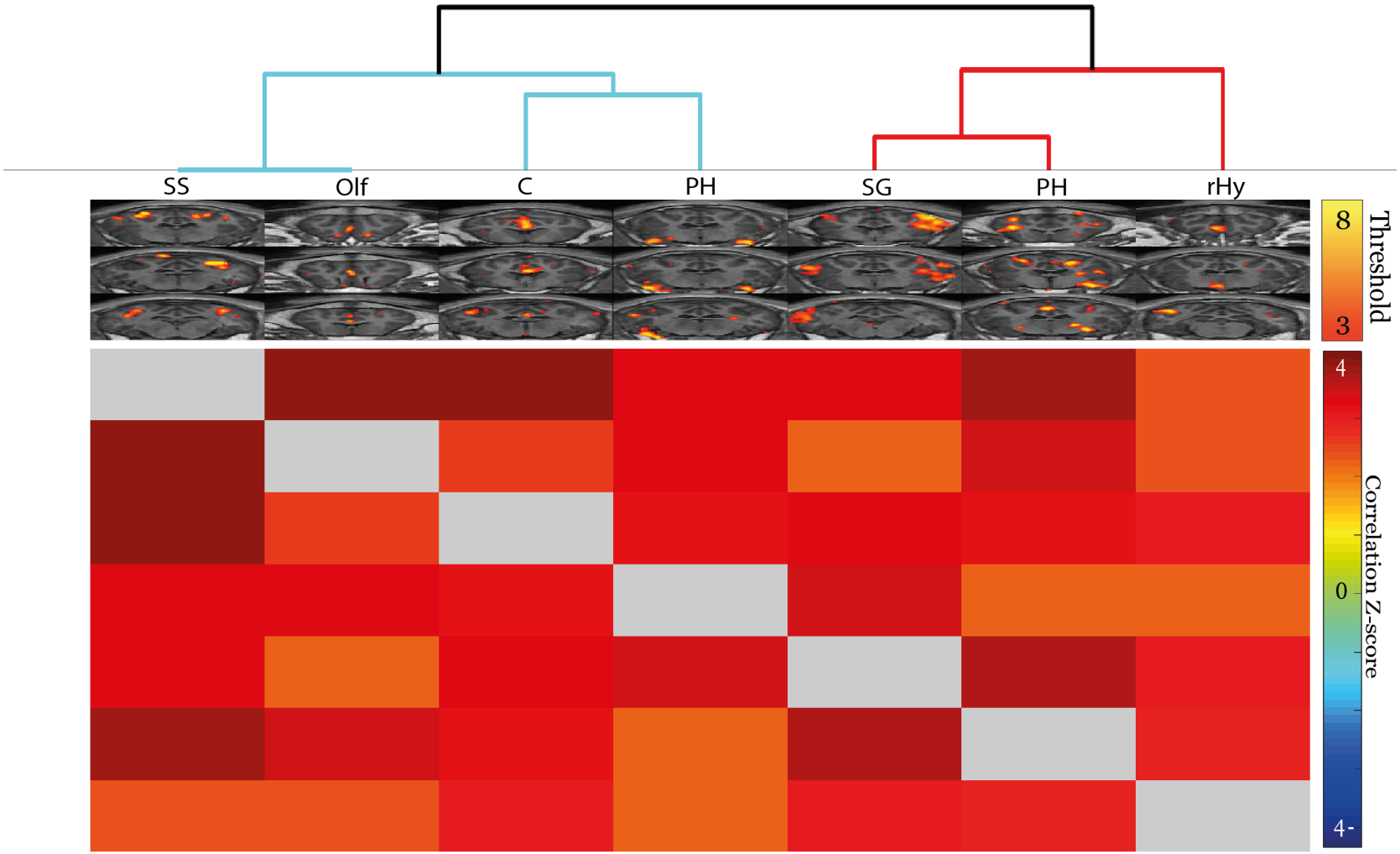


Figure 5. 5. Hierarchy matrix, clustering highly correlated components for the pre-stroke timepoint. Each neurally driven component (n=7) is overlaid onto 3 T_1 weighted images organized into columns (anterior to posterior) from (Ella et al., 2017). The clusters are color coded (blue and red). The matrix displays the correlations between all components. Abbreviations: suprasylvius gyrus (SS), olfactory bulb (Olf), cingulate gyrus (C), parahippocampal gyrus (PH), sylvian gyrus (SG), right hypothalamus (rHy). Note: scale bars refer to the z score threshold and the strength of the z correlation.

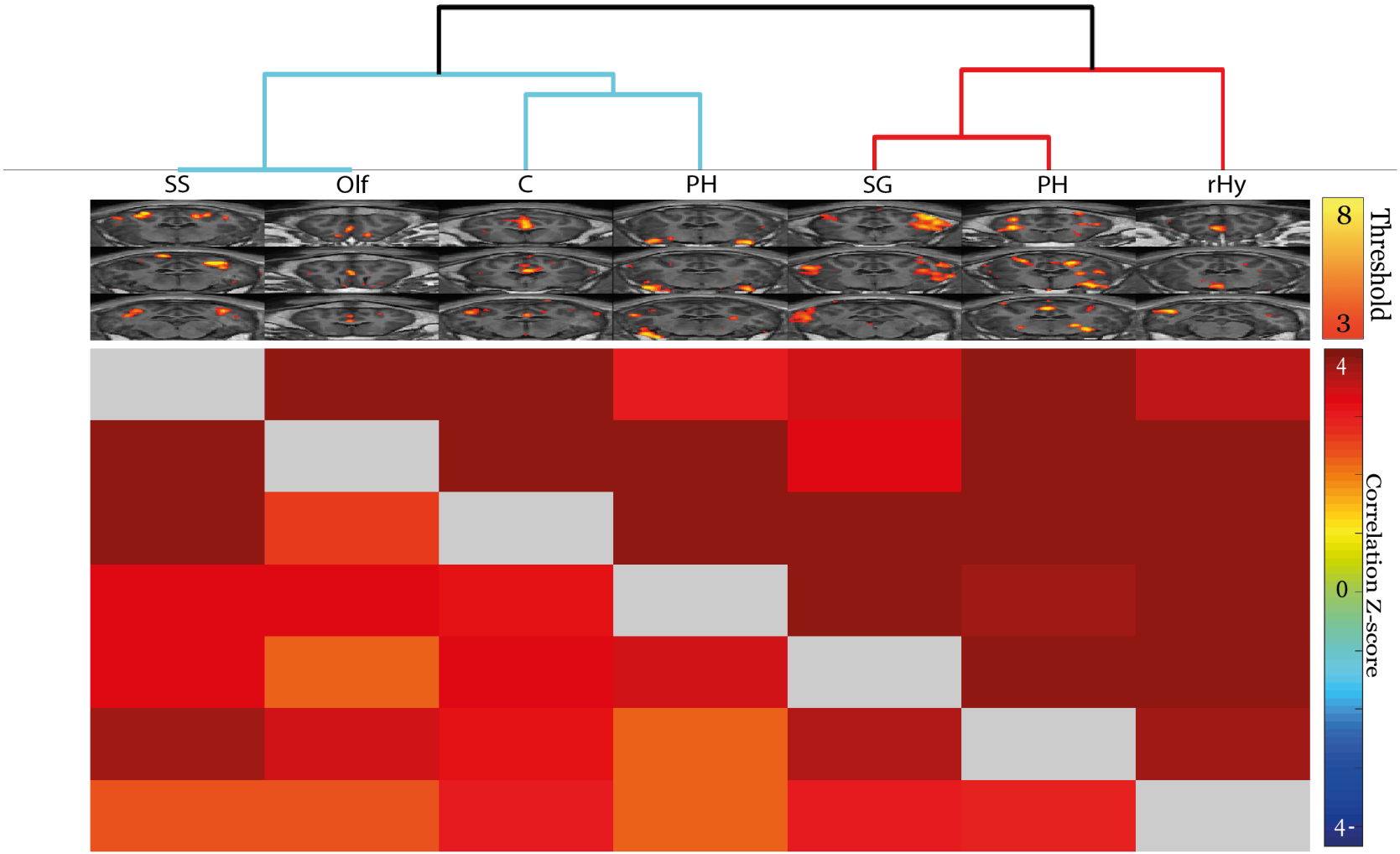


Figure 5. 6. Hierarchy matrix, clustering highly correlated components comparing the pre-stroke and 6-Day post-stroke timepoints. Each neurally driven component (n=7) is overlaid onto 3 T_1 weighted images organized into columns (anterior to posterior) from (Ella et al., 2017). The clusters are color coded (blue and red). The matrix displays the correlations between all components, and the pre-stroke timepoint is displayed in the lower diagonal, whereas the 6-Day post-stroke timepoint is shown in the upper diagonal. Abbreviations: suprasylvius gyrus (SS), olfactory bulb (Olf), cingulate gyrus (C), parahippocampal gyrus (PH), sylvian gyrus (SG), right hypothalamus (rHy). Note: scale bars refer to the z score threshold and the strength of the z correlation.

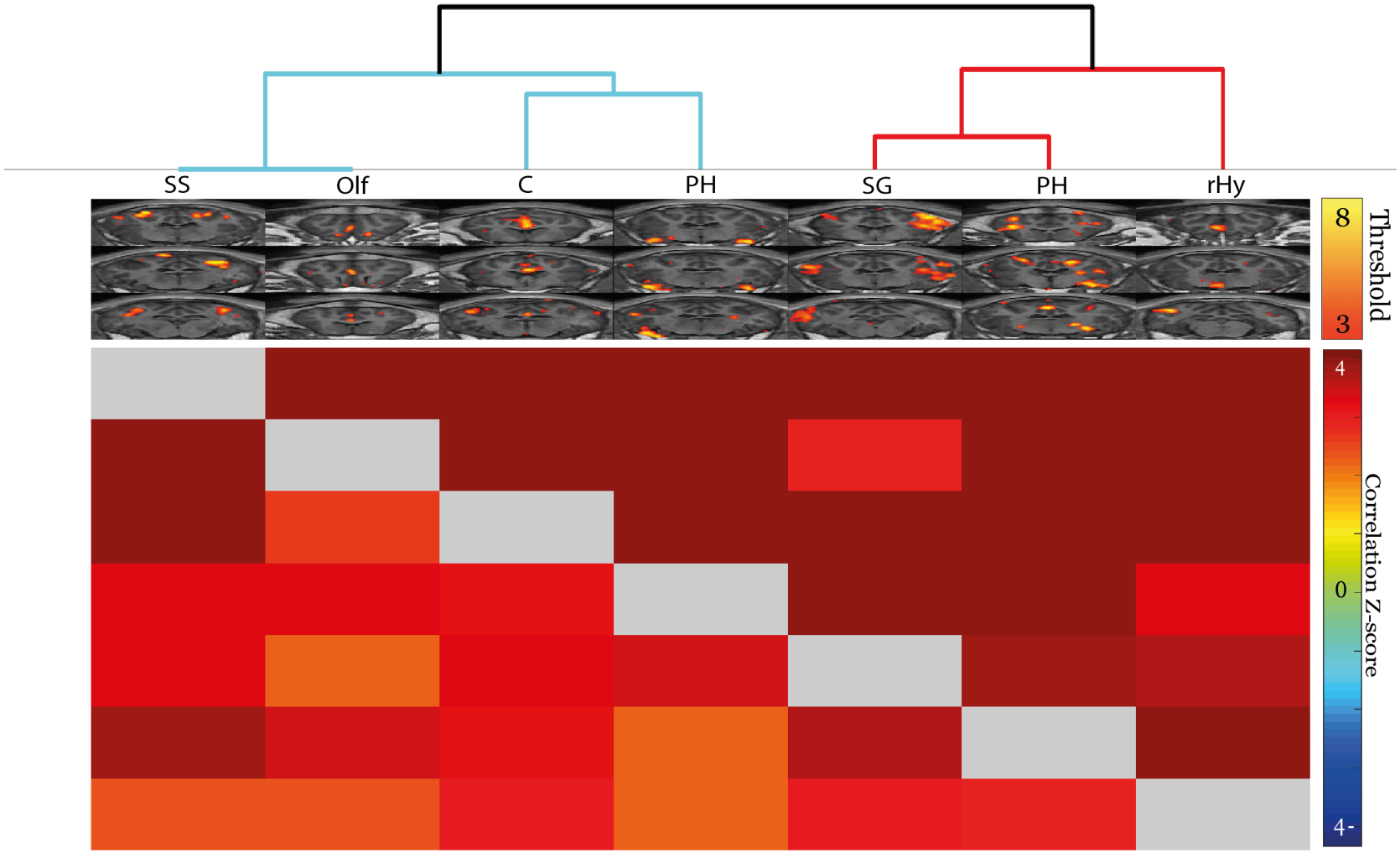


Figure 5. 7. Hierarchy matrix, clustering highly correlated components comparing the pre-stroke and 28-Day post-stroke timepoints. Each neurally driven component (n=7) is overlaid onto 3 T_1 weighted images organized into columns (anterior to posterior) from (Ella et al., 2017). The clusters are color coded (blue and red). The matrix displays the correlations between all components, and the pre-stroke timepoint is displayed in the lower diagonal, whereas the 28-Day post-stroke timepoint is shown in the upper diagonal. Abbreviations: suprasylvius gyrus (SS), olfactory bulb (Olf), cingulate gyrus (C), parahippocampal gyrus (PH), sylvian gyrus (SG), right hypothalamus (rHy). Note: scale bars refer to the z score threshold and the strength of the z correlation.

5.3.1.4. Edge differences between functional matrices

Comparison of the correlational edges revealed significant differences between the pre-stroke and 6-Day post-stroke timepoints. There was a total of 4 significant correlational edges and all significant interactions involved component 22, a RSN primarily driven by bilateral parahippocampal activity. Furthermore, the directional difference in correlation values followed a similar pattern to the hierarchy matrices with a stronger correlational value at the 6-Day post-stroke compared to pre-stroke timepoint. The significant correlations between components were as follows; Component 22 (parahippocampal) and 11 (C) p= 0.029 (Figure 5.8), Component 22 (parahippocampal) and 13 (hypothalamus) p= 0.029 (Figure 5.9), Component 22 (parahippocampal) and 20 (olfactory bulb) p= 0.0048 (Figure 5.10), and Component 22 (parahippocampal) and 24 (primarily right hippocampal cortex) p= 0.039 (Figure 5.11).

Only the correlational edge between Component 20 (olfactory bulb) and 11 (C) was significantly increased between the pre-stroke and 28-Day post-stroke timepoints p= 0.006 (Figure 5.12).

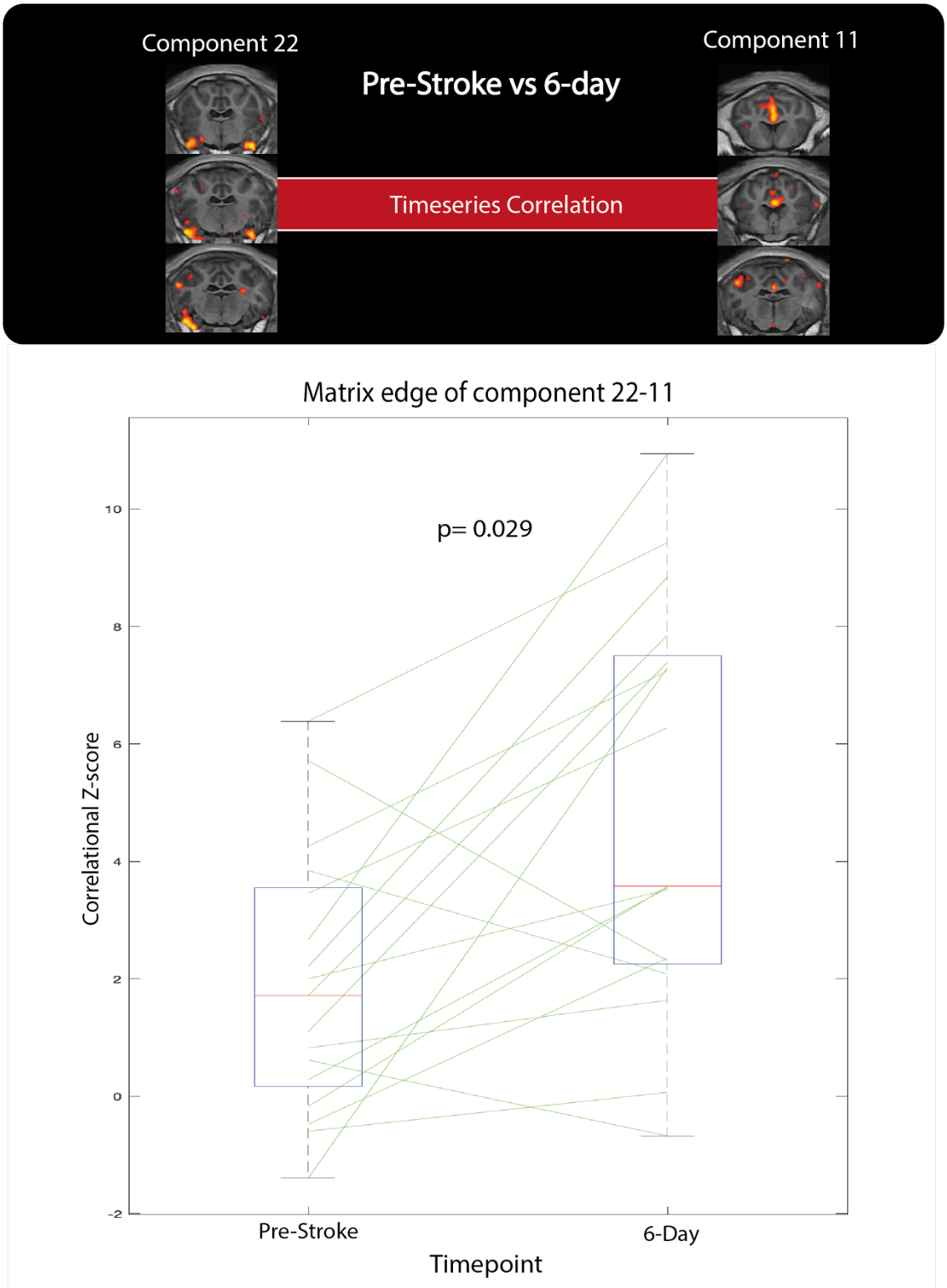


Figure 5. 8. Comparison of significantly different correlational edges prior to and at 6-Day post stroke. Boxplot (median, red) representing the 25th to 75th percentiles (bottom to top) of differences in correlational strength between component 22 (parahippocampal) and 11 (C) prior to surgery and at 6-Day post-stroke. Whiskers represent the highest and lowest data point and + represents outliers. Each green line represents an individual subject.

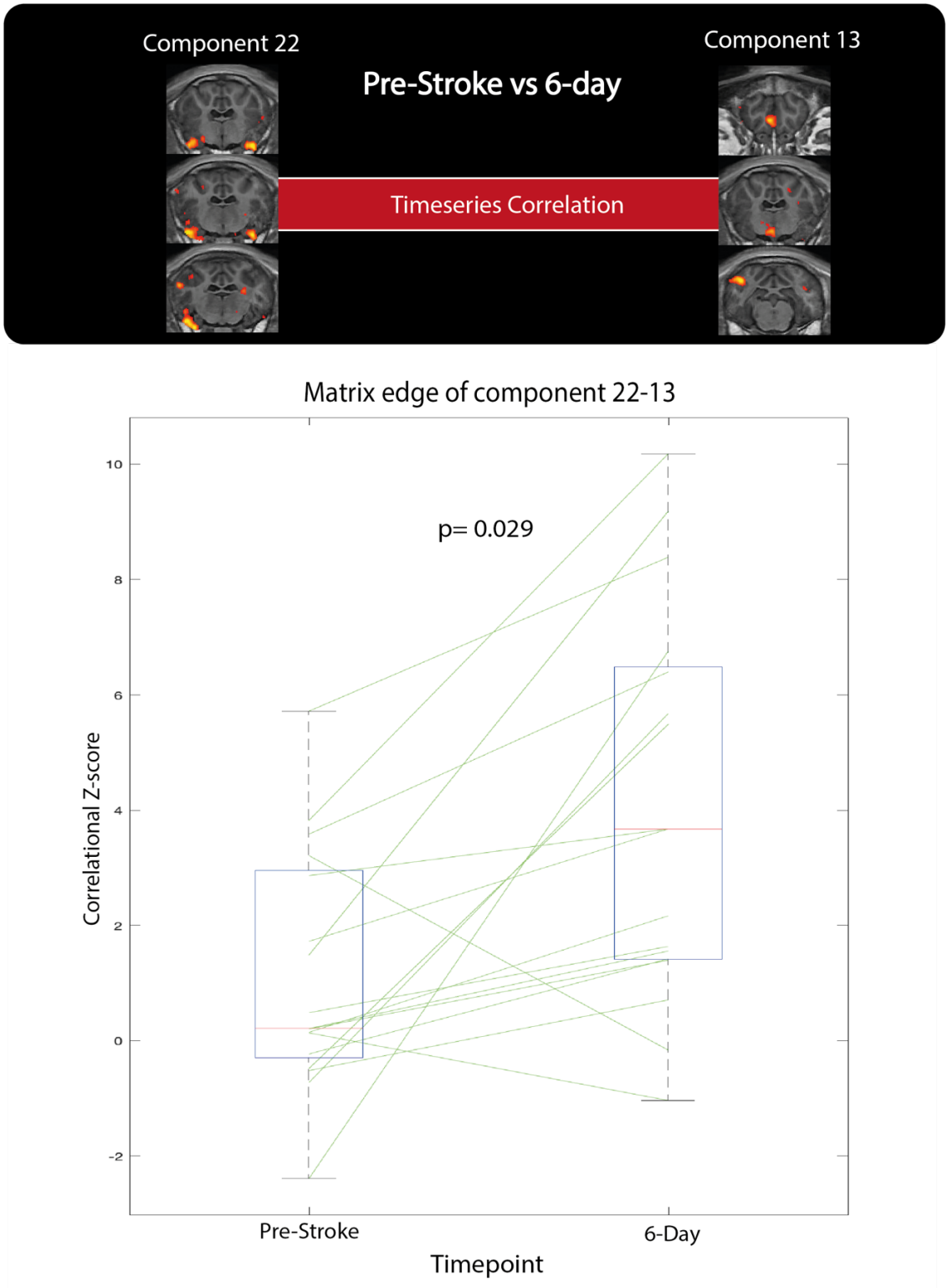
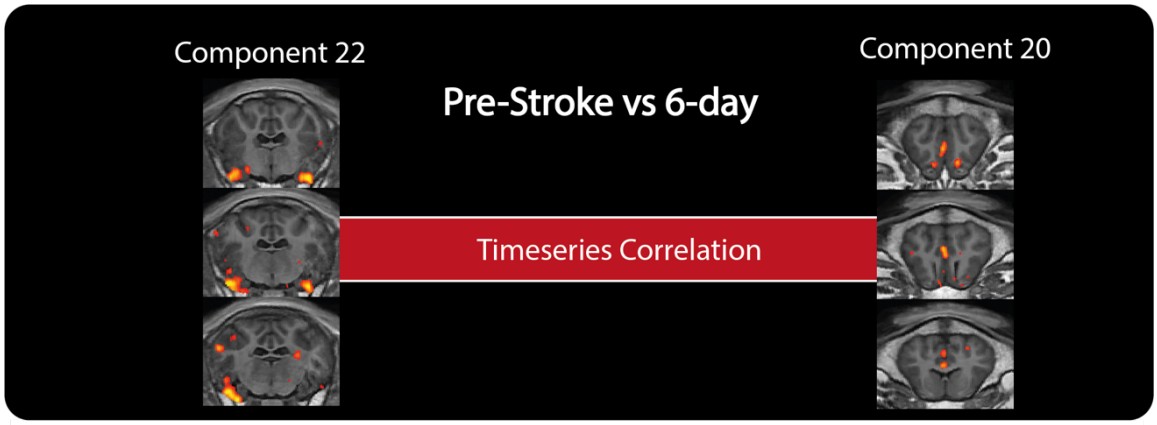


Figure 5. 9. Comparison of significantly different correlational edges prior to and at 6-Day post stroke. Boxplot (median, red) representing the 25th to 75th percentiles (bottom to top) of differences in correlational strength between component 22 (parahippocampal cortex) and 13 (hypothalamus) prior to surgery and at 28-Days. Whiskers represent the highest and lowest data point and + represents outliers. Each green line represents an individual subject.



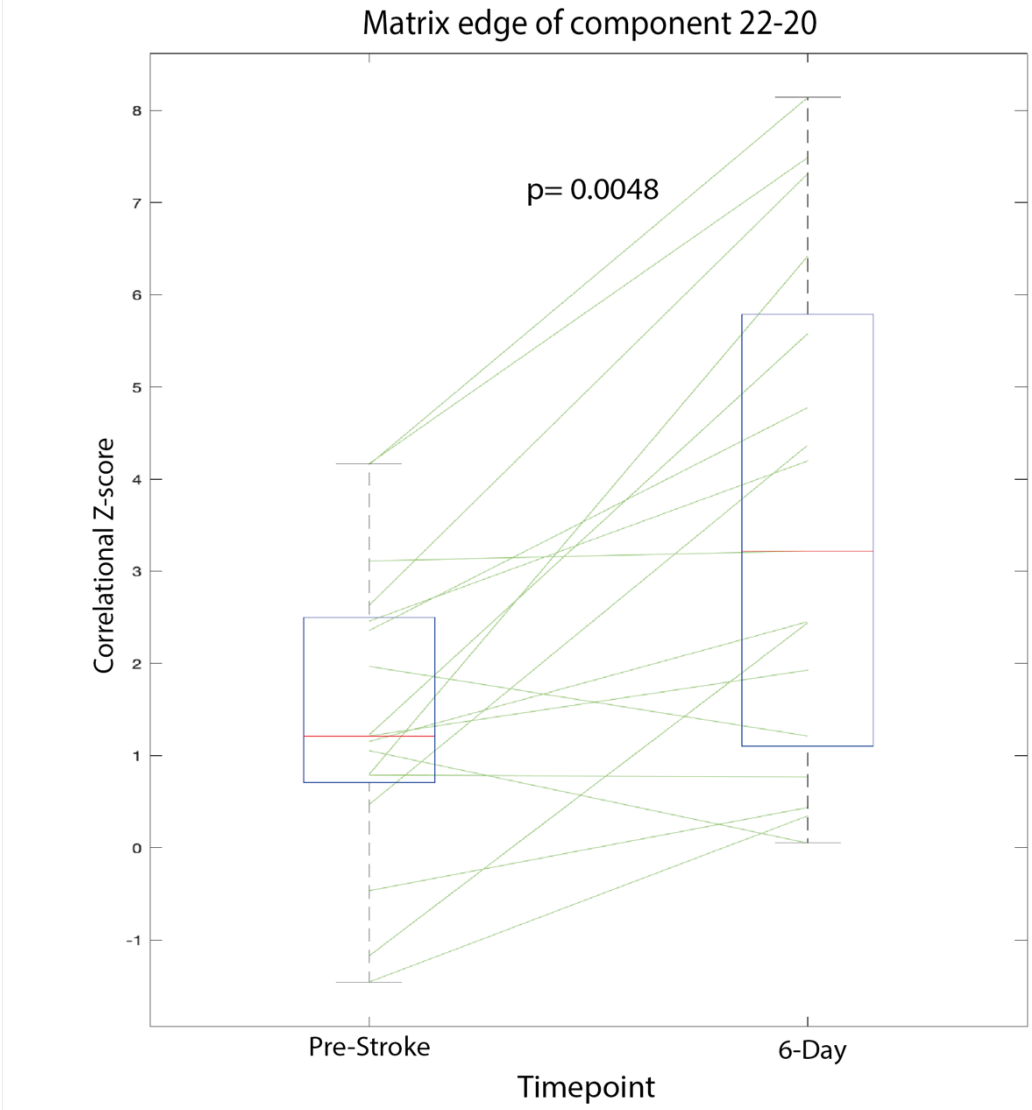


Figure 5. 10. Comparison of significantly different correlational edges prior to and at 6-Day post stroke. Boxplot (median, red) representing the 25th to 75th percentiles (bottom to top) of differences in correlational strength between component 22 (parahippocampal cortex) and 20 (primarily olfactory bulb) prior to surgery and at 28-Days. Whiskers represent the highest and lowest data point and + represents outliers. Each green line represents an individual subject.

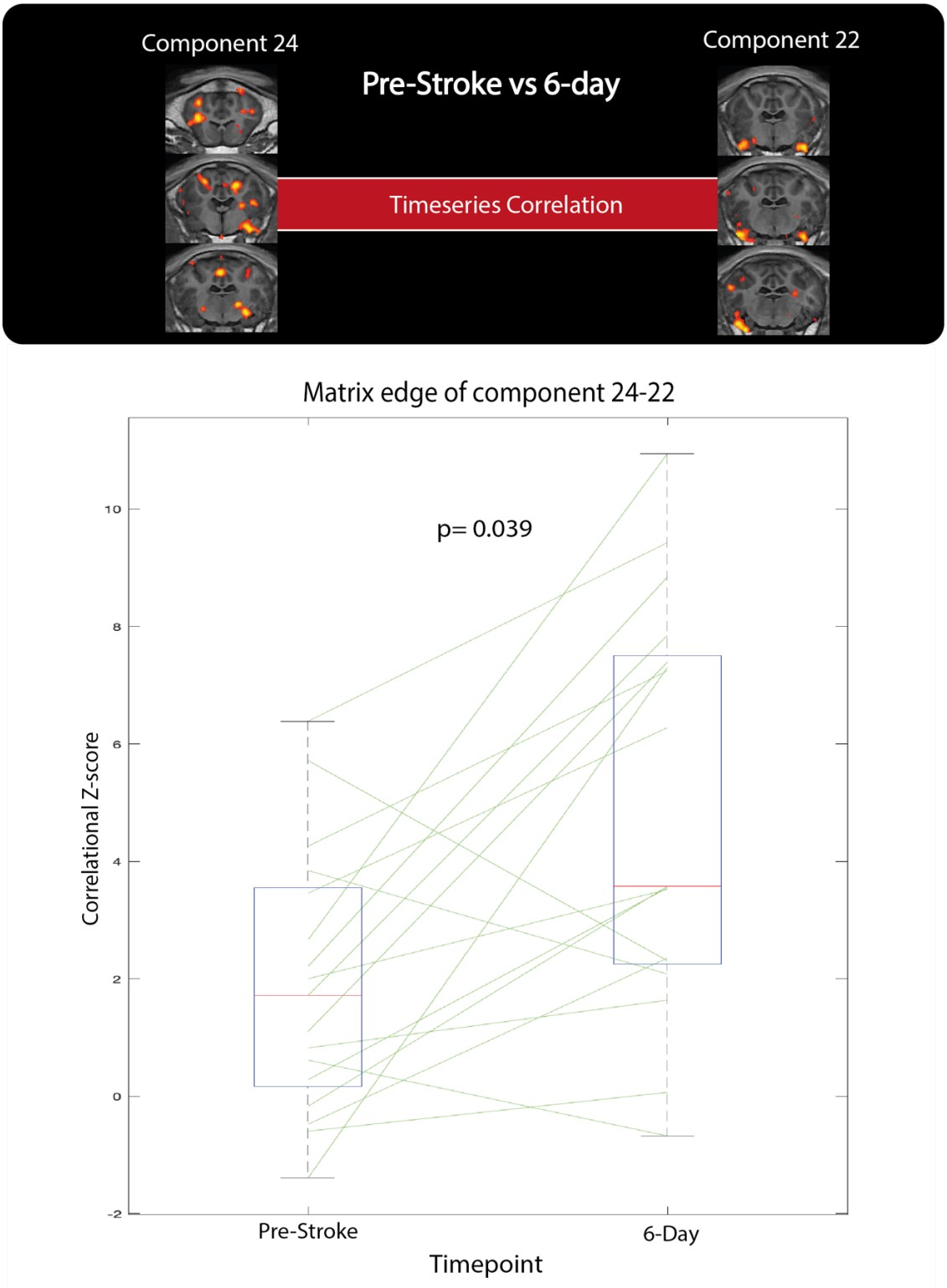
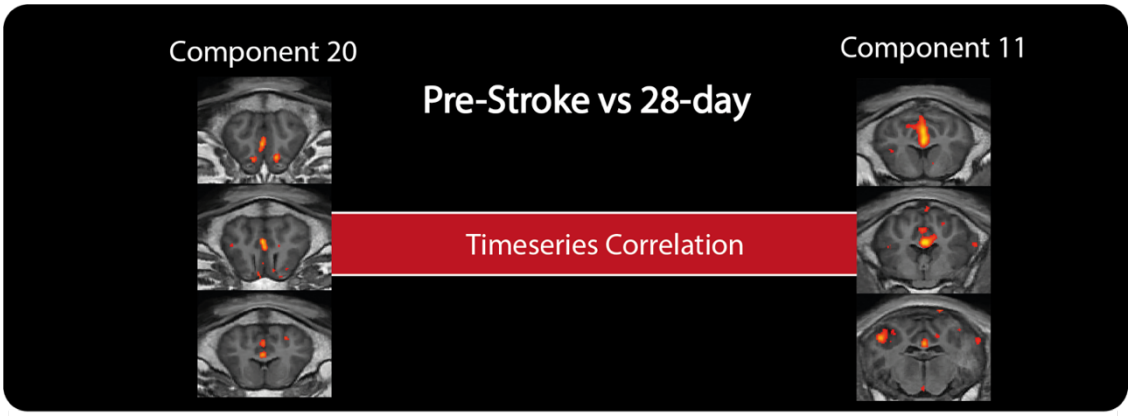


Figure 5. 11. Comparison of significantly different correlational edges prior to and at 6-Day post stroke. Boxplot (median, red) representing the 25th to 75th percentiles (bottom to top) of differences in correlational strength between component 24 (primarily right parahippocampal cortex) and 22 (parahippocampal cortex) prior to surgery and at 6-Days. Whiskers represent the highest and lowest data point and + represents outliers. Each green line represents an individual subject.



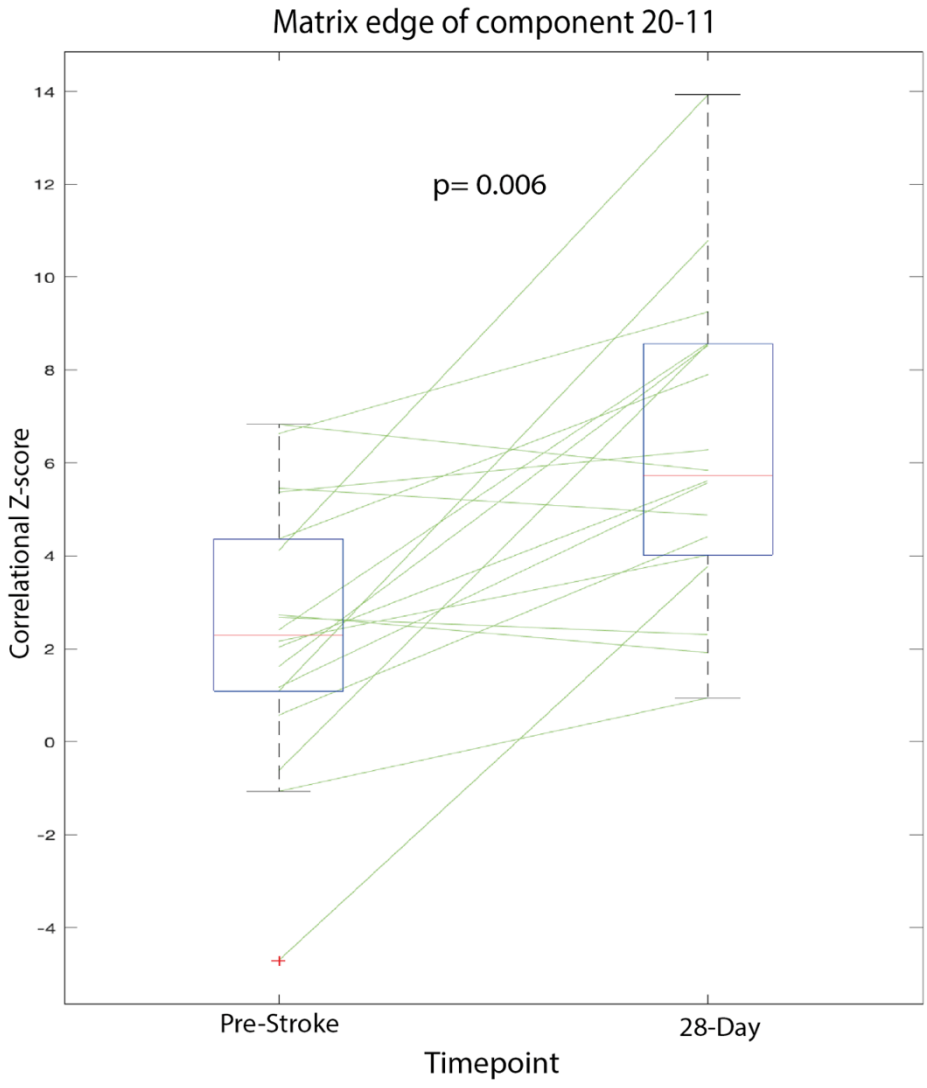


Figure 5. 12. Comparison of significantly different correlational edges prior to and at 28-Day post stroke. Boxplot (median, red) representing the 25th to 75th percentiles (bottom to top) of differences in correlational strength between component 20 (olfactory bulb) and 11 (cingulate gyrus) prior to surgery and at 28-Days. Whiskers represent the highest and lowest data point and + represents outliers. Each green line represents an individual subject.

5.3.1.5. Dual regression

All components were selected for dual-regression analysis (n = 7) and voxelwise testing of the resulting spatial maps. Overall, none of the selected components exhibited voxels that were significantly different in terms of correlations with the other voxels in the brain. This was true for all the timepoint comparisons.

5.3.1.6. Graph theory

Average measures for global efficiency at each timepoint are displayed in Figure 5.13. Paired t-tests reported a significant difference between the pre-stroke and 6-Days post-stroke timepoints $t(16) = -2.84$, $p = 0.036$. This was the result of an increase in global efficiency at 6-Days ($M = 4.97$, $SE = 0.75$) from baseline levels ($M = 2.74$, $SE = 0.43$). After multiple comparison corrections, no differences were present between the pre-stroke and 28-Day post-stroke $t(17) = -2.71$, $p = 0.068$, or 6-Day and 28-Day post-stroke comparisons $t(14) = 0.68$, $p = 0.505$.

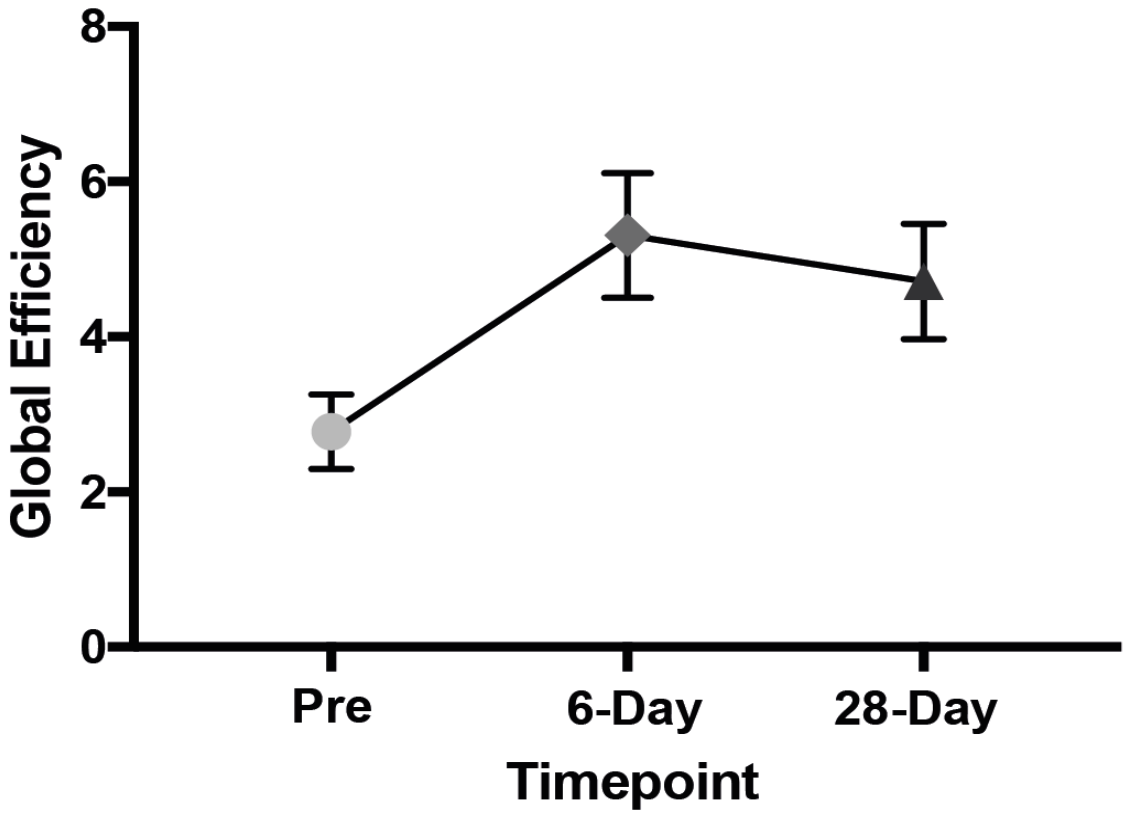


Figure 5. 13. Global efficiency from rs-fMRI data following stroke. Line graph illustrates graph theory values for global efficiency (mean ± standard error) (Pre-stroke, and at 6- and 28-Day post-stroke) (n = 15).

Graph theory measures of modularity are illustrated in Figure 5.14. Although an average reduction in modularity was present at the 6-Day post-stroke timepoint compared to pre-stroke baseline, the paired t-test reported this reduction was not significant $t(16) = 1.29$, $p = 0.615$. Similar non-significant outcomes were reported for comparisons between pre-stroke and 28-Days post-stroke $t(17) = 0.47$, $p = 0.74$ in addition to 6-Days and 28-Day post-stroke $t(14) = -0.34$, $p = 0.74$.

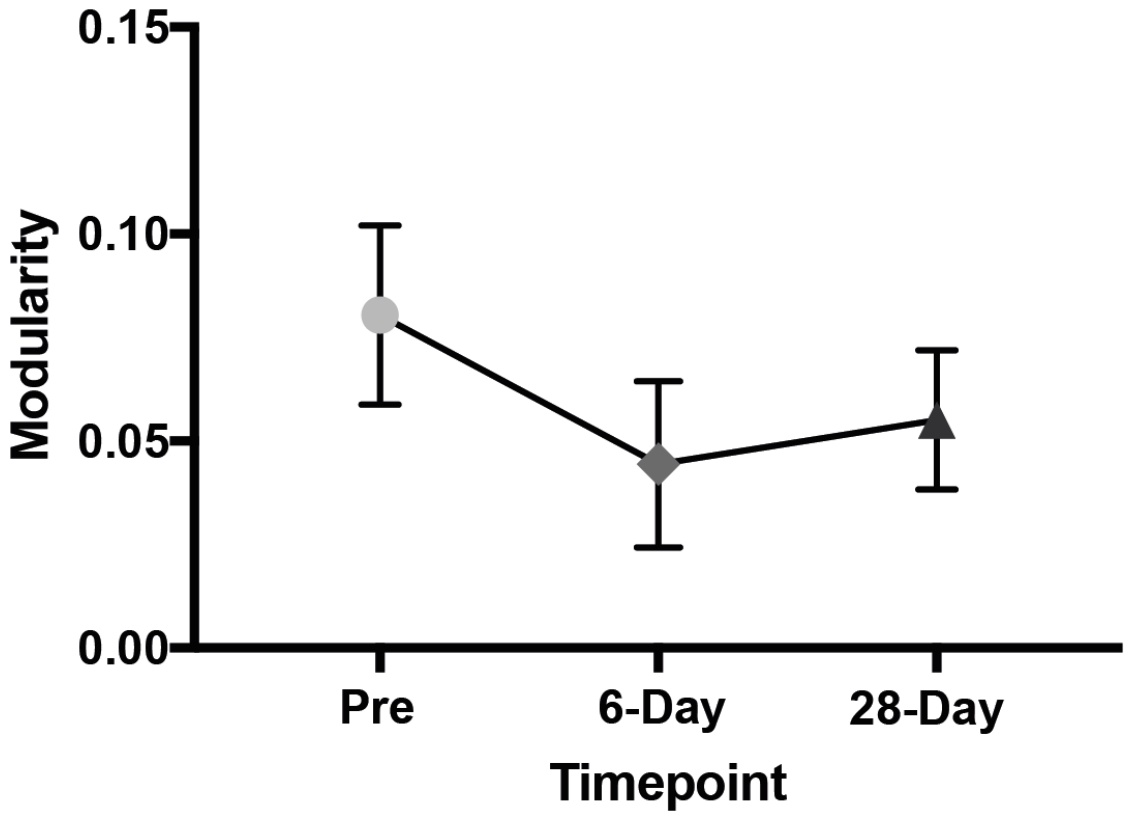


Figure 5. 14. Modularity from rs-fMRI data following stroke. Line graph displaying the graph theory measure of modularity (mean ± standard error) for all timepoints (Pre-stroke, 6- and 28-Day post-stroke) (n = 15).

Average graph theory measures of transitivity at each of the 3 timepoints are shown in Figure 5.15. Paired t-tests reported no significant differences for all timeseries comparisons; pre-stroke against 6-Day post-stroke $t(16) = -1.08$, $p = 0.30$, pre-stroke against 28-Day post-stroke $t(17) = -0.65$, $p = 0.52$, and lastly 6-Day against 28-Day post-stroke $t(14) = 0.42$, $p = 0.68$.

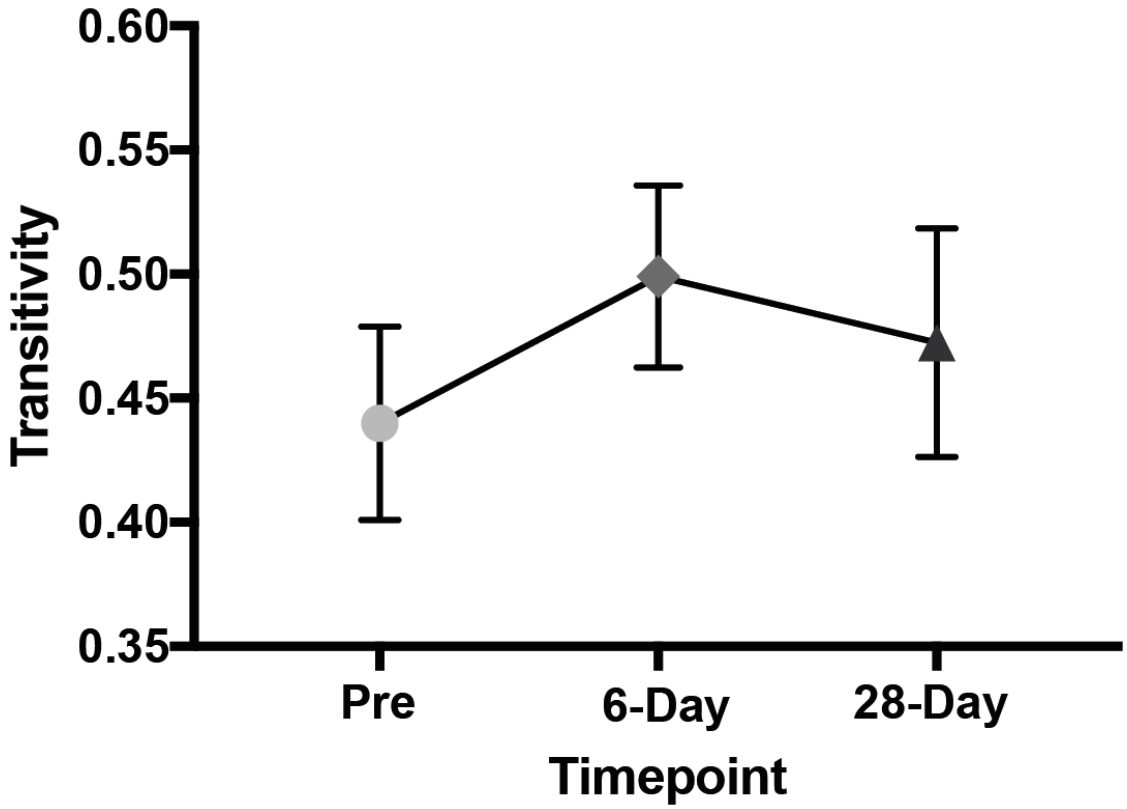


Figure 5. 15. Transitivity from rs-fMRI data following stroke. Line graph displaying the graph theory measure of transitivity (mean ± standard error) for all timepoints (Pre-stroke, 6- and 28-Day post stroke) (n = 15).

Local efficiency values were averaged across all components for each timepoint (Figure 5.16).

There was a significant main effect of time for local efficacy measures $F(2, 196) = 6.87$, $p < 0.001$. Post-hoc analysis with a Bonferroni correction revealed a significant increase from pre-stroke ($M = 0.42$, $SE = 0.02$) to 6-Days post-stroke ($M = 0.51$, $SE = 0.02$) ($p = 0.006$). Furthermore, this significant increase in local efficiency was present between pre-stroke and 28-Days post-stroke ($M = 0.52$, $SE = 0.02$) ($p = 0.005$). No differences were present between the 6 and 28-Day post-stoke timepoints ($p = 1.000$).

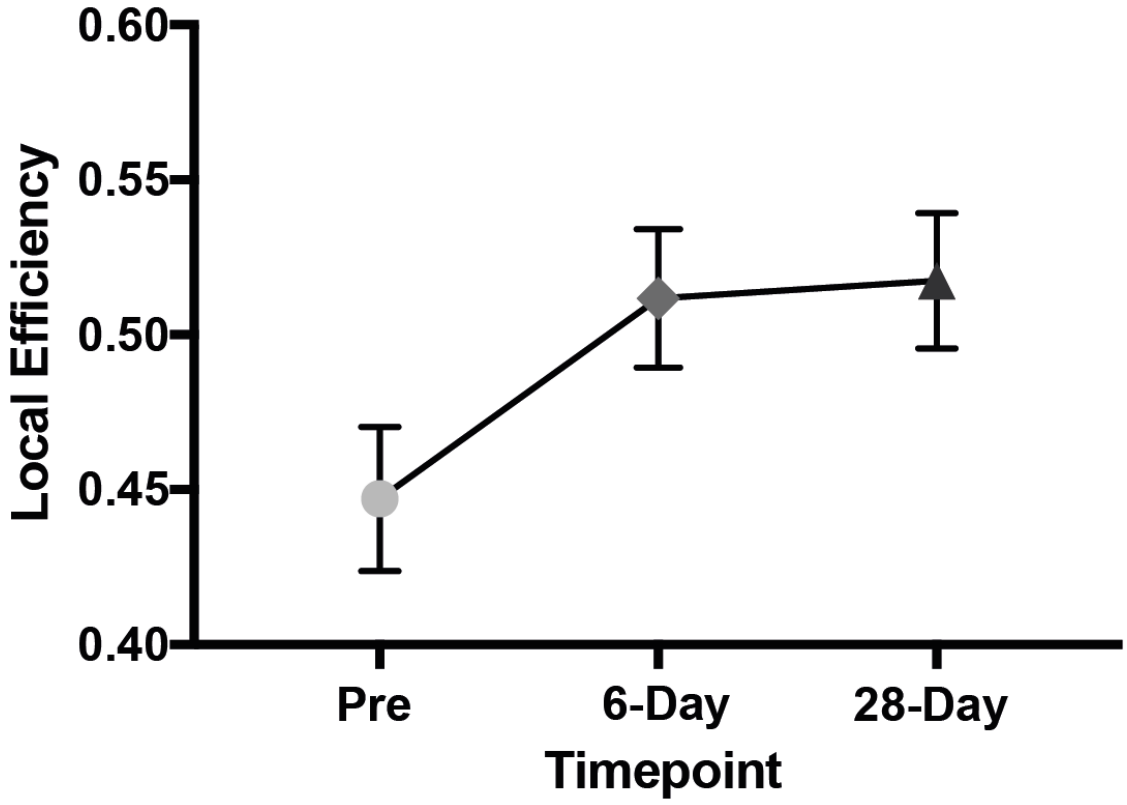


Figure 5. 16. Average local efficiency from rs-fMRI data following stroke. Line graph displaying the graph theory measure of local efficiency (mean ± standard error) for all timepoints (Pre, 6- and 28-Day post stroke) (n = 15).

There was also a significant main effect of component $F(6, 98) = 3.30$, $p < .005$ but no significant interaction between component and time $F(12, 196) = 0.67$, $p = 0.774$. Local efficiency measures for each individual component are displayed in Figure 5.17).

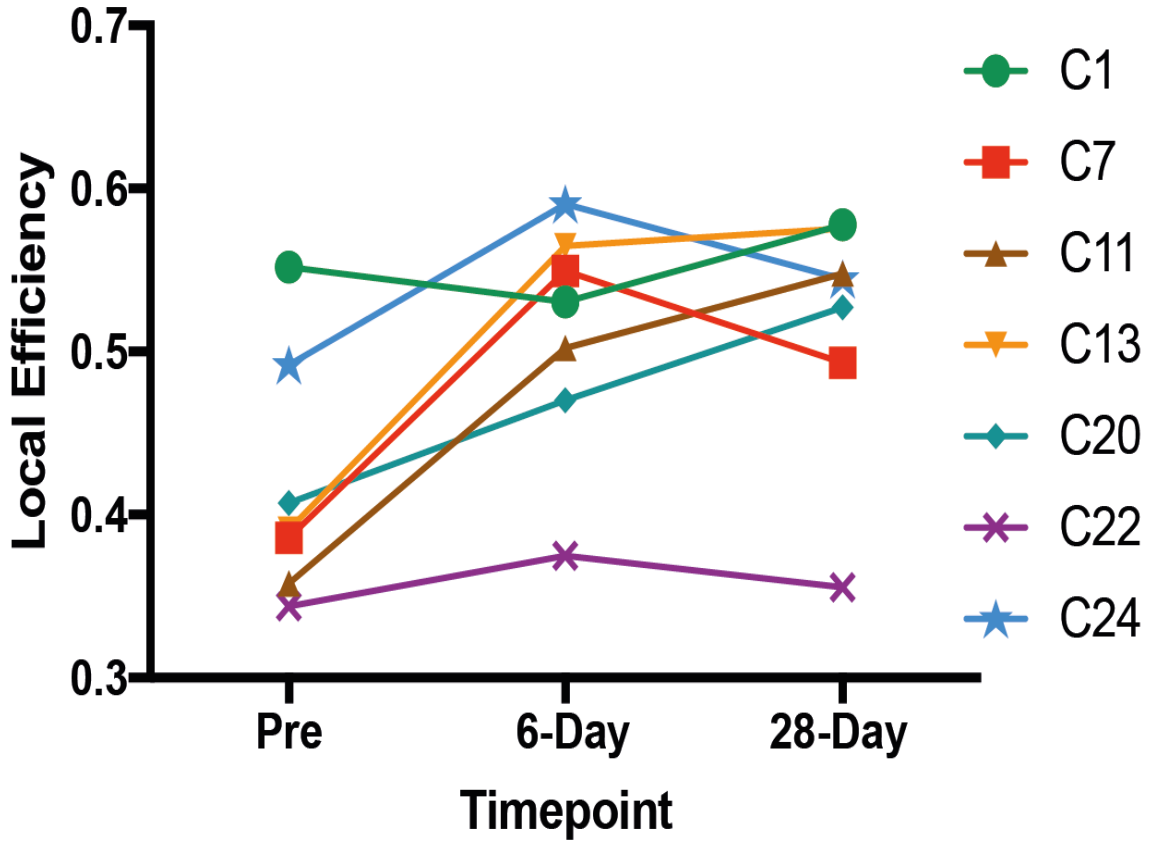


Figure 5. 17. Local efficiency from rs-fMRI data following stroke. Line graph illustrating the local efficiency values (mean ± standard error) for each individual component for all timepoints (Pre, 6- and 28-Day post stroke).

5.3.2. dMRI

5.3.2.1. Tract based spatial statistics

Voxelwise differences in regions of high FA between timepoints are displayed in Figures 5.18 - 5.20. Decreased FA at the 6-Day post stroke compared to the pre-stroke values was extensive throughout the WM of the ipsilateral hemisphere (Figure 5.18, top box). This was most apparent throughout the cortico-spinal tract and internal capsule, and most of these voxels remained significant following multiple comparisons. There were also grey matter cortical regions that exhibited decreased FA at 6-Days: postcruciate, C, insular, SS, posterior sylvian, ectolateralis gyri, and occipital lobe, as well as the olfactory bulb, putamen, caudate nucleus, amygdala and thalamus. Overall, the ectolateralis gyrus showed the strongest reductions in FA at the 6-Day timepoint among the cortical regions. However, none of the voxels in these grey matter regions survived multiple comparisons.

In contrast, there were a few regions, primarily located in sub-cortical grey matter areas, that showed increases of FA at the 6-Day timepoint compared to baseline. These regions included the midbrain, subfornical organ, lateral septal nucleus, preoptic hypothalamic area, bed nucleus of stria terminalis, nucleus of the vertical limb of the diagonal band (Figure 5.18, bottom box). The strongest increases in FA were primarily in the preoptic hypothalamic area. Other WM regions also displayed increases in FA, such as the fornix and the mammillothalamic tract.

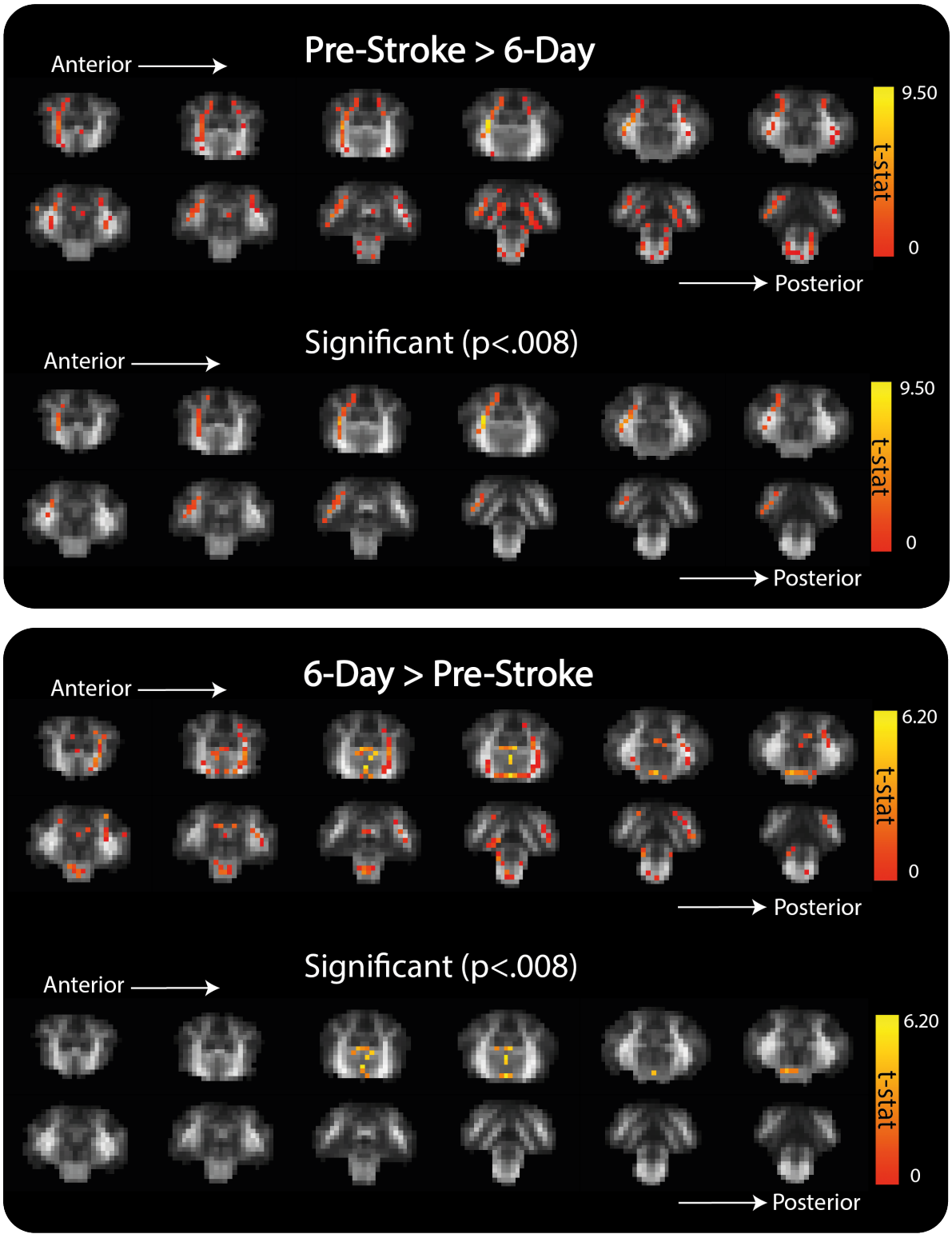


Figure 5. 18. Spatial map differences in FA values between the pre-stroke and 6-Day post stroke time points. Voxelwise differences are illustrated in a sequence of coronal slices from anterior (top left) to posterior (bottom right). The top 2 rows display voxelwise FA differences, whilst the bottom 2 rows display differences that were significant (n = 17). Note: scale bars represent the t-statistic.

There were still reductions in FA at the 28-Day compared to the pre-stroke timepoint, particularly in the WM regions ipsilateral to the stroke (Figure 5.19, top box). This was similar to the reductions seen at 6-Days; the right internal capsule showed the strongest reductions. However, none of these voxelwise decreases remained significant after multiple comparison corrections.

Contrasting increases in FA were also present at the 28-Day timepoint when compared to baseline. These increases were located in WM regions contralateral to the stroke (Figure 5.19, bottom box), such as the left internal capsule and optic tract. There were also some increases in FA noted in the brainstem, but no voxels maintained significance after multiple comparison corrections.

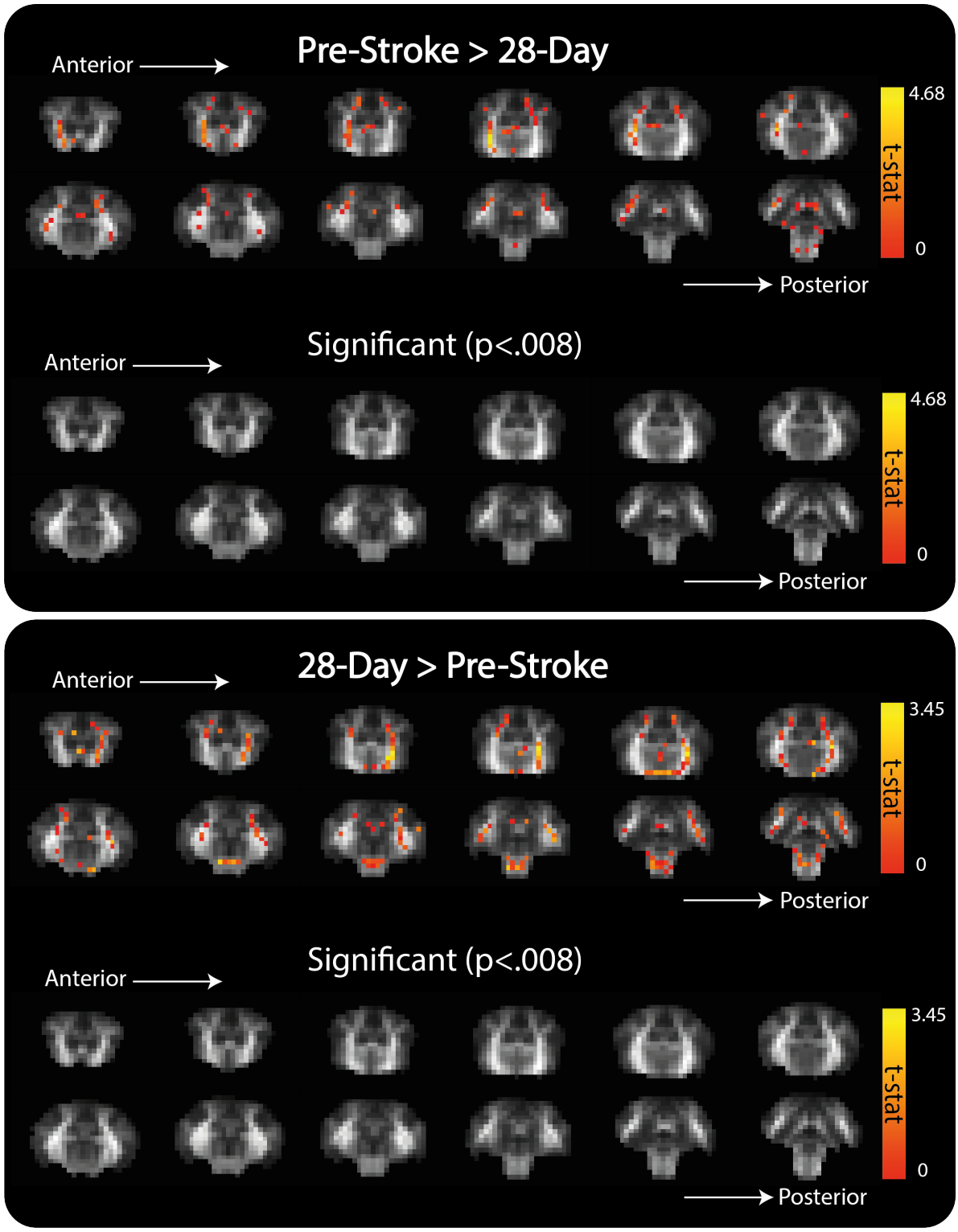


Figure 5. 19. Differences in FA values between the pre-stroke and 28-Day post stroke time points. Voxelwise differences are illustrated in a sequence of coronal slices from anterior (top left) to posterior (bottom right). The top 2 rows display voxelwise FA differences, whilst the bottom 2 rows display differences that were significant (n = 17). Note: scale bars represent the t-statistic.

Comparisons between the 6- and 28-Day post stroke timepoints revealed reductions in FA at 28-Days that were loosely scattered across the WM on both sides of the brain and also in anterior sub-cortical regions such as the caudate, nucleus accumbens, thalamus, and hypothalamus (Figure 5.20, top box). None of these differences survived significance after multiple comparison corrections.

In contrast, there was a widespread bilateral increase in FA at the 28-Day compared to the 6-Day timepoint in many WM voxels with other voxels located in sub-cortical grey matter structures such as the hippocampus, amygdala, globus pallidus, claustrum and putamen (Figure 5.20, bottom box). Overall, the increases in FA were only significant in the superior region of the internal capsule on the ipsilateral side, and in a few voxels in the anterior commissure and globus pallidus.

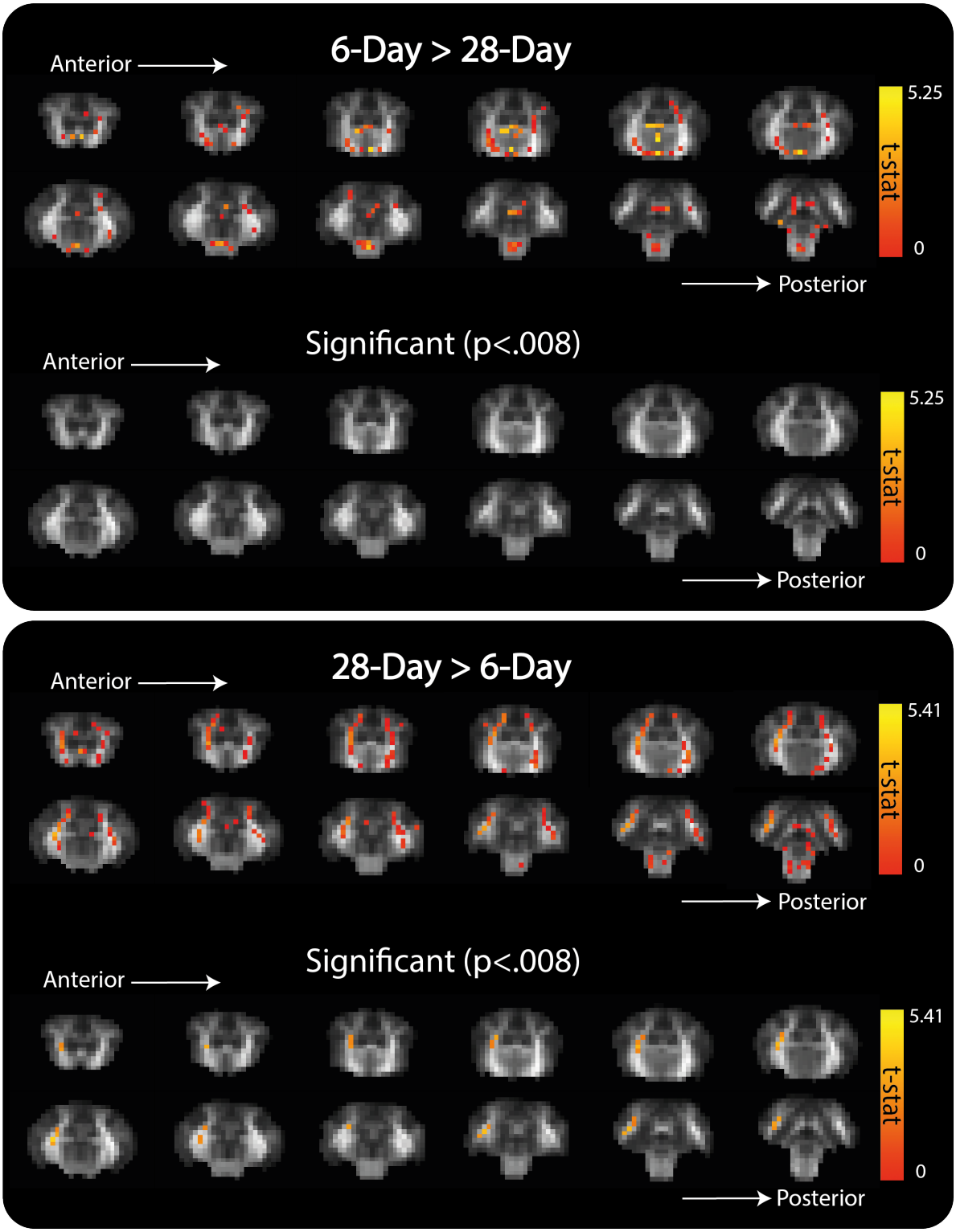


Figure 5. 20. Differences in FA values between the 6 and 28-Day post stroke time points. Voxelwise differences are illustrated in a sequence of coronal slices from anterior (top left) to posterior (bottom right). The top 2 rows display voxelwise FA differences, whilst the bottom 2 rows display differences that were significant (n = 17). Note: scale bars represent the t-statistic.

5.3.2.2. Tractography

5.3.2.2.1. Deterministic tractography

Visual inspection of the deterministic tracts (Figure 5.21) displayed all major WM regions such as the corpus callosum, corona radiata, internal capsule, corticospinal tracts, and fornix prior to stroke. By 6-Days, the WM exhibits a midline shift. This is particularly noticeable in the corpus callosum, which appears to be shifted laterally (towards the left or contralateral side) due to the brain swelling from the stroke, and the internal capsule appears distorted with fewer streamlines contributing to the corticospinal tract. By 28-Days, oedema has resolved, and the WM no longer appears compressed or shifted. Aspects of the corpus callosum have failed to reconstruct, and there appear to be more disorganised or spurious streamlines in the internal capsule, though the corticospinal tract appears more robust.

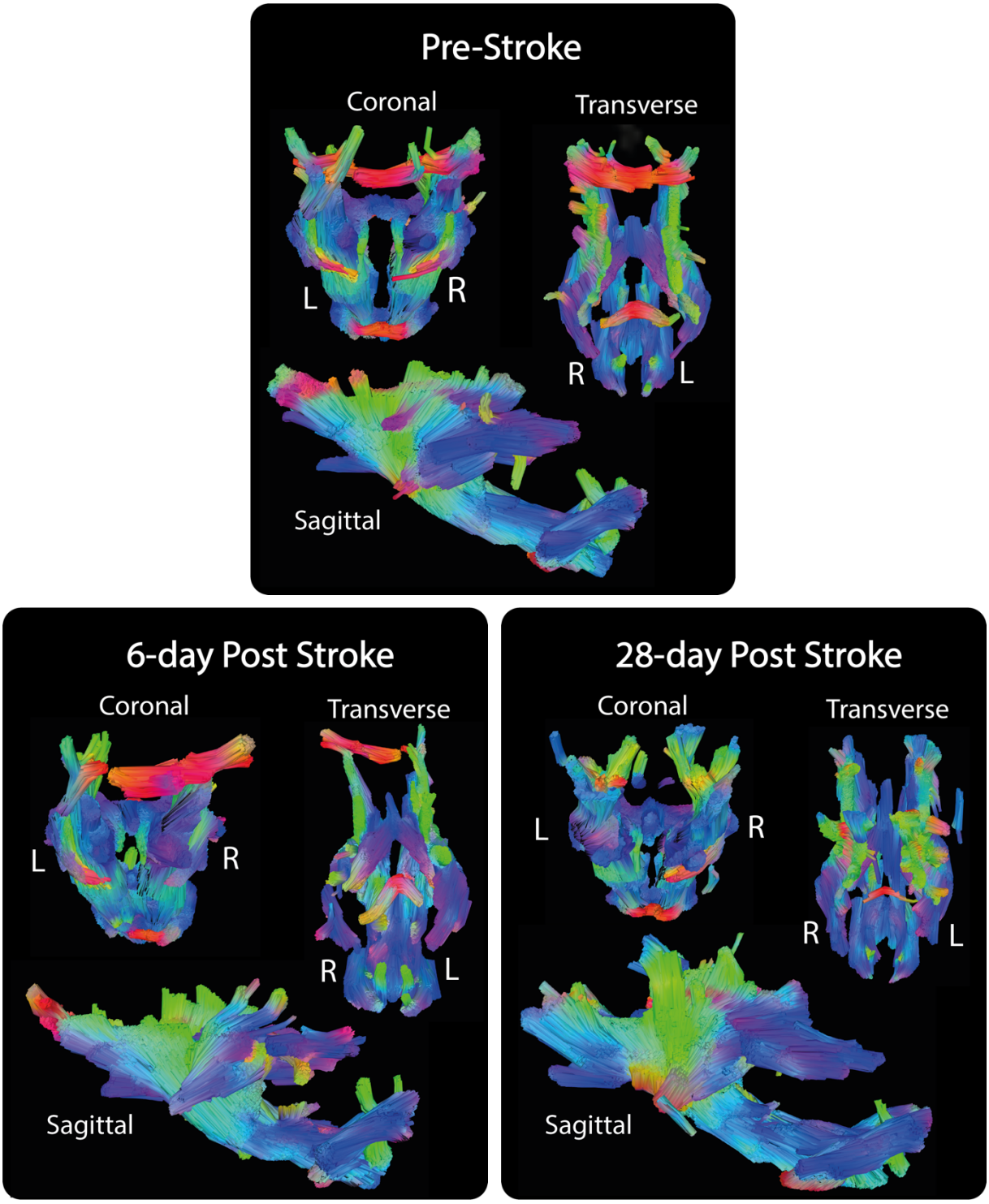


Figure 5. 21. Deterministic tractography WM reconstructions from a representative animal. (Top) The corpus callosum is visible on both coronal and transverse views, as well as the internal capsule, prior to surgery. The sagittal view clearly shows the corona radiata, internal capsule and corticospinal tract. Oedema has impacted WM integrity and position at 6- and 28-Day post-stroke. Note: Colour indicates direction, green: superior/inferior, blue: anterior/posterior, red: left/right.

5.3.2.2.2. Probabilistic tractography

Structural connectivity matrices for each timepoint are displayed in Figures 5.22, 5.23 and 5.24. As would be expected, prior to stroke, streamline connections to regions within the same hemisphere (intra-hemispheric connectivity - whether it be ipsilateral or contralateral) were generally stronger than inter-hemispheric regional connectivity. WM was highly connected to most regions There was also strong connectivity among cortical regions, and the thalamus and basal ganglia were also highly connected to cortical regions. There were also strong connections evident throughout the brain stem

Interestingly, no obvious qualitative differences were evident from comparisons at each timepoint. The 6- and 28-Day post stroke connectivity matrices were similar in overall appearance to the presurgical matrix.

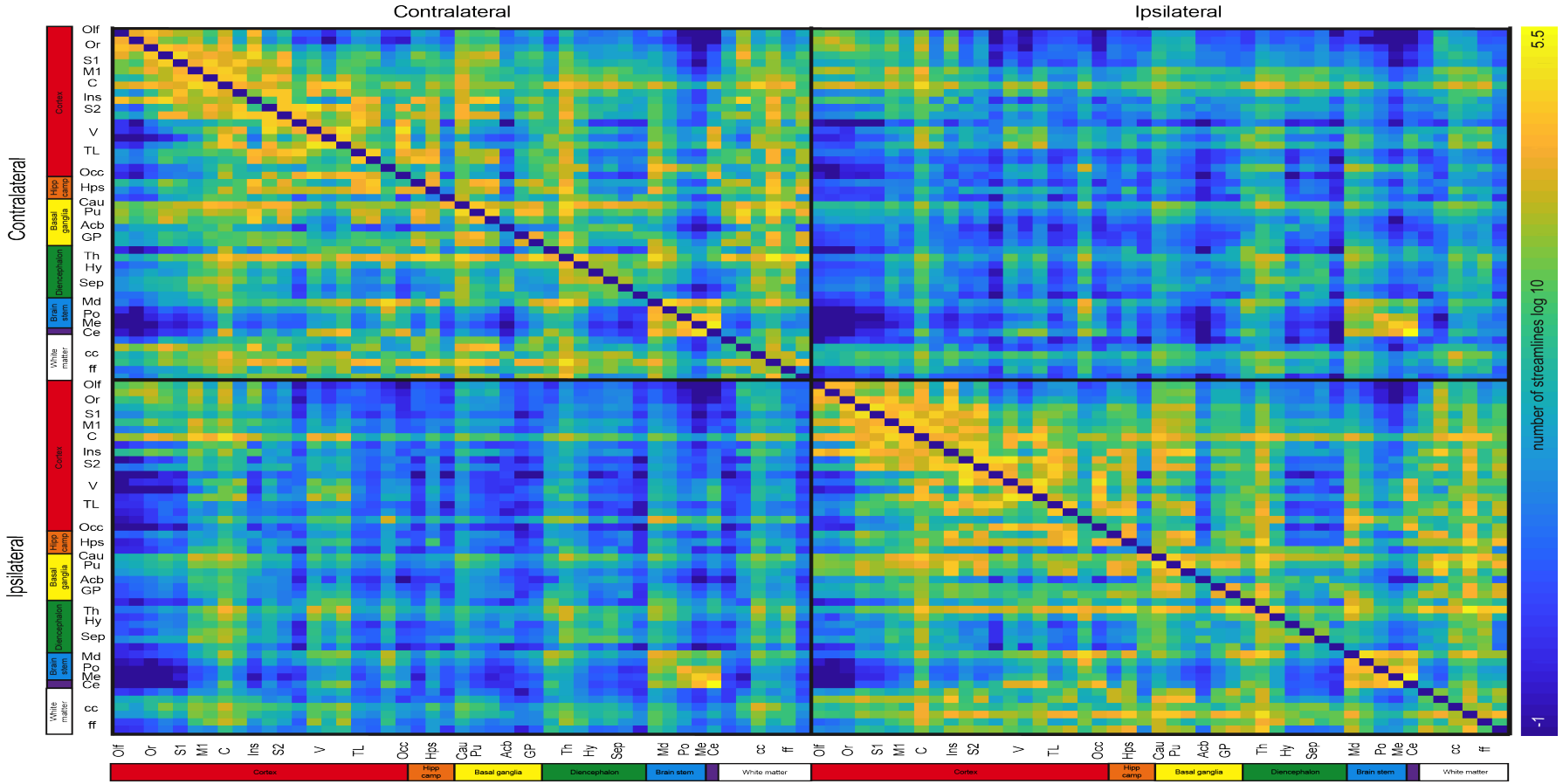


Figure 5. 22. Structural connectivity matrix at the pre-stroke timepoint (n=21). Ipsilateral and contralateral regions are from the modified unilateral ovine atlas (n=94). Note: scale bar represents connectivity strength through the number of streamlines scaled by a factor of $\log_{10}$. Abbreviations: Olfactory (Olf), Orbital frontal (Or), anterior sygmoideus gyrus (S1), pre and post-cruciate gyrus (M1), Cingulate (C), Insular (Ins), Sylvian gyrus (S2), Visual (combination ecto and entolateral gyri) (V1), Temporal (TL), Occipital lobe (Occ), Hippocampus (Hps), Caudate (Cau), Putamen (Pu), Nucleus accumbens (Acb), Globus pallidus (GP), Thalamus (Th), Hypothalamus (Hy), Medial and lateral septal nuclei (Sep), Midbrain (Md), Pons (Po), Medulla (Me), Cerebellum (Ce), Corpus Callosum (CC), fornix (ff).

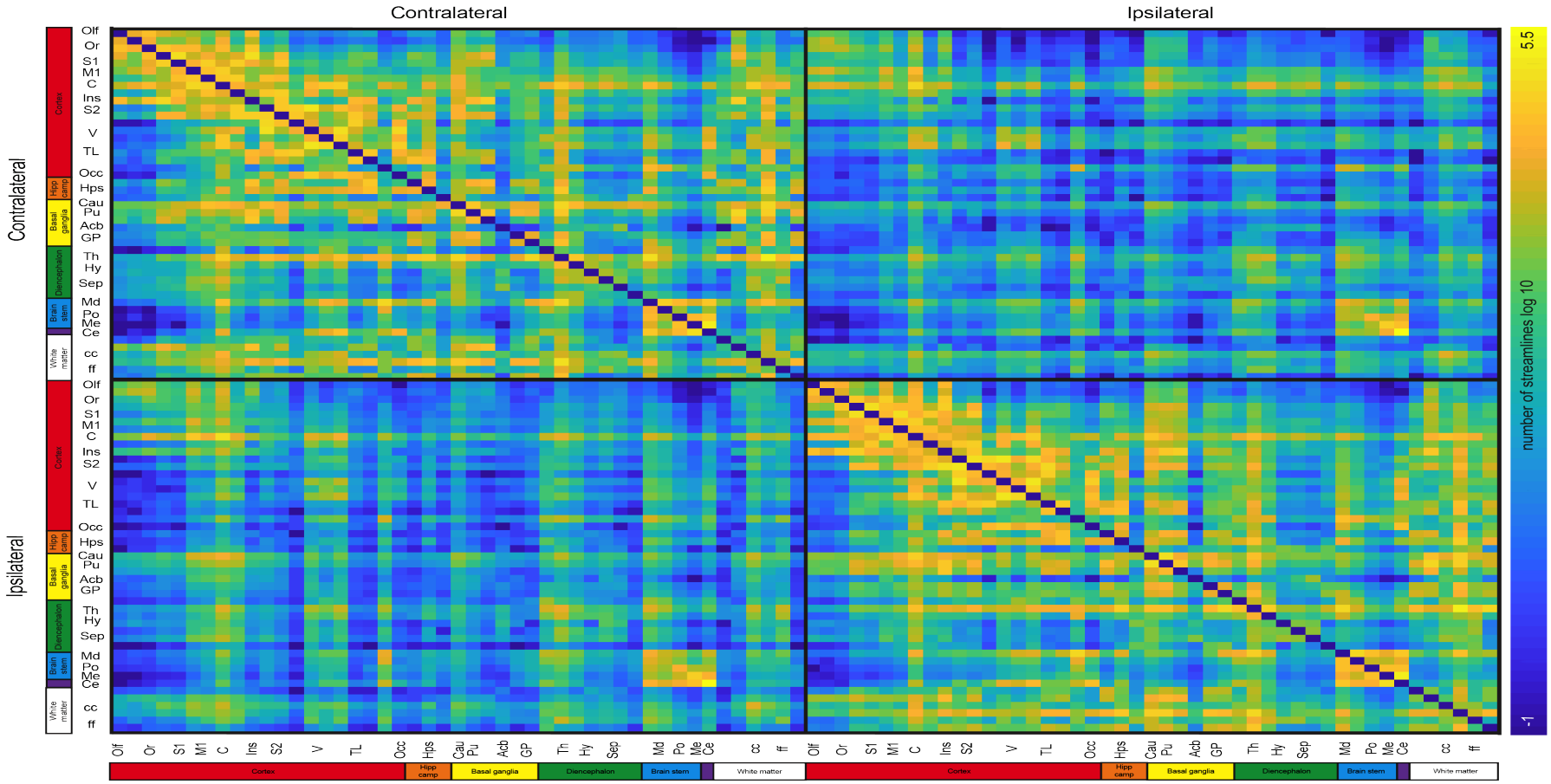


Figure 5. 23. Structural connectivity matrix at the 6-Day post stroke timepoint (n=17). Ipsilateral and contralateral regions are from the modified unilateral ovine atlas (n=94). Note: scale bar represents connectivity strength through the number of streamlines scaled by a factor of $\log_{10}$. Abbreviations: Olfactory (Olf), Orbital frontal (Or), anterior sygmoideus gyrus (S1), pre and post-cruciate gyrus (M1), Cingulate (C), Insular (Ins), Sylvian gyrus (S2), Visual (combination ecto and entolateral gyri) (V1), Temporal (TL), Occipital lobe (Occ), Hippocampus (Hps), Caudate (Cau), Putamen (Pu), Nucleus accumbens (Acb), Globus pallidus (GP), Thalamus (Th), Hypothalamus (Hy), Medial and lateral septal nuclei (Sep), Midbrain (Md), Pons (Po), Medulla (Me), Cerebellum (Ce), Corpus Callosum (CC), fornix (ff).

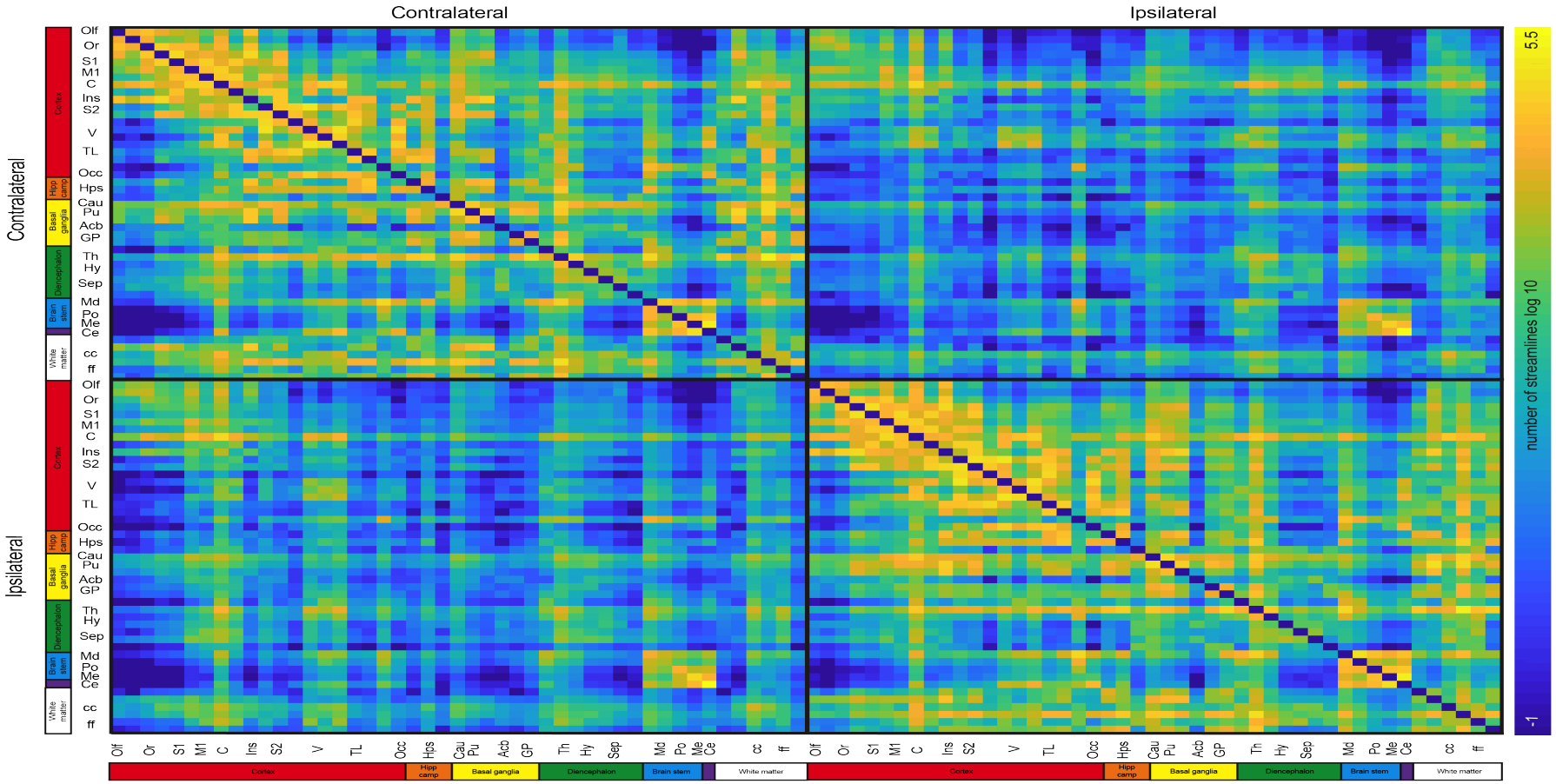


Figure 5. 24. Structural connectivity matrix at the 28-Day post stroke timepoint (n=18). Ipsilateral and contralateral regions are from the modified unilateral ovine atlas (n=94). Note: scale bar represents connectivity strength through the number of streamlines scaled by a factor of $\log_{10}$. Regions are categorised and ordered in their groups from anterior to posterior. Abbreviations: Olfactory (Olf), Orbital frontal (Or), anterior sygmoideus gyrus (S1), pre and post-cruciate gyrus (M1), Cingulate (C), Insular (Ins), Sylvian gyrus (S2), Visual (combination ecto and entolateral gyri) (V1), Temporal (TL), Occipital lobe (Occ), Hippocampus (Hps), Caudate (Cau), Putamen (Pu), Nucleus accumbens (Acb), Globus pallidus (GP), Thalamus (Th), Hypothalamus (Hy), Medial and lateral septal nuclei (Sep), Midbrain (Md), Pons (Po), Medulla (Me), Cerebellum (Ce), Corpus Callosum (CC), fornix (ff).

5.3.2.3. Graph theory

Global efficiency scores at the 3 timepoints are displayed in Figure 5.25. A significant difference was observed between the pre-stroke and 6-Day timepoints $t(16) = -6.1$, $p < 0.01$; global efficiency was slightly higher at 6-Days post stroke ($M = 2.38$, $SE = 0.01$) compared to the pre-stroke timepoint ($M = 2.34$, $SE = 0.01$). No significant differences were reported between the pre-stroke and 28-Day post-stroke timepoints $t(17) = 0.16$, $p = 0.87$. The third contrast between the 6- and 28-Day post stroke timepoints was significantly different, $t(14) = 3.62$, $p < 0.01$; the 6-Day ($M = 2.38$, $SE = 0.01$) timepoint had a higher global efficiency compared to the 28-Day post stroke timepoint ($M = 2.34$, $SE = 0.01$).

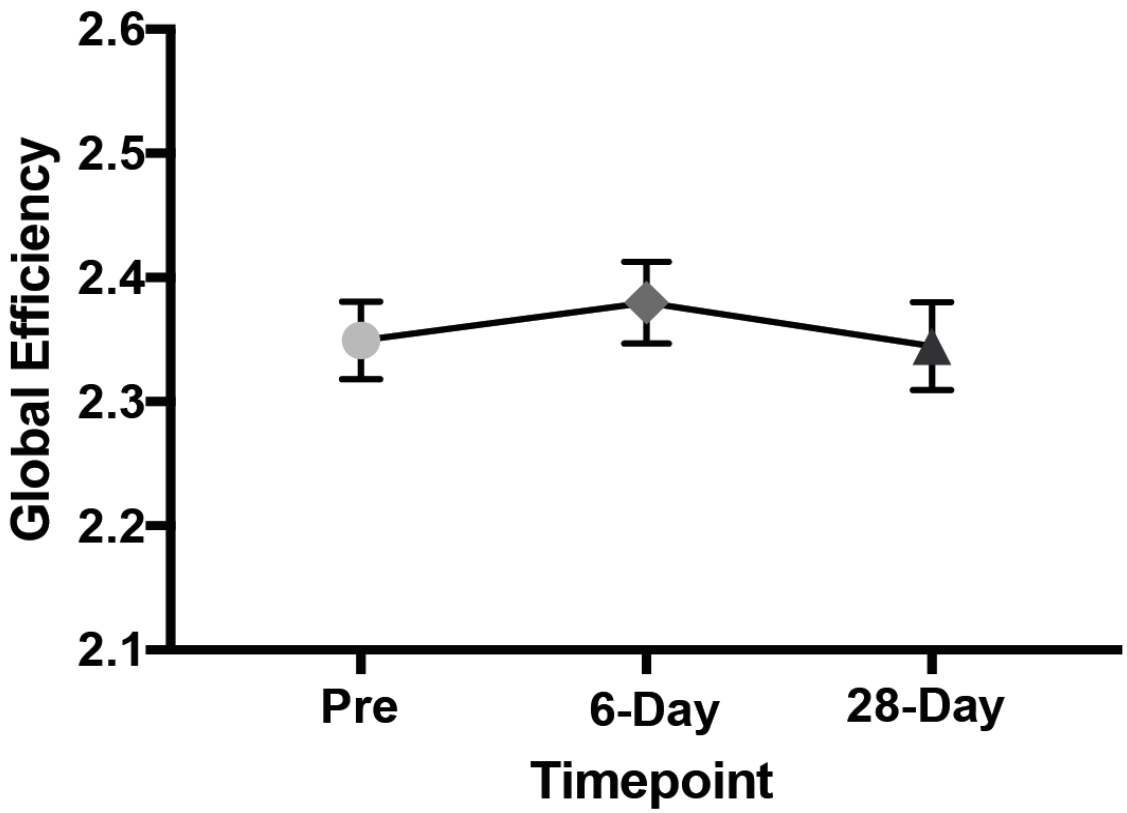


Figure 5. 25. Global efficiency from dMRI data following stroke. Line graph displaying global efficiency (mean ± standard error) at each timepoint (Pre, 6- and 28-day post stroke) (n = 12).

Average local efficiency across all 94 regions is displayed in Figure 5.26. There was a significant main effect for timepoint $F(2, 2632) = 34.66$, $p < .001$, post hoc tests using a Bonferroni correction revealed an average local efficiency increase of 0.01 ($p < .001$) at 6-Days post stroke ($M = 0.60$, $SE = 0.01$) compared to the pre-stroke baseline ($M = 0.59$, $SE = 0.01$). Furthermore, a significant average decrease of 0.01 ($p < .001$) in local efficiency was present at the 28 ($M = 0.59$, $SE = 0.01$) compared to the 6-Day post-stroke ($M = 0.60$, $SE = 0.01$) timepoint. No significant difference was reported between the pre-stroke and 28-Day post-stroke timepoint for average local efficiency ($p = 0.68$).

There was no significant main effect of region or hemispheric side, nor was there a significant interaction between timepoint and hemispheric side $F(2, 2632) = 0.48$, $p = 0.62$, or timepoint and brain region $F(92, 2632) = 0.36$, $p = 0.36$. However, there was a significant interaction between timepoint, hemispheric side and brain region $F(92, 2632) = 1.62$, $p < .001$. Further investigation using a post hoc analysis with FDR corrections, revealed some individual regions survived multiple comparison corrections; all significant post hoc interactions are displayed in Figure 5.27. These include: the right medullary lamina $F(2,28) = 9.46$, $p = 0.03$ (pre-stroke ($M = 0.51$, $SE = 0.01$), 6-Day ($M = 0.54$, $SE = 0.01$), 28-Day ($M = 0.52$, $SE = 0.01$) poststroke), right corpus callosum: $F(2,28) = 8.89$, $p = 0.03$ (pre-stroke ($M = 0.51$, $SE = 0.01$), 6-Day ($M = 0.54$, $SE = 0.01$), 28-Day ($M = 0.52$, $SE = 0.01$) poststroke), right pituitary gland: $F(2,28) = 9.08$, $p = 0.03$, (pre-stroke ($M = 0.55$, $SE = 0.01$), 6-Day ($M = 0.58$, $SE = 0.01$), 28-Day ($M = 0.56$, $SE = 0.01$) poststroke), left hippocampus: $F(2,28) = 6.63$, $p = 0.047$ (pre-stroke ($M = 0.56$, $SE = 0.01$), 6-Day ($M = 0.58$, $SE = 0.01$), 28-Day ($M = 0.57$, $SE = 0.01$) poststroke), left insular cortex: $F(1.38, 19.26) = 8.93$, $p = 0.047$ (pre-stroke ($M = 0.56$, $SE = 0.01$), 6-Day ($M = 0.59$, $SE = 0.01$), 28-Day ($M = 0.57$, $SE = 0.01$) poststroke), right orbital gyrus: $F(2,28) = 8.03$, $p = 0.047$ (pre-stroke ($M = 0.64$, $SE = 0.01$), 6-Day ($M = 0.68$, $SE = 0.01$), 28-Day ($M = 0.63$, $SE = 0.01$) poststroke), and left sylvian gyrus: $F(1.42, 19.92) = 9.11$, $p = 0.047$ (pre-stroke ($M = 0.59$, $SE = 0.01$), 6-Day ($M = 0.61$, $SE = 0.01$), 28-Day ($M = 0.59$, $SE = 0.01$) poststroke). Most of the regions show a similar trend with a slight increase in local efficiency from pre-stroke baseline at the 6-Day post stroke timepoint, and values return to original pre-stroke levels by 28-Days post stroke. The only region that did not follow this trend was the right midbrain: $F(2,28) = 6.66$, $p = 0.047$, which displayed a sharp reduction at 6-Days post-stroke ($M = 0.51$, $SE = 0.01$) compared to pre-stroke ($M = 0.59$, $SE = 0.01$), that persisted at 28-Days post-stroke ($M = 0.49$, $SE = 0.01$).

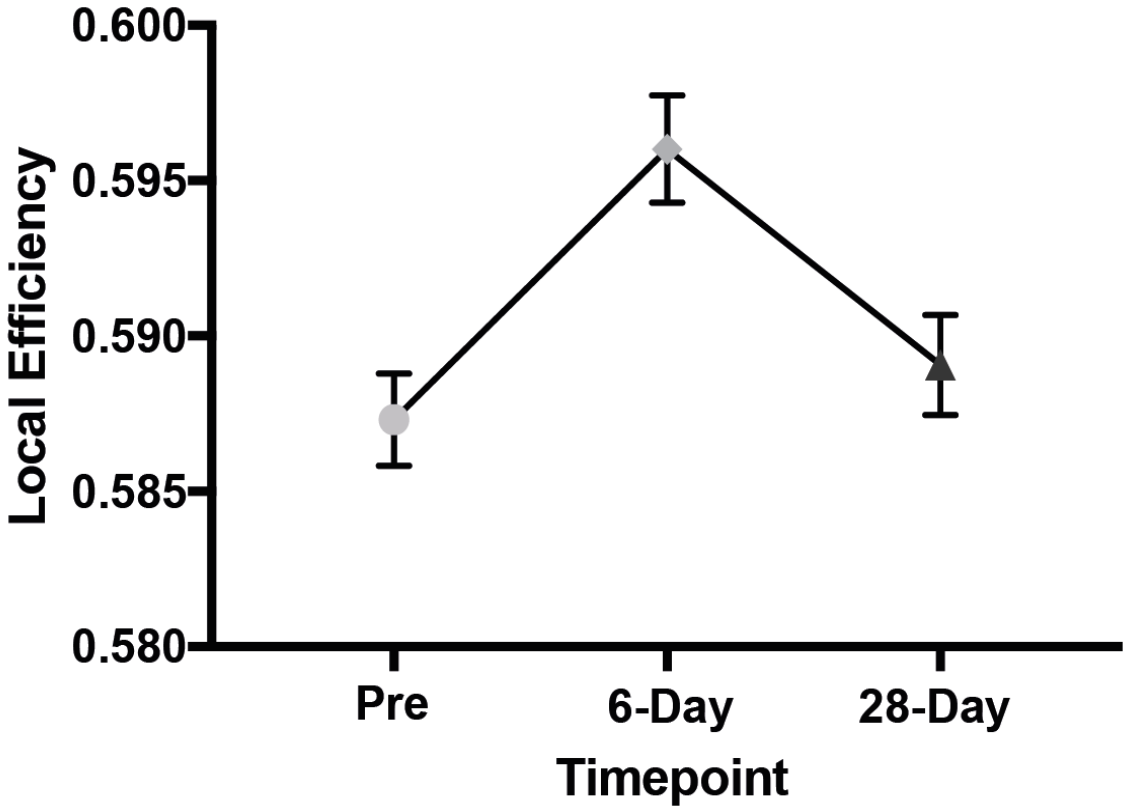


Figure 5. 26. Average local efficiency from dMRI data following stroke. Mean local efficiency values (± standard error) for each timepoint (Pre, 6- and 28-Day post stroke) (n = 12).

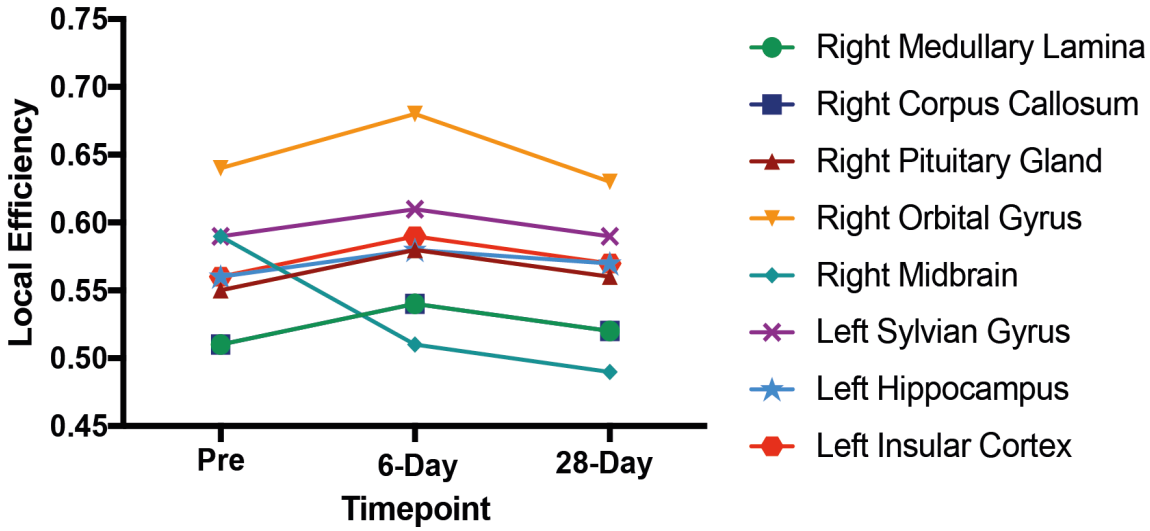


Figure 5. 27. Local efficiency from dMRI data following stroke. Line graph displaying the local efficiency values (mean ± standard error) for all timepoints (Pre, 6- and 28-Day post stroke) of regions that were still significant following multiple comparison corrections.

Transitivity values are displayed in Figure 5.28. Overall no significance was reported for the pre-stroke against 6-Day post-stroke contrast $t(16) = -1.67$, $p = 0.17$, pre-stroke against 28-Day post-stroke contrast $t(17) = -2.34$, $p = 0.10$, or the 6-Day against 28-Day post-stroke contrast $t(14) = 0.55$, $p = 0.59$.

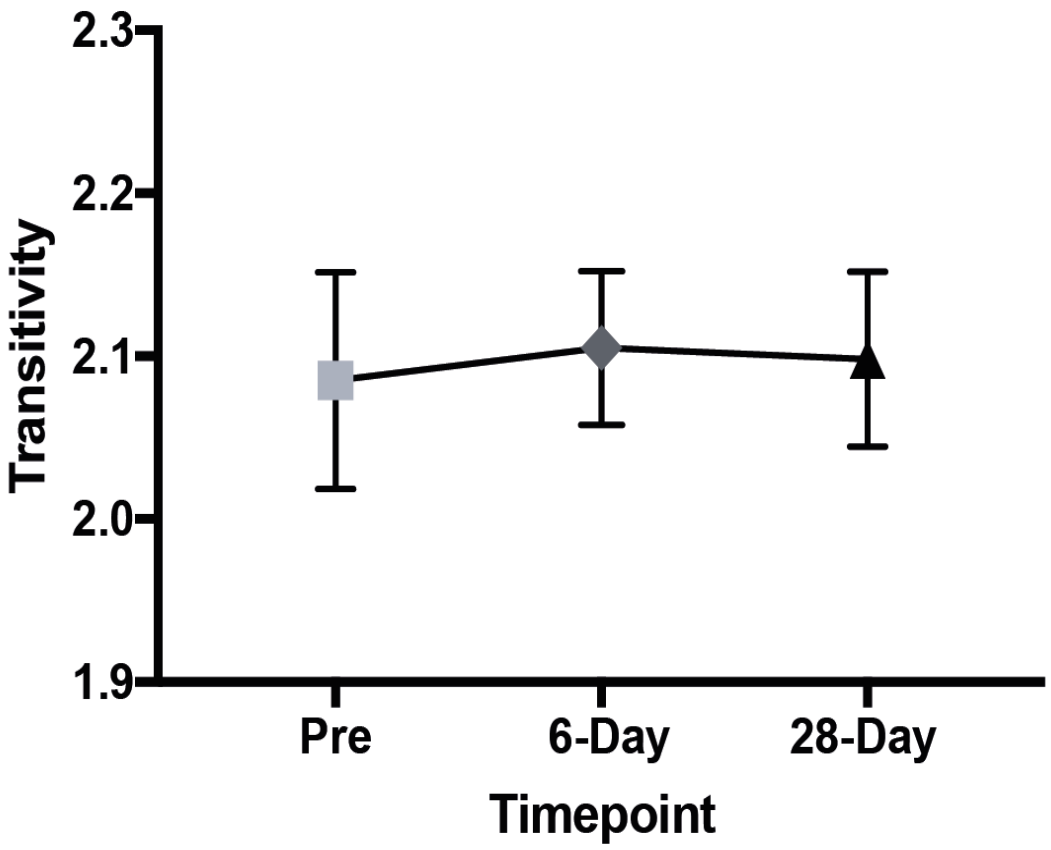


Figure 5. 28. Transitivity from dMRI data following stroke. Line graph displays the transitivity (mean ± standard error) at each timepoint (Pre, 6- and 28-Day post stroke) (n = 12).

Modularity scores from the structural connectome are illustrated in Figure 5.29. Overall no significant differences were reported for the pre-stroke against 6-Day post-stroke contrast $t(16) = 2.28$, $p = 0.11$, pre-stroke against 28-Day post-stroke contrast $t(17) = -1.09$, $p = 0.29$, or the 6-Day against 28-Day post-stroke contrast $t(14) = -1.79$, $p = 0.14$.

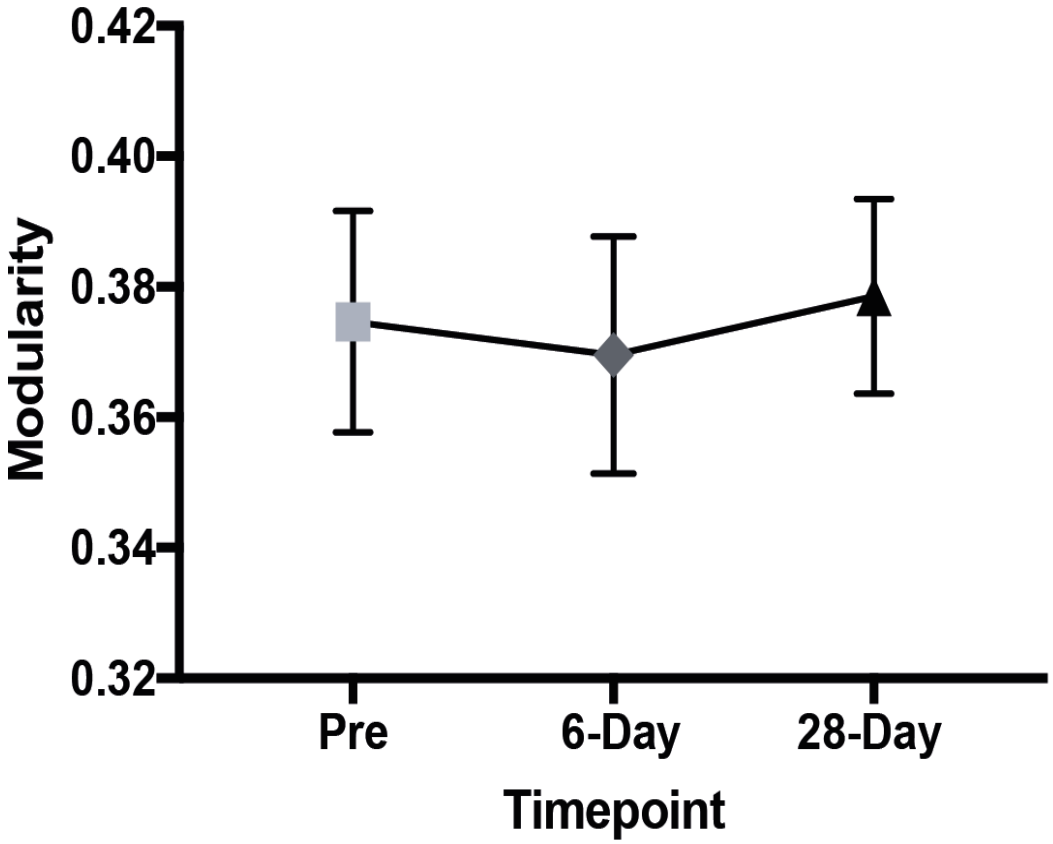


Figure 5. 29. Modularity from dMRI data following stroke. Line graph displays the modularity (mean ± standard error) at each timepoint (Pre, 6- and 28-Day post stroke) (n = 12).

5.4. Discussion

To our knowledge, this was the first time connectivity analysis had been investigated not only in sheep, but in a specific model of cerebrovascular disease. We have characterised functional connectivity prior to stroke in the sheep, and observed some network activity, the overall strength of which was increased after stroke (6- and 28-Day). This was accompanied by a significant increase in global efficiency, and a trend towards a decrease in modularity and increase in transitivity. A predictable pattern of structural connectivity was observed prior to stroke. Despite decreases in FA in the ipsilateral WM corticospinal tract at 6-Day, overall structural connectivity was not dramatically impacted. This is supported by a subtle increase in structural global efficiency at the 6-Day timepoint with no changes in other graph theory measures. Of note, is that local efficiency was slightly increased in a few regions at 6-Day, but dramatically decreased in the ipsilateral midbrain at both 6- and 28-Day.

Due the lack of previous research examining rs-fMRI in sheep, we first wanted to attempt to identify what RSNs are present before further analysing potential change as a result of stroke using ICA. All data driven resting-state components were generated from only the pre-stroke timepoint of each subject. Altogether 32 data driven components were identified, and despite control over physiological parameters and efforts to correct for motion and regress noise, only 7 were identified as neurally driven resting-state components, and 4 of those were contaminated by some noise. The three strongest signal components accounted for the highest amount of variance within the data and were generally associated with the sensory cortex. The strongest consisted of a combination of bilateral sensory (suprasylvius and sylvian gyrus) and, to a lesser degree, the visual regions also (ectolateralis and endolateralis). The sensorimotor and visual RSNs are extensively characterised in the human, reviewed in (Raichle, 2015; Hausman et al., 2020). The second strongest component contained a composite of bilateral sensory regions (the sylvian gyrus), in addition to areas associated with memory (temporal lobe and insular regions). This again shows similarities to the sensorimotor and visual RSNs in addition to aspects of the DMN like the temporal lobes. Interestingly, the majority of Component 11 was located throughout the entire cingulate gyrus, in addition to parietal regions (motor; pre and postcruciate gyrus, somatosensory; sylvian gyrus). Similar to the rodent (Lu et al., 2012; Grandjean et al., 2017a), and monkey (Vincent et al., 2007), it is possible this collection of cingulate and motor and somatosensory

cortices could constitute a potential ovine analogue to the DMN. In humans, the posterior cingulate gyrus, coupled with the neighbouring precuneus and lateral parietal cortices, is also a key component of the DMN along with the ventral medial prefrontal cortex and dorsal medial prefrontal cortices (Raichle, 2015).

The remaining 4 components were less clear in terms of potential functional significance, particularly as they were contaminated by noise. While many still included sensorimotor regions, there was also strong limbic representation. Component 13 had signal located in the hypothalamus, anterior cingulate and posterior sylvian gyrus, whilst Component 20 was primarily driven by the olfactory bulb, anterior cingulate and posterior sygmoideus gyrus. Component 22 had bilateral parahippocampal cortex and hippocampal activity, and Component 24 consisted of unilateral activity scatted throughout the right parahippocampal cortex, left orbitofrontal gyrus, as well as the posterior sygmoideus and suprasylvius gyri. One human study parcellated 7 RSNs from 1000 subjects, and while the visual, somatomotor, DMN and dorsal and ventral attention RSNs were identified, there was another network that included limbic structures such as the temporal lobes and inferior frontal lobes (Yeo et al., 2011). Indeed several studies have identified limbic RSN that are well connected to pre-frontal regions and appear to be perturbed in a variety of mental health conditions (Janes et al., 2012; Pannekoek et al., 2013). As this is the first rs-fMRI study in sheep, it is still very unclear what the functional significance of many of these components could be, whether they are unique to sheep, or a direct result of the anaesthetic used during scanning (isoflurane), or processing decisions.

All signal components generally displayed strong correlations with each other. This suggests there is a high functional connectivity between all signal components, however, hierarchical clustering revealed two sub-clusters. The first was centred around the sensory and visual RSN (Component 1), the olfactory driven component (Component 20), the possible ovine DMN driven by the cingulate (Component 11) and the parahippocampal (Component 22). This may support the possibility that Component 11 is a potential ovine DMN, since it is highly correlated with the somatosensory and memory RSNs.

The second sub-cluster was smaller and consisted of a combination of the sensory and memory RSNs (Component 7), right parahippocampal cortex, left orbitofrontal and posterior sygmoideus and suprasylvius gyri (Component 24), and the right hypothalamus, anterior

cingulate and posterior sylvian gyrus (Component 13), which displayed a reduced strength in correlation compared to the rest of the sub-cluster. The majority of this cluster was composed of the limbic RSNs, and temporal memory regions.

Investigating the effects of acute and chronic stroke on the resting-state components revealed that stroke did not affect the spatial maps of the components or their correlational strength in relation to the other voxels of the brain (dual regression), but rather the correlations between the individual component's time series. At the acute 6-Day post-stroke timepoint, all component time series were much more correlated than they were prior to surgery, and the same pattern was observed to an even greater degree at 28-Day. The node that was most dramatically affected was located bilaterally in the parahippocampal cortices (Component 22). The correlations between Component 22 and subsequent Components 11, 13 and 20 were all significant increased after stroke. The functional hyperconnectivity post-stroke that was evident in this study, has also been observed in populations of stroke patients, particularly when ICA was used to probe the data. For example, 25 patients within 6 months of an internal capsule stroke exhibited increased functional connectivity in the sensorimotor, visual, auditory, dorsal attention and DMN compared to subjects without a stroke (Wang et al., 2014). Similar results were reported for a cohort of patients within 2 weeks of stroke that had moderate to high loss of hand strength. In addition, the increase in correlations was evident in pathways between components that were not present in the healthy controls (Li et al., 2014). A systematic review revealed that, while there are often decreased in functional connectivity in some nodes (particularly acutely and commonly in the sensorimotor RSNs), increased connectivity was highly correlated with improved motor function (Desowska and Turner, 2019). The review discussed the finding that the increased functional connectivity may be associated with increased randomisation of the network. Indeed, graph theory network characteristics like increased centrality (more short-range connections for each node) and reduced clustering coefficients have been reported in stroke patients and interpreted as increased randomisation of the network (Wang et al., 2010). While we did not examine centrality or clustering coefficient, we observed a significant increase in overall connectivity (global efficiency) at 6-Day post-stroke that remained at the 28-Day poststroke timepoint. Another paper has reported a comparable increase in global efficiency in a small cohort of non-disabled stroke patients (Zhu et al., 2017). This was accompanied by other measures that implied increase randomness, including an increase in degree (number of connections) in some nodes, specifically, ones associated with the DMN. We examined local efficiency

across all 7 Components or nodes, and while there was a slight increase in values at the 6-Day post-stroke timepoint compared to baseline, that continued until the 28-Day post-stroke timepoint, no significant differences were present. The somatosensory, visual component (C1) displayed a reduction in localised connections at the 6-Day post-stroke that recovered to slightly higher levels than baseline at the 28-Day timepoint. The segregatory measure of transitivity suggested a small but not significant increase in small triplet connections at the acute 6-Day post-stroke timepoint. This also suggests increased local connectivity in specific hubs and it may have occurred at the expense of modularity.

By far, the majority of papers that have examined changes in functional connectivity following stroke used seed-based approaches to look at inter-hemispheric connectivity. Common seed locations were the primary motor cortex (M1), or areas known to participate in motor function. A very typical finding is that connectivity between the M1 regions decreases, and recovery is correlated with improved motor function (Park et al., 2011; Chen and Schlaug, 2013; Golestani et al., 2013; Liu et al., 2015; Rehme et al., 2015). Additional approaches have used task-based studies to define the M1 (Carter et al., 2010; Baldassarre et al., 2016). Similarly, stroke patients with motor impairments have displayed decreases in interhemispheric connectivity between the primary motor cortices, and this has been coupled with an increase in intrahemispheric connectivity between the M1 and premotor regions. This pattern of change in functional connectivity has been so prominent, it could correctly classify patients with motor and without motor impairments (Rehme et al., 2015). This finding has been replicated in larger clinical cohorts (n = 100, 1-2 weeks post-stroke) compared to age matched controls (n = 27). Reductions were particularly evident in other homotopic regions. Overall, a reduction in integratory values for connections between the hemispheres were correlated with associative functions such as visual and verbal memory (Siegel et al., 2016). Future research could employ seed-analysis between homotopic ovine regions to explore these possibilities.

Interpretation of the dMRI results was more straightforward and our results were similar to what has been previously reported in similar ovine dMRI research (Pieri et al., 2019). Major WM tracts such as the corticospinal tract, corpus callosum, visual pathway, occipitofrontal fasciculus and fornix were evident in the FA maps and via deterministic tractography reconstructions. Structural connectivity matrices also seemed to be anatomically expected, with high connectivity among cortical regions within each hemisphere and slightly lower

connectivity with the corresponding contralateral hemisphere. Medial regions such as the brain stem exhibited equally high connectivity within and between the hemispheres. WM regions displayed an average high connectivity throughout all other brain regions in the matrix.

Qualitative investigation of the deterministic tractography revealed a warping of the internal capsule at the acute 6-Day post stroke timepoint. At the 28-Day post-stroke timepoint, the warping had almost recovered. This warping of the internal capsule into the midline at the acute phase is likely due to oedema. This is a well-known phenomenon, and in severe cases, the corticospinal tract may fail to reconstruct (Seo et al., 2014). In more chronic stages, similar problems may also occur as the loss of brain tissue and replacement with cerebral spinal fluid may affect tractography results (Andersen et al., 2010; Price et al., 2017).

It is much more common to use scalar metrics to infer tract integrity, and FA is the most commonly applied measure. Decreases in FA, particularly in the corticospinal tract, are negatively correlated with functional outcomes acutely, in the sub-acute phase, and even out to as far as 90 days (Puig et al., 2010; Radlinska et al., 2010; Kim et al., 2013; Groisser et al., 2014; Doughty et al., 2016). Indeed, a recent systematic review analysing clinical dMRI research found that cortico-spinal tract FA reductions were not only widespread, but also could accurately predict motor impairment depending on the post-stroke recovery timepoint (66.7% at 4-weeks, 83.3% at 6-months, and 92.3% 2-years post-stroke) (Moura et al., 2019). Quantitative analysis using TBSS revealed strong reductions in FA, particularly in the ipsilateral corticospinal tract and this was most obvious in the internal capsule. This localised damage is in widespread agreement with the clinical research findings. One consideration with regards to voxelwise approaches is that registration to align multiple subjects is even more problematic due to the potential effects of oedema, particularly at acute post-stroke timepoints. There is concern that the reliability of dMRI measures could be comprised as a result of different diffusion values due to oedema (Lin et al., 2018). We sought to overcome this using non-linear registration of WM skeletons, as recommended by Smith and colleagues (2006), and image warping was reduced in the acute phase.

The TBSS approach also allows measurements of WM change at the whole brain level. Decreased FA was prominent throughout the ipsilateral hemisphere and included the following regions: postcruciate, cingulate, insular, suprasylvius, posterior sylvian, and

ectolateralis gyri, occipital lobe, as well as the bulb, and thalamus. The majority of these regions were cortical, sensorimotor and associative memory functions and the ectolateralis gyrus (visual) displayed the strongest reduction. Even though dMRI is ideal for examination of WM, studies have used it to examine grey matter. For example, the apparent diffusion coefficient is well known indicator of cytotoxic and vasogenic oedema acutely and sub-acutely (Bastin et al., 2000; Fiebach et al., 2002). While FA recovers more quickly in ischemic grey matter tissue (Maniega et al., 2004). Intriguingly, increases in FA were also present at the acute 6-Day post-stroke in WM regions such as the fornix and mammillothalamic tract, and subcortical areas such as the thalamus and hypothalamus. Particularly during the acute stages, this increase in FA is likely due to oedema, which would result in a decrease in isotropic diffusion (Alegiani et al., 2017). It has been suggested that long term increases may represent plasticity associated with recovery. However, when comparing pre-stroke with 28-Days post-stroke FA values, no significant differences were present.

Although no clear visual differences were present in our structural connectivity matrices, we have not had the time to explore them further. A recent review reported that the vast majority of structural connectivity studies in stroke patients have focused on networks associated with the corticospinal tract, including the rubrospinal tract, inter-hemispheric connections, and parietal frontal pathways (Koch et al., 2016). Using a structural connectivity matrix derived from FA values, one study showed that stroke patients exhibited widespread decreases in FA in sensorimotor regions, along with interesting increases in some areas such as the contralateral orbitofrontal cortex and anterior cingulate (Wong et al., 2019). Probabilistic tractography was used to reconstruct connectomes from 19 stroke patients and age matched controls, the average number of direct connections to each voxels' neighbour was quantified, and there was a significant correlation with upper extremity function (Kalinosky et al., 2013). A recent study measured connectivity between grey matter regions in a small cohort of chronic stroke patients compared to controls (Sotelo et al., 2020). There was reduced connectivity between the frontal and parietal lobes, as well as ipsilateral subcortical regions and bilateral cerebellum, highlighting the utility of this method to look for connectivity changes beyond the lesion.

Graph theory measures calculated from the number of diffusion streamlines did show changes in network characteristics throughout the timeseries. A significant increase from

baseline was reported for global efficiency at the 6-Day post-stroke timepoint that recovered back to baseline at the 28-Day point. This increase is contradictory to clinical studies that show decreases in global efficiency between 3-5 days post stroke that persisted to chronic phases (30-40 days) and well out to 85-90 days (Schlemm et al., 2020). Another study reported similar findings at 6 months (Chen et al., 2020). Both papers reported increases in modularity, whereas we observed no changes in modularity in the ovine data. Our findings do seem contradictory, as the increase in integration measures and lack of change in segregatory measures also contradict the marked reduction in FA in the major WM tracts of the ipsilateral side. It is therefore possible our measurements may be confounded by oedema, though we did try to mitigate this using non-linear registration techniques to unwarp the images. Interestingly, in a rodent model of stroke, few observable changes were observed in a structural connectivity matrix derived from tractography, and even though global metrics were not calculated, there were increases in connection strengths (centrality) in sensorimotor nodes, which was interpreted as increased connectivity that may underpin recovery (Sinke et al., 2018).

When we examined integratory measures of graph theory at the regional level with local efficiency, there was a significant interactional among timepoint, hemispheric side, and region. This suggests there may be important structural connectivity differences at specific locations. The majority of the significant regions were located ipsilateral to the stroke (medullary lamina, orbital gyrus, midbrain, pituitary gland and corpus callosum) which exhibited a slight increase in local efficiency only at the 6-Day timepoint. In the contralateral side similar effects were observed in hippocampus, insular cortex and sylvian gyrus. Only the ipsilateral midbrain displayed a sharp and predictable decrease in local efficiency at 6-Days that persisted until the 28-Day timepoint. Increased structural communicability (a measure of the number of direct and indirect connections) has been reported in stroke patients in the ipsilateral inferior temporal and cingulate gyri and in the contralateral orbitofrontal cortex (Crofts et al., 2011). It is clear further investigation is required to determine whether these changes are meaningful, and the ovine tissue may assist with this.

Another logical starting point for future work with this data would be to use histological methods to support the inferences made from both structural and functional connectivity studies. Collectively, the clinical findings report reductions in FA in the ipsilateral corticospinal tract that recovers and the degree predicts functional outcome. In addition,

functional connectivity studies have reported decreased connectivity between homotopic cortical regions with increased connectivity within hemispheres. Studies using both methods have reported structural correlates are better predictors (Lin et al., 2018), while others have attempted to use the structural data to support functional findings (for example using dMRI to examine inter-hemispheric connections). The ovine model may help elucidate many of these questions.

Overall, this research has successfully adapted the pre-clinical rodent structural and functional pipeline for cerebrovascular disease to larger animal models. The findings of the present study parallel similar investigation in clinical stroke cohorts in terms of rs-fMRI, but more work is required to confirm the structural connectivity findings and understand the mechanistic changes that underpin structural and functional connectivity.

Chapter 6. General Discussion

6.1. Thesis outcome

The primary aim of this thesis was to develop an automated processing pipeline for non-human preclinical models that incorporates recent advances in data processing for building and evaluating representative connectomes used in human clinical studies. Though the pipeline was successful in terms of data processing, connectome building and network analysis, we found the automation posed more challenges than originally thought. This became apparent early on as software and manufacturer variations between preclinical scanners could alter image information at the conversion to NIFTI format stage. For example, the orientation information of converted scans could vary depending on the software version and the layout of the methods file associated with the sequence. For a fully automated pipeline, the need to change specific commands as a result of software updates, for example, can become impractical for the researcher that does not have a dedicated system in place for maintenance and version control. Therefore, we found the importance of a clear methodological guide that explains the optimal analysis tools for preclinical MRI research, with examples of how to use them, was far more useful. It also has wider implications for a range of researchers, including those without the expertise to update or modify an unfamiliar pipeline if subsequent problems occur. This balanced the project nicely in terms of achieving the secondary thesis aim.

The secondary thesis aim was to identify neuroimaging biomarkers in prominent animal models of cerebrovascular disease. These models not only varied in terms of animal size, but also in the pathology visible on the structural scans; ranging from distinct unilateral lesions present in the ovine MCAO, to atrophy or no clear damage in the mouse BCAS model. The BCAS mouse model demonstrated that the functional network was particularly sensitive to hypoperfusion, with clear qualitative differences present in cortical hubs and reductions in the hippocampus, retrosplenial and visual cortices. In comparison, the structural analysis displayed no qualitative direct differences in major WM regions, though an increase in connectivity was present for the hypoperfusion group, specifically in the visual association area at the 6-month post-surgery timepoint. This suggests the possibility that this region maybe attempting to compensate. These findings not only support the sensitivity of

connectome analysis in detecting subtle changes, but also indicate the ability of the preclinical pipeline to generate biomarker profiles in animal models.

The second biomarker profile developed by adapting the preclinical pipeline was in a larger model of cerebrovascular disease with prominent damage evident in the structural scans. The ovine MCAO model displayed a well-known FA reduction in the ipsilateral corticospinal tract and internal capsule at the acute phase. Analysis of the structural networks revealed additional predictable results in some individual regions. For example, the right midbrain in particular displayed a decrease in average localised connectivity at the acute phase, that continued at the chronic timepoints. This continued reduction demonstrated how graph theory measures can help locate particular vulnerable nodes and also confirm damage present at the voxelwise level, as the cortico-spinal tract was the area with the strongest reduction in the voxel-wise FA comparisons. Interestingly, other significant regions reported an inverse change in localised connectivity, with a sharp increase at the acute phase, recovering to somewhat pre-stroke levels during the chronic timepoint. Similar to the mouse model, the significant changes in functional connectivity were between specific resting-state hubs. Overall an increase in functional connectivity was present post-stroke that was confirmed by raised levels of global and localised connectivity. The biomarker profiles presented from the results of each preclinical model, indicate the pipeline's ability to generate network measures to help further profile pathology.

6.2. dMRI pipeline

When comparing our preclinical pipeline to other research groups building and investigating networks with dMRI, a wide range of similarities can be evident in addition to potential avenues for improvement and expansion. For example in high resolution scanning of *ex-vivo* mouse brains, Calabrese and colleagues (2015) used a similar combination of tools: ANTs (Avants et al., 2014) for registration and FSL (Jenkinson et al., 2012) for dMRI analysis. Some differences were present in the removal of non-brain tissue (skull-stripping) compared to our pipeline, as an automated algorithm previously described was used instead (Badea et al., 2007). This algorithm begins by spatially smoothing the structural image, allowing for a better determinate of the brain shape. Then a combination of thresholding and erosion is performed from a seed placed within the centre of the volume. Dilation of the seed mask is

introduced, and voxels containing values within the fixed threshold range are subsequently added to the brain mask. Combined with erosion at the mask edge, when completed, this process should output a mask containing only brain tissue. Whilst no code was shared, the clear explanation allows for replication using the basic MRI tools provided by FSL and ITK. Our current skull-stripping algorithm is also based on a mask, but instead required initial registration steps to bring the mask into individual subject space and being able to remove these steps could shorten the processing time. When Calabrese and colleagues (2015) benchmarked their high resolution dMRI connectome against the Allen connectome generated via neural tract tracing (Oh et al., 2014), they used injection sites as seed regions for tractography. This was performed at 3 different scales: the finest was seed-to-target voxel, the mid-range was seed to an individual brain structure, and the largest employed seed to the Allen parent region. The strongest correlations with the Allen connectome were evident at the largest scale (99% similarity). This similarity at the parent level was a major factor in this thesis for generating an Allen atlas at the parent level for future pipeline usage. Whilst benchmarking phantom simulations is a prominent feature in terms of testing dMRI tractography (Sarwar et al., 2019). Being able to benchmark dMRI tractography with high-resolution whole brain connectomes such as the Allen mouse brain connectome is a major opportunity for preclinical pipelines to compare with the 'ground-truth'.

In comparison to other preclinical dMRI pipelines, the strongest similarities were surrounding the usage of ANTs (Avants et al., 2014) for pre-processing and registration. For example, Johnson and colleagues (2019) used a similar pipeline, performed registration with ANTs, and achieved similar registration outcomes. Despite the fact that ANTS has been optimised for human brain images, it has been reported to be flexible in terms of adapting parameters to rodent brain images (Feo and Giove, 2019; Ioanas et al., 2020). The pipeline developed by Johnson and colleagues (2019) generated scalar maps using a different Diffusion Toolkit (http://trackvis.org), and connectomics analysis was performed with DSI studio (http://dsi-studio.labsolver.org/). The latter is very widely used for tractography in rodent dMRI research (Wang et al., 2018; Pervolaraki et al., 2019; Wang et al., 2020). Despite the fact that Johnson and colleagues (2019) used the normalized quantitative anisotropy (NQA) tool from the Diffusion Toolkit instead of FA for tractography, our results were similar. Interestingly, this tool has been reported to result in improved performance for deterministic tractography (Yeh et al., 2013) as NQA essentially attempts to identify less salient peaks and resolves them as crossing fibres or removes them as noise. It would be

interesting to compare the NQA value in deterministic tractography against probabilistic tractography in terms of the accuracy of the reconstructions, particularly since tractography has been heavily criticised as it can contain a large proportion of false-positive connections (Maier-Hein et al., 2016).

The current pipeline averages the tractography connectome of all individual subjects at the matrix level, meaning only end-to-end streamlines are averaged instead of the prominent tracts themselves. This is due to the inability of registration techniques to account for differences in gradient angles between subjects, and therefore unable to register average diffusion directionality. Ultimately, this results in visual tractography comparisons at an individual of each group rather than a complete group average. Yeh and colleagues (Yeh et al., 2016) have developed a technique that is able to generate group tractography averages. Termed q space diffeomorphic reconstruction (QSDR), diffusion directionality can be registered and averaged together to generate group-based tractography. Recently used in preclinical dMRI research (Allan Johnson et al., 2019; Badea et al., 2019), future dMRI pipelines could make use of such a tool to generate visually informative tractography biomarkers of group pathologies, rather than visualisations only at the individual subject level.

6.3. rs-fMRI pipeline

Similar to dMRI, a large number of rs-fMRI pipelines in preclinical literature highly vary in terms of the processing tools that are used. A large amount of the rs-fMRI pipeline adapted in this thesis was based on the recommendations described by Bajic and colleagues (2017). We replicated motion correction, spatial smoothing, single subject and group ICA processes. The differences between our pipeline and the one proposed by Bajic and colleagues (2017) were in the data pre-processing stages. For example, we found that converting the raw scanner data straight to NIFTI format required less computational steps than first converting the data to a digital imaging and communications in medicine (DICOM) format. We also preferred the improved performance and adaptability of ANTs for preclinical rodent data against the standard FSL tools designed for humans. This offered the additional advantage of not needing to upscale the data by a factor of 10, as the ANTs registration tools did not require scaling to human-like sizes.

Additional steps were also included for construction and analysis of matrices representing the functional networks. In the preclinical rs-fMRI literature, there are many different toolboxes dedicated to performing ICA. Statistical Parametric Mapping (SPM8) is primarily operated via MATLAB (MathWorks) and was widely used for a majority of earlier pipelines as it also performed well for registration and motion correction (Guilfoyle et al., 2013; Grandjean et al., 2014a; Grandjean et al., 2014b; Nasrallah et al., 2014). Group ICA of fMRI Toolbox (GIFT) (www.nitric.org/projects/gift/) was also a popular choice for generating independent components (Jonckers et al., 2011; Jonckers et al., 2014; Mechling et al., 2014) as it is generally straightforward to use. Some groups, ourselves included, have chosen FSL (Jenkinson et al., 2012) toolboxes (Sforazzini et al., 2014; Wu et al., 2017) with the addition of compatible MATLAB toolboxes that build network matrices such as FSLnets (Zerbi et al., 2015; Bukhari et al., 2017). All of these options have a variety of advantages and disadvantages. These range from the quality of the user interface to the availability of support and documentation for users with a range of expertise. Many of these tools have preferences in terms of pre-processing choices and compatibility with additional analysis tools. Some of the preclinical pipelines have used automated methods of ICA cleaning, for example, the use of machine learning tools to help classify components. One of the first studies to present hierarchy matrices in the mouse (Zerbi et al., 2015) used FSL's automatic classification tool FIX (Griffanti et al., 2014; Salimi-Khorshidi et al., 2014) to identify noise-based components in single-subject ICA. Inputting half of the total dataset as classifiers, FIX was able to successfully classify the remaining data with 100% accuracy for signal, and 98% for noise. Although this tool requires adequate training data specific to the scanner setup and model before it can be considered automatic, it again brings greater possibilities for improvement on future versions of the rs-fMRI pipeline to process high throughput datasets.

Despite all of the different acquisition and pre-processing methods, recent multicentre research comparing over 17 different datasets of mouse rs-fMRI, discovered strong similarities in spatially located networks (Grandjean et al., 2020). Whilst the majority of the datasets displayed similar networks during seed-based analysis, sedation techniques and scanning equipment also played a major role in image quality and signal-to-noise ratio (SNR). Though 'awake' (non-anaesthetized, scanner trained) mice displayed the strongest functional connectivity signal, a combination of sedatives and anesthetics, such as medetomidine and isoflurane coupled with the use of mechanical ventilation, outputted the

most prominent rodent DMN. Although the influence of anesthetic on functional connectivity has been previously been discussed, there is no research that investigates the variability of different types of processing software on pre-clinical rs-fMRI data.

6.4. Both dMRI and rs-fMRI pipelines in combination

Although preclinical studies combining both structural and functional connectivity are less frequent, one of the earliest studies to generate and analyse functional and structural connectomes together was in a transgenic mouse model (Mechling et al., 2016). Ultimately this showcased the potential of combining both structural and functional connectivity. Whilst the rs-fMRI pipeline consisted of a combination of rodent packages in SPM8 and GIFT, a MATLAB toolbox termed ICASSO (Himberg et al., 2004) was also used. ICASSO employs techniques such as bootstrapping and randomisation of different component dimensionalities to estimate an optimal number of components for ICA. Since there is high variability in ICA dimensionality between preclinical mouse studies, it would be interesting to compare this with the automatic dimensionality selection in FSL's MELODIC (Jenkinson et al., 2012) that was used in the current pipeline. Furthermore it would be interesting to explore the output components from each toolbox in the connectivity matrices to help assess the optimal dimensionality value. For dMRI, an in-house pipeline was employed, called the Fibertool package (https://www.uniklinikfreiburg.de/mren/researchgroups/postprocessing/globaltractography.html?L=) that produced dMRI scalar maps and tractography. Interestingly, like our own results, structural connectivity was preserved in the model.

More recently, a python-based rodent pipeline combining both dMRI and rs-fMRI has been published containing a thorough description of all processing stages (Pallast et al., 2019); it is termed 'atlas-based imaging data analysis of structural and functional mouse brain MRI' (AIDAmri). The overall procedures are similar to our approach with some exceptions. The AIDAmri pipeline is also capable to managing re-orientation of the images into a standard space and employs bias-field correction using the multiplicative intrinsic component optimization (MICO) tool. In the publication, the MICO tool was compared against the popular and widely used N4 bias-field correction tool (Tustison et al., 2010). For T_2-weighted and dMRI images, MICO outperformed the N4 bias-field correction tool in terms of the degree of signal homogeneity and the coefficient variance throughout the image. Once the

bias-field correction is complete, an initial up-scale by a factor of 10 is applied to the header information of each scan to prepare the images for skull stripping with FSL's BET tool (Jenkinson et al., 2012) and a robust iterative estimation of the brain centre to successfully remove non-brain tissue. Registration is applied to ultimately align all scans with the ALLEN atlas using a multi-step process of linear and non-linear registrations similar to what was used in this thesis but using the NiftyReg tool (Modat et al., 2010) instead. Throughout the paper, a selection of registration tools were compared (ANTs (Avants et al., 2008), FSL (Jenkinson et al., 2012) and elastiX (Klein et al., 2010)), and the authors concluded that NiftyReg provided the most accurate alignments. For dMRI data, the AIDAmri pipeline ran FSLs MCFLIRT (Jenkinson et al., 2002) to correct for motion, using the option to split each dataset into segments, for correction before merging the motion corrected segments back together. DSI-studio (Yeh et al., 2013) was used for scalar map generation and deterministic tractography to generate structural connectomes. For the rs-fMRI pipeline, tools from the FSL library (Jenkinson et al., 2012), such as; SliceTimer and FEAT (Woolrich et al., 2001) were employed for slice timing correction, spatial smoothing, and application of a standard high-pass filter with frequency of 0.01 Hz. In order to build the functional connectome, nodes represented the average timeseries and edges were the correlations between them. The AIDAmri (Pallast et al., 2019) pipeline offers several future opportunities to compare methodology with the current pipeline in order to find optimal processing steps for preclinical data. This could involve running simple comparisons of registration and skull-stripping techniques or assessing the effectiveness of the additional processing steps included in the current pipeline that were not included in AIDAmri. For example, we employed the Bedpostx tool (Jbabdi et al., 2012) for dMRI tractography, which is superior for resolving of crossing fibres. Though the resolution may be lacking in vivo to obtain this detail, it would be interesting to know whether deterministic versus probabilistic tractography can result in the same structural connectome. Methods of connectome building could also be examined. Whether the use of atlas-based seeding of regions would provide different information than if nodes were identified using components generated from ICA instead.

In addition to the tools already discussed, future updates of the pipeline could also include area under the curve (AUC) statistics for assessing optimal small worldness thresholds of connectomes. Previously employed in preclinical mouse research (Kesler et al., 2018), this method could be particularly effective when thresholding dense matrices where slight changes in thresholding could heavily influence connectivity.

6.5. Conclusion

In conclusion, the primary and secondary aims of the thesis were achieved. The pipeline was successfully implemented, though further research is still required to evaluate a wide range of tools before an optimum pipeline for preclinical use can be identified. In addition, standardisation in preclinical research could be encouraged to allow better comparability across studies – this may be more useful once optimal strategies have been widely assessed and explained. The developed pipeline has effectively allowed characterisation of structural and functional changes in 2 different animal models of cerebrovascular disease: VCI in the mouse and stroke in the sheep.

Appendix A. Scripts

Below are the exact scripts used for each processing step in Terminal. The sections that require individual user specific information (i.e., input or output file directories and options) are listed within the '<' '>' symbols. All scripts were ran in the Terminal program on a iMac (Retina 4K, 21.5-inch, 2017) running on a Catalina operating system (3 GHz Quad-Core Intel Core i5). Toolbox versions, ANTs: 2.3.5, FSL: 6.0.0, BCT: 2017-15-01.

A.1. Pre-processing steps

A.1.1. Data conversion (Br2Nii, Bruker2Nifti, Dcn2niiX)

Paravision 5:

```
./Bru2 -a -p -o <Output_Subject_Path> <Input_Subject_Path>
```

Paravision 6:

```
bruker2nifti -i <Input_Subject_Path> -o <Output_Directory> -
study_name <Overall_Study_Name>
```

DICOM:

```
dcm2niix -z y -f %p -o <Output_Path> <DICOM folder pathway>
```

Note: Bru2 (for Paravision 5) program uses an executable file, therefore it is important that the user is in the correct directory when using the script.

A.1.2. Orientation deletion, change and confirmation (FSL)

Orientation Deletion:

```
fslorient -deleteorient <Input_Imagename.nii.gz>
```

Note: This will delete the input image, therefore it is always useful to make a backup image copy first, before deleting the original orientation.

Changing Orientation:

```
fslswapdim <Input_Imagename.nii.gz> x y z <Output_Imagename.nii.gz>
```

Note: The x y z are the orientation options that can be reordered (e.g., y z x), for example if sagittal is labelled in the coronal plane. Furthermore, the x y z option can be inversed to flip the orientation (e.g., x -y z), if the axial anterior posterior direction requires flipping.

Setting the changed orientation labels:

```
fslorient -setqformcode 1 <Input_Imagename.nii.gz>
```

Note: Sets the changed orientation information into the display settings

A.1.3. Structural template creation (ANTs)

Creating template from individual non-registered T2 weighted images:

```
antsMultivariateTemplateConstruction2.sh -d 3 -o
<Output_directory_name> <Input_images> or <Input_'.csv'_list>
```

Note: The first option ('-d') selects the dimensionality of the input images, since all the structural MRI images we used were 3-D, this option was set to 3. The information after the ('-o') option flag is the name of the directory that will contain the template image (usually template image name ends with '_template0.nii.gz'). The input images can be the images input one by one, or instead a .csv list that contains all the input directories of each image.

A.1.4. Bias correction (ANTs)

Bias Correction

```
N4BiasFieldCorrection -d <Input_dimensionality> -i
<Input_image.nii.gz> -o <Output_image.nii.gz>
```

Note: Again, the first option ('-d') selections the dimensionality of the input images (e.g., single structural image would be set to 3, rs-fMRI timeseries would be set to 4).

A.1.5. Skull stripping (ANTs & FSL)

Registration of individual subject structural image to study generated template:

```
antsRegistrationSyN.sh -d 3 -f <Subject_template_T2.nii.gz> -m
<Subject_image_T2.nii.gz> -o <Subject_template_output_>
```

Registration of study generated template to Allen template:

```
antsRegistrationSyN.sh -d 3 -f <Allen_Template.nii.gz> -m
<Subject_Template_T2.nii.gz> -o <SubjectTemp_AllenSpace_Output_> -x
<ALLEN_Grey+WM_Mask.nii.gz>
```

Moving the mask of the Allen template into the subject template space:

```
antsApplyTransforms -d 3 -i <Allen_mask.nii.gz> -r
<Subject_template_T2.nii.gz> -o <Subject_template_T2_mask.nii.gz> -n
MultiLabel -t [<SubjectTemp_AllenSpace_Output_0GenericAffine.mat,1]>
-t <SubjectTemp_AllenSpace_Output_1InverseWarp.nii.gz>
```

Moving the mask of the Allen template space into the individual subject space:

```
antsApplyTransforms -d 3 -i <Subject_Template_T2_mask.nii.gz> -r
<Subject_Image_T2.nii.gz> -o <Subject_Image_T2_mask.nii.gz> -n
MultiLabel -t <[Subject_Temmplate_Output_0GenericAffine.mat,1]> -t
<Subject_Temmplate_Output_1InverseWarp.nii.gz>
```

Skull stripping the individual structural T2 images:

```
fslmaths <Subject_Image_T2.nii.gz> -mul
<Subject_Image_T2_Mask.nii.gz> <Subject_Image_T2_Stripped.nii.gz>
```

Note: During the study template registration, due to differing tissue contrasts between the Allen and study template, a combined grey and WM tissue mask was used to ignore the CSF regions at registration.

A.2. rs-fMRI pipeline

A.2.1. Unwarp EPI data (FSL)

Changing the fieldmap from Hz to rad/s (Ovine):

```
fsl_prepare_fieldmap SIEMENS <Phase_image.nii.gz>
<Magnitude_image.nii.gz> <Output_image> <2.46>
```

Unwarping of the EPI images using the T1 image and fieldmap (Ovine):

```
epi_reg --epi=<dMRI_data.nii.gz> --t1=<T1w_image> --
t1brain=<Extracted_T1_image> --out=<Unwarped_Output> --
```

```
fmap=<Prepared_fieldmap.nii.gz> --
fmapmag=<Magnitude_of_fieldmap.nii.gz> --
fmapmagbrain=<Skull_stripped_magnitude_of_fieldmap.ii.gz> --
echospacing=<0.448> --pedir=<-y> -v
```

Changing the fieldmap from Hz to rad/s (rodent):

```
fslmaths <fieldmap_Hz.nii.gz> -mul 6.28 <fieldmap_rads.nii.gz>
```

Smoothing the fieldmap (rodent):

```
fugue --loadfmap=<fieldmap_rads.nii.gz> -s <1> --
savefmap=<fieldmap_rads_smoothed.nii.gz>
```

Despiking the fieldmap (rodent):

```
fugue --loadfmap=<fieldmap_rads_smoothed.nii.gz> --despike
savefmap=<fieldmap_rads_smoothed_despike.nii.gz>
```

Median filter of the fieldmap (rodent):

```
fugue --loadfmap=<fieldmap_rads_smoothed_despike.nii.gz> -m
savefmap=<fieldmap_rads_smoothed_despike_filtered.nii.gz>
```

Unwarping the EPI image (rodent):

```
fugue -i <EPI_timeseries.nii.gz> --dwell=<0.448>
loadfmap=<fieldmap_rads_smoothed_despike_filtered.nii.gz> -u
<Unwarped_EPI_timeseries.nii.gz>
```

Note: Before unwarping the data, the fieldmap usually needs processing to change the units to radians per second and remove potential sharp signal spikes that may make the process fail. The reason why the ovine data was different, was due to the presence of a $T1_w$ structural image meant the 'epi_reg' tool could be used.

A.2.2. rs-fMRI mask creation and skull stripping (ANTs & FSL)

Extracting a single 3D image from the 4D stack for resampling:

```
fslroi <rs-fMRI_Timeseries.nii.gz> <single_rs-fMRI_volume.nii.gz>
<0> <1>
```

Resampling the mask in subject T_2 weighted space into EPI space:

```
antsApplyTransforms -d 3 -i <Subject_Structural_Mask.nii.gz> -r
<Single_rs-fMRI_volume.nii.gz> -o <Subject_rs-fMRI_mask.nii.gz> -n
MultiLabel
```

Note: As a 4D dataset cannot be used during the resampling process, therefore an EPI volume is first removed from the dataset. During the resampling stage the '-r' option is the resolution we want to resample too, also the multi label interpolation option keeps the mask in a binary state (preserving all integers).

A.2.3. Motion, slice timing (FSL)

Motion correction:

```
mcflirt -in=<Input_file_name.nii.gz> -out=<Output_file_name.nii.gz>
```

Slice timing correction:

```
slicetimer -i <Input_file_name.nii.gz> -r 1 -d y --odd -o
<Output_file_name.nii.gz>
```

Note: Slice timing correction is set to interleaved order.

A.2.4. Single subject ICA (FSL)

```
melodic -i <Subject_rs-fMRI_timeseries.nii.gz> -o
<Subject_rs_fMRI_output> -m <rs-fMRI_mask.nii.gz> --report --nobet -
-tr=<1> -v
```

Note: This is ran for every individual subject. The dimensionality flag '-d' is not set, therefore automatic dimensionality is selected.

A.2.5. Single subject component cleaning (FSL)

Opening FSLeyes melodic view for single subject cleaning:

```
fsleyes --scene melodic -ad <filtered_func_data.ica>
```

Opening the list generated through the classification stage:

```
tail -1 <labels>
```

Regressing out the artefactual components:

```
fsl_regfilt -I <filtered_func_data.nii.gz> -d <melodic_mix> -o
<output.nii.gz> -f "<List_output_from_tail_command e.g., 1, 3, 7,
12>"
```

Note: After all the components are classified, then it is important to save the list, or the classification will be lost. The output generated from the 'tail' stage just contains the components selected to regress out of the data.

A.2.6. rs-fMRI timeseries registration (FSL & ANTs)

Extraction of single volume from rs-fMRI timeseries:

```
fslroi <rs-fMRI_timeseries.nii.gz> <rs-fMRI_output_volume> 0 1
```

Registration of that single volume to the selected space (M001 in this example):

```
antsRegistrationSyN.sh -d 3 -f <M001_rs-fMRI_volume.nii.gz> -m <rs-
fMRI_output_volume> -o <Registered_rs-fMRI_volume>
```

Applying the transformation of the registration to the whole subject rs-fMRI timeseries:

```
antsApplyTransforms -d 3 -e 3 -i <rs-fMRI_timeseries.nii.gz> -r <
Registered_rs-fMRI_volume.nii.gz> -o <Output_registered_rs-
fMRI_timeseries.nii.gz> -n NearestNeighbor -t <[Registered_rs-
fMRI_volume_0GenericAffine.mat,0]> -t <Registered_rs-
fMRI_volume_1InverseWarp.nii.gz>
```

Note: Since the complete 4D timeseries cannot be directly registered, we extracted a single volume, registered it to the common space for analysis, and then applied the transformation to the whole timeseries with the nearest neighbour interpolation to best preserve the data throughout the applied transformation.

A.2.7. Smoothing EPI data (FSL)

```
fslmaths <Input_image_name.nii.gz> -s <0.7>
<Output_image_name.nii.gz>
```

Note: The number after the '-s' flag is the smoothing kernel in mm.

A.2.8. Group level ICA (FSL)

```
melodic -i <file_pathways_of_input_images.txt> -o
<output_directory_name> --tr=1 --nobet -a concat --report -v
```

Note: The '.txt' file just contains all the pathways of the pre-processed rs-fMRI timeseries, if we wanted to select a set dimensionality then the '-d' flag would be used.

A.2.9. Component analysis (FSL)

```
dual_regression <group_IC_spatial_maps.nii.gz> 1 <GLM_pathway.mat>
<GLM_pathway.con> <5000> <output_directory> grot `cat pathways.txt`
```

Note: The stage 3 'DR_stage_3' of the dual regression output contains the t-stat differences and the p-vals 'corrp'. 5000 is the number of random permutations to be ran, this number is generally considered acceptable.

A.3. dMRI pipeline

A.3.1. EPI unwarping (FSL)

If a B0 was collected with an opposite B0 phase encoding direction then follow step would be attempted, if not, then we would unwarp with tools explained in A.2.1:

Creating the fieldmap:

```
topup --imain=<Both_B0_images.nii.gz> --datain=<acqp_info.txt> --
config=b02b0.cnf --out=<Topup_Output>
```

Unwarping to test the correction in a single 3D image:

```
applytopup --imain=<B0_normal.nii.gz,B0_reverse.nii.gz> --
inindex=2,1 --datatin=acq_info.txt --topup=<Topup_Output> --
out=<Output_Unwarped_Image>
```

Note: The actual correction to the dMRI timeseries was applied during the eddy step. The 'applytopup' step was a check to see if the unwarping was successful on the B0 images.

A.3.2. Motion and eddy correction (FSL)

```
eddy --imain=<dMRI_data_input.nii.gz> --mask=<Mask_EPI_space>
--index=<index_of_volumes.txt> --acqp=<scanning_parameters_file.txt>
--bvecs=<bvecs.txt> --bvals=<bvals.txt> --out=<Output_Directory>
```

If fieldmap was collected using Topup:

```
eddy --imain=<dMRI_data_input.nii.gz> --mask=<Mask_EPI_space>
--index=<index_of_volumes.txt> --acqp=<scanning_parameters_file.txt>
--bvecs=<bvecs.txt> --bvals=<bvals.txt> --out=<Output_Directory> --
topup=<Prefix_Topup_names>
```

A.3.3. dMRI mask creation and skull stripping (FSL & ANTs)

Exact same as the rs-fMRI process specified in A.2.2.

A.3.4. Remove B0 image and average (FSL)

Removal of B0 images from the 4D dataset:

```
fslroi <dMRI_data.nii.gz> <B0_only.nii.gz> <0> <5>
```

Averaging the B0s together to generate one B0 image for each subject:

```
fslmaths <B0_only.nii.gz> -Tmean <Average_B0_only.nii.gz>
```

Note: In this example the first 5 were removed, counting begins at 0 not 1 however. Then subsequent B0 images were averaged together '-Tmean'.

A.3.5. Creating B0 template (ANTs)

```
antsMultivariateTemplateConstruction2.sh -d 3 -o
<Output_directory_name> <Input_B0_images> or <input_'.csv'_list>
```

Note: Similar script used previously, just inputting the B0 images instead for probabilistic tractography alignment.

A.3.6. Tensor fitting and making scalar maps (FSL)

```
dtifit --data=<dMRI_data.nii.gz> --out=<Output_Prefix> --
mask=<Mask_EPI_space.nii.gz> --bvecs=<b_vector.txt> --
bvals=<b_value.txt>
```

Note: This will output all the scalar maps for subsequent TBSS analysis.

A.3.7. Creating FA template (ANTs)

```
antsMultivariateTemplateConstruction2.sh -d 3 -o
<Output_directory_name> <Input_FA_images> or <input_'.csv'_list>
```

A.3.8. TBSS scripts (FSL)

Erosion of brain edges and end slices (TBSS stage 1):

```
tbss_1_preproc <Input_FA_Image_Subject_1>
```

Registration and creating mask and mean FA images (replacement of TBSS stage 2 and 3):

```
antsRegistrationSyN.sh -d 3 -f <FA_Template.nii.gz> -m
<Individual_Subject_FA.nii.gz> -o <Registered_Subject_FA_>

fslmerge -t all_FA <Input_FA_Image_Subject_1>
<Input_FA_Image_Subject_2>...

fslmaths <all_FA.nii.gz> -max 0 -Tmin -bin <mean_FA_mask> -odt char

fslmaths <all_FA.nii.gz> -mas <mean_FA_mask.nii.gz> <all_FA>
```

```
fslmaths <all_FA.nii.gz> -Tmean <mean_FA>
```

Thresholding FA images (TBBS stage 4):

```
tbss_4_prestats <0.3>
```

Note: Specific naming is important for stage 4 and randomise steps, therefore outputs (i.e., during the fslmerge and fslmaths stages) were kept to the same naming output from TBSS stage 2 and 3.

A.3.9. Voxelwise analysis of TBSS skeletons (FSL)

```
randomise -i <all_FA_skeletonised> -o <tbss_analysis> -m
<mean_FA_skeleton_mask> -d <design.mat> -t <design.con> -n 500 --T2
-v
```

Note: Similar to the output of the dual-regression, this outputs the t-stat and p-value spatial maps indicating potential significant differences.

A.3.10. Registration of B0 images (ANTs)

```
antsRegistrationSyN.sh -d 3 -f <B0_Template.nii.gz> -m
<Subject_B0_Average.nii.gz> -o <Registered_Subject_B0_>
```

Note: Registering the individual subject average B0 images to a template for tractography analysis.

A.3.11. Local modelling of diffusion parameters (FSL)

```
bedpostx <dMRI_subject_directory>
```

Note: The bedpostx command is simple to call, however it is name sensitive, therefore the dMRI files should be named correctly. The required names are as follows: dMRI file ‘data.nii.gz’, an associated mask named ‘nodif_brain_mask.nii.gz, and b-vector and b-value information in a text file format named ‘b-vecs’ and ‘b-vals’ respectively.

A.3.12. Probabilistic tractography (FSL)

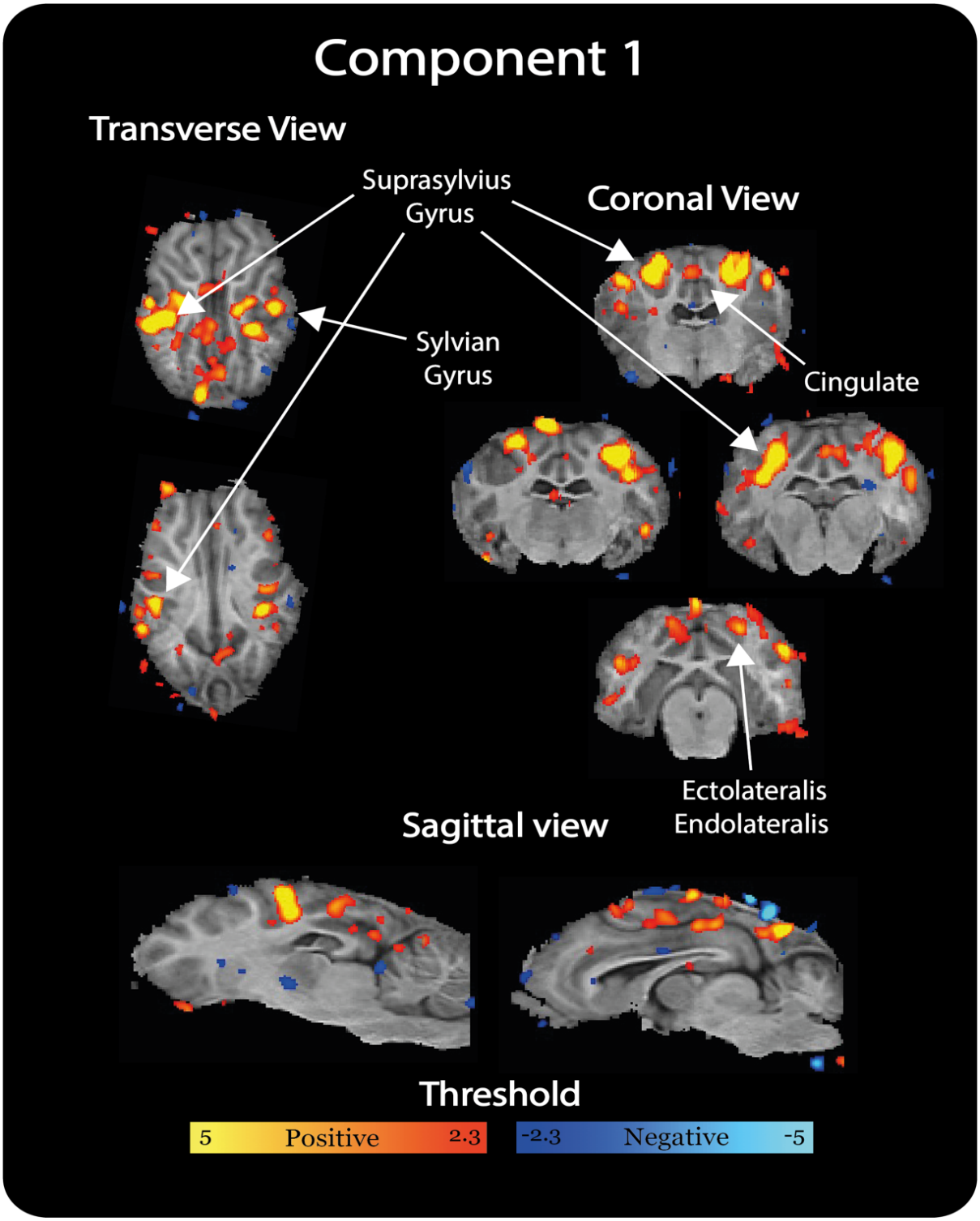
```
Probtrackx2 –s <bedpost_subject_directory> –m
<brain_mask_EPI_space.nii.gz> –x <File_containing_
Atlas_Pathways.txt> ––network –l ––onewaycondition –c 0.60 –
steplength=0.113 ––opd ––forcedir –dir=<Output_Directory> ––omatrix1
–distthresh1=0.5 ––savepaths ––opathdir
```

Note: The '--network' option will only keep streamlines running to other atlas regions. The output of this call should generate a text file 'fdt_network_matrix' containing the matrix ready to be imported into MATLAB for graph theory analysis.

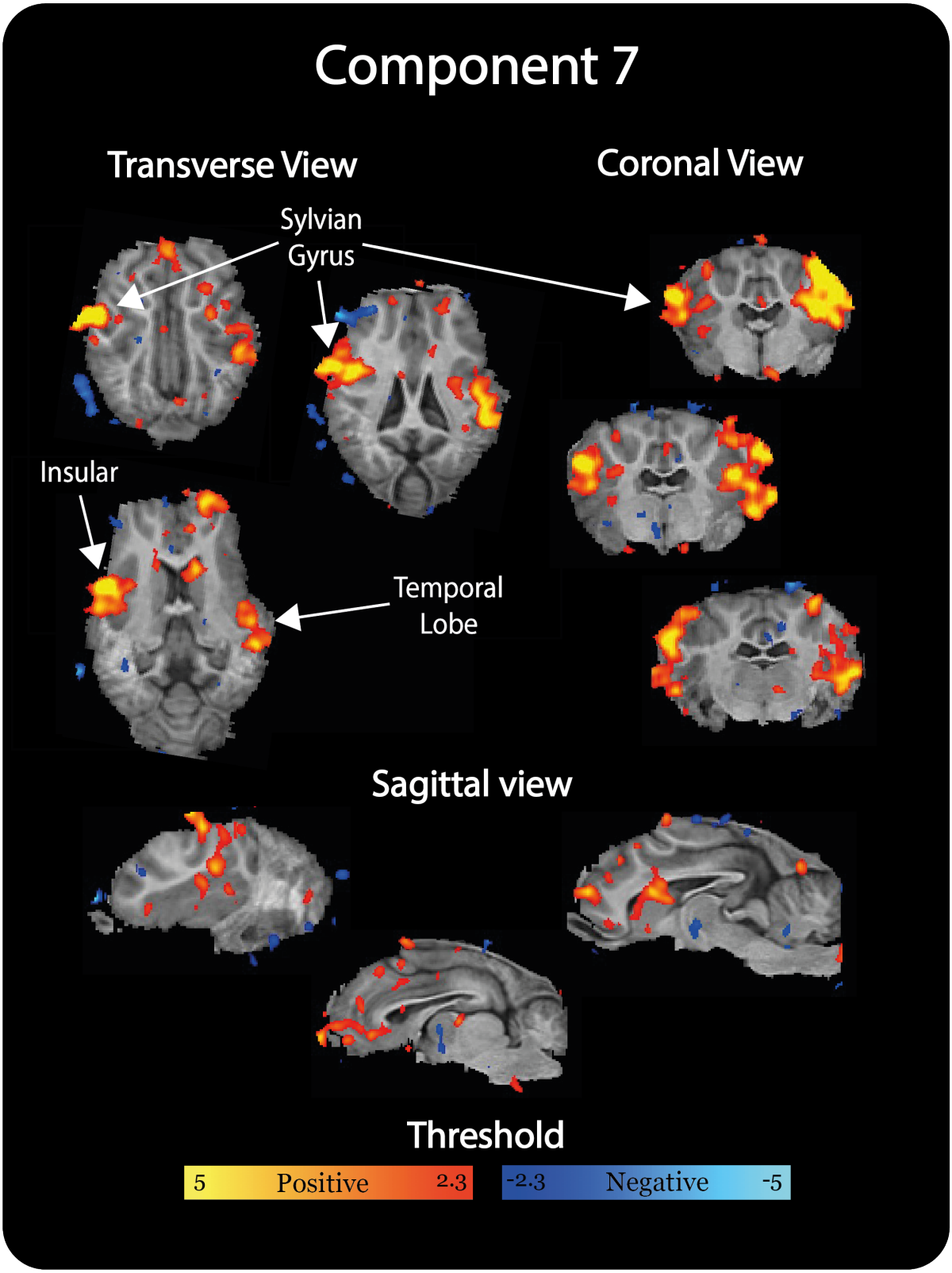
Appendix B. Ovine resting state components

Below are the ovine resting-state components classified as neurally driven signal or at least a mix of signal with noise. Components were generated from the pre-stroke group (n = 21) using MELODIC set at automatic dimensionality.

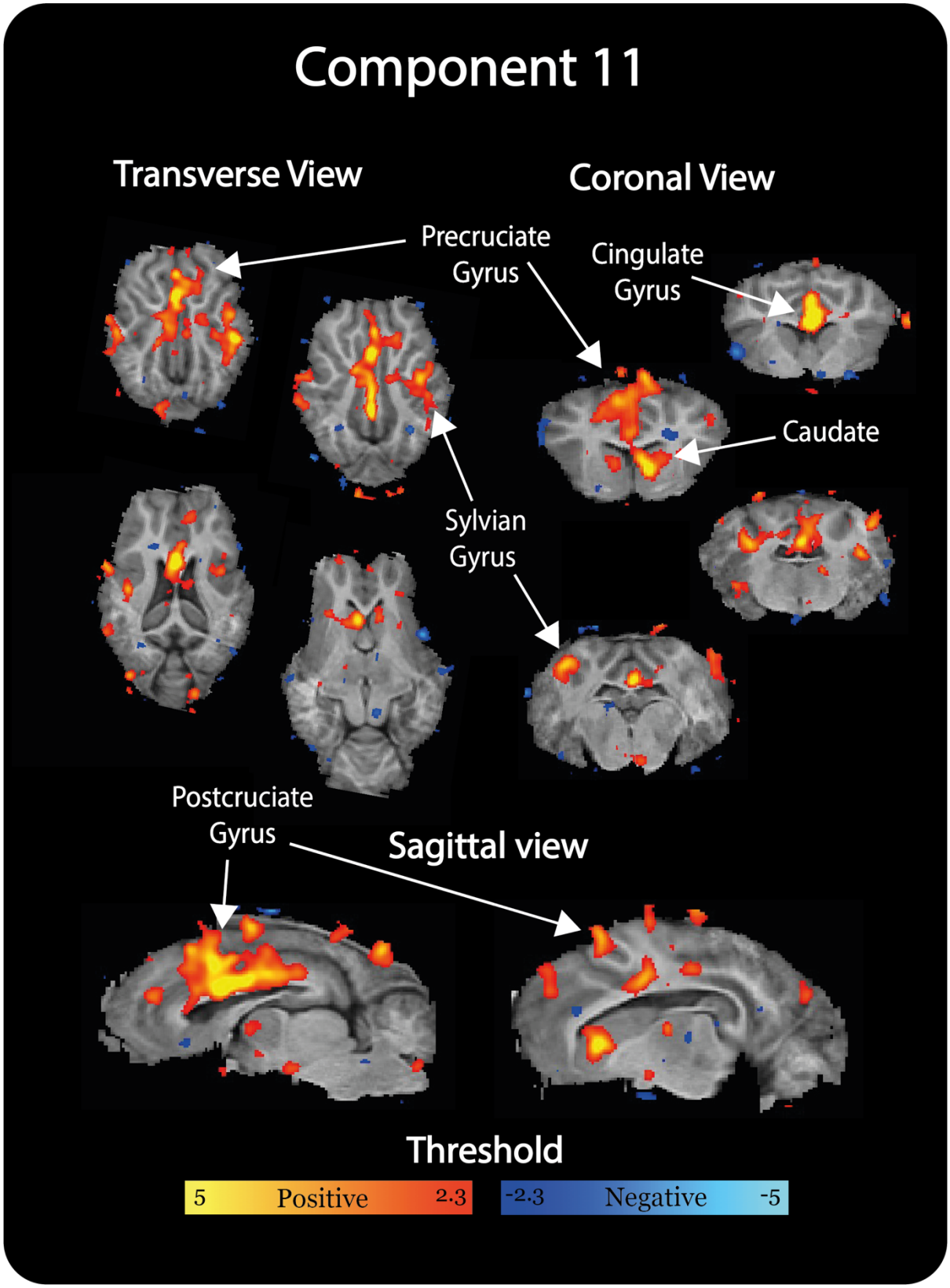
B.1. Ovine Component 1: Sensory, visual network



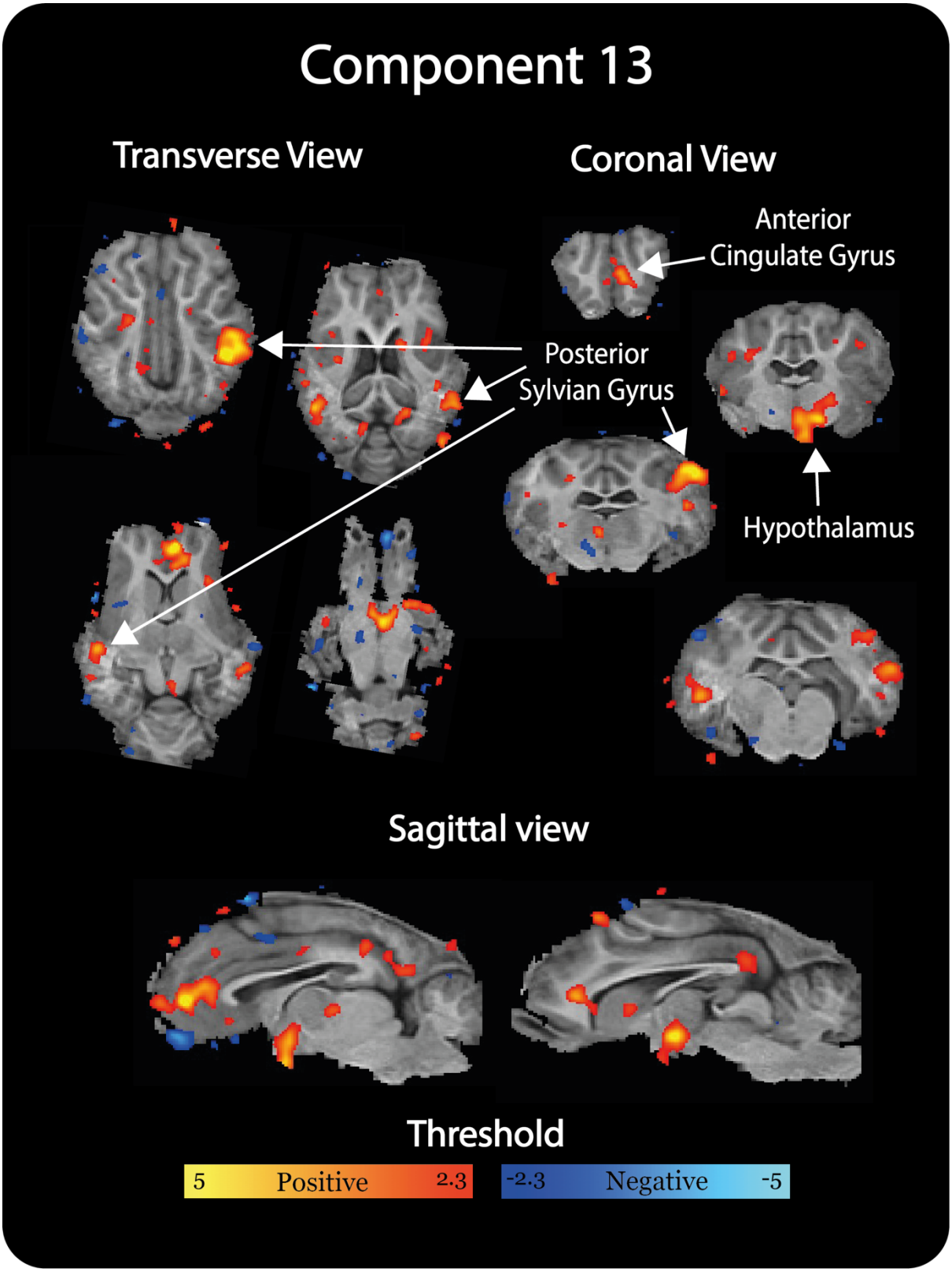
B.2. Ovine Component 7: Sensory, memory network



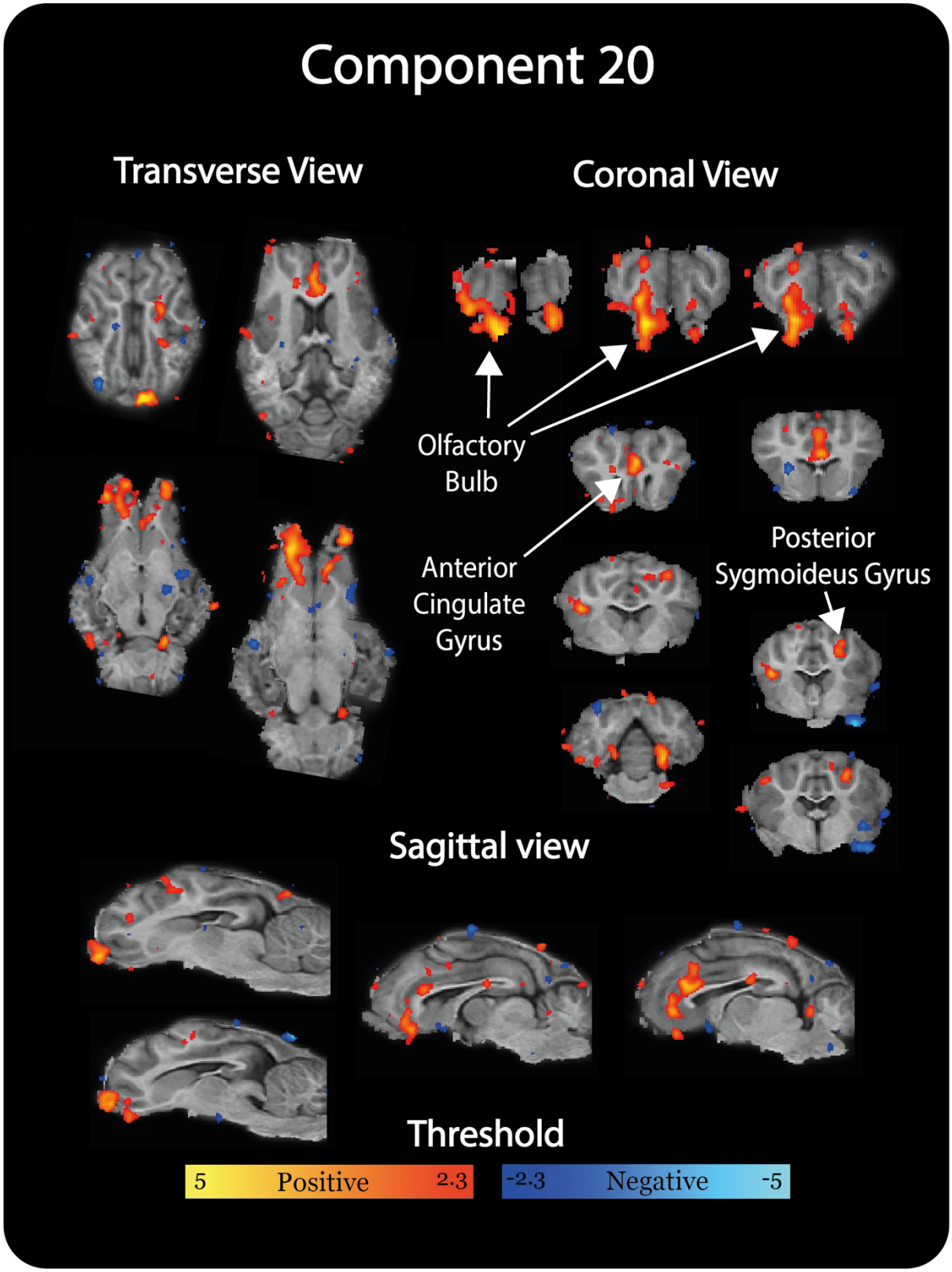
B.3. Ovine Component 11: Potential DMN



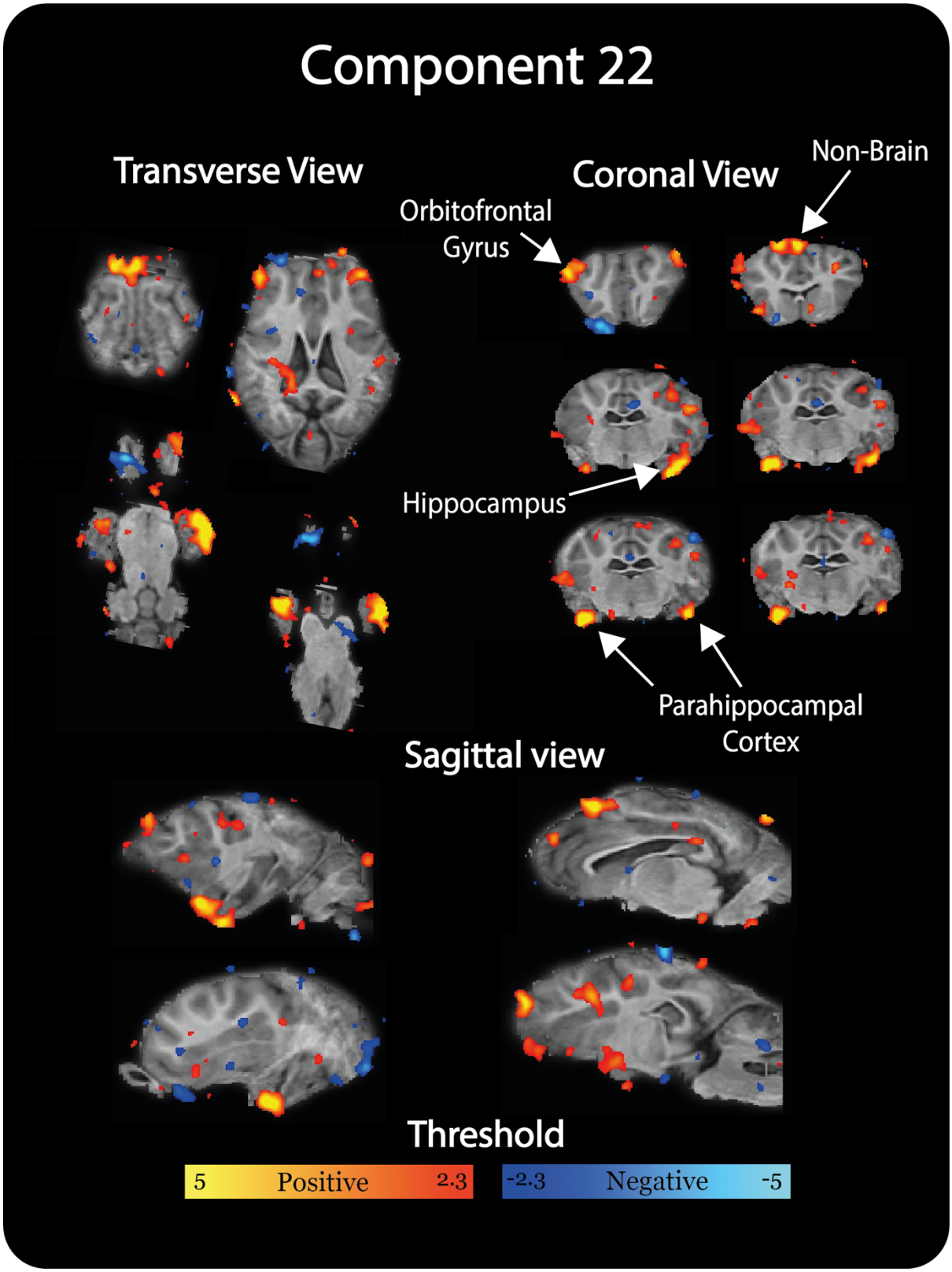
B.4. Ovine Component 13: Unclear functional association



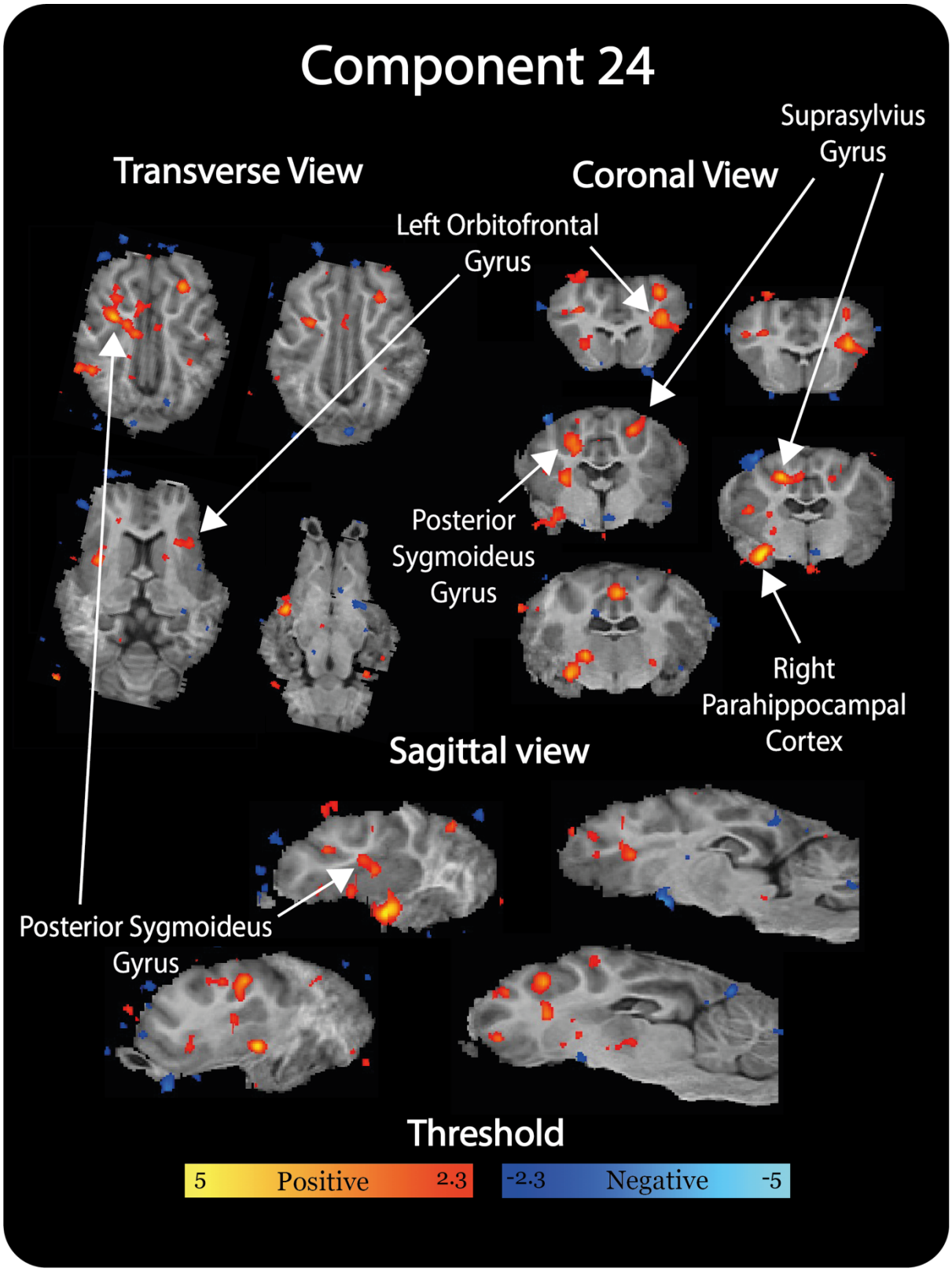
B.5. Ovine Component 20: Unclear functional association



B.6. Ovine Component 22: Unclear functional association



B.7. Ovine Component 24: Unclear functional association



References

Alegiani AC, MacLean S, Braass H, Siemonsen S, Gerloff C, Fiehler J, Cho T-H, Derex L, Hermier M, Berthezene Y (2017) Comprehensive analysis of early fractional anisotropy changes in acute ischemic stroke. PloS one 12:e0188318.

Alexander AL, Lee JE, Lazar M, Field AS (2007) Diffusion tensor imaging of the brain. Neurotherapeutics 4:316-329.

Allan Johnson G, Wang N, Anderson RJ, Chen M, Cofer GP, Gee JC, Pratson F, Tustison N, White LE (2019) Whole mouse brain connectomics. J Comp Neurol 527:2146-2157.

Allen EA et al. (2011) A baseline for the multivariate comparison of resting-state networks. Front Syst Neurosci 5:2.

Alsop DC, Dai W, Grossman M, Detre JA (2010) Arterial spin labeling blood flow MRI: its role in the early characterization of Alzheimer's disease. J Alzheimers Dis 20:871-880.

Alves GS, de Carvalho LA, Sudo FK, Briand L, Laks J, Engelhardt E (2017) A panel of clinical and neuropathological features of cerebrovascular disease through the novel neuroimaging methods. Dement Neuropsychol 11:343-355.

Andersen SM, Rapcsak SZ, Beeson PM (2010) Cost function masking during normalization of brains with focal lesions: still a necessity? Neuroimage 53:78-84.

Andersson JL, Sotiropoulos SN (2016) An integrated approach to correction for off-resonance effects and subject movement in diffusion MR imaging. Neuroimage 125:1063-1078.

Andersson JL, Skare S, Ashburner J (2003) How to correct susceptibility distortions in spin-echo echo-planar images: application to diffusion tensor imaging. Neuroimage 20:870-888.

Anstey KJ, Cherbuin N, Budge M, Young J (2011) Body mass index in midlife and late-life as a risk factor for dementia: a meta-analysis of prospective studies. Obes Rev 12:e426-437.

Appleton JP, Scutt P, Sprigg N, Bath PM (2017) Hypercholesterolaemia and vascular dementia. Clin Sci (Lond) 131:1561-1578.

Avants BB, Epstein CL, Grossman M, Gee JC (2008) Symmetric diffeomorphic image registration with cross-correlation: evaluating automated labeling of elderly and neurodegenerative brain. Med Image Anal 12:26-41.

Avants BB, Tustison NJ, Song G, Cook PA, Klein A, Gee JC (2011) A reproducible evaluation of ANTs similarity metric performance in brain image registration. Neuroimage 54:2033-2044.

Avants BB, Tustison NJ, Stauffer M, Song G, Wu B, Gee JC (2014) The Insight ToolKit image registration framework. Front Neuroinform 8:44.

Badea A, Ali-Sharief AA, Johnson GA (2007) Morphometric analysis of the C57BL/6J mouse brain. Neuroimage 37:683-693.

Badea A, Wu W, Shuff J, Wang M, Anderson RJ, Qi Y, Johnson GA, Wilson JG, Koudoro S, Garyfallidis E, Colton CA, Dunson DB (2019) Identifying Vulnerable Brain Networks in Mouse Models of Genetic Risk Factors for Late Onset Alzheimer's Disease. Front Neuroinform 13:72.

Bajic D, Craig MM, Mongerson CRL, Borsook D, Becerra L (2017) Identifying Rodent Resting-State Brain Networks with Independent Component Analysis. Front Neurosci 11:685.

Baldassarre A, Ramsey LE, Siegel JS, Shulman GL, Corbetta M (2016) Brain connectivity and neurological disorders after stroke. Curr Opin Neurol 29:706-713.

Baliki MN, Mansour AR, Baria AT, Apkarian AV (2014) Functional reorganization of the default mode network across chronic pain conditions. PLoS One 9:e106133.

Bastin ME, Rana AK, Wardlaw JM, Armitage PA, Keir SL (2000) A study of the apparent diffusion coefficient of grey and white matter in human ischaemic stroke. Neuroreport 11:2867-2874.

Bastin ME, Clayden JD, Pattie A, Gerrish IF, Wardlaw JM, Deary IJ (2009) Diffusion tensor and magnetization transfer MRI measurements of periventricular white matter hyperintensities in old age. Neurobiol Aging 30:125-136.

Batty GD, Shipley MJ, Kvaavik E, Russ T, Hamer M, Stamatakis E, Kivimaki M (2018) Biomarker assessment of tobacco smoking exposure and risk of dementia death: pooling of individual participant data from 14 cohort studies. J Epidemiol Community Health.

Beckmann CF, Smith SM (2004) Probabilistic independent component analysis for functional magnetic resonance imaging. IEEE Trans Med Imaging 23:137-152.

Beckmann CF, Mackay CE, Filippini N, Smith SM (2009) Group comparison of resting-state FMRI data using multi-subject ICA and dual regression. Neuroimage 47:S148.

Behrens TE, Berg HJ, Jbabdi S, Rushworth MF, Woolrich MW (2007) Probabilistic diffusion tractography with multiple fibre orientations: What can we gain? Neuroimage 34:144-155.

Biesbroek JM, Leemans A, den Bakker H, Duering M, Gesierich B, Koek HL, van den Berg E, Postma A, Biessels GJ (2017) Microstructure of Strategic White Matter Tracts and Cognition in Memory Clinic Patients with Vascular Brain Injury. Dement Geriatr Cogn Disord 44:268-282.

Bijsterbosch J, Smith SM, Beckmann CF (2017) Introduction to resting state fMRI functional connectivity: Oxford University Press.

Bink DI, Ritz K, Aronica E, van der Weerd L, Daemen MJ (2013) Mouse models to study the effect of cardiovascular risk factors on brain structure and cognition. J Cereb Blood Flow Metab 33:1666-1684.

Biswal B, Yetkin FZ, Haughton VM, Hyde JS (1995) Functional connectivity in the motor cortex of resting human brain using echo-planar MRI. Magn Reson Med 34:537-541.

Boehm-Sturm P, Fuchtemeier M, Foddis M, Mueller S, Trueman RC, Zille M, Rinnenthal JL, Kypraios T, Shaw L, Dirnagl U, Farr TD (2017) Neuroimaging Biomarkers Predict Brain Structural Connectivity Change in a Mouse Model of Vascular Cognitive Impairment. Stroke 48:468-475.

Boltze J, Nitzsche F, Jolkkonen J, Weise G, Posel C, Nitzsche B, Wagner DC (2017) Concise Review: Increasing the Validity of Cerebrovascular Disease Models and Experimental Methods for Translational Stem Cell Research. Stem Cells 35:1141-1153.

Bowler JV (2007) Modern concept of vascular cognitive impairment. Br Med Bull 83:291-305.

Bucur B, Madden DJ, Spaniol J, Provenzale JM, Cabeza R, White LE, Huettel SA (2008) Age-related slowing of memory retrieval: contributions of perceptual speed and cerebral white matter integrity. Neurobiol Aging 29:1070-1079.

Bukhari Q, Schroeter A, Rudin M (2018) Increasing isoflurane dose reduces homotopic correlation and functional segregation of brain networks in mice as revealed by resting-state fMRI. Sci Rep 8:10591.

Bukhari Q, Schroeter A, Cole DM, Rudin M (2017) Resting State fMRI in Mice Reveals Anesthesia Specific Signatures of Brain Functional Networks and Their Interactions. Front Neural Circuits 11:5.

Bullmore E, Sporns O (2009) Complex brain networks: graph theoretical analysis of structural and functional systems. Nat Rev Neurosci 10:186-198.

Buzsaki G, Logothetis N, Singer W (2013) Scaling brain size, keeping timing: evolutionary preservation of brain rhythms. Neuron 80:751-764.

Calabrese E, Badea A, Cofer G, Qi Y, Johnson GA (2015) A Diffusion MRI Tractography Connectome of the Mouse Brain and Comparison with Neuronal Tracer Data. Cereb Cortex 25:4628-4637.

Camandola S, Mattson MP (2017) Brain metabolism in health, aging, and neurodegeneration. EMBO J 36:1474-1492.

Carter AR, Astafiev SV, Lang CE, Connor LT, Rengachary J, Strube MJ, Pope DL, Shulman GL, Corbetta M (2010) Resting interhemispheric functional magnetic resonance imaging connectivity predicts performance after stroke. Annals of neurology 67:365-375.

Chang TY, Huang KL, Ho MY, Ho PS, Chang CH, Liu CH, Chang YJ, Wong HF, Hsieh IC, Lee TH, Liu HL (2016) Graph theoretical analysis of functional networks and its relationship to cognitive decline in patients with carotid stenosis. J Cereb Blood Flow Metab 36:808-818.

Chao LL, Buckley ST, Kornak J, Schuff N, Madison C, Yaffe K, Miller BL, Kramer JH, Weiner MW (2010) ASL perfusion MRI predicts cognitive decline and conversion from MCI to dementia. Alzheimer Dis Assoc Disord 24:19-27.

Chen H, Zhao Y, Zhang T, Zhang H, Kuang H, Li M, Tsien JZ, Liu T (2014) Construct and assess multimodal mouse brain connectomes via joint modeling of multi-scale DTI and neuron tracer data. Med Image Comput Comput Assist Interv 17:273-280.

Chen H, Liu T, Zhao Y, Zhang T, Li Y, Li M, Zhang H, Kuang H, Guo L, Tsien JZ, Liu T (2015) Optimization of large-scale mouse brain connectome via joint evaluation of DTI and neuron tracing data. Neuroimage 115:202-213.

Chen HJ, Gao YQ, Che CH, Lin H, Ruan XL (2018) Diffusion Tensor Imaging With Tract-Based Spatial Statistics Reveals White Matter Abnormalities in Patients With Vascular Cognitive Impairment. Front Neuroanat 12:53.

Chen JL, Schlaug G (2013) Resting state interhemispheric motor connectivity and white matter integrity correlate with motor impairment in chronic stroke. Frontiers in neurology 4:178.

Chen K, Azeez A, Chen DY, Biswal BB (2020) Resting-State Functional Connectivity: Signal Origins and Analytic Methods. Neuroimaging Clin N Am 30:15-23.

Chen L, Zhang Y, Li D, Zhang N, Liu R, Han B, Wei C, Liu H, Xu X, Hao J (2016) Everolimus (RAD001) ameliorates vascular cognitive impairment by regulating

microglial function via the mTORC1 signaling pathway. J Neuroimmunol 299:164-171.

Chen YF, Wang H, Chu Y, Huang YC, Su MY (2006) Regional quantification of white matter hyperintensity in normal aging, mild cognitive impairment, and Alzheimer's disease. Dement Geriatr Cogn Disord 22:177-184.

Coltman R, Spain A, Tsenkina Y, Fowler JH, Smith J, Scullion G, Allerhand M, Scott F, Kalaria RN, Ihara M, Daumas S, Deary IJ, Wood E, McCulloch J, Horsburgh K (2011) Selective white matter pathology induces a specific impairment in spatial working memory. Neurobiol Aging 32:2324 e2327-2312.

Constantinides C, Mean R, Janssen BJ (2011) Effects of isoflurane anesthesia on the cardiovascular function of the C57BL/6 mouse. ILAR J 52:e21-31.

Corriveau RA, Bosetti F, Emr M, Gladman JT, Koenig JI, Moy CS, Pahigiannis K, Waddy SP, Koroshetz W (2016) The Science of Vascular Contributions to Cognitive Impairment and Dementia (VCID): A Framework for Advancing Research Priorities in the Cerebrovascular Biology of Cognitive Decline. Cell Mol Neurobiol 36:281-288.

Cox RW (1996) AFNI: software for analysis and visualization of functional magnetic resonance neuroimages. Comput Biomed Res 29:162-173.

Crofts JJ, Higham DJ, Bosnell R, Jbabdi S, Matthews PM, Behrens T, Johansen-Berg H (2011) Network analysis detects changes in the contralesional hemisphere following stroke. Neuroimage 54:161-169.

de Guzman AE, Wong MD, Gleave JA, Nieman BJ (2016) Variations in post-perfusion immersion fixation and storage alter MRI measurements of mouse brain morphometry. Neuroimage 142:687-695.

Deary IJ, Leaper SA, Murray AD, Staff RT, Whalley LJ (2003) Cerebral white matter abnormalities and lifetime cognitive change: a 67-year follow-up of the Scottish Mental Survey of 1932. Psychol Aging 18:140-148.

Debette S, Beiser A, DeCarli C, Au R, Himali JJ, Kelly-Hayes M, Romero JR, Kase CS, Wolf PA, Seshadri S (2010) Association of MRI markers of vascular brain injury with incident stroke, mild cognitive impairment, dementia, and mortality: the Framingham Offspring Study. Stroke 41:600-606.

Desowska A, Turner DL (2019) Dynamics of brain connectivity after stroke. Reviews in the Neurosciences 30:605-623.

Di Martino A, Scheres A, Margulies DS, Kelly A, Uddin LQ, Shehzad Z, Biswal B, Walters JR, Castellanos FX, Milham MP (2008) Functional connectivity of human striatum: a resting state FMRI study. Cerebral cortex 18:2735-2747.

Dichgans M, Zietemann V (2012) Prevention of vascular cognitive impairment. Stroke 43:3137-3146.

Dichgans M, Leys D (2017) Vascular Cognitive Impairment. Circ Res 120:573-591.

Dong YF, Kataoka K, Toyama K, Sueta D, Koibuchi N, Yamamoto E, Yata K, Tomimoto H, Ogawa H, Kim-Mitsuyama S (2011) Attenuation of brain damage and cognitive impairment by direct renin inhibition in mice with chronic cerebral hypoperfusion. Hypertension 58:635-642.

Doughty C, Wang J, Feng W, Hackney D, Pani E, Schlaug G (2016) Detection and predictive value of fractional anisotropy changes of the corticospinal tract in the acute phase of a stroke. Stroke 47:1520-1526.

Duncombe J, Kitamura A, Hase Y, Ihara M, Kalaria RN, Horsburgh K (2017) Chronic cerebral hypoperfusion: a key mechanism leading to vascular cognitive impairment and dementia. Closing the translational gap between rodent models and human vascular cognitive impairment and dementia. Clin Sci (Lond) 131:2451-2468.

Elbaz A, Vicente-Vytopilova P, Tavernier B, Sabia S, Dumurgier J, Mazoyer B, Singh-Manoux A, Tzourio C (2013) Motor function in the elderly: evidence for the reserve hypothesis. Neurology 81:417-426.

Ella A, Keller M (2015) Construction of an MRI 3D high resolution sheep brain template. Magn Reson Imaging 33:1329-1337.

Ella A, Delgadillo JA, Chemineau P, Keller M (2017) Computation of a high-resolution MRI 3D stereotaxic atlas of the sheep brain. J Comp Neurol 525:676-692.

Ercsey-Ravasz M, Markov NT, Lamy C, Van Essen DC, Knoblauch K, Toroczkai Z, Kennedy H (2013) A predictive network model of cerebral cortical connectivity based on a distance rule. Neuron 80:184-197.

Farkas E, Luiten PG, Bari F (2007) Permanent, bilateral common carotid artery occlusion in the rat: a model for chronic cerebral hypoperfusion-related neurodegenerative diseases. Brain Res Rev 54:162-180.

Feo R, Giove F (2019) Towards an efficient segmentation of small rodents brain: A short critical review. J Neurosci Methods 323:82-89.

Ferraris S, Shakir D, Van Der Merwe J, Gsell W, Deprest J, Vercauteren T (2017) Bruker2nifti: Magnetic resonance images converter from bruker ParaVision to NIfTI format. Journal of Open Source Software 2:354.

Fiebach J, Jansen O, Schellinger P, Heiland S, Hacke W, Sartor K (2002) Serial analysis of the apparent diffusion coefficient time course in human stroke. Neuroradiology 44:294-298.

Floel A, de Vries MH, Scholz J, Breitenstein C, Johansen-Berg H (2009) White matter integrity in the vicinity of Broca's area predicts grammar learning success. Neuroimage 47:1974-1981.

Fornito A, Zalesky A, Bullmore E (2016) Fundamentals of brain network analysis: Academic Press.

Fuchtemeier M, Brinckmann MP, Foddis M, Kunz A, Po C, Curato C, Dirnagl U, Farr TD (2015) Vascular change and opposing effects of the angiotensin type 2 receptor in a mouse model of vascular cognitive impairment. J Cereb Blood Flow Metab 35:476-484.

Fukuda M, Vazquez AL, Zong X, Kim SG (2013) Effects of the alpha(2)-adrenergic receptor agonist dexmedetomidine on neural, vascular and BOLD fMRI responses in the somatosensory cortex. Eur J Neurosci 37:80-95.

Glenner GG, Wong CW (1984) Alzheimer's disease: initial report of the purification and characterization of a novel cerebrovascular amyloid protein. Biochem Biophys Res Commun 120:885-890.

Glud AN, Bech J, Tvilling L, Zaer H, Orlowski D, Fitting LM, Ziedler D, Geneser M, Sangill R, Alstrup AKO, Bjarkam CR, Sorensen JCH (2017) A fiducial skull marker for precise MRI-based stereotaxic surgery in large animal models. J Neurosci Methods 285:45-48.

Golestani AM, Tymchuk S, Demchuk A, Goodyear BG, Group V-S (2013) Longitudinal evaluation of resting-state FMRI after acute stroke with hemiparesis. Neurorehabil Neural Repair 27:153-163.

Gooch J, Wilcock DM (2016) Animal Models of Vascular Cognitive Impairment and Dementia (VCID). Cell Mol Neurobiol 36:233-239.

Gorelick PB et al. (2011) Vascular contributions to cognitive impairment and dementia: a statement for healthcare professionals from the american heart association/american stroke association. Stroke 42:2672-2713.

Gorges M, Roselli F, Muller HP, Ludolph AC, Rasche V, Kassubek J (2017) Functional Connectivity Mapping in the Animal Model: Principles and Applications of Resting-State fMRI. Front Neurol 8:200.

Gozzi A, Schwarz AJ (2016) Large-scale functional connectivity networks in the rodent brain. Neuroimage 127:496-509.

Grandjean J, Schroeter A, Batata I, Rudin M (2014a) Optimization of anesthesia protocol for resting-state fMRI in mice based on differential effects of anesthetics on functional connectivity patterns. Neuroimage 102 Pt 2:838-847.

Grandjean J, Zerbi V, Balsters JH, Wenderoth N, Rudin M (2017a) Structural Basis of Large-Scale Functional Connectivity in the Mouse. J Neurosci 37:8092-8101.

Grandjean J, Preti MG, Bolton TAW, Buerge M, Seifritz E, Pryce CR, Van De Ville D, Rudin M (2017b) Dynamic reorganization of intrinsic functional networks in the mouse brain. Neuroimage 152:497-508.

Grandjean J, Schroeter A, He P, Tanadini M, Keist R, Krstic D, Konietzko U, Klohs J, Nitsch RM, Rudin M (2014b) Early alterations in functional connectivity and white matter structure in a transgenic mouse model of cerebral amyloidosis. J Neurosci 34:13780-13789.

Grandjean J et al. (2020) Common functional networks in the mouse brain revealed by multi-centre resting-state fMRI analysis. Neuroimage 205:116278.

Green C, Minassian A, Vogel S, Diedenhofen M, Beyrau A, Wiedermann D, Hoehn M (2018) Sensorimotor Functional and Structural Networks after Intracerebral Stem Cell Grafts in the Ischemic Mouse Brain. J Neurosci 38:1648-1661.

Greve DN, Fischl B (2009) Accurate and robust brain image alignment using boundary-based registration. Neuroimage 48:63-72.

Griffanti L, Douaud G, Bijsterbosch J, Evangelisti S, Alfaro-Almagro F, Glasser MF, Duff EP, Fitzgibbon S, Westphal R, Carone D, Beckmann CF, Smith SM (2017) Hand classification of fMRI ICA noise components. Neuroimage 154:188-205.

Griffanti L, Salimi-Khorshidi G, Beckmann CF, Auerbach EJ, Douaud G, Sexton CE, Zsoldos E, Ebmeier KP, Filippini N, Mackay CE, Moeller S, Xu J, Yacoub E, Baselli G, Ugurbil K, Miller KL, Smith SM (2014) ICA-based artefact removal and accelerated fMRI acquisition for improved resting state network imaging. Neuroimage 95:232-247.

Groisser BN, Copen WA, Singhal AB, Hirai KK, Schaechter JD (2014) Corticospinal tract diffusion abnormalities early after stroke predict motor outcome. Neurorehabilitation and neural repair 28:751-760.

Guilfoyle DN, Gerum SV, Sanchez JL, Balla A, Sershen H, Javitt DC, Hoptman MJ (2013) Functional connectivity fMRI in mouse brain at 7T using isoflurane. J Neurosci Methods 214:144-148.

Gusnard DA, Akbudak E, Shulman GL, Raichle ME (2001) Medial prefrontal cortex and self-referential mental activity: relation to a default mode of brain function. Proc Natl Acad Sci U S A 98:4259-4264.

Hachinski V, Iadecola C, Petersen RC, Breteler MM, Nyenhuis DL, Black SE, Powers WJ, DeCarli C, Merino JG, Kalaria RN, Vinters HV, Holtzman DM, Rosenberg GA, Wallin A, Dichgans M, Marler JR, Leblanc GG (2006) National Institute of Neurological Disorders and Stroke-Canadian Stroke Network vascular cognitive impairment harmonization standards. Stroke 37:2220-2241.

Hachinski VC, Bowler JV (1993) Vascular dementia. Neurology 43:2159-2160; author reply 2160-2151.

Hainsworth AH, Allan SM, Boltze J, Cunningham C, Farris C, Head E, Ihara M, Isaacs JD, Kalaria RN, Lesnik Oberstein SA, Moss MB, Nitzsche B, Rosenberg GA, Rutten JW, Salkovic-Petrisic M, Troen AM (2017) Translational models for vascular cognitive impairment: a review including larger species. BMC Med 15:16.

Ham T, Leff A, de Boissezon X, Joffe A, Sharp DJ (2013) Cognitive control and the salience network: an investigation of error processing and effective connectivity. Journal of Neuroscience 33:7091-7098.

Harris JJ, Attwell D (2012) The energetics of CNS white matter. J Neurosci 32:356-371.

Hase Y, Horsburgh K, Ihara M, Kalaria RN (2018a) White matter degeneration in vascular and other ageing-related dementias. J Neurochem 144:617-633.

Hase Y, Craggs L, Hase M, Stevenson W, Slade J, Chen A, Liang D, Ennaceur A, Oakley A, Ihara M, Horsburgh K, Kalaria RN (2018b) The effects of environmental enrichment on white matter pathology in a mouse model of chronic cerebral hypoperfusion. J Cereb Blood Flow Metab 38:151-165.

Hase Y, Craggs L, Hase M, Stevenson W, Slade J, Lopez D, Mehta R, Chen A, Liang D, Oakley A, Ihara M, Horsburgh K, Kalaria RN (2017) Effects of environmental enrichment on white matter glial responses in a mouse model of chronic cerebral hypoperfusion. J Neuroinflammation 14:81.

Hausman HK, O'Shea A, Kraft JN, Boutzoukas EM, Evangelista ND, Van Etten EJ, Bharadwaj PK, Smith SG, Porges E, Hishaw GA (2020) The role of resting-state network functional connectivity in cognitive aging. Frontiers in Aging Neuroscience 12:177.

Hernandez-Fernandez M, Reguly I, Jbabdi S, Giles M, Smith S, Sotiropoulos SN (2019) Using GPUs to accelerate computational diffusion MRI: From microstructure estimation to tractography and connectomes. Neuroimage 188:598-615.

Himberg J, Hyvarinen A, Esposito F (2004) Validating the independent components of neuroimaging time series via clustering and visualization. Neuroimage 22:1214-1222.

Holland PR, Bastin ME, Jansen MA, Merrifield GD, Coltman RB, Scott F, Nowers H, Khallout K, Marshall I, Wardlaw JM, Deary IJ, McCulloch J, Horsburgh K (2011) MRI is a sensitive marker of subtle white matter pathology in hypoperfused mice. Neurobiol Aging 32:2325 e2321-2326.

Holland PR, Searcy JL, Salvadores N, Scullion G, Chen G, Lawson G, Scott F, Bastin ME, Ihara M, Kalaria R, Wood ER, Smith C, Wardlaw JM, Horsburgh K (2015) Gliovascular disruption and cognitive deficits in a mouse model with features of small vessel disease. J Cereb Blood Flow Metab 35:1005-1014.

Hubner NS, Mechling AE, Lee HL, Reisert M, Bienert T, Hennig J, von Elverfeldt D, Harsan LA (2017) The connectomics of brain demyelination: Functional and structural patterns in the cuprizone mouse model. Neuroimage 146:1-18.

Iadecola C (2013) The pathobiology of vascular dementia. Neuron 80:844-866.

Ihara M, Tomimoto H (2011) Lessons from a mouse model characterizing features of vascular cognitive impairment with white matter changes. J Aging Res 2011:978761.

Ingalhalikar M, Parker D, Ghanbari Y, Smith A, Hua K, Mori S, Abel T, Davatzikos C, Verma R (2015) Connectome and Maturation Profiles of the Developing Mouse Brain Using Diffusion Tensor Imaging. Cereb Cortex 25:2696-2706.

Ioanas H-I, Marks M, Zerbi V, Yanik MF, Rudin M (2020) An optimized registration workflow and standard geometric space for small animal brain imaging. BioRxiv:619650.

Iwanami J, Mogi M, Tsukuda K, Wang XL, Nakaoka H, Kan-no H, Chisaka T, Bai HY, Shan BS, Kukida M, Horiuchi M (2015) Direct angiotensin II type 2 receptor stimulation by compound 21 prevents vascular dementia. J Am Soc Hypertens 9:250-256.

Janes AC, Nickerson LD, Frederick Bde B, Kaufman MJ (2012) Prefrontal and limbic resting state brain network functional connectivity differs between nicotine-dependent smokers and non-smoking controls. Drug Alcohol Depend 125:252-259.

Jbabdi S, Sotiropoulos SN, Savio AM, Graña M, Behrens TE (2012) Model-based analysis of multishell diffusion MR data for tractography: how to get over fitting problems. Magnetic resonance in medicine 68:1846-1855.

Jellinger KA (2006) Alzheimer 100--highlights in the history of Alzheimer research. J Neural Transm (Vienna) 113:1603-1623.

Jenkinson M, Bannister P, Brady M, Smith S (2002) Improved optimization for the robust and accurate linear registration and motion correction of brain images. Neuroimage 17:825-841.

Jenkinson M, Beckmann CF, Behrens TE, Woolrich MW, Smith SM (2012) Fsl. Neuroimage 62:782-790.

Jiwa NS, Garrard P, Hainsworth AH (2010) Experimental models of vascular dementia and vascular cognitive impairment: a systematic review. J Neurochem 115:814-828.

Jokinen H, Schmidt R, Ropele S, Fazekas F, Gouw AA, Barkhof F, Scheltens P, Madureira S, Verdelho A, Ferro JM, Wallin A, Poggesi A, Inzitari D, Pantoni L, Erkinjuntti T, Group LS (2013) Diffusion changes predict cognitive and functional outcome: the LADIS study. Ann Neurol 73:576-583.

Jonckers E, Van Audekerke J, De Visscher G, Van der Linden A, Verhoye M (2011) Functional connectivity fMRI of the rodent brain: comparison of functional connectivity networks in rat and mouse. PLoS One 6:e18876.

Jonckers E, Delgado y Palacios R, Shah D, Guglielmetti C, Verhoye M, Van der Linden A (2014) Different anesthesia regimes modulate the functional connectivity outcome in mice. Magn Reson Med 72:1103-1112.

Jones DK, Knosche TR, Turner R (2013) White matter integrity, fiber count, and other fallacies: the do's and don'ts of diffusion MRI. Neuroimage 73:239-254.

Kalaria RN (2017) The pathology and pathophysiology of vascular dementia. Neuropharmacology.

Kalaria RN, Perry RH, O'Brien J, Jaros E (2012) Atheromatous disease in small intracerebral vessels, microinfarcts and dementia. Neuropathol Appl Neurobiol 38:505-508.

Kalinosky BT, Schindler-Ivens S, Schmit BD (2013) White matter structural connectivity is associated with sensorimotor function in stroke survivors. NeuroImage: Clinical 2:767-781.

Kang J, Lemaire HG, Unterbeck A, Salbaum JM, Masters CL, Grzeschik KH, Multhaup G, Beyreuther K, Muller-Hill B (1987) The precursor of Alzheimer's disease amyloid A4 protein resembles a cell-surface receptor. Nature 325:733-736.

Kesler SR, Acton P, Rao V, Ray WJ (2018) Functional and structural connectome properties in the 5XFAD transgenic mouse model of Alzheimer's disease. Netw Neurosci 2:241-258.

Khanna N, Altmeyer W, Zhuo J, Steven A (2015) Functional Neuroimaging: Fundamental Principles and Clinical Applications. Neuroradiol J 28:87-96.

Kim E, Lee SH, Lee KS, Cheong HK, Namkoong K, Hong CH, Oh BH (2012) AMPK gamma2 subunit gene PRKAG2 polymorphism associated with cognitive impairment as well as diabetes in old age. Psychoneuroendocrinology 37:358-365.

Kim EH, Lee J, Jang SH (2013) Motor outcome prediction using diffusion tensor tractography of the corticospinal tract in large middle cerebral artery territory infarct. NeuroRehabilitation 32:583-590.

Kim HJ, Im K, Kwon H, Lee JM, Ye BS, Kim YJ, Cho H, Choe YS, Lee KH, Kim ST, Kim JS, Lee JH, Na DL, Seo SW (2015) Effects of amyloid and small vessel disease on white matter network disruption. J Alzheimers Dis 44:963-975.

King JA, Garelick TS, Brevard ME, Chen W, Messenger TL, Duong TQ, Ferris CF (2005) Procedure for minimizing stress for fMRI studies in conscious rats. J Neurosci Methods 148:154-160.

Kitamura A, Manso Y, Duncombe J, Searcy J, Koudelka J, Binnie M, Webster S, Lennen R, Jansen M, Marshall I, Ihara M, Kalaria RN, Horsburgh K (2017) Long-term cilostazol treatment reduces gliovascular damage and memory impairment in a mouse model of chronic cerebral hypoperfusion. Sci Rep 7:4299.

Klein S, Staring M, Murphy K, Viergever MA, Pluim JP (2010) elastix: a toolbox for intensity-based medical image registration. IEEE Trans Med Imaging 29:196-205.

Koch P, Schulz R, Hummel FC (2016) Structural connectivity analyses in motor recovery research after stroke. Annals of clinical and translational neurology 3:233-244.

Laubach M, Amarante LM, Swanson K, White SR (2018) What, if anything, is rodent prefrontal cortex? eneuro 5.

Laufs H (2010) Multimodal analysis of resting state cortical activity: what does EEG add to our knowledge of resting state BOLD networks? Neuroimage 52:1171-1172.

Lawrence AJ, Chung AW, Morris RG, Markus HS, Barrick TR (2014) Structural network efficiency is associated with cognitive impairment in small-vessel disease. Neurology 83:304-311.

Lawrence AJ, Patel B, Morris RG, MacKinnon AD, Rich PM, Barrick TR, Markus HS (2013) Mechanisms of cognitive impairment in cerebral small vessel disease: multimodal MRI results from the St George's cognition and neuroimaging in stroke (SCANS) study. PLoS One 8:e61014.

Lawrence AJ, Zeestraten EA, Benjamin P, Lambert CP, Morris RG, Barrick TR, Markus HS (2018) Longitudinal decline in structural networks predicts dementia in cerebral small vessel disease. Neurology 90:e1898-e1910.

Lee W, Lee SD, Park MY, Foley L, Purcell-Estabrook E, Kim H, Yoo SS (2015) Functional and diffusion tensor magnetic resonance imaging of the sheep brain. BMC Vet Res 11:262.

Lerch JP, Gazdzinski L, Germann J, Sled JG, Henkelman RM, Nieman BJ (2012) Wanted dead or alive? The tradeoff between in-vivo versus ex-vivo MR brain imaging in the mouse. Front Neuroinform 6:6.

Li J, Biswal BB, Wang P, Duan X, Cui Q, Chen H, Liao W (2019) Exploring the functional connectome in white matter. Hum Brain Mapp 40:4331-4344.

Li W, Li Y, Zhu W, Chen X (2014) Changes in brain functional network connectivity after stroke. Neural Regen Res 9:51-60.

Lin LY, Ramsey L, Metcalf NV, Rengachary J, Shulman GL, Shimony JS, Corbetta M (2018) Stronger prediction of motor recovery and outcome post-stroke by cortico-spinal tract integrity than functional connectivity. PLoS One 13:e0202504.

Liska A, Galbusera A, Schwarz AJ, Gozzi A (2015) Functional connectivity hubs of the mouse brain. Neuroimage 115:281-291.

Liu B, Li J, Yu C, Li Y, Liu Y, Song M, Fan M, Li K, Jiang T (2010) Haplotypes of catechol-O-methyltransferase modulate intelligence-related brain white matter integrity. Neuroimage 50:243-249.

Liu J, Qin W, Zhang J, Zhang X, Yu C (2015) Enhanced interhemispheric functional connectivity compensates for anatomical connection damages in subcortical stroke. Stroke 46:1045-1051.

Liu Q, Zhu Z, Teipel SJ, Yang J, Xing Y, Tang Y, Jia J (2017) White Matter Damage in the Cholinergic System Contributes to Cognitive Impairment in Subcortical Vascular Cognitive Impairment, No Dementia. Front Aging Neurosci 9:47.

Liyanage KA, Steward C, Moffat BA, Opie NL, Rind GS, John SE, Ronayne S, May CN, O'Brien TJ, Milne ME, Oxley TJ (2016) Development and Implementation of a Corriedale Ovine Brain Atlas for Use in Atlas-Based Segmentation. PLoS One 11:e0155974.

Logothetis NK (2008) What we can do and what we cannot do with fMRI. Nature 453:869-878.

Lu H, Zou Q, Gu H, Raichle ME, Stein EA, Yang Y (2012) Rat brains also have a default mode network. Proc Natl Acad Sci U S A 109:3979-3984.

Ma Y, Smith D, Hof P, Foerster B, Hamilton S, Blackband S, Yu M, Benveniste H (2008) In vivo 3D digital atlas database of the adult C57BL/6J mouse brain by magnetic resonance microscopy. Frontiers in Neuroanatomy 2.

Madan CR (2015) Creating 3D visualizations of MRI data: A brief guide. F1000Res 4:466.

Madigan JB, Wilcock DM, Hainsworth AH (2016) Vascular Contributions to Cognitive Impairment and Dementia: Topical Review of Animal Models. Stroke 47:1953-1959.

Maier-Hein K, Neher P, Houde J-C, Côté M-A, Garyfallidis E, Zhong J, Chamberland M, Yeh F-C, Lin Y-C, Ji Q (2016) Tractography-based connectomes are dominated by false-positive connections.

Maki T, Ihara M, Fujita Y, Nambu T, Miyashita K, Yamada M, Washida K, Nishio K, Ito H, Harada H, Yokoi H, Arai H, Itoh H, Nakao K, Takahashi R, Tomimoto H (2011) Angiogenic and vasoprotective effects of adrenomedullin on prevention of cognitive decline after chronic cerebral hypoperfusion in mice. Stroke 42:1122-1128.

Maniega SM, Bastin M, Armitage P, Farrall A, Carpenter T, Hand P, Cvoro V, Rivers C, Wardlaw J (2004) Temporal evolution of water diffusion parameters is different in grey and white matter in human ischaemic stroke. Journal of Neurology, Neurosurgery & Psychiatry 75:1714-1718.

Manouchehrian O, Arner K, Deierborg T, Taylor L (2015) Who let the dogs out?: detrimental role of Galectin-3 in hypoperfusion-induced retinal degeneration. J Neuroinflammation 12:92.

McQueen J, Reimer MM, Holland PR, Manso Y, McLaughlin M, Fowler JH, Horsburgh K (2014) Restoration of oligodendrocyte pools in a mouse model of chronic cerebral hypoperfusion. PLoS One 9:e87227.

Mechling AE, Hubner NS, Lee HL, Hennig J, von Elverfeldt D, Harsan LA (2014) Fine-grained mapping of mouse brain functional connectivity with resting-state fMRI. Neuroimage 96:203-215.

Mechling AE, Arefin T, Lee H-L, Bienert T, Reisert M, Hamida SB, Darcq E, Ehrlich A, Gaveriaux-Ruff C, Parent MJ (2016) Deletion of the mu opioid receptor gene in mice reshapes the reward–aversion connectome. Proceedings of the National Academy of Sciences 113:11603-11608.

Minassian A, Green C, Diedenhofen M, Vogel S, Hess S, Stoeber M, Radmilovic MD, Wiedermann D, Kloppenburg P, Hoehn M (2020) Human Neural Stem Cell Induced Functional Network Stabilization After Cortical Stroke: A Longitudinal Resting-State fMRI Study in Mice. Front Cell Neurosci 14:86.

Mitchell AS, Czajkowski R, Zhang N, Jeffery K, Nelson AJ (2018) Retrosplenial cortex and its role in spatial cognition. Brain and neuroscience advances 2:2398212818757098.

Miyamoto N, Maki T, Pham LD, Hayakawa K, Seo JH, Mandeville ET, Mandeville JB, Kim KW, Lo EH, Arai K (2013) Oxidative stress interferes with white matter renewal after prolonged cerebral hypoperfusion in mice. Stroke 44:3516-3521.

Mizrahi EH, Waitzman A, Blumstein T, Arad M, Adunsky A (2010) Diabetes mellitus predicts cognitive impairment in patients with ischemic stroke. Am J Alzheimers Dis Other Demen 25:362-366.

Modat M, Ridgway GR, Taylor ZA, Lehmann M, Barnes J, Hawkes DJ, Fox NC, Ourselin S (2010) Fast free-form deformation using graphics processing units. Comput Methods Programs Biomed 98:278-284.

Montine TJ et al. (2014) Recommendations of the Alzheimer's disease-related dementias conference. Neurology 83:851-860.

Moura LM, Luccas R, de Paiva JPQ, Amaro E, Jr., Leemans A, Leite CDC, Otaduy MCG, Conforto AB (2019) Diffusion Tensor Imaging Biomarkers to Predict Motor Outcomes in Stroke: A Narrative Review. Front Neurol 10:445.

Muller J, Alizadeh M, Mohamed FB, Riley J, Pearce JJ, Trieu B, Liang T-W, Romo V, Sharan A, Wu C (2018) Clinically applicable delineation of the pallidal sensorimotor region in patients with advanced Parkinson’s disease: study of probabilistic and deterministic tractography. Journal of neurosurgery 131:1520-1531.

Murphy K, Fox MD (2017) Towards a consensus regarding global signal regression for resting state functional connectivity MRI. Neuroimage 154:169-173.

Nasrallah FA, Tay HC, Chuang KH (2014) Detection of functional connectivity in the resting mouse brain. Neuroimage 86:417-424.

Neto CJ, Paganelli RA, Benetoli A, Lima KC, Milani H (2005) Permanent, 3-stage, 4-vessel occlusion as a model of chronic and progressive brain hypoperfusion in rats: a neurohistological and behavioral analysis. Behav Brain Res 160:312-322.

Nickerson LD, Smith SM, Ongur D, Beckmann CF (2017) Using Dual Regression to Investigate Network Shape and Amplitude in Functional Connectivity Analyses. Front Neurosci 11:115.

Nishio K, Ihara M, Yamasaki N, Kalaria RN, Maki T, Fujita Y, Ito H, Oishi N, Fukuyama H, Miyakawa T, Takahashi R, Tomimoto H (2010) A mouse model characterizing features of vascular dementia with hippocampal atrophy. Stroke 41:1278-1284.

Nitzsche B, Frey S, Collins LD, Seeger J, Lobsien D, Dreyer A, Kirsten H, Stoffel MH, Fonov VS, Boltze J (2015) A stereotaxic, population-averaged T1w ovine brain atlas including cerebral morphology and tissue volumes. Front Neuroanat 9:69.

O'Brien JT, Thomas A (2015) Vascular dementia. Lancet 386:1698-1706.

Oh SW et al. (2014) A mesoscale connectome of the mouse brain. Nature 508:207-214.

Pallast N, Diedenhofen M, Blaschke S, Wieters F, Wiedermann D, Hoehn M, Fink GR, Aswendt M (2019) Processing Pipeline for Atlas-Based Imaging Data Analysis of Structural and Functional Mouse Brain MRI (AIDAmri). Front Neuroinform 13:42.

Pannekoek JN, Veer IM, van Tol MJ, van der Werff SJ, Demenescu LR, Aleman A, Veltman DJ, Zitman FG, Rombouts SA, van der Wee NJ (2013) Resting-state functional connectivity abnormalities in limbic and salience networks in social anxiety disorder without comorbidity. Eur Neuropsychopharmacol 23:186-195.

Park CH, Chang WH, Ohn SH, Kim ST, Bang OY, Pascual-Leone A, Kim YH (2011) Longitudinal changes of resting-state functional connectivity during motor recovery after stroke. Stroke 42:1357-1362.

Patel A, Moalem A, Cheng H, Babadjouni RM, Patel K, Hodis DM, Chandegara D, Cen S, He S, Liu Q, Mack WJ (2017) Chronic cerebral hypoperfusion induced by bilateral carotid artery stenosis causes selective recognition impairment in adult mice. Neurol Res 39:910-917.

Paxinos G, Franklin KB (2019) Paxinos and Franklin's the mouse brain in stereotaxic coordinates: Academic press.

Pervolaraki E, Tyson AL, Pibiri F, Poulter SL, Reichelt AC, Rodgers RJ, Clapcote SJ, Lever C, Andreae LC, Dachtler J (2019) The within-subject application of diffusion tensor MRI and CLARITY reveals brain structural changes in Nrxn2 deletion mice. Molecular autism 10:1-13.

Petersen MV, Lund TE, Sunde N, Frandsen J, Rosendal F, Juul N, Østergaard K (2017) Probabilistic versus deterministic tractography for delineation of the cortico-subthalamic hyperdirect pathway in patients with Parkinson disease selected for deep brain stimulation. Journal of neurosurgery 126:1657-1668.

Pieri V, Trovatelli M, Cadioli M, Zani DD, Brizzola S, Ravasio G, Acocella F, Di Giancamillo M, Malfassi L, Dolera M, Riva M, Bello L, Falini A, Castellano A (2019) In vivo Diffusion Tensor Magnetic Resonance Tractography of the Sheep Brain: An Atlas of the Ovine White Matter Fiber Bundles. Front Vet Sci 6:345.

Pizoli CE, Shah MN, Snyder AZ, Shimony JS, Limbrick DD, Raichle ME, Schlaggar BL, Smyth MD (2011) Resting-state activity in development and maintenance of normal brain function. Proc Natl Acad Sci U S A 108:11638-11643.

Price CJ, Hope TM, Seghier ML (2017) Ten problems and solutions when predicting individual outcome from lesion site after stroke. Neuroimage 145:200-208.

Puig J, Pedraza S, Blasco G, Daunis-I-Estadella J, Prats A, Prados F, Boada I, Castellanos M, Sánchez-González J, Remollo S (2010) Wallerian degeneration in the corticospinal tract evaluated by diffusion tensor imaging correlates with motor deficit 30 days after middle cerebral artery ischemic stroke. American Journal of Neuroradiology 31:1324-1330.

Radlinska B, Ghinani S, Leppert I, Minuk J, Pike G, Thiel A (2010) Diffusion tensor imaging, permanent pyramidal tract damage, and outcome in subcortical stroke. Neurology 75:1048-1054.

Raichle ME (2015) The brain's default mode network. Annu Rev Neurosci 38:433-447.

Rehme AK, Volz LJ, Feis DL, Bomilcar-Focke I, Liebig T, Eickhoff SB, Fink GR, Grefkes C (2015) Identifying Neuroimaging Markers of Motor Disability in Acute Stroke by Machine Learning Techniques. Cereb Cortex 25:3046-3056.

Reijmer YD, Fotiadis P, Martinez-Ramirez S, Salat DH, Schultz A, Shoamanesh A, Ayres AM, Vashkevich A, Rosas D, Schwab K, Leemans A, Biessels GJ, Rosand J, Johnson KA, Viswanathan A, Gurol ME, Greenberg SM (2015) Structural network alterations and neurological dysfunction in cerebral amyloid angiopathy. Brain 138:179-188.

Reimer MM, McQueen J, Searcy L, Scullion G, Zonta B, Desmazieres A, Holland PR, Smith J, Gliddon C, Wood ER, Herzyk P, Brophy PJ, McCulloch J, Horsburgh K (2011) Rapid disruption of axon-glial integrity in response to mild cerebral hypoperfusion. J Neurosci 31:18185-18194.

Rodríguez M, Abdala P, Barroso-Chinea P, González-Hernández T (2001) The deep mesencephalic nucleus as an output center of basal ganglia: morphological and electrophysiological similarities with the substantia nigra. Journal of Comparative Neurology 438:12-31.

Rosenberg GA, Wallin A, Wardlaw JM, Markus HS, Montaner J, Wolfson L, Iadecola C, Zlokovic BV, Joutel A, Dichgans M, Duering M, Schmidt R, Korczyn AD, Grinberg LT, Chui HC, Hachinski V (2016) Consensus statement for diagnosis of subcortical small vessel disease. J Cereb Blood Flow Metab 36:6-25.

Rubinov M, Sporns O (2010) Complex network measures of brain connectivity: uses and interpretations. Neuroimage 52:1059-1069.

Rusanen M, Kivipelto M, Quesenberry CP, Jr., Zhou J, Whitmer RA (2011) Heavy smoking in midlife and long-term risk of Alzheimer disease and vascular dementia. Arch Intern Med 171:333-339.

Sachdev P et al. (2014) Diagnostic criteria for vascular cognitive disorders: a VASCOG statement. Alzheimer Dis Assoc Disord 28:206-218.

Saggu R, Schumacher T, Gerich F, Rakers C, Tai K, Delekate A, Petzold GC (2016) Astroglial NF-kB contributes to white matter damage and cognitive impairment in a mouse model of vascular dementia. Acta Neuropathol Commun 4:76.

Salimi-Khorshidi G, Douaud G, Beckmann CF, Glasser MF, Griffanti L, Smith SM (2014) Automatic denoising of functional MRI data: combining independent component analysis and hierarchical fusion of classifiers. Neuroimage 90:449-468.

Sarti C, Pantoni L, Bartolini L, Inzitari D (2002) Cognitive impairment and chronic cerebral hypoperfusion: what can be learned from experimental models. J Neurol Sci 203-204:263-266.

Sarwar T, Ramamohanarao K, Zalesky A (2019) Mapping connectomes with diffusion MRI: deterministic or probabilistic tractography? Magn Reson Med 81:1368-1384.

Schaefer A, Quinque EM, Kipping JA, Arelin K, Roggenhofer E, Frisch S, Villringer A, Mueller K, Schroeter ML (2014) Early small vessel disease affects frontoparietal and cerebellar hubs in close correlation with clinical symptoms--a resting-state fMRI study. J Cereb Blood Flow Metab 34:1091-1095.

Schlemm E, Schulz R, Bonstrup M, Krawinkel L, Fiehler J, Gerloff C, Thomalla G, Cheng B (2020) Structural brain networks and functional motor outcome after stroke-a prospective cohort study. Brain Commun 2:fcaa001.

Schneider JA, Arvanitakis Z, Bang W, Bennett DA (2007) Mixed brain pathologies account for most dementia cases in community-dwelling older persons. Neurology 69:2197-2204.

Seabrook TA, Burbridge TJ, Crair MC, Huberman AD (2017) Architecture, function, and assembly of the mouse visual system. Annual review of neuroscience 40:499-538.

Sedeno L et al. (2017) Tackling variability: A multicenter study to provide a gold-standard network approach for frontotemporal dementia. Hum Brain Mapp 38:3804-3822.

Seo JH, Miyamoto N, Hayakawa K, Pham LD, Maki T, Ayata C, Kim KW, Lo EH, Arai K (2013) Oligodendrocyte precursors induce early blood-brain barrier opening after white matter injury. J Clin Invest 123:782-786.

Seo JP, Do KH, Jung GS, Seo SW, Kim K, Son SM, Kim YK, Jang SH (2014) The difference of gait pattern according to the state of the corticospinal tract in chronic hemiparetic stroke patients. NeuroRehabilitation 34:259-266.

Sethi SS, Zerbi V, Wenderoth N, Fornito A, Fulcher BD (2017) Structural connectome topology relates to regional BOLD signal dynamics in the mouse brain. Chaos 27:047405.

Sforazzini F, Schwarz AJ, Galbusera A, Bifone A, Gozzi A (2014) Distributed BOLD and CBV-weighted resting-state networks in the mouse brain. Neuroimage 87:403-415.

Shah A, Jhawar SS, Goel A (2012) Analysis of the anatomy of the Papez circuit and adjoining limbic system by fiber dissection techniques. J Clin Neurosci 19:289-298.

Shah D, Jonckers E, Praet J, Vanhoutte G, Delgado YPR, Bigot C, D'Souza DV, Verhoye M, Van der Linden A (2013) Resting state FMRI reveals diminished functional connectivity in a mouse model of amyloidosis. PLoS One 8:e84241.

Shannon BJ, Dosenbach RA, Su Y, Vlassenko AG, Larson-Prior LJ, Nolan TS, Snyder AZ, Raichle ME (2013) Morning-evening variation in human brain metabolism and memory circuits. J Neurophysiol 109:1444-1456.

Shibata M, Ohtani R, Ihara M, Tomimoto H (2004) White matter lesions and glial activation in a novel mouse model of chronic cerebral hypoperfusion. Stroke 35:2598-2603.

Shibata M, Yamasaki N, Miyakawa T, Kalaria RN, Fujita Y, Ohtani R, Ihara M, Takahashi R, Tomimoto H (2007) Selective impairment of working memory in a mouse model of chronic cerebral hypoperfusion. Stroke 38:2826-2832.

Shirer WR, Jiang H, Price CM, Ng B, Greicius MD (2015) Optimization of rs-fMRI Pre-processing for Enhanced Signal-Noise Separation, Test-Retest Reliability, and Group Discrimination. Neuroimage 117:67-79.

Shulman GL, Corbetta M, Buckner RL, Fiez JA, Miezin FM, Raichle ME, Petersen SE (1997) Common Blood Flow Changes across Visual Tasks: I. Increases in Subcortical Structures and Cerebellum but Not in Nonvisual Cortex. J Cogn Neurosci 9:624-647.

Siegel JS, Ramsey LE, Snyder AZ, Metcalf NV, Chacko RV, Weinberger K, Baldassarre A, Hacker CD, Shulman GL, Corbetta M (2016) Disruptions of network connectivity predict impairment in multiple behavioral domains after stroke. Proc Natl Acad Sci U S A 113:E4367-4376.

Sigfridsson E, Marangoni M, Johnson JA, Hardingham GE, Fowler JH, Horsburgh K (2018) Astrocyte-specific overexpression of Nrf2 protects against optic tract damage and behavioural alterations in a mouse model of cerebral hypoperfusion. Sci Rep 8:12552.

Simpson JR, Jr., Snyder AZ, Gusnard DA, Raichle ME (2001) Emotion-induced changes in human medial prefrontal cortex: I. During cognitive task performance. Proc Natl Acad Sci U S A 98:683-687.

Sinke MR, Otte WM, van Meer MP, van der Toorn A, Dijkhuizen RM (2018) Modified structural network backbone in the contralesional hemisphere chronically after stroke in rat brain. J Cereb Blood Flow Metab 38:1642-1653.

Skrobot OA, O'Brien J, Black S, Chen C, DeCarli C, Erkinjuntti T, Ford GA, Kalaria RN, Pantoni L, Pasquier F, Roman GC, Wallin A, Sachdev P, Skoog I, group V, Ben-Shlomo Y, Passmore AP, Love S, Kehoe PG (2017) The Vascular Impairment of Cognition Classification Consensus Study. Alzheimers Dement 13:624-633.

Skrobot OA, Black SE, Chen C, DeCarli C, Erkinjuntti T, Ford GA, Kalaria RN, O'Brien J, Pantoni L, Pasquier F, Roman GC, Wallin A, Sachdev P, Skoog I, group V, Ben-Shlomo Y, Passmore AP, Love S, Kehoe PG (2018) Progress toward standardized diagnosis of vascular cognitive impairment: Guidelines from the Vascular Impairment of Cognition Classification Consensus Study. Alzheimers Dement 14:280-292.

Smith E (2016) Vascular Cognitive Impairment. Continuum (Minneap Minn) 22:490-509.

Smith SM, Jenkinson M, Woolrich MW, Beckmann CF, Behrens TE, Johansen-Berg H, Bannister PR, De Luca M, Drobnjak I, Flitney DE (2004a) Advances in functional and structural MR image analysis and implementation as FSL. Neuroimage 23:S208-S219.

Smith SM, Jenkinson M, Johansen-Berg H, Rueckert D, Nichols TE, Mackay CE, Watkins KE, Ciccarelli O, Cader MZ, Matthews PM (2006) Tract-based spatial statistics: voxelwise analysis of multi-subject diffusion data. Neuroimage 31:1487-1505.

Smith SM, Vidaurre D, Beckmann CF, Glasser MF, Jenkinson M, Miller KL, Nichols TE, Robinson EC, Salimi-Khorshidi G, Woolrich MW, Barch DM, Ugurbil K, Van Essen DC (2013) Functional connectomics from resting-state fMRI. Trends Cogn Sci 17:666-682.

Smith SM, Jenkinson M, Woolrich MW, Beckmann CF, Behrens TE, Johansen-Berg H, Bannister PR, De Luca M, Drobnjak I, Flitney DE, Niazy RK, Saunders J, Vickers J, Zhang Y, De Stefano N, Brady JM, Matthews PM (2004b) Advances in functional and structural MR image analysis and implementation as FSL. Neuroimage 23 Suppl 1:S208-219.

Soares JM, Marques P, Alves V, Sousa N (2013) A hitchhiker's guide to diffusion tensor imaging. Front Neurosci 7:31.

Song SK, Sun SW, Ramsbottom MJ, Chang C, Russell J, Cross AH (2002) Dysmyelination revealed through MRI as increased radial (but unchanged axial) diffusion of water. Neuroimage 17:1429-1436.

Song SK, Yoshino J, Le TQ, Lin SJ, Sun SW, Cross AH, Armstrong RC (2005) Demyelination increases radial diffusivity in corpus callosum of mouse brain. Neuroimage 26:132-140.

Sood R, Yang Y, Taheri S, Candelario-Jalil E, Estrada EY, Walker EJ, Thompson J, Rosenberg GA (2009) Increased apparent diffusion coefficients on MRI linked with matrix metalloproteinases and edema in white matter after bilateral carotid artery occlusion in rats. J Cereb Blood Flow Metab 29:308-316.

Sotelo MR, Kalinosky BT, Goodfriend K, Hyngstrom AS, Schmit BD (2020) Indirect structural connectivity identifies changes in brain networks after stroke. Brain Connectivity 10:399-410.

Sotiropoulos SN, Zalesky A (2017) Building connectomes using diffusion MRI: why, how and but. NMR Biomed.

Stafford JM, Jarrett BR, Miranda-Dominguez O, Mills BD, Cain N, Mihalas S, Lahvis GP, Lattal KM, Mitchell SH, David SV, Fryer JD, Nigg JT, Fair DA (2014) Large-scale topology and the default mode network in the mouse connectome. Proc Natl Acad Sci U S A 111:18745-18750.

Sun SW, Liang HF, Cross AH, Song SK (2008) Evolving Wallerian degeneration after transient retinal ischemia in mice characterized by diffusion tensor imaging. Neuroimage 40:1-10.

Sun YW, Qin LD, Zhou Y, Xu Q, Qian LJ, Tao J, Xu JR (2011) Abnormal functional connectivity in patients with vascular cognitive impairment, no dementia: a resting-state functional magnetic resonance imaging study. Behav Brain Res 223:388-394.

Takeuchi H, Taki Y, Sassa Y, Hashizume H, Sekiguchi A, Fukushima A, Kawashima R (2010) White matter structures associated with creativity: evidence from diffusion tensor imaging. Neuroimage 51:11-18.

The LSG, Poggesi A, Pantoni L, Inzitari D, Fazekas F, Ferro J, O'Brien J, Hennerici M, Scheltens P, Erkinjuntti T, Visser M, Langhorne P, Chabriat H, Waldemar G, Wallin A, Wahlund A (2011) 2001-2011: A Decade of the LADIS (Leukoaraiosis And DISability) Study: What Have We Learned about White Matter Changes and Small-Vessel Disease? Cerebrovasc Dis 32:577-588.

Toledo JB, Arnold SE, Raible K, Brettschneider J, Xie SX, Grossman M, Monsell SE, Kukull WA, Trojanowski JQ (2013) Contribution of cerebrovascular disease in autopsy confirmed neurodegenerative disease cases in the National Alzheimer's Coordinating Centre. Brain 136:2697-2706.

Tomimoto H, Ihara M, Wakita H, Ohtani R, Lin JX, Akiguchi I, Kinoshita M, Shibasaki H (2003) Chronic cerebral hypoperfusion induces white matter lesions and loss of oligodendroglia with DNA fragmentation in the rat. Acta Neuropathol 106:527-534.

Toyama K, Spin JM, Deng AC, Huang TT, Wei K, Wagenhauser MU, Yoshino T, Nguyen H, Mulorz J, Kundu S, Raaz U, Adam M, Schellinger IN, Jagger A, Tsao PS (2018) MicroRNA-Mediated Therapy Modulating Blood-Brain Barrier Disruption Improves Vascular Cognitive Impairment. Arterioscler Thromb Vasc Biol 38:1392-1406.

Tsai TH, Sun CK, Su CH, Sung PH, Chua S, Zhen YY, Leu S, Chang HW, Yang JL, Yip HK (2015) Sitagliptin attenuated brain damage and cognitive impairment in mice with chronic cerebral hypo-perfusion through suppressing oxidative stress and inflammatory reaction. J Hypertens 33:1001-1013.

Tuladhar AM, van Norden AG, de Laat KF, Zwiers MP, van Dijk EJ, Norris DG, de Leeuw FE (2015) White matter integrity in small vessel disease is related to cognition. Neuroimage Clin 7:518-524.

Tuladhar AM, van Dijk E, Zwiers MP, van Norden AG, de Laat KF, Shumskaya E, Norris DG, de Leeuw FE (2016) Structural network connectivity and cognition in cerebral small vessel disease. Hum Brain Mapp 37:300-310.

Tustison NJ, Avants BB, Cook PA, Zheng Y, Egan A, Yushkevich PA, Gee JC (2010) N4ITK: improved N3 bias correction. IEEE Trans Med Imaging 29:1310-1320.

Ueno M, Tomimoto H, Akiguchi I, Wakita H, Sakamoto H (2002) Blood-brain barrier disruption in white matter lesions in a rat model of chronic cerebral hypoperfusion. J Cereb Blood Flow Metab 22:97-104.

Upadhyay J, Baker SJ, Chandran P, Miller L, Lee Y, Marek GJ, Sakoglu U, Chin CL, Luo F, Fox GB, Day M (2011) Default-mode-like network activation in awake rodents. PLoS One 6:e27839.

Valdes Hernandez Mdel C, Gonzalez-Castro V, Ghandour DT, Wang X, Doubal F, Munoz Maniega S, Armitage PA, Wardlaw JM (2016) On the computational assessment of white matter hyperintensity progression: difficulties in method selection and bias field correction performance on images with significant white matter pathology. Neuroradiology 58:475-485.

Vincent JL, Patel GH, Fox MD, Snyder AZ, Baker JT, Van Essen DC, Zempel JM, Snyder LH, Corbetta M, Raichle ME (2007) Intrinsic functional architecture in the anaesthetized monkey brain. Nature 447:83-86.

Voorn P, Vanderschuren LJ, Groenewegen HJ, Robbins TW, Pennartz CM (2004) Putting a spin on the dorsal–ventral divide of the striatum. Trends in neurosciences 27:468-474.

Wang C, Qin W, Zhang J, Tian T, Li Y, Meng L, Zhang X, Yu C (2014) Altered functional organization within and between resting-state networks in chronic subcortical infarction. J Cereb Blood Flow Metab 34:597-605.

Wang J, Chen Y, Liang H, Niedermayer G, Chen H, Li Y, Wu M, Wang Y, Zhang Y (2019) The Role of Disturbed Small-World Networks in Patients with White Matter Lesions and Cognitive Impairment Revealed by Resting State Function Magnetic Resonance Images (rs-fMRI). Med Sci Monit 25:341-356.

Wang L, Yu C, Chen H, Qin W, He Y, Fan F, Zhang Y, Wang M, Li K, Zang Y (2010) Dynamic functional reorganization of the motor execution network after stroke. Brain 133:1224-1238.

Wang N, White LE, Qi Y, Cofer G, Johnson GA (2020) Cytoarchitecture of the mouse brain by high resolution diffusion magnetic resonance imaging. Neuroimage 216:116876.

Wang N, Anderson RJ, Badea A, Cofer G, Dibb R, Qi Y, Johnson GA (2018) Whole mouse brain structural connectomics using magnetic resonance histology. Brain Struct Funct 223:4323-4335.

Wang Y, Wang Q, Haldar JP, Yeh FC, Xie M, Sun P, Tu TW, Trinkaus K, Klein RS, Cross AH, Song SK (2011) Quantification of increased cellularity during inflammatory demyelination. Brain 134:3590-3601.

Washida K, Ihara M, Nishio K, Fujita Y, Maki T, Yamada M, Takahashi J, Wu X, Kihara T, Ito H, Tomimoto H, Takahashi R (2010) Nonhypotensive dose of telmisartan attenuates cognitive impairment partially due to peroxisome proliferator-activated receptor-gamma activation in mice with chronic cerebral hypoperfusion. Stroke 41:1798-1806.

Watts DJ, Strogatz SH (1998) Collective dynamics of 'small-world' networks. Nature 393:440-442.

Wells AJ, Vink R, Blumbergs PC, Brophy BP, Helps SC, Knox SJ, Turner RJ (2012) A surgical model of permanent and transient middle cerebral artery stroke in the sheep. PLoS One 7:e42157.

Werner CJ, Dogan I, Sass C, Mirzazade S, Schiefer J, Shah NJ, Schulz JB, Reetz K (2014) Altered resting-state connectivity in Huntington's disease. Hum Brain Mapp 35:2582-2593.

Winkler AM, Ridgway GR, Webster MA, Smith SM, Nichols TE (2014) Permutation inference for the general linear model. Neuroimage 92:381-397.

Wong WW, Fang Y, Chu WCW, Shi L, Tong KY (2019) What Kind of Brain Structural Connectivity Remodeling Can Relate to Residual Motor Function After Stroke? Front Neurol 10:1111.

Woolrich MW, Ripley BD, Brady M, Smith SM (2001) Temporal autocorrelation in univariate linear modeling of FMRI data. Neuroimage 14:1370-1386.

Woolrich MW, Jbabdi S, Patenaude B, Chappell M, Makni S, Behrens T, Beckmann C, Jenkinson M, Smith SM (2009) Bayesian analysis of neuroimaging data in FSL. Neuroimage 45:S173-186.

Wortmann M (2012) Dementia: a global health priority - highlights from an ADI and World Health Organization report. Alzheimers Res Ther 4:40.

Wu T, Grandjean J, Bosshard SC, Rudin M, Reutens D, Jiang T (2017) Altered regional connectivity reflecting effects of different anaesthesia protocols in the mouse brain. Neuroimage 149:190-199.

Yang J, Wong A, Wang Z, Liu W, Au L, Xiong Y, Chu WW, Leung EY, Chen S, Lau C, Chan AY, Lau AY, Fan F, Ip V, Soo Y, Leung T, Ho CL, Wong LK, Mok VC (2015) Risk factors for incident dementia after stroke and transient ischemic attack. Alzheimers Dement 11:16-23.

Yang Y, Kimura-Ohba S, Thompson J, Rosenberg GA (2016) Rodent Models of Vascular Cognitive Impairment. Transl Stroke Res 7:407-414.

Yeh FC, Badre D, Verstynen T (2016) Connectometry: A statistical approach harnessing the analytical potential of the local connectome. Neuroimage 125:162-171.

Yeh FC, Verstynen TD, Wang Y, Fernandez-Miranda JC, Tseng WY (2013) Deterministic diffusion fiber tracking improved by quantitative anisotropy. PLoS One 8:e80713.

Yeo BT, Krienen FM, Sepulcre J, Sabuncu MR, Lashkari D, Hollinshead M, Roffman JL, Smoller JW, Zöllei L, Polimeni JR (2011) The organization of the human cerebral cortex estimated by intrinsic functional connectivity. Journal of neurophysiology.

Yi LY, Liang X, Liu DM, Sun B, Ying S, Yang DB, Li QB, Jiang CL, Han Y (2015) Disrupted topological organization of resting-state functional brain network in subcortical vascular mild cognitive impairment. CNS Neurosci Ther 21:846-854.

Yu Y, Zhou X, Wang H, Hu X, Zhu X, Xu L, Zhang C, Sun Z (2015) Small-World Brain Network and Dynamic Functional Distribution in Patients with Subcortical Vascular Cognitive Impairment. PLoS One 10:e0131893.

Zerbi V, Grandjean J, Rudin M, Wenderoth N (2015) Mapping the mouse brain with rs-fMRI: An optimized pipeline for functional network identification. Neuroimage 123:11-21.

Zhang J, Aggarwal M, Mori S (2012) Structural insights into the rodent CNS via diffusion tensor imaging. Trends Neurosci 35:412-421.

Zheng L, Vinters HV, Mack WJ, Zarow C, Ellis WG, Chui HC (2013) Cerebral atherosclerosis is associated with cystic infarcts and microinfarcts but not Alzheimer pathologic changes. Stroke 44:2835-2841.

Zhou Y, Qun X, Qin LD, Qian LJ, Cao WW, Xu JR (2011) A primary study of diffusion tensor imaging-based histogram analysis in vascular cognitive impairment with no dementia. Clin Neurol Neurosurg 113:92-97.

Zhu Y, Bai L, Liang P, Kang S, Gao H, Yang H (2017) Disrupted brain connectivity networks in acute ischemic stroke patients. Brain Imaging Behav 11:444-453.

Zieren N, Duering M, Peters N, Reyes S, Jouvent E, Herve D, Gschwendtner A, Mewald Y, Opherk C, Chabriat H, Dichgans M (2013) Education modifies the relation of vascular pathology to cognitive function: cognitive reserve in cerebral autosomal dominant arteriopathy with subcortical infarcts and leukoencephalopathy. Neurobiol Aging 34:400-407.